A search for neutral high-mass Higgs bosons decaying into pairs of hadronically decaying tau leptons in 13 TeV collisions recorded by the ATLAS detector

Mark Andrew Pickering
Keble College, Oxford

Thesis submitted in fulfilment of the requirements
for the degree of Doctor of Philosophy at the University of Oxford

Hilary Term, 2016

A search for neutral high-mass Higgs bosons decaying into pairs of hadronically decaying tau leptons in 13 TeV collisions recorded by the ATLAS detector

Mark Andrew Pickering
Keble College, Oxford

Thesis submitted in fulfilment of the requirements
for the degree of Doctor of Philosophy at the University of Oxford.

Hilary Term, 2016

Abstract

This thesis outlines the search for neutral Higgs bosons in a mass range of $m_{H/A} = 200$ GeV $-$ 1.2 TeV, decaying to a pair of hadronically decaying tau leptons. The search is performed using $\sqrt{s} = 13$ TeV proton-proton collision data, corresponding to an integrated luminosity of 3.21 fb^{-1}, recorded by the ATLAS detector. No excess over the predicted Standard Model background is observed and upper limits are placed on the production cross section times branching fraction as a function of the mass of the scalar resonance. When combined with the results of the analysis where one of the tau leptons decays to either a muon or electron, the 95% confidence level upper limit on the cross section times branching fraction ranges from 1.4 pb at $m_{H/A} = 200$ GeV to 0.025 pb at $m_{H/A} = 1.2$ TeV for a scalar boson produced via gluon-gluon fusion, and 1.6 pb at $m_{H/A} = 200$ GeV to 0.028 pb at $m_{H/A} = 1.2$ TeV for a scalar boson produced via b-associated production. The results are interpreted in the Minimal Supersymmetric extension to the Standard Model (MSSM) as a limit on the value of tanβ, as a function of the mass of the neutral CP-odd MSSM Higgs boson. In the $m_h^{\text{mod+}}$ scenario, the 95% confidence level upper limit is tan$\beta < 7.6$ for $m_A = 200$ GeV, and tan$\beta < 47$ for $m_A = 1$ TeV. For the mass range $m_A > 500$ GeV, the upper limit on tanβ is improved in comparison to previous ATLAS searches.

I think I can safely say that nobody understands quantum mechanics.

- *Richard Feynman*

To my family.

Acknowledgements

I would like to extend a great thanks to the entire Oxford particle physics department that has made this work a success. Particular thanks go to the ATLAS academics and students, especially my supervisor Chris Hays. My appreciation extends to the collaborators and researchers I worked with at CERN, particularly those of the tau trigger working group, the tau working group, and those involved in the MSSM Higgs/$Z' \to \tau\tau$ analysis group, without whom the work in this thesis would not have been possible. This includes, but is certainly not limited to, Allison, Carl, Damian, Daniele, Dirk, Eric, Guillermo, Hao, Lei, Lorenz, Luca, Masahiro, Matthew, Nikos, Pedro, Quentin, Sinead, Takashi, Viviana, Zinonas and the indomitable POW (Pier-Olivier and Will).

This work would also not have been possible without those that have helped me maintain something resembling work-life balance during my DPhil. This was achieved through festivals, drinks, energetic debates, family gatherings and mountain-based activities, with friends I have made throughout my life, from Nottingham, London, Toronto, Chile, Oxford and Geneva. Beginning my work in particle physics with an excellent cohort of colleagues, Chris, Faye, Kathrin, Katharina, Lydia, Olli, Soof, Will^2 and many more, has given me the motivation to come to work each day, even if their lunching hour and grammar preferences are misguided (though helpful during thesis writing). Particular thanks go to Eluned, for reading theses and conference notes, listening to talks, and keeping me sane during the last two years.

There are a lot of people, too many to name, that have played a huge role in my education and development along this journey. This ranges from answering my silly questions to those who have directed the course of my work and education. Particular thanks in this regard goes to my family, Andrew, Sharon, Matthew and Helena, and relatives. Finally my work at CERN was made possible by STFC, the University of Oxford and the European and international collaboration that enables projects such as CERN to exist.

Contents

Preface 1

1 Introduction 5

2 Theoretical background 7
- 2.1 Standard Model Overview . . . 7
- 2.2 Standard Model Theory . . . 9
  - 2.2.1 Quantum electrodynamics . . . 10
  - 2.2.2 Electroweak physics . . . 11
  - 2.2.3 Quantum chromodynamics . . . 12
  - 2.2.4 The Higgs Mechanism . . . 13
  - 2.2.5 Fermion masses . . . 16
- 2.3 Supersymmetry . . . 17
  - 2.3.1 SUSY overview . . . 17
  - 2.3.2 SUSY motivation . . . 18
  - 2.3.3 The MSSM Higgs sector . . . 19
- 2.4 Experimental searches for MSSM Higgs bosons . . . 21

3 The ATLAS experiment 27
- 3.1 The ATLAS detector . . . 28
  - 3.1.1 Magnets . . . 30
  - 3.1.2 The inner detector . . . 31
  - 3.1.3 The Calorimeters . . . 33
  - 3.1.4 Muon Spectrometer . . . 36
  - 3.1.5 Trigger and data acquisition . . . 37
- 3.2 Object reconstruction and identification . . . 40
  - 3.2.1 Inner detector tracks . . . 41
  - 3.2.2 Electrons . . . 41
  - 3.2.3 Muons . . . 42
  - 3.2.4 Jets . . . 44
  - 3.2.5 *b*-jets . . . 44
  - 3.2.6 Overlap removal . . . 45
  - 3.2.7 Missing transverse momentum . . . 46
- 3.3 Data . . . 46
  - 3.3.1 Event cleaning . . . 47
- 3.4 ATLAS simulation . . . 48

4 The reconstruction and identification of hadronic tau decays 51
4.1 The reconstruction of tau candidates . . . 53
4.1.1 Formation of tau candidates . . . 53
4.1.2 Tau vertex . . . 53
4.1.3 Track association . . . 53
4.1.4 Reconstruction efficiency . . . 54
4.2 The energy calibration of tau candidates . . . 55
4.2.1 Tau energy scale calibration . . . 55
4.3 The identification of hadronic tau decays . . . 56
4.3.1 Variables used in the tau identification BDT . . . 57
4.3.2 Tau BDT score . . . 58
4.4 Tau discrimination against electrons . . . 60
4.5 High-p_{T} tau candidates . . . 62
4.5.1 Simulation and event selection . . . 63
4.5.2 Misidentification rate of tau particles . . . 68
4.5.3 High-p_{T} tau uncertainty inflation . . . 68

5 The Run-2 tau trigger system 73
5.1 Overview of the Run-2 tau trigger system . . . 74
5.1.1 L1 tau trigger . . . 75
5.1.2 HLT tau trigger . . . 75
5.1.3 Trigger strategy and nomenclature . . . 77
5.1.4 Preparation for Run-2 data-taking . . . 79
5.2 Early Run-2 commissioning of the tau trigger . . . 80
5.2.1 Tag and probe method . . . 81
5.2.2 $Z \rightarrow \tau_{\mu}\tau_{h}$ tag and probe . . . 82
5.2.3 $W(\rightarrow \mu\nu)$+jets tag and probe . . . 84
5.2.4 Early Run-2 trigger efficiency . . . 86
5.3 Measurement of the tau trigger efficiency . . . 89
5.3.1 Event selection . . . 90
5.3.2 Estimation of signal and background processes . . . 92
5.3.3 Signal region distributions . . . 95
5.3.4 Sources of systematic uncertainty . . . 96
5.3.5 Results . . . 98

6 The search for neutral high-mass Higgs bosons 101
6.1 Signal and background processes . . . 102
6.1.1 Signal processes . . . 102
6.1.2 Background processes . . . 103
6.2 Event selection . . . 107
6.2.1 Trigger . . . 107
6.2.2 Analysis selection . . . 108
6.2.3 Analysis validation and control regions . . . 109
6.2.4 Di-tau mass reconstruction . . . 113
6.3 Estimation of background processes . . . 115

6.3.1 Multi-jet estimation . . . 115
6.3.2 W + jets estimation . . . 120
6.3.3 Top background estimation . . . 125
6.3.4 Z+jets and diboson background estimation . . . 127
6.3.5 Validation of the background estimation in the SS validation region . . . 128
6.4 Results of the event selection and background estimation . . . 133
6.4.1 Kinematic distributions in the b-veto signal region . . . 133
6.4.2 Kinematic distributions in the b-tag signal region . . . 135
6.5 Sources of systematic uncertainty . . . 140
6.5.1 Luminosity . . . 140
6.5.2 Pile-up . . . 140
6.5.3 Multi-jet estimation via fake factors . . . 140
6.5.4 Jet $\rightarrow \tau$ fake rate . . . 143
6.5.5 W+jets reweighting . . . 143
6.5.6 Tau candidates . . . 143
6.5.7 Jet reconstruction . . . 143
6.5.8 Electron and muon candidates and $E_{\mathrm{T}}^{\mathrm{miss}}$ . . . 144
6.5.9 Cross section uncertainties for simulated backgrounds . . . 144
6.5.10 Top background modelling . . . 144
6.5.11 Signal modelling . . . 145
6.6 Statistical interpretation of the results . . . 147
6.6.1 Profile likelihood method . . . 148
6.6.2 Limit Setting . . . 149

7 Conclusions **155**

Appendix 157

A Simulated Samples **159**

B Misidentification rate of high-p_{T} tau candidates **165**

C Early Run-2 trigger monitoring **171**

D Extra SS control region validation figures **173**

E Extra signal region kinematic distributions **177**

F Distributions of the total transverse mass in the $A/H \rightarrow \tau_{\mathrm{lep}}\tau_{\mathrm{had}}$ analysis **181**

G Impact of systematic uncertainties on the signal strength **183**

H Updated Run-2 limits **187**

Bibliography **191**

Glossary

$E_{\mathrm{T}}^{\mathrm{miss}}$ Missing Transverse Momentum : the magnitude of the negative sum of the visible momenta of ATLAS objects in the plane transverse to the beamline.

1-prong : refers to tau particles which have decayed via a single charged hadron, and thus have a single charged track associated with their decay (also referred to as 1p).

2HDM : Two Higgs Doublet Model : a Higgs sector extension model in which an extra Higgs doublet is introduced.

3-prong : refers to tau particles which have decayed via three charged hadrons, and thus have three charged tracks associated with their decay (also referred to as 3p).

ATLAS A Toroidal LHC ApparatuS : a general purpose particle detector located at the LHC.

BDT Boosted Decision Tree : a method in machine learning in which a set of discriminating variables between signal and background processes is combined to produce a single discriminating variable, the BDT output.

BSM Beyond the Standard Model : theories of particle physics that postulate new particles and/or interactions, which can explain some of the deficiencies of the Standard Model.

CERN : The European Organization for Nuclear Research.

CMS Compact Muon Solenoid : a general purpose particle physics detector based at the LHC.

CP Charge-Parity : the combination of the symmetries of charge conjugation and parity.

CSC Cathode Strip Chamber : component of the MS used in the precision measurements of muon tracks.

CTP Central Trigger Processor : the final stage of the L1 trigger processing.

EM Electromagnetic.

EMCAL : Electromagnetic Calorimeter.

EOYE End Of Year Event : a public unveiling of results of the ATLAS and CMS experiments.

FTK Fast TracKer : a hardware based tracking system undergoing commissioning during 2016.

HCAL : Hadronic Calorimeter.

HLT High Level Trigger : the final stage of the ATLAS trigger. Events that pass HLT are recorded.

IBL Insertable B-Layer : an ATLAS pixel tracking system located closest to the beamline.

ID Identification : a requirement placed on objects measurement by the ATLAS detector using discriminating variables to computationally select a specific type of particle with a high efficiency and reject backgrounds to the particle with a large rejection rate. Various levels of identification are used, commonly referred to as *loose*, *medium* and *tight* depending on the identification efficiency.

IP Interaction Point : the central point of the ATLAS detector, where proton beams cross.

JER Jet Energy Resolution : the accuracy at which the energy of any given jet can be resolved.

JES Jet Energy Scale : a calibration applied to reconstructed jets in order to correct for detector effects.

JVF Jet Vertex Fraction : the proportion of momentum associated with jet tracks that comes from tracks associated with the PV.

L1 Level 1 : the first tier of the ATLAS trigger system, utilising calorimeter and MS information.

L1Topo L1 Topological : the processor converting L1 topological information into information for the CTP.

LAr : Liquid Argon Calorimeter.

LC Local Hadronic Calibration : a calorimeter calibration scheme for hadronic objects.

LEP : The Large Electron Positron collider.

LHC : The Large Hadron Collider.

LO Leading Order : a scattering calculation taking into account the lowest order Feynman diagram.

LS1 Long Shutdown 1 : an approximately 2 year hiatus of LHC collisions between February 2013 and April 2015, during which time a series of upgrades took place.

MDT Monitored Drift Tube : component of the MS used in the precision measurements of muon tracks.

MS Muon Spectrometer : the outer ATLAS tracking subsystem, optimised for the tracking of muons.

MSSM Minimal Supersymmetric extension of the Standard Model : a supersymmetric extension of the SM that includes a minimal number of new particles.

MUCTPI Muon to CTP Interface : the processor converting trigger level MS information into information for the CTP.

NLO Next-to-Leading Order : a scattering calculation taking into account the lowest and next to lowest order Feynman diagrams.

NNLO Next-to-Next-to-Leading Order : a scattering calculation taking into account the lowest and next to lowest, and next-to-next-to-lowest order Feynman diagrams.

offline : the algorithms and reconstruction of objects taking place after the data has been recorded.

online : referring to the trigger level algorithms and reconstruction of objects.

OS Opposite Sign : refers to scenarios in which the decay objects carry opposite sign charges.

PDF Parton Distribution Function : the momentum distribution functions of the partons inside the proton.

PU Pile-Up : the average number of proton-proton interactions per bunch crossing.

PV Primary Vertex : the identified position of the reconstructed vertex with the highest scalar-sum p_{T} of tracks.

QCD Quantum Chromodynamics : a quantum field theory describing the strong interaction.

QED Quantum Electrodynamics : a quantum field theory describing the electromagnetic interaction.

QFT Quantum Field Theory : a field theory that unifies the theories of quantum mechanics and special relativity.

ROD Readout Drivers : electronics taking information from the subdetectors for further processing.

RoI Region of Interest : an area of the ATLAS detector containing L1 reconstructed objects that pass the L1 trigger.

RPC Resistive-Plate Chamber : component of the MS used in the muon trigger.

Run-1 : The first phase of operation of the LHC with pp collisions at $\sqrt{s} = 7$ TeV between 2010 and 2011, and $\sqrt{s} = 8$ TeV in 2012.

Run-2 : The second phase of operation of the LHC with pp collisions at $\sqrt{s} = 13$ TeV. The first data recording period occurred between June 2015 and November 2015, and is the focus of this thesis.

SCT Semi-Conductor Tracker : one of the ATLAS tracking subsystems, consisting of silicon strip modules.

SM Standard Model : a quantum field theory describing the known matter particles and their interactions through the electroweak and strong forces.

SS Same Sign : refers to scenarios in which the decay objects carry the same sign charge.

STT Single Tau Trigger : the trigger system that records events passing the online algorithms related to the detection of a single tau object.

SUSY Supersymmetry : a candidate extension of the SM in which a new degree of symmetry between bosons and fermions is introduced.

SV Secondary Vertex : a vertex displaced from the beamline, potentially resulting from the in-flight decay of a particle.

T&P Tag and Probe : an analysis method often used in calibration and performance measurement. In a well understood SM decay to at least two objects, one of the objects is 'tagged', undergoing strict identification requirements, and the other object is 'probed' to investigate its properties further.

TDAQ Trigger and Data Acquisition.

TES Tau Energy Scale : a calibration applied to candidate taus in order to correct the energy deposition measured in the detector to the average value of the energy carried by the measured decay products.

TGC Thin-Gap Chamber : component of the MS used in the muon trigger.

TRT Transition Radiation Tracker : one of the ATLAS tracking subsystems, consisting of inert gas filled straw tubes.

TV Tau Vertex : the primary vertex candidate associated with the largest fraction of transverse momentum from tracks associated with a tau candidate.

Preface

The work presented in this thesis has been carried out in collaboration between the author and other members of the ATLAS experiment unless otherwise stated. The figures shown are produced by the author unless otherwise stated, and those that are publicly available are labelled **ATLAS**. Further information on the contributions of the author to the ATLAS experiment is given below.

Efficiency of the Fast TracKer system in tau trigger chains

The majority of the work conducted at the beginning of this DPhil involved the Fast TracKer (FTK) [1] upgrade to the tau trigger system. The FTK is a L1 hardware based tracking system designed to provide particle tracks as input variables to the HLT. This work involved designing potential trigger chains that involve the FTK for searches involving Higgs boson decays to tau particles, and testing the efficiency of such chains. The FTK was in the commissioning stage during 2016 and as such does not feature in the analysis central to this thesis.

xTau software framework development

In preparation for Run-2, a new analysis model and data format was developed in order to reduce resource use and storage space after the reconstruction of physics objects from the raw detector readout information. A combined framework, the ‘xTau framework’, was developed for the various analyses which contained tau leptons in the final state and the author assisted in the development of this framework from the very early stages.

The software framework takes the reconstructed object information and applies the various ATLAS object corrections, recommendations and analysis selections required to produce a data format ready at a plotting level. Key contributions came in the addition of trigger related variables, and role as the 'trigger contact', as well as leading the development of the channels used in the $A/H \to \tau_{\text{had}}\tau_{\text{had}}$ analysis, trigger efficiency measurement, and early Run-2 monitoring.

Preparation and monitoring of the Run-2 tau trigger system

During LS1 several improvements to the tau trigger algorithms were attempted and implemented. Extensive testing of the L1 tau trigger algorithms, in particular the L1Topo algorithms, was completed and the effect on the SM $H \to \tau\tau$ analysis studied. An emulation tool was also developed in order to independently check decisions made by the trigger software. This was integrated into the tau trigger monitoring software.

Tau trigger 'expert on-call' and trigger control room shifts were carried out during the 2015 preparations and data-taking. With a colleague, Takashi Mitani, the first public Run-2 ATLAS plots of the tau trigger HLT trigger chain variables were produced and subsequently presented during the summer conferences [2–5]. With the same colleague, the tau trigger efficiency performance measurement was made [6, 7].

High-p_{T} tau recommendations

The efficiency of the tau identification algorithm is measured in $Z \to \tau\tau$ events, however the measurement is constrained to 'low-p_{T}' tau candidates where $p_{\text{T}}^{\tau} < 100$ GeV. In order to test the identification algorithms in regimes where the hadronic tau has a higher transverse momentum, a tag and probe analysis was performed using dijet events to investigate the p_{T} dependence of the misidentification of jet objects as tau particles. The results of this analysis forms part of the recommended ATLAS tau object corrections to be applied when analysing simulated Run-2 data.

$A/H \rightarrow \tau_{\text{had}}\tau_{\text{had}}$ analysis

Two analyses were completed in the search for $A/H \rightarrow \tau_{\text{had}}\tau_{\text{had}}$ decays. The first was a b-jet-inclusive search conducted in time for the first unveiling of ATLAS Run-2 results and described in Ref. [8]. It was later presented at the LHCP conference [9]. The second analysis, documented in Ref. [10], has a further categorisation depending on the presence of b-jets and is described in this thesis. The analysis selection and framework, data set production, and background estimation techniques generally overlap with those used in the search for $Z' \rightarrow \tau_{\text{had}}\tau_{\text{had}}$, also documented in Ref. [10]. The $Z' \rightarrow \tau_{\text{had}}\tau_{\text{had}}$ analysis is not described in this thesis.

The author took part in all stages of the $A/H \rightarrow \tau_{\text{had}}\tau_{\text{had}}$ analysis from the analysis framework development to the cutflow and background estimation, with the exception of the W+jets reweighting and fake rate correction studies, Section 6.3.2, and the post-fit plot production and limit setting, Section 6.6. Systematic studies affecting the result were completed by the author, a collaborator, or a member of the relevant object working group. The list of contributors to the analysis can be found in Ref. [11].

Chapter 1

Introduction

J. J. Thomson's discovery of the electron in 1897 marked the first observation of what we now consider to be elementary particles, and in the 119 years that have followed, the work of tens of thousands of mathematicians, scientists and engineers has enabled us to add many more. Equally importantly, we have been able to develop theories of how these particles interact, allowing us to build models of the particle world. The direct work of particle physicists has enabled advances in fields as diverse as medicine, precision engineering and computing and led to technologies such as radiation therapy, crystallography and the world wide web, whilst the knowledge gained has made possible many more advancements that define the modern era.

The fundamental reason that particle physics is studied though, is in order to learn more about the universe we inhabit, and what drives most physicists is the quest to understand the laws that govern our existence. During the latter half of the 20^{th} century, most of our knowledge of particle physics was combined into a single theory, the Standard Model. Its success is demonstrated by the prediction of many particles and their properties, later confirmed through experiment. It was to this end that the Large Hadron Collider (LHC) was constructed, with one of its principle motivations being the search for the Higgs boson, the final unobserved particle predicted by the Standard Model. In 2012, after two years of analysing proton-proton collision data, the ATLAS and CMS detectors independently confirmed a first observation of the Higgs boson [12, 13].

We know that the Standard Model is not the end of the journey however. Many physics phenomena are not explained by the Standard Model, and many theories attempt to explain the physics that exists beyond the Standard Model. One such theory, Supersymmetry, explains some of the known issues of the Standard Model, and predicts many more particles and Higgs bosons, potentially accessible with the LHC. It is in the search for new physics that the LHC is currently engaged, and the search for additional Higgs bosons beyond the Standard Model forms the subject of this thesis.

This thesis begins by introducing the theoretical framework of the Standard Model in Chapter 2, and also gives an overview of Supersymmetry. The analysis presented in this thesis is specifically searching for neutral high-mass Higgs bosons decaying to pairs of hadronically decaying tau leptons in collisions recorded by the ATLAS detector. As such, the ATLAS detector, one of the main LHC experiments, is used in the collection of the data analysed in this thesis, and is described in Chapter 3. The success of searches and measurements is dependent on the efficient reconstruction of physics objects and the functioning of the data recording system, a role carried out by the trigger system. The reconstruction of the hadronic decays of tau leptons is described in Chapter 4, while the successful operation of the tau trigger system is described in Chapter 5. Finally, in Chapter 6, the analysis of data in the search for high-mass neutral Higgs bosons is presented, constituting an important component of the search for physics beyond the Standard Model.

Chapter 2

Theoretical background

This chapter discusses the theoretical background to the work in this thesis. First an overview of the Standard Model (SM), the underlying theoretical framework of particle physics, is given in Section 2.1. The theory itself is introduced in more detail in Section 2.2. Some of the issues with the SM are discussed in Section 2.3, where Supersymmetry (SUSY) is introduced as a candidate extension theory to the SM, with extra focus placed on the Minimal Supersymmetric extension to the Standard Model (MSSM) and its Higgs sector. An overview of experimental searches for high-mass MSSM Higgs bosons is given in Section 2.4.

2.1 Standard Model Overview

The Standard Model is a theory developed in the 1960s that describes the interactions of all known fundamental particles. It describes matter and the forces that govern the interactions of matter, in terms of particles. The particles contained in the SM are considered to be point-like, and can be classified into two types: bosons and fermions.

The fundamental bosons are particles which have an integer-valued intrinsic angular momentum, or spin, a conserved quantum property of all particles. The bosons can also be classified into the gauge boson force carriers, with a spin value of 1, and scalar bosons, of which the Higgs boson is the only one, with spin value 0. The gauge bosons are considered as

Particle type		Generation	Particle	Symbol	Charge	Mass [MeV]
Fermions	Quarks	1^{st}	up	u	$+\frac{2}{3}$	2.3
			down	d	$-\frac{1}{3}$	4.8
		2^{nd}	charm	c	$+\frac{2}{3}$	1.28×10^3
			strange	s	$-\frac{1}{3}$	95
		3^{rd}	top	t	$+\frac{2}{3}$	173.2×10^3
			bottom	b	$-\frac{1}{3}$	4.18×10^3
	Leptons	1^{st}	e neutrino	ν_e	0	-
			electron	e	-1	0.5110
		2^{nd}	μ neutrino	ν_μ	0	-
			muon	μ	-1	105.7
		3^{rd}	τ neutrino	ν_τ	0	-
			tau	τ	-1	1.777×10^3
Bosons	Gauge bosons		photon	γ	0	-
			Z boson	Z	0	90.19×10^3
			W boson	$W^\pm$	±1	80.38×10^3
			gluon	g	0	-
	Scalar bosons		Higgs boson	h	0	125.1×10^3

Table 2.1: The particles of the SM. Experimentally determined masses are shown for particles that are not assumed massless in the SM, and are taken from [14], with the exception of the Higgs boson mass, taken from [15].

force carrying particles, through which the fermions, and indeed the bosons themselves, may interact. The photon is responsible for the electromagnetic force, the W and Z bosons for the weak interaction and the gluon for the strong nuclear force. The Higgs boson meanwhile plays a role in how the other SM particles acquire mass, and is the final particle of the SM to have been discovered.

The fermions, on the other hand, have a half integer spin value, and can be classified into quarks and leptons by the types of interactions they undergo. The charged leptons are able to interact through the electromagnetic and weak forces while the uncharged leptons, known as neutrinos, interact through the weak force only. In addition to weak and electromagnetic interactions, the quarks interact through the strong force. The different types of quarks and leptons can be further paired into three generations of particles with the different pairs undergoing a common set of interactions. For each particle there exists an equal mass anti-particle with opposite sign internal quantum numbers.

Table 2.1 displays these classifications of particles in the Standard Model and the particle masses.

2.2 Standard Model Theory

The Standard Model is a quantum field theory (QFT), formed from the unification of special relativity and quantum mechanics. The theory mathematically describes the interactions of particles as interactions between fields.

The dynamics of the fields in the SM are described best using the Lagrangian formalism. The SM Lagrangian (more specifically Lagrangian density) can be split into the separate components:

$$\mathcal{L}_{\text{SM}} = \mathcal{L}_{\text{EWK}} + \mathcal{L}_{\text{QCD}} + \mathcal{L}_{\text{Higgs}} + \mathcal{L}_{\text{Yukawa}}, \tag{2.1}$$

where $\mathcal{L}_{\text{EWK}}$ describes the dynamics of the electroweak force, $\mathcal{L}_{\text{QCD}}$ describes the dynamics of the strong force, and $\mathcal{L}_{\text{Higgs}}$ and $\mathcal{L}_{\text{Yukawa}}$ describe the introduction of mass to the gauge bosons and fermions respectively.

The SM is based on an $SU(3) \times SU(2) \times U(1)$ gauge group, where $U(N)$ refers to a group of $N \times N$ unitary matrices, and $SU(N)$ is the subset with determinant equal to 1. Symmetries under transformations of the gauge groups results in the conservation of charges. The $SU(3)$ group describes the strong force, while the $SU(2) \times U(1)$ group describes the unified electromagnetic and weak interactions, referred to as the electroweak force.

This section gives an overview of the terms that make up the SM Lagrangian, after first giving an example of how a gauge theory can be constructed from the requirement of gauge invariance.

2.2.1 Quantum electrodynamics

The theory of quantum electrodynamics (QED) provides an simple example of how a gauge theory can be constructed through the requirement of gauge invariance under a $U(1)$ transformation. The Lagrangian of a fermion field, $\psi(x)$, is given by the Dirac Lagrangian:

$$\mathcal{L}_{\text{Dirac}} = i\bar{\psi}(x)\gamma^{\mu}\partial_{\mu}\psi(x) - m\bar{\psi}(x)\psi(x), \tag{2.2}$$

where γ^{μ} refers to the gamma matrices, m the fermion mass and ∂_{μ} the partial derivative 4-vector. Under a global gauge transformation through the introduction of a phase shift $\psi \to e^{-i\alpha}\psi$, the Lagrangian is invariant.

If however, the phase shift contains a local, positional dependence, $\alpha(x)$, then the invariance is broken, as shown by the result:

$$\mathcal{L}'_{\text{Dirac}} = i\bar{\psi}(x)\gamma^{\mu}\partial_{\mu}\psi(x) - i\bar{\psi}(x)\gamma^{\mu}\psi(x)\partial_{\mu}\alpha(x) - m\bar{\psi}(x)\psi(x). \tag{2.3}$$

In order to recover invariance under the local gauge transformation, a new gauge field, A_{μ}, is introduced, and the derivative ∂_{μ} is replaced by the covariant derivative D_{μ}:

$$\partial_{\mu} \to D_{\mu} = \partial_{\mu} + ieA_{\mu}, \tag{2.4}$$

where e is a constant. The A_{μ} field transforms as:

$$A_{\mu} \to A_{\mu} - \frac{1}{e}\partial_{\mu}\alpha(x), \tag{2.5}$$

under local gauge transformations.

In QED, the gauge field A_{μ} is interpreted as the electromagnetic field, and the massless free field introduces the extra term:

$$-\frac{1}{4}F_{\mu\nu}F^{\mu\nu}, \tag{2.6}$$

and so completes the QED Lagrangian:

$$\mathcal{L}_{\text{QED}} = i\bar{\psi}(x)\gamma^{\mu}D_{\mu}\psi(x) - m\bar{\psi}(x)\psi(x) - \frac{1}{4}F_{\mu\nu}F^{\mu\nu}, \tag{2.7}$$

where $F_{\mu\nu}$ is the electromagnetic field tensor, $F_{\mu\nu} = \partial_\mu A_\nu - \partial_\nu A_\mu$. The constant e is the coupling strength between the two fields. The QED Lagrangian is invariant under local $U(1)$ transformations, and can be used to derive Maxwell's equations.

2.2.2 Electroweak physics

The electromagnetic and weak interactions are unified in the SM, and the Lagrangian is invariant under $SU(2) \times U(1)$ gauge transformations. It is observed that only left-handed fermions participate in weak interactions, and assumed in the Standard Model that the neutrino only exists in the left-handed state. The lepton fields are therefore grouped into three generations of isospin doublets ($T_3 = \pm\frac{1}{2}$ for the upper and lower members) in the left-handed case, χ_L, whilst right-handed leptons are represented by isospin singlets ($T_3 = 0$), χ_R. The quark fields are similarly grouped into three generations of left-handed doublets and right-handed singlets.

The electroweak Lagrangian is given by:

$$\mathcal{L}_{\text{EWK}} = \bar{\chi}_L \gamma^\mu D^L_\mu \chi_L + \bar{\chi}_R \gamma^\mu D^R_\mu \chi_R - \frac{1}{4}\vec{W}_{\mu\nu}\vec{W}^{\mu\nu} - \frac{1}{4}B_{\mu\nu}B^{\mu\nu}. \tag{2.8}$$

The first two terms describe the interaction of the left- and right-handed fermion fields with the gauge boson fields. The covariant derivatives used to recover the invariance of the Lagrangian under local gauge transformations are given by:

$$\begin{aligned} D^L_\mu &= i\partial_\mu - \frac{g}{2}\vec{\sigma}\cdot\vec{W}_\mu - \frac{g'}{2}YB_\mu, \\ D^R_\mu &= i\partial_\mu - \frac{g'}{2}YB_\mu. \end{aligned} \tag{2.9}$$

The four gauge fields introduced are denoted by $\vec{W}^{\mu\nu}$ (W^i_μ, $i = 1,\ 2,\ 3$) and $B_{\mu\nu}$, with the couplings to the fermion fields related to g and g'. The group generator of $SU(2)$ is the weak isospin operator, formed from the Pauli matrices, $\vec{\sigma}$. The Pauli matrices are non-commuting, and so result in a non-abelian gauge theory. In the $U(1)$ group transformations meanwhile, weak hypercharge, $Y = 2Q - 2T_3$, where Q is the electric charge, is conserved.

The final two terms are the Lagrangians of the free vector boson fields, under the assumption that the gauge bosons are massless, and describe the self-interactions of the bosons. The field strength tensors are defined by:

$$\begin{aligned} \vec{W}_{\mu\nu} &= \partial_\mu \vec{W}_\nu - \partial_\nu \vec{W}_\mu - g\vec{W}_\nu \times \vec{W}_\mu, \\ B_{\mu\nu} &= \partial_\mu B_\nu - \partial_\nu B_\mu. \end{aligned} \tag{2.10}$$

The $\vec{W}^i_\mu$ and B_μ fields can be written in terms of the $W^\pm_\mu$, Z_μ, and A_μ fields, whose quantised oscillations correspond to the physical gauge bosons:

$$\begin{aligned} W^1_\mu &= \frac{1}{\sqrt{2}}(W^+_\mu + W^-_\mu), \\ W^2_\mu &= \frac{i}{\sqrt{2}}(W^-_\mu - W^+_\mu), \\ W^3_\mu &= \cos\theta_W Z_\mu + \sin\theta_W A_\mu, \\ B_\mu &= -\sin\theta_W Z_\mu + \cos\theta_W A_\mu, \end{aligned} \tag{2.11}$$

where θ_W is the weak mixing angle:

$$\tan(\theta_W) = \frac{g'}{g}. \tag{2.12}$$

2.2.3 Quantum chromodynamics

Quantum chromodynamics (QCD) governs the interaction of particles through the strong force. The Lagrangian of QCD is given by:

$$\mathcal{L}_{\text{QCD}} = \bar{\psi}(i\gamma^\mu D_\mu - m)\psi - \frac{1}{4}G^a_{\mu\nu}G^{\mu\nu,a}, \tag{2.13}$$

where, in similarity to the QED case, the covariant derivative is:

$$D_\mu = \partial_\mu + ig_s T^a G^a_\mu, \tag{2.14}$$

and the field strength tensor is:

$$G^a_{\mu\nu} = \partial_\mu G^a_\nu - \partial_\nu G^a_\mu - g_s f^{abc} G^b_\mu G^c_\mu. \tag{2.15}$$

The gauge group is $SU(3)$ and there are correspondingly eight generators, $T^a = \lambda^a/2$ (where λ^a refer to the Gell-Mann matrices), and eight gluons of varying "colour charge". The quarks are the only fermions to interact through the strong force, and the corresponding fields are denoted by ψ. The quarks also come in various colours forming a triplet, and are referred to as R (red), G (green) and B (blue). The coupling strength between the quark and gluon fields is given by g_s.

The self-interaction of the gluons is embodied mathematically in the final term of Equation (2.15), where f^{abc} are structure constants, and are antisymmetric in the three indices. As different gluons contain different colour charges, the theory is non-abelian, and the order of interaction is important. The self-interaction results in confinement of the particles into colour singlet states, such that free quarks and gluons are not observed.

2.2.4 The Higgs Mechanism

The invariance of the electroweak Lagrangian under local gauge transformations in Section 2.2.2 is based on the assumption that the gauge bosons $W^{\pm}, Z$, and γ are massless. Massive bosons would introduce extra terms into the Lagrangian of the form $m_V^2 V_\mu V^\nu$ (where V_μ is the vector field) and so break the gauge invariance. As seen in Table 2.1 the $W^{\pm}$ and Z bosons are observed to have mass and so the theory is not complete.

Particle masses enter the SM through the process of spontaneous symmetry breaking. As with the QED example, the principles of spontaneous symmetry breaking can be introduced under a $U(1)$ gauge transformation. Taking a complex scalar field:

$$\phi = \frac{1}{\sqrt{2}}(\phi_1 + i\phi_2) \tag{2.16}$$

and the Lagrangian:

$$\begin{aligned} \mathcal{L} &= (\partial_\mu \phi)^\dagger (\partial^\mu \phi) - V(\phi), \\ V(\phi) &= \mu^2(\phi^\dagger \phi) + \lambda(\phi^\dagger \phi)^2, \end{aligned} \tag{2.17}$$

we observe invariance under global gauge transformations of the form $\phi \rightarrow e^{i\alpha}\phi$. The second

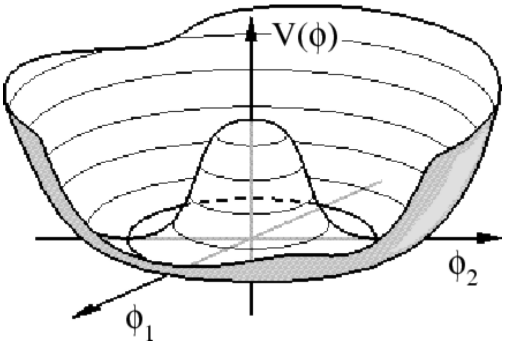

Figure 2.1: Visualisation of the potential described in Equation (2.17). Taken from [16].

term in the Lagrangian can be taken as a potential, as visualised in Figure 2.1, and has a non-zero ground state when $\mu^2 < 0$, $\lambda > 0$. The minimum of the field is given by:

$$\phi^\dagger \phi|_{min} = \frac{1}{2}(\phi_1^2 + \phi_2^2)|_{min} = \frac{-\mu^2}{2\lambda} \equiv \frac{v^2}{2}, \tag{2.18}$$

which forms a circle of minima around the origin in the $\phi_1 - \phi_2$ plane, with an infinite number of states. In the process of spontaneous symmetry breaking, the gauge invariance is broken by the selection of a solution to the minimum, which we choose as $\phi_1 = \frac{v}{\sqrt{2}}, \phi_2 = 0$. The scalar field can be redefined in terms of two new fields, ξ and η, as an excitation around the vacuum state:

$$\phi = \frac{1}{\sqrt{2}}(v + \xi + i\eta). \tag{2.19}$$

When substituted back into Equation (2.17), the Lagrangian contains the term $\mu^2\xi^2$, and so denotes a mass term for the scalar field, ξ, $m_\xi = \sqrt{-2\mu^2}$. The η field does not contain a similar term in the Lagrangian and so corresponds to a massless scalar field. According to Goldstone's theorem, each broken generator of a symmetry group results in a massless spin-0 particle, or 'Goldstone boson'. The massless field describes excitations along the direction of constant potential about the minimum (i.e. along the circle of minima in Figure 2.1).

Particle masses in the Standard Model enter via the Higgs mechanism, where we introduce a Lagrangian with gauge invariance under $SU(2) \times U(1)$ transformations, which can be spontaneously broken, producing Goldstone fields as above. A scalar 'Higgs' field, Φ, able to interact with the electroweak gauge boson fields, is introduced and comprises of an $SU(2)$

complex doublet of scalar fields, ϕ, as defined by:

$$\Phi = \begin{pmatrix} \phi^+ \\ \phi^0 \end{pmatrix} = \frac{1}{\sqrt{2}} \begin{pmatrix} \phi_1 + i\phi_2 \\ \phi_3 + i\phi_4 \end{pmatrix}. \tag{2.20}$$

The Lagrangian is given by:

$$\mathcal{L}_{\text{Higgs}} = (D_\mu \Phi)^\dagger (D^\mu \Phi) - \mu^2 (\Phi^\dagger \Phi) - \lambda (\Phi^\dagger \Phi)^2, \tag{2.21}$$

with the covariant derivative defined as:

$$D_\mu = \partial_\mu + \frac{ig}{2} \vec{\sigma} \cdot \vec{W}_\mu + \frac{ig'}{2} Y B_\mu \tag{2.22}$$

where the doublet has weak hypercharge $Y = 1$. The first term of the Lagrangian contains the interactions of the Higgs field and the electroweak gauge fields. As in the previous example, the final two terms of the Lagrangian form a scalar potential with parameters $\mu^2 < 0$ and $\lambda > 0$. The minima of the potential are determined by the equation

$$\Phi^\dagger \Phi|_{min} = \frac{1}{2}(\phi_1^2 + \phi_2^2 + \phi_3^2 + \phi_4^2)|_{min} = \frac{-\mu^2}{2\lambda}. \tag{2.23}$$

In the process of spontaneous symmetry breaking, we choose to set the direction of the minimum (or 'vacuum expectation value') such that three components of Φ (ϕ_1, ϕ_2, ϕ_4) are zero, such that the vacuum expectation value in the remaining component, ϕ_3, is given by:

$$\phi_3 = \sqrt{\frac{-\mu^2}{\lambda}} = v. \tag{2.24}$$

The symmetry of $SU(2)$ is broken, resulting in three Goldstone bosons. This enables us to rewrite the Higgs field as:

$$\Phi = \frac{1}{\sqrt{2}} \begin{pmatrix} 0 \\ v + h \end{pmatrix}, \tag{2.25}$$

in a gauge defined as the unitary gauge, with h a scalar field oscillating about the vacuum perpendicular to the direction of constant potential. Under local $SU(2)$ transformations, the massless fields can be 'gauged away' and absorbed by the $W^\pm$ and Z fields, leading them to acquire mass terms.

With the substitution of Equation (2.25) into the Higgs Lagrangian in Equation (2.21), the Lagrangian can be rewritten:

$$\begin{aligned}\mathcal{L}_{\text{Higgs}} = &\frac{1}{2}\partial_\mu h \partial^\mu h + \mu^2 h^2 + \frac{\lambda}{4}h^4 + \lambda v h^3 \\ &+ \frac{g^2}{4}(v+h)^2 W^+_\mu W^{-\mu} + \frac{1}{8}(g^2+g'^2)(v+h)^2 Z_\mu Z^\mu,\end{aligned} \tag{2.26}$$

where we have also utilised Equation (2.11) and Equation (2.12). From this we can identify the masses of the $W^\pm$ and Z bosons (the photon does not pick up a mass term as the $U(1)$ symmetry is unbroken), as well as the Higgs boson:

$$\begin{aligned} M_W &= \frac{1}{2}gv, \\ M_Z &= \frac{v}{2}\sqrt{g^2+g'^2} = \frac{M_W}{\cos\theta_W}, \\ M_h &= \sqrt{2}|\mu| = v\sqrt{2\lambda}. \end{aligned} \tag{2.27}$$

The remaining terms in Equation (2.26) relate to the interactions between the $W^\pm$, Z, and h bosons. It is important to note that the Higgs mass is not predicted by the theory.

2.2.5 Fermion masses

In the electroweak Lagrangian the inclusion of fermion masses would break the gauge symmetry due to the different transformation properties of the left- and right-handed fields. Assuming massless neutrinos, the observation of charged lepton masses is instead accounted for by an extra term in the SM Lagrangian:

$$\mathcal{L}^l_{\text{Yukawa}} = -g_l(\bar{\chi}_L \Phi \chi_R + \bar{\chi}_R \Phi^\dagger \chi_L), \tag{2.28}$$

where g_l is the Yukawa coupling, and the fields are as defined previously. Substituting in the Higgs field using Equation (2.25), the Lagrangian is rewritten:

$$\mathcal{L}^l_{\text{Yukawa}} = -\frac{g_l}{\sqrt{2}}(h+v)\bar{\chi}\chi. \tag{2.29}$$

The masses of the leptons are read off as $m_l = \frac{g_l v}{\sqrt{2}}$, whilst the coupling to the Higgs field is proportional to the lepton mass $\frac{g_l}{\sqrt{2}} = \frac{m_l}{v}$. The quark masses can be obtained in a similar manner, with a corresponding Lagrangian, $\mathcal{L}^q_{\text{Yukawa}}$, resulting in masses of the form $m_q = \frac{g_q v}{\sqrt{2}}$. The Higgs interaction mass eigenstates of the quarks are however not flavour eigenstates, and are instead related by the CKM (Cabbibo-Kobayashi-Maskawa) matrix, resulting in the mixing of quark generations during weak interactions.

2.3 Supersymmetry

The Standard Model is by no means a final theory of physics. For example, there is no SM explanation for gravity or the observations of dark matter and neutrino masses (though it can be modified to accommodate neutrino masses), and it provides no explanation as to why we observe the universe to be matter-dominated. Additionally, the SM requires the input of 19 parameters, constrained by experiment, and the generational grouping of the fermions over a mass range of several orders of magnitude appears arbitrary. This has motivated the search for theories beyond the Standard Model (BSM) that seek to incorporate these phenomena.

Supersymmetry (SUSY) is a proposed candidate extension to the SM. This section gives an overview of the phenomenology and motivation of SUSY [17].

2.3.1 SUSY overview

In the supersymmetric SM the number of particles is extended by introducing a symmetry between fermions and bosons such that for each fermion chirality, there is a corresponding 'superpartner' spin-0 particle, and for each boson there is corresponding spin-$\frac{1}{2}$ superpartner. In the common nomenclature of SUSY, the fermion scalar partners are referred to as 'sfermions', with prefix 's' (e.g. sleptons and squarks), whilst the boson superpartners or 'gauginos' contain the suffix '-ino' (e.g. gluinos). The binos and the winos (superpartners of the electroweak bosons) together mix with the Higgsinos to form four neutral fermions, the neutralinos, $\tilde{\chi}$, and four charged fermions, the charginos, $\tilde{\chi}^{\pm}$. A tilde over the particle symbols denotes the supersymmetric partner particles.

Whilst the particles of the SM contain supersymmetric partners, the symmetry is inexact. From experiment, it is observed that, in general, the masses of the superpartners must be higher than those of the SM particles, and there are various proposed models for the symmetry breaking. In the context of this thesis, only the Minimal Supersymmetric extension to the Standard Model (MSSM) is considered. The MSSM is a subset of SUSY models that introduces the minimal number of possible interactions and particles, and is considered the simplest SUSY extension to the SM.

2.3.2 SUSY motivation

Supersymmetry provides a natural extension to the Standard Model that resolves some of its problems.

One of these issues is referred to as the hierarchy problem. Quantum corrections from fermion loops such as the one shown in Figure 2.2 alter the Higgs mass. In the SM, the divergences that result from loop corrections can be absorbed into the measurable SM parameters in the process of renormalisation. Calculating the corrections to the Higgs mass up to a cut-off scale, Λ, which in the absence of new physics is the Planck scale, results in extremely large mass corrections, far beyond the observed Higgs mass, so that fine tuning is required to obtain the value of the Lagrangian parameter that cancels the corrections. In an exact SUSY theory, the loop contribution from the supersymmetric fermion partner, also shown in Figure 2.2, cancels the fermion contribution exactly, and in an inexact theory the 'fine-tuning' of parameters to reconcile the two masses is significantly reduced.

Supersymmetry also provides candidate dark matter particles. The MSSM conserves a quantity known as 'R-parity', which constrains the decay rate of the proton in SUSY models. R-parity is defined as:

$$P_R = (-1)^{3(B-L)+2s}, \tag{2.30}$$

where B is the baryon number, L the lepton number, and s the particle spin, and has a

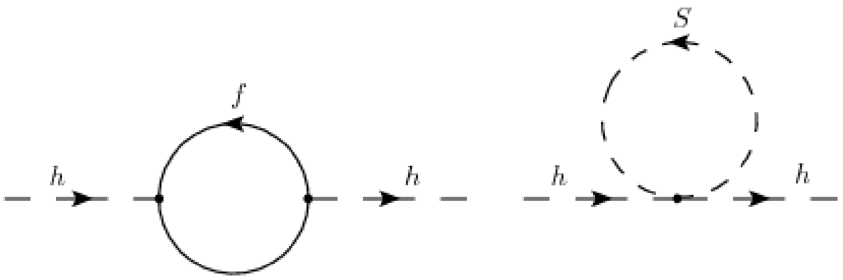

Figure 2.2: Quantum loop corrections to the Higgs mass from (left) fermions and (right) supersymmetric fermion partners. Taken from [18].

value of +1 for particles and −1 for sparticles. The conservation of R-parity means that the lightest SUSY particle must be stable, since in cannot decay solely to SM particles, and could be a candidate dark matter particle.

2.3.3 The MSSM Higgs sector

The Higgs sector of the MSSM is described by a two Higgs doublet model (2HDM). The 2HDM is type-II, meaning that one of the doublets, $h_u = (h_u^+, h_u^0)$, couples with and gives mass to the up-type quarks (i.e. u, c, t), and the other, $h_d = (h_d^0, h_d^-)$, couples to the down-type quarks (i.e d, s, b) and the charged leptons.

The Higgs potential in the model is given by [17]:

$$\begin{aligned} V = {} & (|\mu|^2 + m_{h_u}^2)(|h_u^0|^2 + |h_u^+|^2) + (|\mu|^2 + m_{h_d}^2)(|h_d^0|^2 + |h_d^-|^2) \\ & + [b(h_u^+ h_d^- - h_u^0 h_d^0) + h.c.] \\ & + \frac{1}{8}(g^2 + g'^2)(|h_u^0|^2 + |h_u^+|^2 - |h_d^0|^2 - |h_d^-|^2)^2 + \frac{1}{2}g^2 |h_u^+ h_d^{0*} + h_u^0 h_d^{-*}|^2, \end{aligned} \tag{2.31}$$

where m_{h_u}, m_{h_d} and b are SUSY breaking contributions to the Higgs potential, and $h.c.$ refers to the hermitian conjugate of the term. In order for the potential to have a stable minimum, the parameters are bound by the conditions:

$$\begin{aligned} & 2b < 2|\mu|^2 + m_{h_u}^2 + m_{h_d}^2, \\ & b^2 > (|\mu|^2 + m_{h_u}^2)(|\mu|^2 + m_{h_d}^2). \end{aligned} \tag{2.32}$$

As in the SM case, the two Higgs fields acquire vacuum expectation values, which are selected as v_u and v_d for the h_u^0 and h_d^0 components, respectively. The values are related to each other by the parameter tanβ:

$$\begin{aligned} \tan\beta &= \frac{v_u}{v_d}, \\ v^2 &= v_u^2 + v_d^2, \end{aligned} \tag{2.33}$$

where v is the SM vacuum expectation value. The Higgs doublets have four degrees of freedom each, and in the process of spontaneous symmetry breaking three of these are absorbed in the form of the Goldstone bosons (with fields G^0 and $G^{\pm}$) into the gauge boson masses, resulting in five physical Higgs bosons.

Assuming the conservation of CP-symmetry[1], two of the Higgs bosons are neutral and CP-even, h and H (with the lighter boson conventionally taken as h), one is neutral and CP-odd, A, and two are charged, $H^{\pm}$. At tree level and with the potential minimised, the fields of the physical Higgs and Goldstone bosons can be related to the Higgs doublets by [17]:

$$\begin{gathered} \begin{pmatrix} H_u^0 \\ H_d^0 \end{pmatrix} = \begin{pmatrix} v_u \\ v_d \end{pmatrix} + \frac{1}{\sqrt{2}} \begin{pmatrix} \cos\alpha & \sin\alpha \\ -\sin\alpha & \cos\alpha \end{pmatrix} \begin{pmatrix} h \\ H \end{pmatrix} + \frac{i}{\sqrt{2}} \begin{pmatrix} \sin\beta & \cos\beta \\ -\cos\beta & \sin\beta \end{pmatrix} \begin{pmatrix} G^0 \\ A \end{pmatrix}, \\ \begin{pmatrix} H_u^+ \\ H_d^{-*} \end{pmatrix} = \begin{pmatrix} \sin\beta & \cos\beta \\ -\cos\beta & \sin\beta \end{pmatrix} \begin{pmatrix} G^+ \\ H^+ \end{pmatrix}, \end{gathered} \tag{2.34}$$

with $G = G^{+*}$, $H^- = H^{+*}$ and mixing angle α, and the masses of the Higgs bosons are related through:

$$\begin{aligned} m_{H^\pm}^2 &= m_A^2 + m_W^2, \\ m_{h,H}^2 &= \frac{1}{2}\left(m_A^2 + m_Z^2 \mp \sqrt{(m_A^2 - m_Z^2)^2 + 4m_Z^2 m_A^2 \sin^2(2\beta)}\ \right), \\ m_A^2 &= \frac{2b}{\sin(2\beta)}. \end{aligned} \tag{2.35}$$

The MSSM Higgs sector can therefore be described in terms of two extra parameters compared to the SM. For high values of m_A ($m_A >> m_Z$), the masses of four of the Higgs

---

[1] The parity operator '$\hat{P}$' inverts positions about an axis, i.e. P L(x,t) = L(-x,t). The charge-conjugation operator '$\hat{C}$' takes a charge to an anticharge. The Lagrangian is CP-symmetric if $\hat{CP}$ L = L

bosons, A, H and $H^{\pm}$, are nearly degenerate. There is a limit on the mass of the lightest neutral Higgs boson of $m_h < m_Z$, however radiative corrections, particularly from the quantum loops of top quarks and their superpartners, modify the observed mass such that $m_h \lesssim 135$ GeV. In many models this lightest neutral Higgs is taken to be the recently observed Higgs boson.

In comparison with the mass terms given in Sections 2.2.4 and 2.2.5, the mass terms of the gauge bosons and fermions are given by:

$$\begin{gathered} M_W = \frac{1}{2} g \sqrt{v_u^2 + v_d^2}, \quad M_Z = \frac{1}{2} \sqrt{(g^2 + g'^2)(v_u^2 + v_d^2)} \\ m_u = \frac{g_u v_u}{\sqrt{2}}, \quad m_d = \frac{g_d v_d}{\sqrt{2}}, \quad m_l = \frac{g_l v_d}{\sqrt{2}}. \end{gathered} \tag{2.36}$$

where g_u, g_d and g_l are the Yukawa couplings for the up- and down-type quarks, and the charged leptons, respectively. For larger values of tanβ there is an increased coupling of the Higgs field to the down-type quarks and leptons.

2.4 Experimental searches for MSSM Higgs bosons

No supersymmetric particles have been observed so far using the ATLAS or CMS detectors [19, 20], and limits are placed on the parameter space. As there are many models of supersymmetric physics, benchmark scenarios which constrain some of the parameters are used to interpret and compare experimental results from direct searches. The two extra parameters used to describe the MSSM Higgs sector are conventionally chosen as tanβ and m_A.

As mentioned in Section 2.3.3, the mass of the lightest Higgs boson is modified by radiative corrections, and the correction is particularly dependent on the contributions from the top quarks and the stop squarks, the scalar partners to the top quark. The stop mixing parameter, which defines the relative contribution of left- and right-handed stops to the stop mass eigenstates and affects the predicted Higgs boson mass, can be chosen such that the mass of the lightest Higgs boson is maximised, and this benchmark scenario is referred

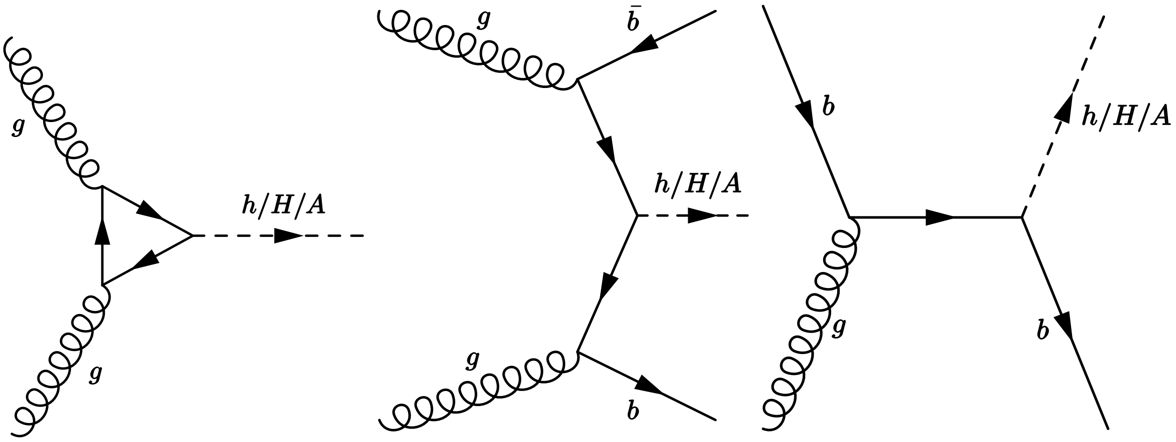

(a) Gluon fusion production (b) b-associated production (four-flavour scheme) (c) b-associated production (five-flavour scheme)

Figure 2.3: Leading order Feynman diagrams for the production of neutral high-mass Higgs bosons at the LHC. Taken from [10].

to as m_h^{max} [21]. In a similar scenario, the stop mixing parameter is modified so that the mass of the lightest MSSM Higgs boson is consistent with the recently observed 125 GeV Higgs boson, and is referred to as the modified m_h^{max} scenario, or $m_h^{\text{mod+}}$ [22]. An alternative method is employed in the hMSSM scenario [23], where the properties of the lightest Higgs are chosen to be those of the observed Higgs boson, and the mass is used to set the dominant radiative corrections.

Feynman diagrams for neutral high-mass Higgs boson production at the LHC are shown in Figure 2.3. As the gluon does not couple directly to the Higgs boson, the production occurs via a quark loop, particularly the loop involving top quarks as a result of their large Yukawa coupling. The coupling to down-type fermions such as b-quarks and tau leptons is enhanced in comparison to SM Higgs bosons, particularly at high tanβ values. As such, the cross section of the b-associated production mechanism, where the Higgs boson is produced in association with b-quarks, becomes increasingly dominant at high values of tanβ. Figure 2.4 shows the production cross sections of the MSSM Higgs bosons in the $m_h^{\text{mod+}}$ scenario as a function of the mass of the boson during for $\sqrt{s} = 8$ TeV proton-proton collisions at the LHC.

Various final states can be used in the search for MSSM Higgs bosons and the branching ratio as a function of the mass of the CP-odd Higgs boson, A, is shown in figure 2.5 for the

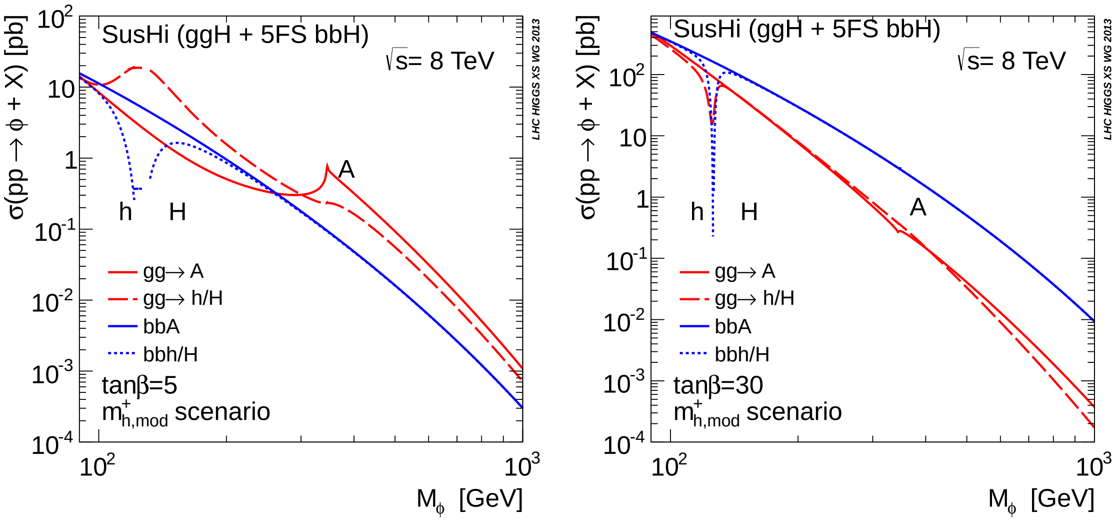

Figure 2.4: Production cross sections for neutral MSSM Higgs bosons in the $m_h^{\text{mod}+}$ scenario for tanβ =5 (left) and tanβ = 30 (right), as a function of the mass of the scalar boson. Taken from [24].

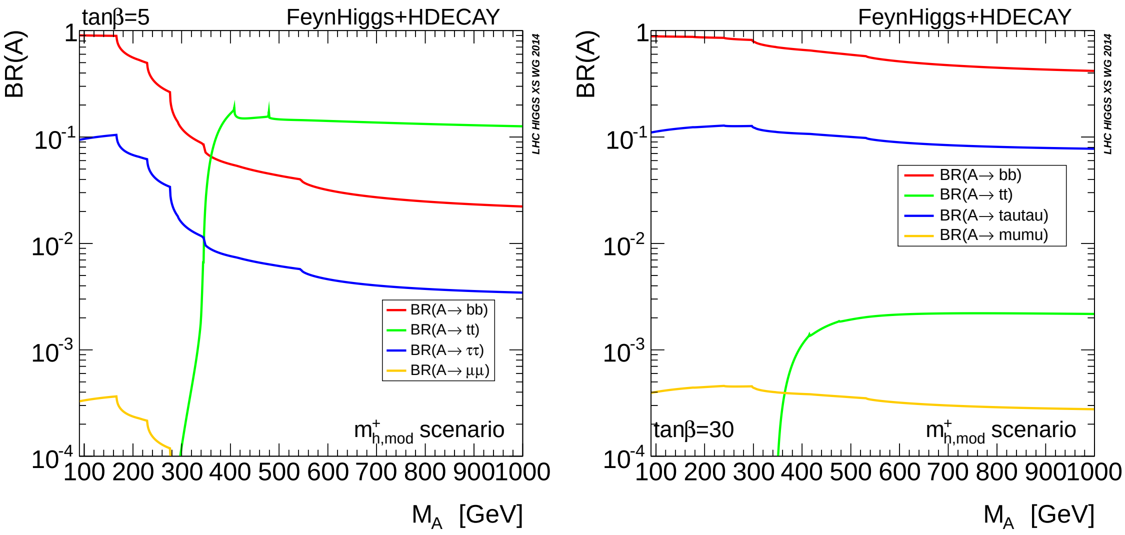

Figure 2.5: Branching ratios for the CP-odd MSSM Neutral Higgs boson, A, in the $m_h^{\text{mod}+}$ scenario for tanβ =5 (left) and tanβ = 30 (right), as a function of the mass of the boson, m_A. Taken from [24].

$m_h^{\text{mod}+}$ scenario. At high tanβ, the coupling of heavy Higgs bosons to down-type quarks and charged leptons is enhanced. As the coupling is dependent also on the mass of the particle, final states containing b-quarks and tau leptons are favoured as search channels, with the tau lepton final state particularly sensitive due to a lower contribution from background QCD processes mimicking the final state.

The LEP [25], Tevatron [26] and LHC [27] collider experiments have all placed limits on the production of neutral heavy resonances decaying to b-quarks and tau lepton final states, and the results have been interpreted in the $m_A - \tan\beta$ MSSM plane, with no excesses observed above the SM prediction [28–34]. The results of searches for neutral high-mass Higgs bosons decaying to tau lepton pairs using the ATLAS [35] and CMS [36] detectors are shown in the $m_h^{\text{mod+}}$ scenario in Figure 2.6, for data collected prior to this thesis. In the case of the ATLAS search, performed using $\sqrt{s} = 8$ TeV proton-proton collision data, corresponding to an integrated luminosity of 19.5-20.3 fb^{-1} (depending on the subsequent tau lepton decay channels), a 95% confidence level upper limit is set of $\tan\beta \lesssim 7.5$ for $m_A = 200$ GeV, and $\tan\beta \lesssim 59$ for $m_A = 1$ TeV.

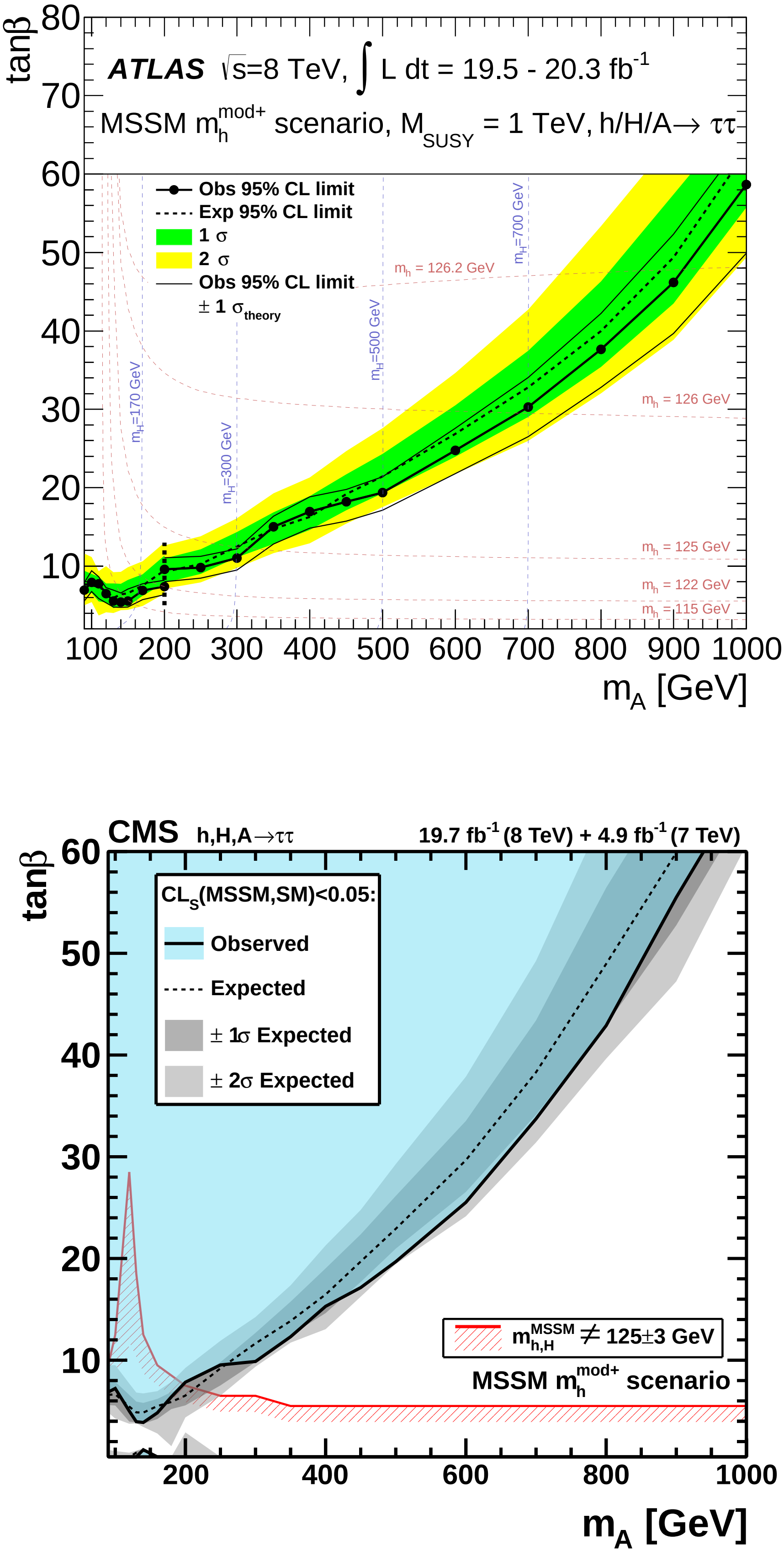

Figure 2.6: The observed and expected 95% confidence level limits on tanβ as a function of the mass of the neutral MSSM Higgs boson, m_A, in the $m_h^{\mathrm{mod}+}$ scenario, as measured in $A/H \to \tau\tau$ decays in the ATLAS detector (top), and the CMS detector (bottom). Taken from [31] and [32].

Chapter 3

The ATLAS experiment

The ATLAS (A Toroidal LHC ApparatuS) detector [35] is one of two general purpose particle detectors, along with CMS (Compact Muon Solenoid) [36], designed to study high energy physics collisions at the European Organization for Nuclear Research, also known as CERN. After passing through a series of smaller accelerators, proton bunches are accelerated by the LHC (Large Hadron Collider) [37] in two anti-clockwise beams, 27 km in circumference. A schematic diagram of the accelerator and main particle detectors is shown in Figure 3.1. These two beams cross at the centre of the ATLAS detector, at a point known as the interaction point (IP). The bunches contain around 100 billion protons and collisions occur at up to every 25 ns, with each beam containing up to 2808 bunches.

During the first operation of the ATLAS detector, referred to as Run-1, the collision energy in the centre of mass frame was $\sqrt{s} = 7$ TeV between 2010 and 2011, where 5.08 fb^{-1} of data was collected, followed by a collision energy of $\sqrt{s} = 8$ TeV in 2012, and the collection of 21.3 fb^{-1} of data [41]. The detector then entered ‘long shutdown 1’ (LS1), a series of upgrades between 2013 and 2015. During the first period of data collection in Run-2, between June and November 2015, the ATLAS detector recorded 3.9 fb^{-1} of proton-proton collision data with a centre of mass energy of $\sqrt{s} = 13$ TeV, and peak instantaneous luminosities of $5 \times 10^{33}\text{cm}^{-2}\text{s}^{-1}$ [42]. This thesis contains measurements performed after LS1 in this first period of data collection.

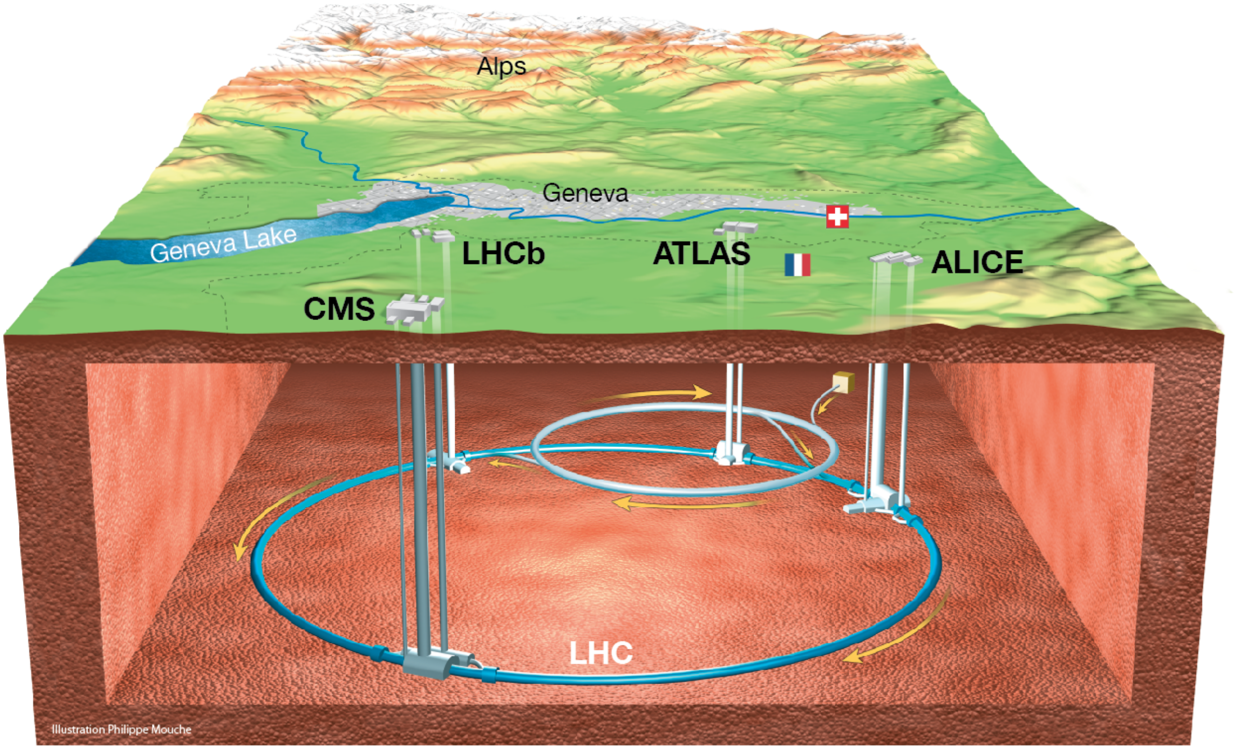

Figure 3.1: Schematic layout of the LHC accelerator system below Geneva, Switzerland. The positions of the four main LHC detectors are shown: ATLAS, ALICE [38], CMS and LHCb [39]. Taken from [40].

This chapter describes the different components that make up the post-LS1 ATLAS detector, in Section 3.1. It goes on to explain how the detector signals are interpreted as physics 'objects', such as tracks and particles, in Section 3.2, before discussing the data collected by the detector in Section 3.3. Also discussed is the simulation of the detector, in Section 3.4.

3.1 The ATLAS detector

The ATLAS detector, shown in Figure 3.2, is made up of a series of cylindrical subsystems in layers about the central interaction point. The coordinate system is right-handed, with the origin and centre of the detector located at the IP. The z-axis is directed along the beam pipe, the x-axis points from the IP to the centre of the LHC ring, and the y-axis

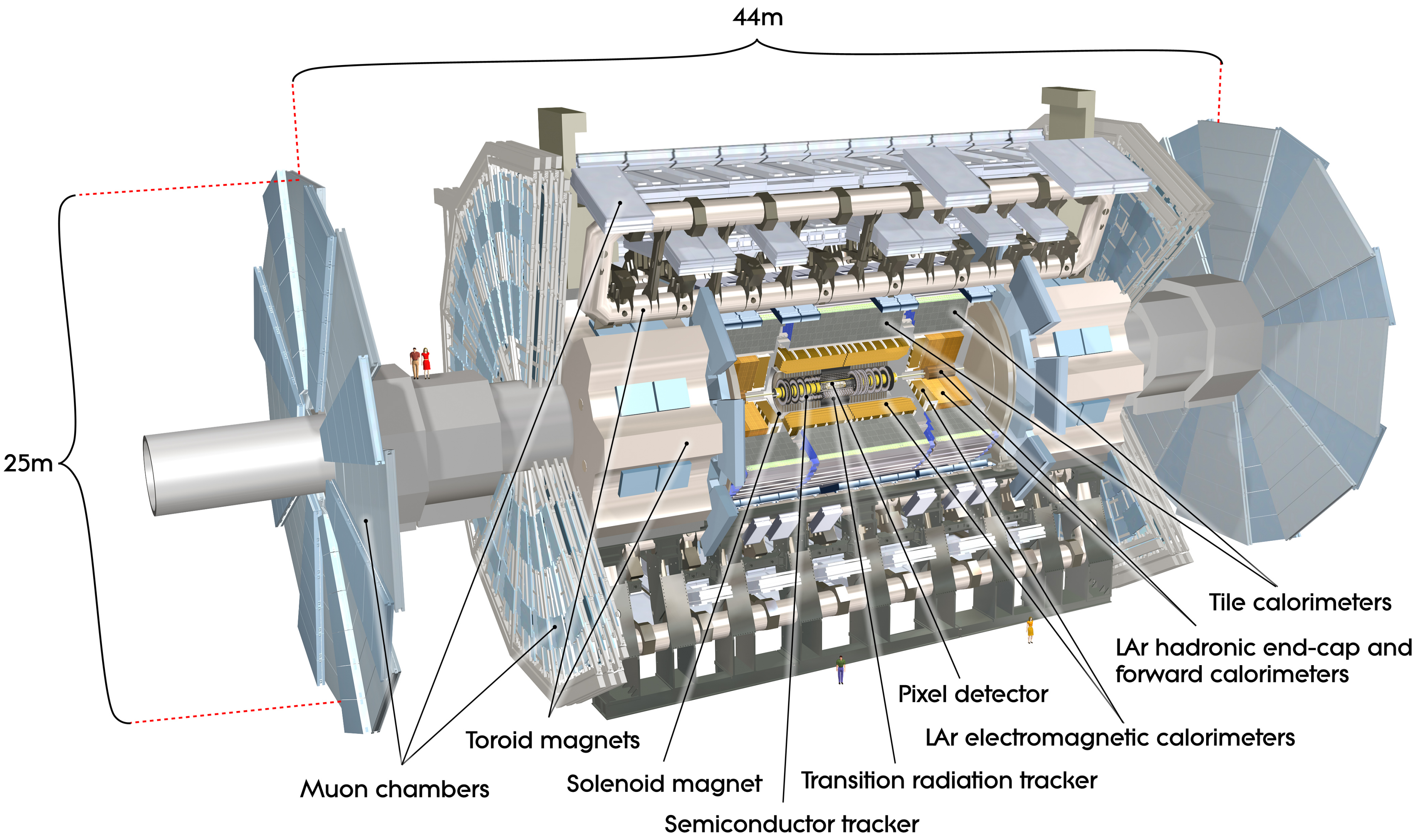

Figure 3.2: The ATLAS detector and its labelled subsystems. Taken from [43].

points upwards. Cylindrical coordinates (r, ϕ) are used in the transverse plane for a given z position, ϕ being the azimuthal angle around the beam pipe, and r the direction radially outwards.

The pseudorapidity is defined in terms of the polar angle, θ, as $\eta = -\ln \tan(\theta/2)$, and in the high energy limit, particle production in η is approximately constant and Lorentz-invariant under longitudinal boosts. Angular separations between physics objects in the detector are measured in units of $\Delta R \equiv \sqrt{(\Delta\eta)^2 + (\Delta\phi)^2}$. As the initial longitudinal momentum of colliding partons within the proton is not known, it is useful to refer to conserved quantities in the transverse plane, such as the transverse momentum p_{T} and transverse energy E_{T}.

The detector is 46 metres long, 25 metres in diameter, and weighs approximately 7,000 tonnes, making it the largest detector ever built to study particle collisions [44]. The innermost part of the detector consists of a series of tracking layers surrounded by a solenoid magnet. This inner detector system is designed to measure the paths and momenta of charged particles showering through. Electromagnetic (EMCAL) and hadronic (HCAL) calorimeters comprise the next detector layers, and enable the measurement of energy deposited by passing particles. Moving radially outwards from the IP, the muon spectrometer surrounds the calorimeter and includes a set of toroidal magnets to measure the paths of muons. Each detector subsystem consists of a 'barrel' layer surrounding the beam pipe, and 'endcap' layers, capping the high $|\eta|$ regions in layers along the direction of the beam pipe. The rest of this section describes in detail the different detector components.

3.1.1 Magnets

Two superconducting magnet systems create magnetic fields inside the ATLAS detector, exerting a force on moving charged particles that enables precision momentum measurements. Surrounding the inner detector tracking systems is a central solenoid, 2.46 m in diameter and 5.8 m long, creating an almost uniform 2 T field. The solenoid is made up of tightly wound wires with an operational current of 7.730 kA. The second system is comprised of

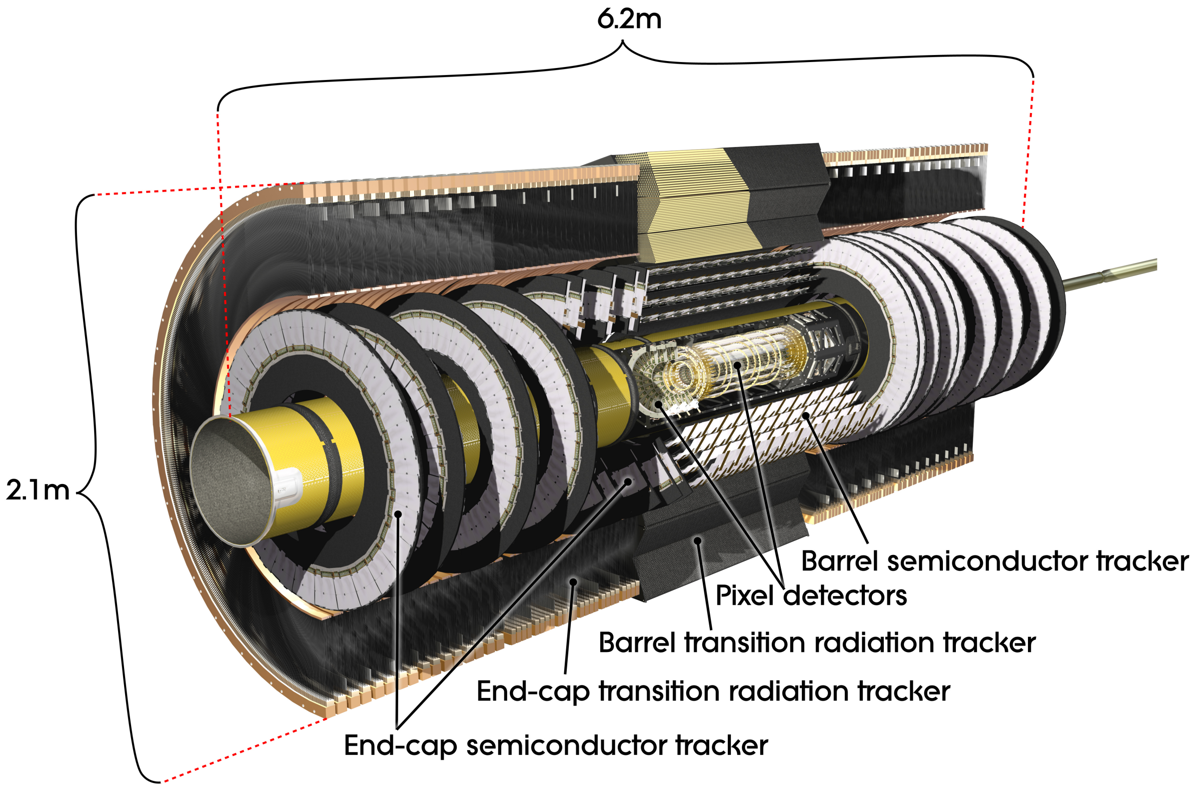

Figure 3.3: The inner detector tracking system of the ATLAS detector, showing the pixel detector and the SCT and the TRT systems. Not shown is the IBL system. Taken from [45].

three air-core toroid systems made up of eight coils, one in the barrel region spanning 25.3 m in length, and one in each endcap. These produce a non-uniform field inside and outside the system, with a peak field of around 4 T in the coil windings.

3.1.2 The inner detector

The inner detector is designed to provide precise measurements of the trajectories (tracks) and momenta of charged particles up to $|\eta| < 2.5$, and is shown in Figure 3.3. The detector enables accurate track reconstruction in dense environments, as well as identification of the primary vertex (PV), defined as the vertex with the largest value of $\sum_{tracks} p_T^2$ for all tracks associated to the vertex. Accurate tracking is also important for the reconstruction of each secondary vertex (SV), which is the location of the decay of a particle displaced from the beam line. The inner detector consists of several subsystems: the pixel detector, the insertable B-layer, the semiconductor tracker, and the transition-radiation tracker.

Pixel detector

In the barrel region, three concentric cylinders form the pixel detector [46], each 400 mm long and with radii between 50.5 mm and 122.5 mm, encircling the beam-axis. In the endcap region, three disks are placed longitudinally along the beam line to ensure that particles with $|\eta| < 2.5$ hit at least three layers. Radiation-hard silicon sensors make up the pixel detector, and are divided into pixels with approximately 80 million readout channels in total. These provide a resolution of the order of 10 μm in r-ϕ and 110 μm along the beam direction, for the barrel layers.

The insertable *B*-layer

The 'Insertable B-Layer' (IBL) [47] is a single cylindrical detector layer encircling the beam line at an average radius of 33 mm. This layer, additional to the pixel detector system, was installed during LS1 and contains around 6 million pixels. The position measurement has an 8 μm resolution in r-ϕ and 40 μm along the z-axis. The addition of the IBL for Run-2 is designed to improve the impact parameter resolution, that is, the lateral and longitudinal displacement of tracks from the primary vertex. This forms an important contribution to the identification of b-jets and hadronic tau lepton decays. The layer maintains efficient reconstruction of high-resolution tracks in the more dense environments of high-energy and high-luminosity LHC collisions.

Semi-conductor tracker

The semi-conductor tracker (SCT) [48], like the pixel layers, uses silicon sensors, but provides a coarser resolution. Four cylindrical layers, between 299 and 514 mm in radius, give a resolution of 17 μm in r-ϕ and 580 μm in the z-direction. Along the beam-axis, nine endcap disks on each side provide the same resolution in the z-ϕ and r-directions respectively, and ensure that at least four layers of SCT are crossed for particles with $|\eta| < 2.5$. The SCT contains over 6 million readout channels.

Transition radiation tracker

The transition radiation tracker (TRT) [49] uses thin-walled proportional drift tubes to detect the passage of charged particles that ionise the contained gas. Additionally, transition radiation occurs as relativistic particles traverse the straw walls. The 4 mm diameter tubes contain mostly xenon gas (with some straws replaced with argon gas due to leaks [50]) and a central wire anode. In the barrel region, 73 straw planes parallel to the beam-axis have radii between 0.5 and 1.0 m, whilst the endcaps contain a total of 160 straw planes. The tracker provides measurements only in r-ϕ in the barrel, and with a resolution of 130 μm per straw. The TRT has a coverage of $|\eta| < 2$ and around 350,000 readout channels.

3.1.3 The Calorimeters

Two calorimeters surround the ATLAS inner detector and solenoid, as shown in Figure 3.4. These measure the energy deposition and location of particles as they create showers upon interaction with the material. The EMCAL primarily determines the energy of particles interacting electromagnetically, whilst the HCAL is optimised for particle interactions via the strong nuclear force. Both calorimeters are sampling calorimeters, using different materials in the showering and measurement of the particles. The energy is collected in segments referred to as cells, defined by the resolution in r, η, and ϕ.

The combination of calorimeters covers a region of $|\eta| < 4.9$. A minimum radiation-length depth of 22 χ_0 in the EMCAL contains a very high fraction of electron and photon showers. A minimum interaction-length of at least 9 λ_I suppresses the passage of high energy particles into the muon spectrometer.

The electromagnetic calorimeter

The EMCAL is a sampling calorimeter with liquid argon (LAr) as the active material and lead as the passive material, and is designed to give coverage up to $|\eta| < 1.475$ in the barrel region, and between $1.375 < |\eta| < 3.2$ in the endcap, such that there is some overlap

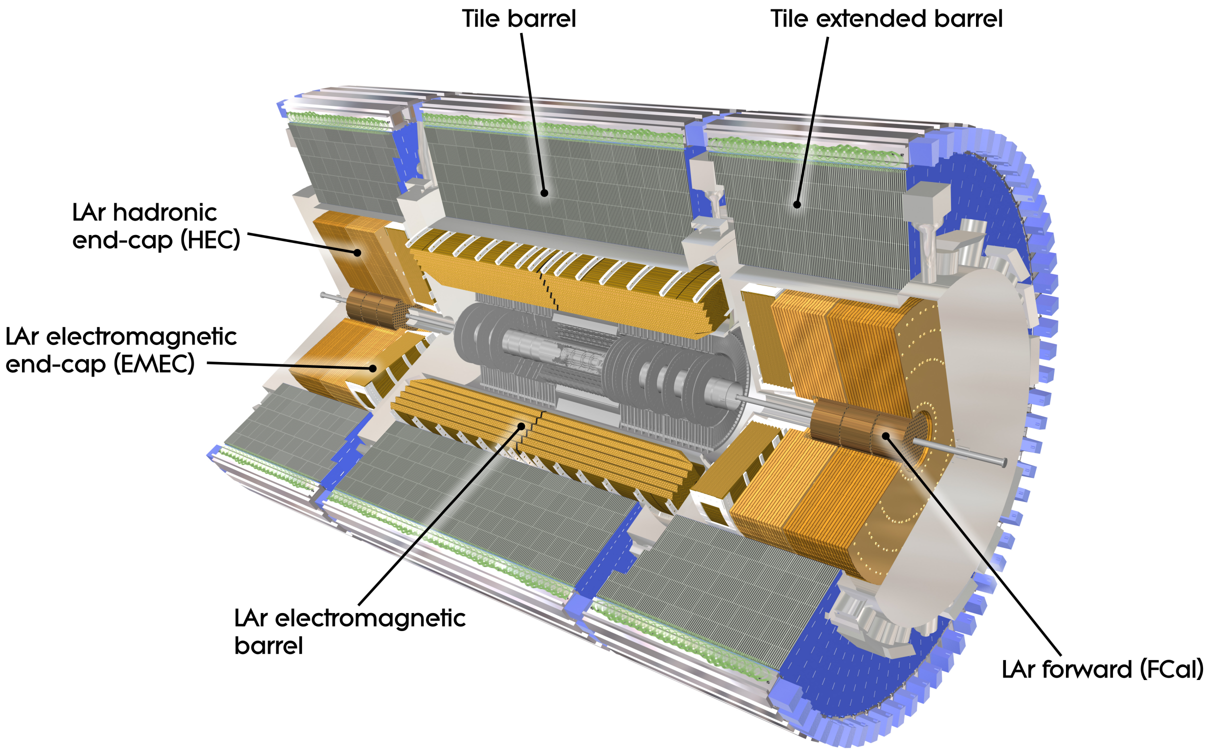

Figure 3.4: The calorimeter system of the ATLAS detector. Taken from [51].

between the two sections [52]. The lead layers have a thickness of between 1.13 and 2.2 mm (dependent on $|\eta|$) and are designed with an accordion geometrical structure such that they are symmetrical across ϕ as incident particles from the IP shower electromagnetically. The electromagnetic shower consists primarily of bremsstrahlung radiation and electron pair-production. In the sampling layers, the liquid argon is ionised by traversing electrons and the current is collected by copper wires. A single layer of liquid argon, the active material, is also present in front of the calorimeter for $|\eta| < 1.8$, in order to recover energy from showers occurring before the EMCAL is reached.

The EMCAL in the barrel region is split into two identical halves on either side of $\eta = 0$, each 3.2 m long and with diameters of 2.8 m on the inside and 4 m on the outside. The calorimeter is split into three sections along the radial direction, with coarser granularity in the sections further from the IP, as can be seen in the segment in Figure 3.5. Each endcap is made up of two wheels 630 mm thick and covering a radial distance from 330 mm to 2.1 m. The granularity in the endcap ranges from 0.0031-0.1 in η and 0.025-0.1 in ϕ.

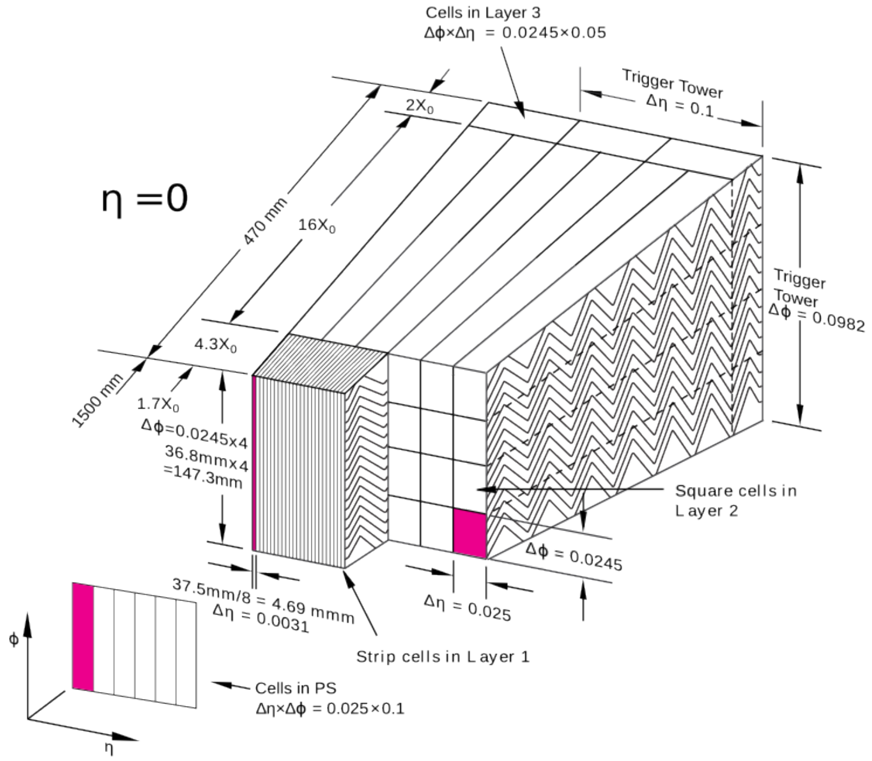

Figure 3.5: Schematic view of a section of the electromagnetic calorimeter system in the barrel region of the ATLAS detector. The dimensions and granularity in units of $\Delta\eta \times \Delta\phi$ are also shown. Taken from [53].

The hadronic calorimeter

The ATLAS HCAL is made up of three separate systems, a tile calorimeter [54] in the barrel region ($|\eta| < 1.7$), a copper-LAr endcap calorimeter similar to that described previously ($1.5 < |\eta| < 3.2$), and a set of forward calorimeters with either tungsten or copper absorbers, and a liquid argon active material ($3.1 < |\eta| < 4.9$). The calorimeter is designed to locate showering particles and measure and contain their energy as they interact either electromagnetically or hadronically with the material.

The tile calorimeter has a steel absorber and uses scintillating tiles as the active material. The granularity is coarser than the EMCAL, with a minimum of $\Delta\eta \times \Delta\phi = 0.1 \times 0.1$. The light from the tiles travels to a series of photomultiplier tubes and the signal is recorded. The barrel has a radius of 2.28 m on the inside and 4.25 m on the outside. The central barrel is 5.8 m long, whilst two further tile calorimeter barrels, 2.6 m long, surround the endcaps.

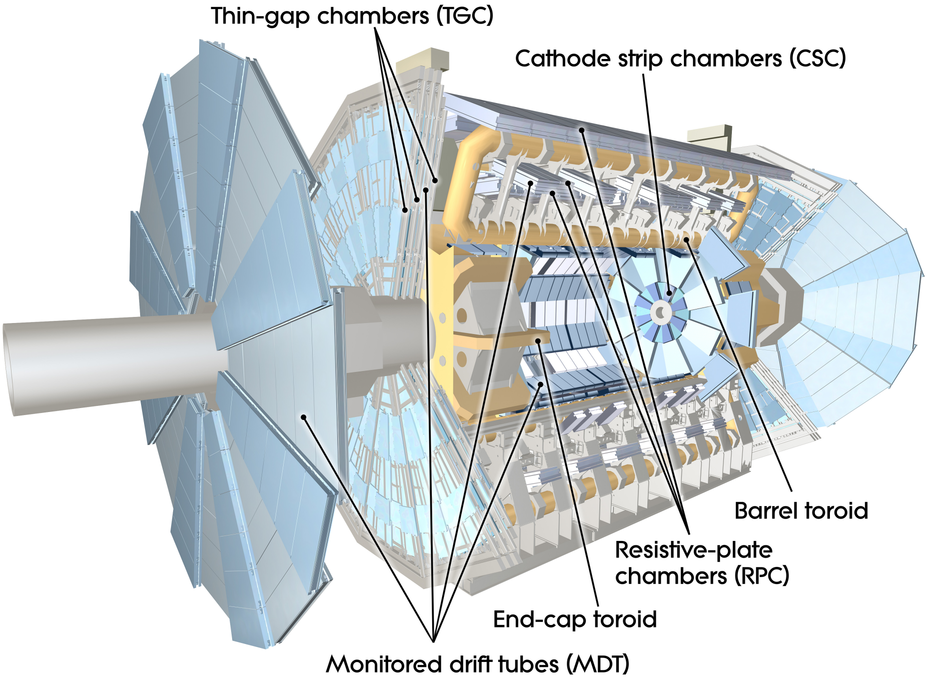

Figure 3.6: Schematic layout of the muon spectrometer and toroid magnet system. Taken from [55].

3.1.4 Muon Spectrometer

The MS [56], shown in detail in Figure 3.6 with the toroidal magnets, is the outermost subdetector of ATLAS and is composed of a set of different tracking systems. These tracking systems are designed to measure the position and, from the track curvature through the high magnetic field, the momentum of muons within $|\eta| < 2.7$. Within the region $|\eta| < 2.4$, the MS provides input to the muon trigger.

Precision momentum measurements within the full η range are carried out by three to eight layers of monitored drift tubes (MDTs). These are separated into three chambers in the barrel region ($|\eta| < 1.05$) up to a radius of 10 m, and four large wheels that form the endcap. Like the TRTs, the MDTs are comprised of a pressurised gas, in this case Argon, in 30 mm diameter tubes with wire anodes. The passage of charged particles is detected by the ionisation of the gas, with an average single-hit spatial resolution of 80 μm. Cathode-strip chambers (CSCs), with single-hit spatial resolutions of around 60 μm, supplement the MDTs in the region $2.0 < |\eta| < 2.7$ due to their improved resolution in high particle densities. These are multi-wire proportional chambers and operate similarly to the MDTs, with a similar gas mixture.

Resistive-plate chambers (RPCs) and thin-gap chambers (TGCs) are used as inputs to the trigger in the barrel ($|\eta| < 1.05$) and endcap ($1.05 < |\eta| < 2.4$) regions, respectively. The use of different detectors for the trigger is motivated by shorter the readout times of the trigger. The smaller readout volumes also require coarser resolution at the trigger level than offline. The RPCs are made up of two gaseous parallel electrode plates and incoming charged particles cause ionisation. The TGCs work on the same principle as the CSCs. During LS1 extra RPCs were added to increase acceptance, and the innermost wheel of the endcap region was replaced [57].

3.1.5 Trigger and data acquisition

The ATLAS trigger and data acquisition (TDAQ) system underwent many significant changes in preparation for the Run-2 data-taking period in order to cope with increases in rate, instantaneous luminosity, and pile-up (PU) [58]. Pile-up refers to the effect of additional interactions on the detector response, and is typically equated with the average number of proton interactions. The trigger system [59] is designed to reduce a ~ 30 MHz rate of proton bunch crossings in the LHC to a rate of 1 kHz for data storage. A ‘menu’ of many different trigger algorithms select physics processes of interest for the various working groups that use the ATLAS detector data.

A two-tier trigger system is used and a schematic diagram can be seen in Figure 3.7. Following a decision at the first tier, detector-specific readout drivers (RODs) send information from the detector front ends to the readout system, where it is made available for the second tier. A positive decision here results in the event data being sent by the ‘sub-farm output’ data logger for storage.

The reconstruction of physics objects during the trigger-level event processing is referred to as online, in contrast to the offline reconstruction, carried out after an event is recorded. This section gives an overview of the functioning of the trigger system, and details how jets

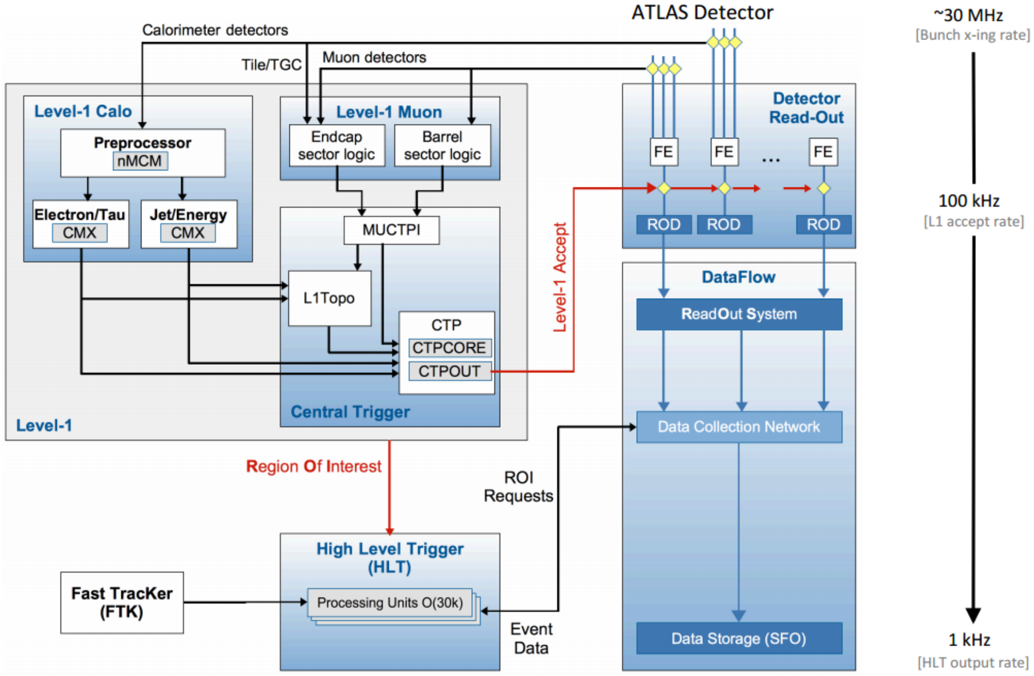

Figure 3.7: Schematic layout of the trigger and data acquisition system. The FTK (fast tracker) hardware-based tracking system was not operational at the time of writing this thesis. Taken from [60].

and muons are reconstructed in the trigger. The trigger may be prescaled or unprescaled. Unprescaled refers to the fact that no cap is placed on the data rate from the trigger, in contrast to prescaled triggers, in which an artificial reduction in the rate is produced by selecting only 1 in x passed events, where x is the prescale value. Chapter 5 details the algorithms used in the tau trigger as well as the performance measurements carried out.

The level 1 trigger

The first tier, level 1 (L1), is hardware based. Regions of interest (RoIs) are identified using coarse information from the muon spectrometer and the calorimeters. The L1 calorimeter transverse energy is measured in $\eta \times \phi = 0.1 \times 0.1$ 'trigger towers', as seen in Figure 3.8, with RoIs defined from several towers combined together. Trigger decisions are made by placing requirements on the transverse energy in a sum of calorimeter towers or on the measured muon p_{T}.

The information is passed to a central trigger processor (CTP) and a decision is made

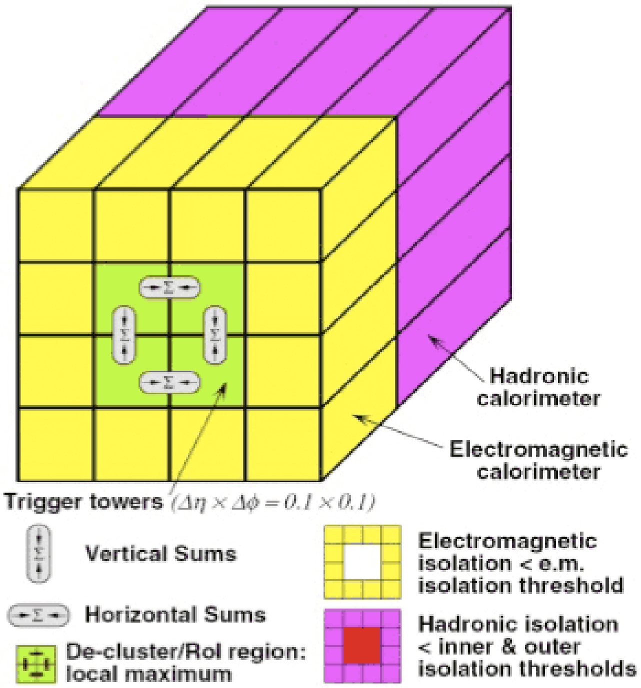

Figure 3.8: Schematic layout of the calorimeter system at L1 of the ATLAS trigger, showing how the calorimeter is divided up into towers in η and ϕ. Energy requirements can be placed on sums of towers, and isolation regions of low energy defined. Taken from [35].

within 2.5 µs [60]. In the case of the muon system the information is passed via the Muon-to-CTP-Interface (MUCTPI). Information from an L1 Topological Processor (L1Topo) is also sent to the CTP, enabling decisions based on topological calorimeter information, such as the structure or separation of energy deposits. The L1Topo system is currently undergoing commissioning, and aims to be operational in 2016.

The high level trigger

The RoIs found at L1 are passed on to the high level trigger (HLT) at a rate of up to 100 kHz. The HLT is software-based and has access to all sub-systems of the detector within the RoI with full granularity. A single processing farm is used with an average processing time of 0.2 s. Here object reconstruction takes place using algorithms similar to those used offline.

The jet trigger

At L1 the jet trigger decision is made by a requirement on the transverse energy deposited in a calorimeter RoI. The RoI is defined as a sum in EMCAL and HCAL energy of 8x8 trigger towers. At HLT jets are reconstructed using the anti-k_t jet clustering algorithm [61], described further in Section 3.2.4, with a distance parameter of $R = 0.4$, and follow a calibration similar to that used offline. The various jet triggers have different requirements on the transverse momentum of the reconstructed jet.

The muon trigger

At L1 the muon trigger requires a spatial and temporal coincidence of hits in either the RPCs or TGCs, with tracks extrapolating back to the beam interaction area. The p_{T} associated with the L1 muon must be above a threshold value, and the RoI is passed to the HLT. Here the muon is reconstructed with added information from the MDTs, the inner detector tracking systems, and information on the tracks found in a geometric region around the muon ('isolation' criteria). Identification algorithms similar to those used offline in Section 3.2.3 combine this information into different muon identification working points referred to as *loose, medium* or *tight*, depending on the selection purity.

3.2 Object reconstruction and identification

This section describes how information in the ATLAS detector is classified into 'objects' offline (i.e. after data taking). These objects are ATLAS interpretations of the information taken from the tracking and calorimeter systems originating from specific particles or types of particles. The object definitions include algorithms designed to reject backgrounds to the desired object, and calibrations to obtain the energy of the originating particle(s). The offline reconstruction and identification of the hadronic decays of tau leptons, referred to as tau candidates, of particular importance in the context of this thesis, is discussed in depth in Chapter 4.

3.2.1 Inner detector tracks

The principle of track reconstruction is to convert the hits from a single charged particle passing through the IBL, pixel detector, SCT and TRT, into a helical path. The hits of the IBL, pixel and SCT form space points, and a set of three space points in different layers forms a seed, with momenta and impact parameters roughly estimated from the helical parameters [62]. The further processing of seeds is subject to various momentum and impact parameter criteria. The seeds enter a track fitting algorithm which adds hits based on the estimated track position in each layer of these detectors. Duplicate tracks are removed, so that only the optimal track is chosen from hits sharing similar positions. The tracks are extended to the TRT, whose hits along the track trajectory are incorporated into a refitting of the full track.

The tracks are extrapolated in the direction of the collision point to reconstruct vertices (including the PV and SV), and find displacements from the beam line (the impact parameter). Track parameters often form an input to the reconstruction of particles.

3.2.2 Electrons

Formation of candidate electrons

Electrons are reconstructed by matching an energy deposit in the EMCAL to an inner detector track, and must be within $|\eta| < 2.47$. The EMCAL is divided into towers corresponding to the granularity of the middle layer, and the energy in the longitudinal layers is summed [63]. These energy towers are then clustered together via a sliding-window algorithm [64], and matched with an inner detector track based on $\Delta\eta$ and $\Delta\phi$ requirements. The energy and position of the candidate electron is then reconstructed and calibrated using information from the calorimeter deposits and the best matched track (decided by the number of pixel detector hits and distance to the EMCAL energy cluster).

Identification of electrons

Electrons are identified using the signal and background probability density functions for several discriminating variables detailed in Ref. [65]. This includes variables relating to the shape of the calorimeter particle shower and the ‘quality’ of the best matched track (for example the transverse impact parameter to the beamspot). A likelihood function is constructed, and several levels of selection are available, referred to as the electron ID ‘working points’ *loose*, *medium* and *tight*, which correspond to cuts on the likelihood score with different levels of signal efficiency and background rejection, using different discriminating variables. The tight working point has the highest level of background rejection and a lower selection efficiency than the medium and loose working points.

3.2.3 Muons

Muon reconstruction

In the reconstruction of muons [66], information is accessed from all subdetector systems, and tracks are reconstructed separately in the inner detector, as described in Section 3.2.1, and in the MS. In the MS muon track candidates are built from hit segments in the MDT, CSC, RPC and TGC layers, with overlapping tracks or tracks failing certain fit quality requirements removed.

Four types of muon are defined:

- Combined muon - created from matching extrapolated tracks in the inner detector with tracks in the MS.
- Segment-tagged muon - created from inner detector tracks extrapolated to the MS, matched with at least one track segment in the MS.

- Calorimeter-tagged muon - created from an inner detector track matched to a calorimeter energy deposit consistent with a minimally ionising particle.

- Extrapolated muon - created from an MS track compatible with the PV or SV.

Muons of different types are used in analyses with the order of priority dictated by the reconstruction performance, as follows: combined, segment-tagged, calorimeter-tagged, and finally extrapolated. The majority of muons are combined muons. A calibration is performed to correct for the muon's energy loss through the detector.

Muon identification

The identification of muons aims to reject fake muon candidates, particularly from charged pions and kaons. Four ID working points are used, *loose*, *medium*, *tight*, and *high-p_{T}*, in order of increasing purity, and the ID is dependent on the muon type. Variables used in the identification algorithms include the number of inner detector and MS hits and the quality of the fit.

Muons may also be required to be 'isolated', with two definitions considered in this thesis, 'gradient' and 'fixed-threshold'. Gradient requires that the scalar sum of the transverse momenta of tracks within a cone of p_{T}-dependent size, $\Delta R <\min\,(10\ \ \mathrm{GeV}/p_{\mathrm{T}}, 0.3)$, centred on the lepton candidate track and excluding the lepton track, is required to be less than a p_{T}-dependent fraction of the muon transverse momentum. Additionally, the sum of the calorimeter energy deposits in a cone of size $\Delta R < 0.2$ around the lepton, excluding energy associated with the lepton candidate, must be less than a p_{T} dependent percentage of the lepton energy. Fixed-threshold isolation uses a similar definition, except with a fixed cone size of $\Delta R < 0.4$ for tracks and with the threshold values fixed at 1% and 4% for the sum of track momenta, and the sum of the calorimeter energy deposits, respectively.

3.2.4 Jets

Due to the limitations of the ATLAS detector, individual hadrons cannot be reconstructed, and instead, energy deposits in the calorimeter cells are clustered into 'jets' , narrow cones of hadronic activity produced by high energy quarks and gluons. The anti-k_t jet clustering algorithm [61], with a distance parameter of $R = 0.4$, is used to cluster calorimeter deposits into jets for the majority of ATLAS analyses, and is used in this thesis. It is infrared and collinear safe meaning the emission of soft or small angle particles from the hadrons does not affect the clustering result.

In constructing ATLAS jets, calorimeter cells with measured energies above a threshold 'expected noise' value are first grouped in topoclusters [64] with adjacent cells that register energies above a lower noise threshold. The topoclusters are calibrated at the EM-scale [67], a calibration derived from electron beam studies, and assuming an electromagnetic shower behaviour in the calorimeter. A PU correction is also applied before an additional local hadronic calibration [68] (LC-scale), a correction for hadronic energy deposits. These topoclusters form the inputs to the anti-k_t algorithm.

A set of calibrations known as the jet energy scale (JES) [69] is then applied. The JES aims to correct the jet four-vector so as to reproduce the particle level energies of the jet constituents, and takes into account effects such as energy losses due to dead material and leakage, as well as the non-compensating nature of the calorimeter (the incomplete measurement of energy deposited by hadrons). Both the jet energy and jet direction are calibrated in this stage. The jet is required to originate from the hard scatter by applying a cut on the jet vertex fraction (JVF), which is the proportion of momentum associated with jet tracks that comes from tracks associated with the PV.

3.2.5 *b*-jets

Jets associated with the production of a b-quark (referred to as b-jets), are detected or 'tagged' via a dedicated b-tagging algorithm [70]. The b-quarks are confined within B-mesons, and the b-tagging algorithm makes use of their measurable lifetimes and decay lengths. This is done by the combination of information relating to the jet track impact parameters (the lateral and longitudinal displacement from the PV), the reconstructed secondary vertex (SV) and the decay chain of particles in the jet. A Boosted Decision Tree (BDT) [71] [72] algorithm combines this information to produce an output variable that discriminates b-jets from lighter flavour jets, and is trained on simulated $t\bar{t}$ events. The ID algorithm aims to achieve a 70% efficiency in selecting b-jets. Figure 3.9 shows the acceptance efficiency of b-jets, and of jets associated with the decay of lighter flavour quarks, as a function of jet p_{T}.

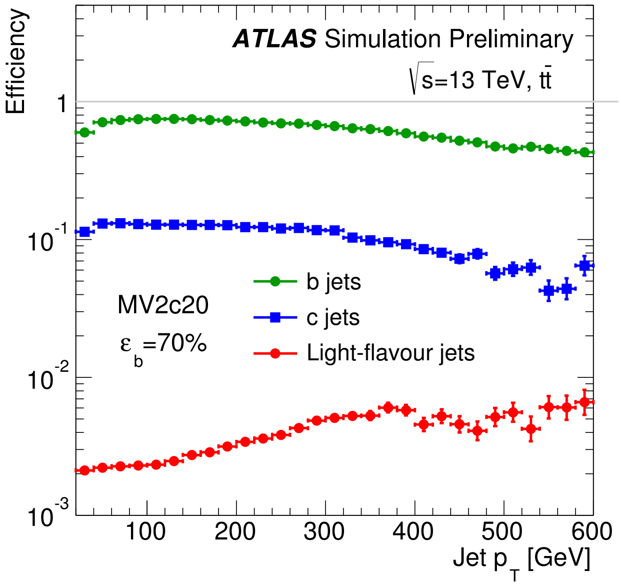

Figure 3.9: Efficiency of the b-tagging algorithm in accepting b-jets, jets associated with the decay of charm quarks (c-jets) and jets associated with up down and strange quarks (light-flavour jets) as a function of the jet p_{T} [70]. The efficiency is measured in simulated $t\bar{t}$ events.

3.2.6 Overlap removal

There can be some ambiguity in the identity of physics objects due to the overlap in object definitions. For example, the calorimeter deposit associated with an electron may also be reconstructed as a jet. Overlapping objects are removed depending on their geometric distance (ΔR) with an order of priority defined by:

- Jets within a $\Delta R = 0.2$ cone of tau candidates selected for an analysis are excluded.

- Jets within a $\Delta R = 0.4$ cone of an electron or muon are excluded.
- Tau candidates within a $\Delta R = 0.2$ cone of electrons or muons are excluded.
- Electrons within a $\Delta R = 0.2$ cone of muons are excluded.

with the identification level and p_{T} of an object dependent on the analysis. Tau candidates are described in detail in Chapter 4.

3.2.7 Missing transverse momentum

It is not possible to measure the properties of neutrinos with the ATLAS detector, and they are instead reconstructed as a 'missing transverse momentum' [73], with magnitude denoted by $E_{\mathrm{T}}^{\mathrm{miss}}$. It is formed from reconstructed and calibrated physics objects in the event:

$$E_{x(y)}^{\mathrm{miss}} = E_{x(y)}^{\mathrm{miss},e} + E_{x(y)}^{\mathrm{miss},\gamma} + E_{x(y)}^{\mathrm{miss},\tau_{\mathrm{had}}} + E_{x(y)}^{\mathrm{miss},jet} + E_{x(y)}^{\mathrm{miss},\mu} + E_{x(y)}^{\mathrm{miss,soft}}, \tag{3.1}$$

where each $E_{x(y)}^{\mathrm{miss}}$ term for a given object (e.g. electrons or muons) in the x- or y-direction, is the negative sum of the momentum of the respective objects in the event. The term $E_{x(y)}^{\mathrm{miss,soft}}$ is constructed from the transverse momentum of tracks associated with the PV but not associated with any reconstructed object above a certain p_{T} threshold. The term $E_{x(y)}^{\mathrm{miss},\gamma}$ uses reconstructed photons, which are not considered in the studies in this thesis. A sum of the transverse momenta of all objects considered in an event can similarly be defined.

3.3 Data

Between June and November 2015, the ATLAS detector recorded proton-proton collisions with a centre of mass energy of $\sqrt{s} = 13$ TeV. As can be seen in Figure 3.10, a total of 4.2 fb^{-1} of collision data was delivered by the LHC, of which 3.9 fb^{-1} was recorded by the trigger system described in Section 3.1.5 [42]. This data was recorded at a computing centre based at CERN, and distributed via a computing 'GRID' for further processing. Figure 3.10

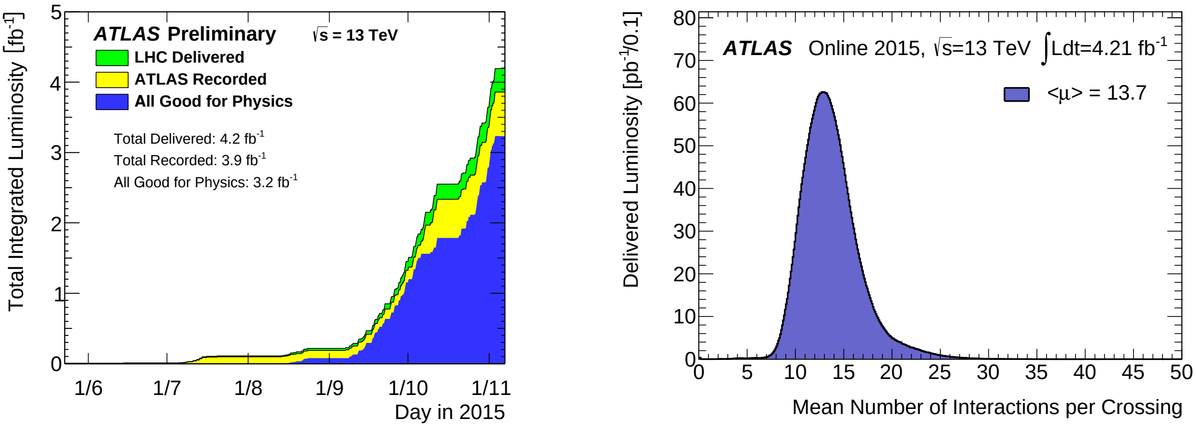

Figure 3.10: The total integrated luminosity (left) and PU distribution (right) measured by the ATLAS detector in the 2015 Run-2 proton-proton collisions. Taken from [42].

also shows the pile-up profile of the recorded data. In general, only the hard scatter, the vertex and process associated with the highest p_{T} tracks, is of interest for physics analysis, with the rest dominated by low energy QCD processes.

This section describes the data quality requirements placed on the data, as well as further quality criteria applied to the objects used.

3.3.1 Event cleaning

The data used in this thesis has the following requirements placed on it in order to mitigate the effect of detector defects:

Data quality

The data recorded in the ATLAS detector is divided up into periods in which the detector conditions are stable; these are referred to as ‘luminosity blocks’. For each block all detector subsystems are required to be operating satisfactorily. Of the recorded data, 3.21 fb^{-1} of 25 ns data taken between August and November 2015 is considered of a quality sufficient for the performance of physics measurements [74].

Collision cleaning

It is required that the primary vertex (PV) of all events contain at least two associated tracks.

Jet cleaning

Requirements are placed on reconstructed jets to reduce the possibility that the energy deposits in the calorimeter occur as a result of problems in the hardware, such as calorimeter noise. This includes requirements on the timing of the energy deposit, and on the fraction of the jet momentum attributable to tracks in the inner detector.

3.4 ATLAS simulation

It is useful in physics analyses to make comparisons between the ATLAS data and simulated proton-proton collisions. The simulation of events uses Monte Carlo generators, named after the random sampling technique, and undergoes several stages of computation. Generators calculate the matrix element of the physics processes of interest either at leading order (LO) or higher orders, with the kinematics of the partons involved selected from parton distribution functions (PDFs). Intermediate particles are then decayed according to their branching fractions. The showering of initial and final state partons involved in the process is also simulated, as is their hadronisation into observable particles. Finally, the underlying event, the remnants of the incoming particles and their interactions, is simulated.

In order to practically compare data with simulated collisions, the simulated particles must be passed through a virtual reconstruction of the ATLAS detector, created by the ATLAS simulation infrastructure [75]. Unless otherwise stated, all simulated events in this thesis reconstruct the ATLAS detector using `GEANT4` [76], a package which simulates the passage of particles through matter. These particle-detector interactions, or hits, are then interpreted in the form of detector signals. Detector noise is included, as is the effect of PU in the same and neighbouring bunch crossings, which is added by overlaying simulated events generated with `Pythia 8.186` [77, 78]. The trigger decisions are emulated, by simulation of the digital inputs to the RODs.

As with data, the object reconstruction algorithms can be used to reconstruct the simulated particles as the ATLAS 'objects' described in Section 3.2. The reconstructed objects in simulation may also have correction factors, also known as scale factors, applied as a weighting to the simulated event, in order to account for differences between data and simulation. These scale factors are often computed with the aid of well understood physics processes as a 'standard candle' to investigate the data-simulation discrepancies. The simulation of events is often completed before the final pileup (PU) distribution of the data collection period, shown in Figure 3.10 for the 2015 data, is well understood. Therefore a correction is applied to simulated events in order to weight the events to a more data-like PU profile. The properties of simulated events at generator level (also known as 'truth level'), without the application of the ATLAS simulation infrastructure, are also stored.

Chapter 4

The reconstruction and identification of hadronic tau decays

Tau leptons are detected via their decay products, and decay either leptonically, that is to a muon or electron and associated neutrinos, or to charged and possibly neutral hadrons (principally pions) and an associated tau neutrino. Since the neutrino passes undetected through the ATLAS detector, only the neutral and charged hadrons associated with the hadronic decay are measured. Throughout this thesis hadronic tau refers to hadronically decaying tau leptons (also denoted by τ_{had} and $\tau_{\text{had-vis}}$) unless otherwise stated, whilst tau lepton or tau particle refers to the particle itself. Correspondingly, in the context of this thesis, 'lepton' alone refers to electrons and muons exclusively, unless otherwise stated. The hadronic mode of tau lepton decays is almost exclusively to one or three charged hadrons, hereafter referred to as 1-prong and 3-prong. The branching fractions of selected tau lepton decay modes are shown in Table 4.1.

This chapter discusses the hadronic tau decay reconstruction, energy calibration, and identification algorithms, in Section 4.1, Section 4.2 and Section 4.3, respectively. These algorithms were developed in Run-1 [79], before being optimised for Run-2 [80]. The major background to the identification of hadronic tau decays in proton-proton collisions comes from quark- or gluon-initiated jets, and a dedicated algorithm, is developed in order to

Decay mode	Branching fraction [%]
Hadronic decay modes	
$\tau^{\pm} \rightarrow \pi^{\pm}\nu_{\tau}$	10.83
$\tau^{\pm} \rightarrow \pi^{\pm}\pi^{0}\nu_{\tau}$	25.52
$\tau^{\pm} \rightarrow \pi^{\pm}2\pi^{0}\nu_{\tau}$	9.30
$\tau^{\pm} \rightarrow \pi^{\pm}3\pi^{0}\nu_{\tau}$	1.05
$\tau^{\pm} \rightarrow \pi^{\pm}\pi^{\pm}\pi^{\mp}\nu_{\tau}$	8.99
$\tau^{\pm} \rightarrow \pi^{\pm}\pi^{\pm}\pi^{\mp}\pi^{0}\nu_{\tau}$	2.70
Leptonic decay modes	
$\tau^{\pm} \rightarrow \mu^{\pm}\nu_{\mu}\nu_{\tau}$	17.41
$\tau^{\pm} \rightarrow e^{\pm}\nu_{e}\nu_{\tau}$	17.83

Table 4.1: The branching fractions of selected tau lepton decay modes [14].

identify hadronic tau decays and reject quark- and gluon-initiated jets. Following the reconstruction and/or identification stages, objects interpreted as hadronically decaying tau leptons are often referred to as 'tau candidates'.

In the following description of the reconstruction, energy calibration and identification of tau candidates, various sources of systematic uncertainty are considered, and include:

- Uncertainty on the amount of detector material.
- Uncertainty on the calorimeter performance and calibration.
- Uncertainty on the amount of pile-up (PU).
- Uncertainty due to the choice of generator and shower model.

The uncertainties are evaluated in different $|\eta|$ regions of the detector, and as a function of the tau candidate p_{T}.

The development of the reconstruction, energy calibration and identification algorithms was conducted primarily on low-p_{T} ($p_{\mathrm{T}} \lesssim 100$ GeV) hadronically decaying taus resulting from Z boson decays. The application of the algorithms to high-p_{T} hadronic taus is discussed in Section 4.5.

4.1 The reconstruction of tau candidates

4.1.1 Formation of tau candidates

Candidate hadronic taus are first formed from jets reconstructed using the anti-k_t clustering algorithm [61] with a distance parameter $R = 0.4$, as described in Section 3.2.4, and prior to calibration. These jets seed candidate taus if the requirements $p_{\mathrm{T}} > 10$ GeV and $|\eta| < 2.5$ (with the poorly instrumented transition region of the detector, $1.37 < |\eta| < 1.52$, excluded) are satisfied.

4.1.2 Tau vertex

The chosen event primary vertex (PV) and the vertex with the tau candidate may not be the same, particularly under high PU conditions. A separate tau vertex (TV) is chosen from the primary vertex candidates for a given candidate tau, and is the vertex associated with the largest fraction of the $\Sigma p_T^2(track)$ of all tracks within a geometric region $\Delta R < 0.2$ around the axis of the seeding jet. The TV is used to define the direction of the candidate tau, and impact parameters are defined with respect to the TV.

4.1.3 Track association

A ‘core region’ of the candidate tau is defined as the geometric region $\Delta R < 0.2$ around the tau axis, and a second ‘isolation region’ is defined as $0.2 < \Delta R < 0.4$. Tracks are then associated to these two regions providing the following criteria are satisfied:

- $p_{\mathrm{T}} > 1$ GeV.
- Total pixel detector (including the IBL) hits > 2.
- Total pixel + SCT detector hits > 7.

- The shortest distance from the track to the TV in the transverse plane, d_0, satisfies $|d_0| < 1$ mm.
- The shortest distance from the track to the TV in the longitudinal plane, Δz_0, satisfies $\Delta z_0 \sin(\theta) < 1.5$ mm.

Inefficiencies in track finding can result in the reconstructed number of tracks differing from the true number of charged hadrons in a given region.

4.1.4 Reconstruction efficiency

The efficiency of reconstructing a hadronic tau decay via the method described above is shown in Figure 4.1 as a function of the transverse momentum of the simulated particle. In this efficiency measurement, the reconstructed hadronic tau must have the same number of reconstructed charged tracks as the number of charged pions associated with the simulated decay.

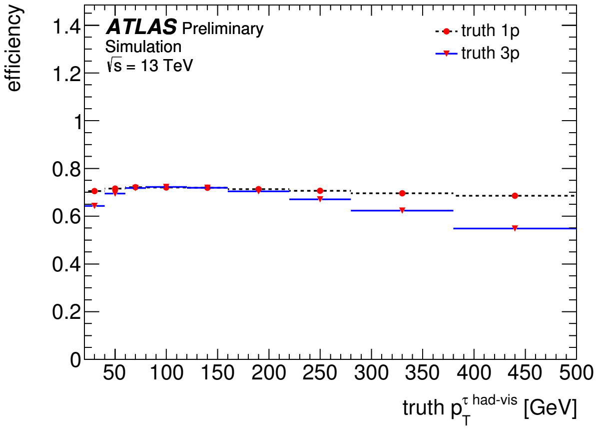

Figure 4.1: The efficiency of reconstructing tau candidates from simulated tau leptons as a function of the transverse momentum of the simulated tau lepton. The efficiency is shown separately for simulated tau particles decaying to 1 and 3 charged hadrons (denoted 1p and 3p) and requires that the number of reconstructed tracks associated to the candidate tau be 1 or 3 respectively [80].

Inefficiencies in hadronic tau reconstruction predominantly result from inefficiencies in the selection of the TV and in the track reconstruction, the latter being particularly important for high-p_T 3-prong tau candidates. A systematic uncertainty of between 2% and 5% depending on the p_{T} and number of tracks is associated with the reconstruction of tau particles. This is driven by the uncertainty related to the selection of the TV particularly as a result of PU tracks, and uncertainty in the simulation of the detector material, which affects the reconstruction of tracks.

4.2 The energy calibration of tau candidates

As discussed in Section 3.2.4, the seed jet is formed from topological clusters of calorimeter cells calibrated at the LC-scale. The 4-momentum of the candidate tau is calculated from the 4-momentum sum of the energy deposited in the region $\Delta R < 0.2$ around the jet seed. In place of the JES a separate tau energy scale (TES) calibration is then applied to correct the measured energy of the tau candidate [81].

4.2.1 Tau energy scale calibration

The candidate tau energy is calibrated via the equation:

$$E_{\mathrm{calib}} = \frac{E_{\mathrm{LC}} - E_{\mathrm{PU}}}{\mathcal{R}\left(E_{\mathrm{LC}} - E_{\mathrm{PU}}, |\eta|, \mathrm{n-prong}\right)} \quad , \tag{4.1}$$

where E_{LC} refers to the measured tau candidate energy described above. E_{PU} is a correction based on the number of reconstructed primary vertices in an event, and as such corrects for PU contributions to the energy. The term $\mathcal{R}$, the detector response function, gives a correction dependent on the measured tau candidate energy and $|\eta|$, and the number of charged tracks (n-prong, where $n = 1$ or 3) of the tau candidate. The response is determined via simulation from the Gaussian mean of the distribution $\frac{E_{\mathrm{LC}} - E_{\mathrm{PU}}}{E_{\mathrm{true}}}$ where E_{true} is the 'true' energy of the simulated tau lepton decay hadrons (that is, the generator-level energy of the simulated tau lepton decay products before passage through the detector simulation software).

Figure 4.2 shows the TES detector response values for 1-prong tau candidates, and for tau candidates associated with multiple charged tracks. Systematic uncertainties on the TES are calculated as shifts in the Gaussian mean. The major contribution to the TES uncertainty comes from the data measurements of the response of single hadrons (i.e. the individual components of the hadronic tau decay) in low luminosity runs. The procedure of estimating the tau candidate energy uncertainty using the uncertainty on single-pion measurements is referred to as the 'particle deconvolution method' [81].

At the time of the studies contained in this thesis, a Run-2 measurement of the TES performance, the TES 'in-situ' measurement, had not been completed. As the ATLAS detector has not significantly changed during the LS1 upgrade, the Run-1 performance measurement and correction between data and simulation is used, and the uncertainty is inflated by a precautionary factor of two [79].

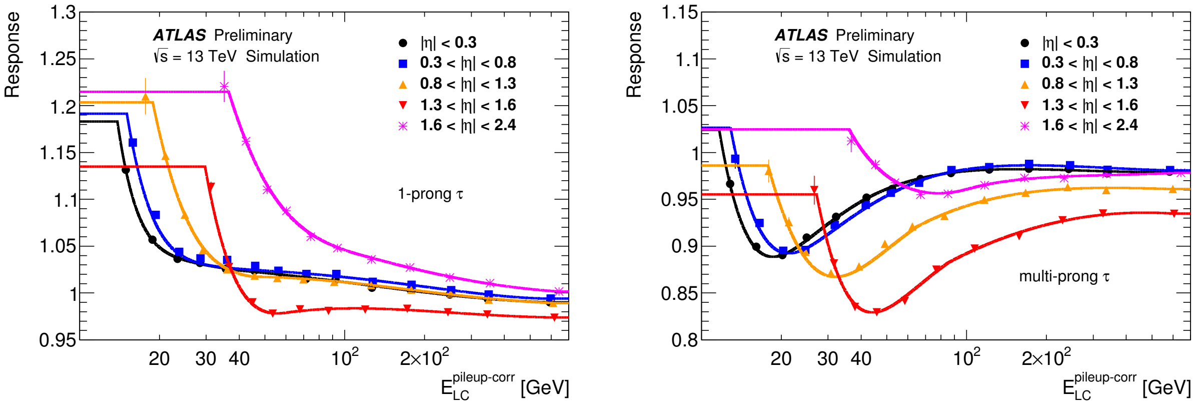

(a) 1-prong tau candidate (b) Multi-prong tau candidate

Figure 4.2: Detector response values used in the calculation of the TES as a function of the PU-corrected energy of the tau candidate [80].

4.3 The identification of hadronic tau decays

The major background to hadronically decaying tau leptons comes from quark- and gluon-initiated jets. The tau identification (ID) algorithm aims to reject this background using a Boosted Decision Tree (BDT) [71] [72] trained on simulated $Z \to \tau\tau$ and dijet events. A set of variables that discriminate 1-prong and 3-prong hadronic tau decays from QCD jets are combined by the tau BDT to produce a more strongly discriminating single variable referred to as the BDT output, or BDT score.

4.3.1 Variables used in the tau identification BDT

Discriminating variables used in the separation of hadronic tau decays and QCD jets use information on the tracks and energy deposits in the core and isolation regions of tau candidate, and are corrected for PU. In general, these variables rely on the following characteristics: tau-initiated jets (i.e. hadronic tau lepton decays) are more collimated than QCD jets; there is a separation between the tau vertex and that of the decay products; and QCD jets generally contain more particles. A full list of the variables, with a brief description, is summarised below, whilst Figures 4.3 and 4.4 show the distributions of selected variables [80].

Central energy fraction (f_{cent}) : The fraction of the transverse energy deposited in topoclusters in the region $\Delta R < 0.1$ around the candidate tau, compared to the total in the core region ($\Delta R < 0.2$).

Leading track momentum fraction ($f^{-1}_{\mathrm{leadtrack}}$) : The ratio of the topocluster transverse energy sum deposited in the core region to the transverse momentum of the highest-p_{T} charged particle in the core region.

Track radius ($R^{0.2}_{\mathrm{track}}$) : The p_{T}-weighted ΔR sum of the core tracks, divided by the p_{T} sum of the core tracks.

Leading track IP significance ($|S_{\mathrm{leadtrack}}|$) : (1-prong tau candidates only) The magnitude of the impact parameter from the TV of the leading core-region track, divided by its estimated uncertainty.

Fraction of track p_{T} in the isolation-region ($f^{\mathrm{track}}_{\mathrm{iso}}$) : (1-prong tau candidates only) The fraction of the p_{T} magnitude sum of isolation-region ($0.2 < \Delta R < 0.4$) tracks to the p_{T} magnitude sum of all tracks ($\Delta R < 0.4$) associated to the tau candidate.

Maximum ΔR (ΔR_{Max}) : (3-prong tau candidates only) The maximum ΔR between the tau direction and a core region track.

Transverse flight path significance ($\boldsymbol{S_{\mathrm{T}}^{\mathrm{flight}}}$) : (3-prong tau candidates only) The transverse distance between the TV and the secondary vertex (the vertex reconstructed from core region tracks) divided by the uncertainty on the distance.

Track mass ($\boldsymbol{m_{\mathrm{track}}}$) : (3-prong tau candidates only) The invariant mass given by the sum of the 4-momenta of all tracks associated to the tau candidate (each track is assumed to have pion mass).

Fraction of EM energy from charged hadrons ($\boldsymbol{f_{\mathrm{EM}}^{\mathrm{track-HAD}}}$) : The difference between the sum of track momenta and the sum of topocluster energy deposited in the hadronic calorimeter (an estimate of the energy in the EMCAL from charged hadrons), divided by the sum of topocluster energy deposition in the electromagnetic calorimeter, for the core region of the candidate tau.

Ratio of EM energy to track momentum ($\boldsymbol{f_{\mathrm{track}}^{\mathrm{EM}}}$) : The ratio of the sum of tau topocluster energy deposited in the electromagnetic calorimeter to the sum of core region track momentum.

Track-plus-EM-system mass ($\boldsymbol{m_{\mathrm{EM+track}}}$) : Invariant mass of the core region tracks and the two most energetic core region topocluster energy deposits in the electromagnetic calorimeter (with mass set to zero).

Ratio of track-plus-EM-system to $\boldsymbol{p_{\mathrm{T}}}$ ($\boldsymbol{p_{\mathrm{T}}^{\mathrm{EM+track}}/p_{\mathrm{T}}}$) : Ratio of vector sum of the core region track momenta and the two most energetic core region topocluster electromagnetic energy deposits, to the calorimeter measurement of the tau candidate p_{T}.

4.3.2 Tau BDT score

The tau ID BDT output scores for simulated $Z \rightarrow \tau\tau$ and multi-jet events are shown in Figure 4.5 for 1-prong and 3-prong tau candidates. The separation for the combination of variables is much more significant than for the individual variables. Figure 4.6 shows the inverse of the efficiency for misidentifying (mis-ID) jets as hadronic tau decays in background

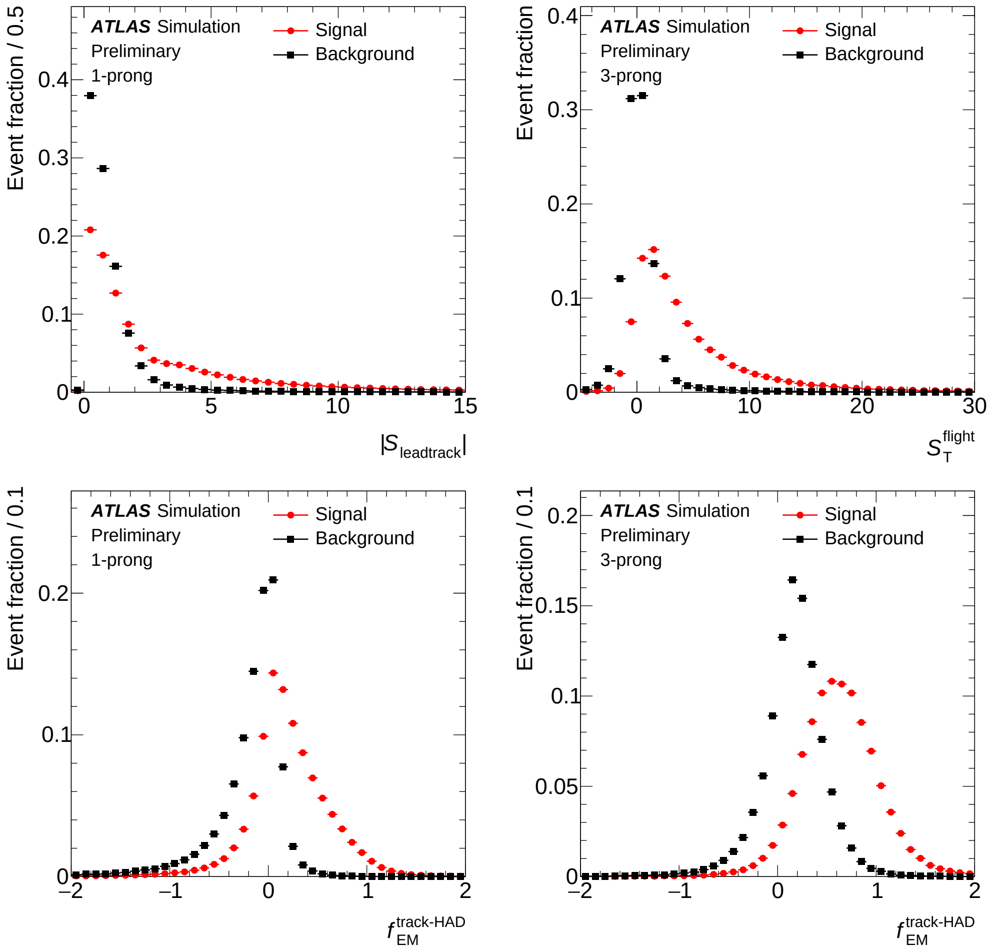

Figure 4.3: The distributions of selected input variables to the tau ID BDT for 1-prong (left) and 3-prong (right) tau candidates in simulated $Z \to \tau\tau$ events (signal) and multi-jet (background) events [80].

multi-jet events as a function of the efficiency for correctly identifying reconstructed tau candidates from $Z \to \tau\tau$ events (calculated in simulated events). Three cuts on the BDT output, referred to as working points and labelled *tight*, *medium* and *loose*, are provided, and correspond to different $p_{\rm T}$-dependent tau ID efficiency values, and consequently different levels of background rejection. The $p_{\rm T}$ dependence aims to maintain a stable efficiency of the combined reconstruction and ID stages across the $p_{\rm T}$-range, with combined efficiencies of 60%, 55% and 45% respectively for loose, medium and tight 1-prong tau candidates, and corresponding efficiencies of 50%, 40% and 30% for 3-prong tau candidates.

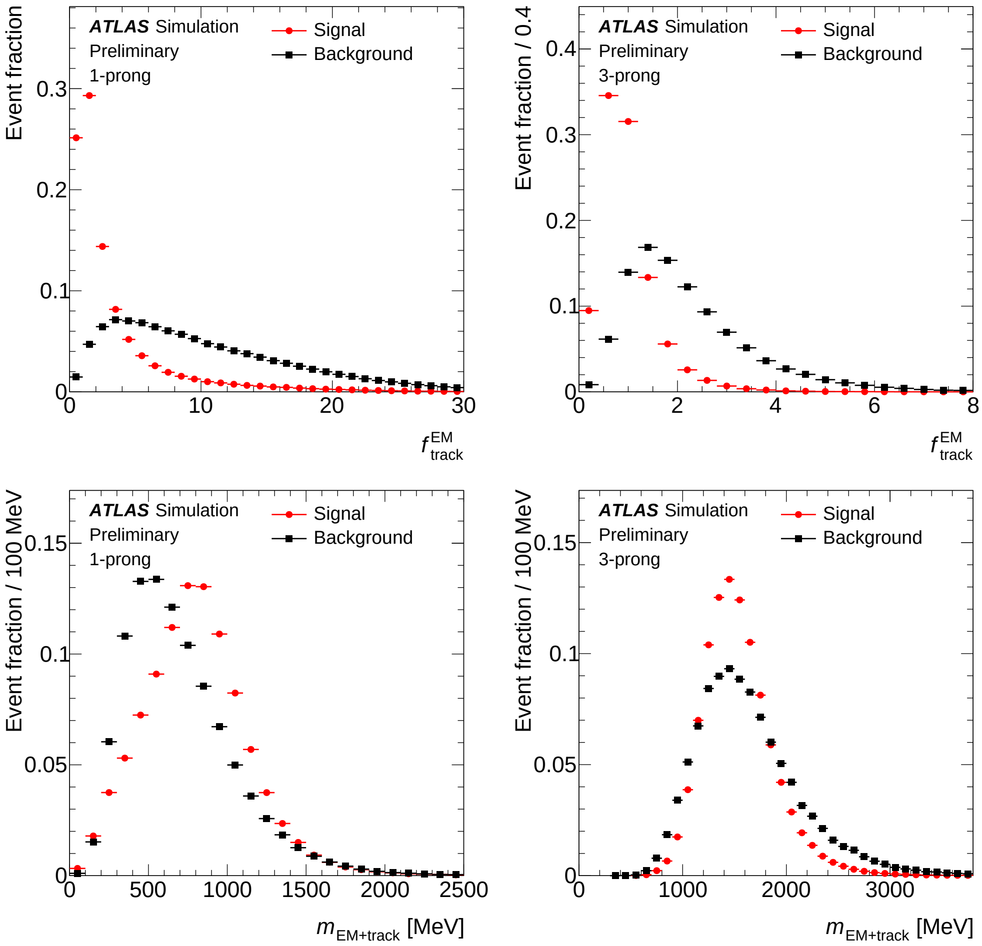

Figure 4.4: The distributions of selected input variables to the tau ID BDT for 1-prong (left) and 3-prong (right) tau candidates in simulated $Z \rightarrow \tau\tau$ events (signal) and multi-jet (background) events [80].

4.4 Tau discrimination against electrons

The electron, with ATLAS reconstruction and identification described in Section 3.2.2, forms a significant background to the identification of 1-prong tau candidates, due to the single charged track linked to energy deposits in the EM calorimeter. To reduce the electron background, candidate taus which are within a geometric region of $\Delta R < 0.4$ from a reconstructed candidate electron with $p_{\mathrm{T}} > 5$ GeV have a cut placed on the electron likelihood score, referred to as the electron veto. The likelihood score cut value is dependent on the track $|\eta|$ and p_{T}, and is set to give a 95% efficiency for candidate taus passing the loose tau BDT ID. Candidate taus with no matched candidate electron are given an artificially low likelihood score. The electron likelihood scores for 1-prong candidate taus from simulated

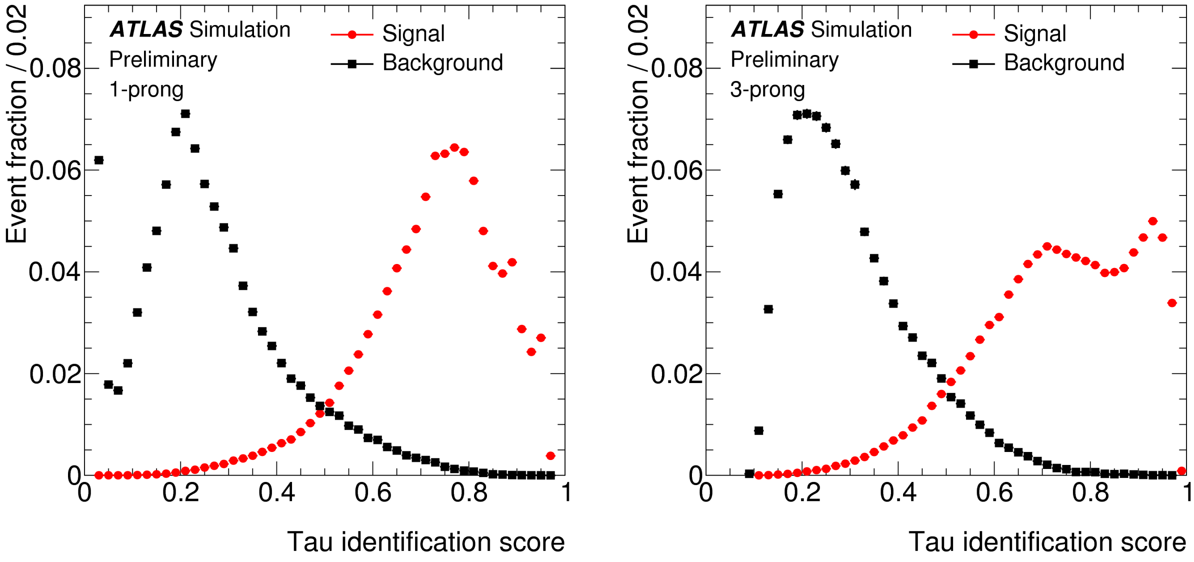

(a) 1-prong

(b) 3-prong

Figure 4.5: Tau ID BDT scores for 1-prong (left) and 3-prong (right) tau candidates from simulated $Z \to \tau\tau$ events (signal) and multi-jet (background) events [80].

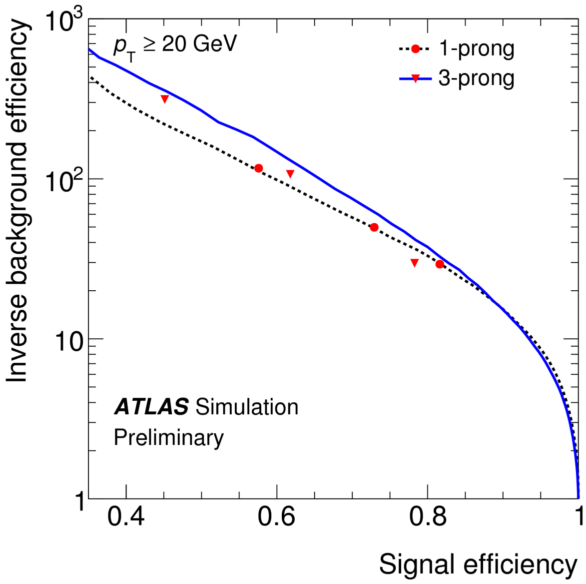

Figure 4.6: The inverse mis-ID efficiency of candidate hadronic taus in dijet events as a function of the ID efficiency of taus with $p_T > 20$ GeV in $Z \to \tau\tau$ events, for 1-prong and 3-prong candidate taus. The three working points are shown, as well as lines of a constant threshold BDT score requirement. The working points are shifted slightly due to the p_T-dependent nature of the BDT score cut [80].

signal $Z \to \tau\tau$ events and simulated background $Z \to ee$ events are shown in Figure 4.7.

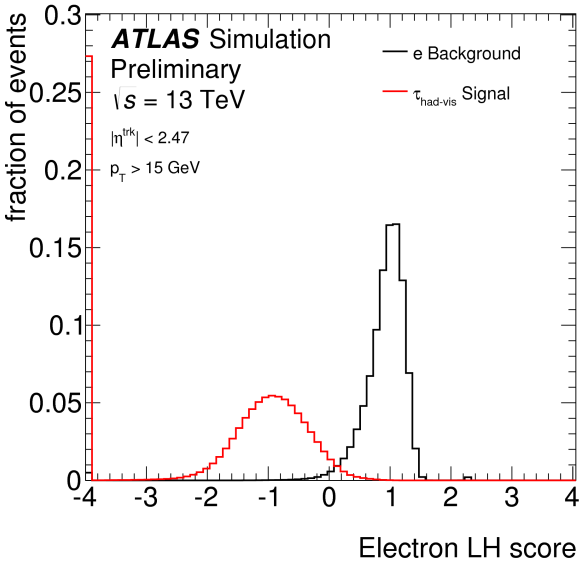

Figure 4.7: Electron likelihood (LH) scores for candidate taus in simulated $Z \to \tau\tau$ (signal) and $Z \to ee$ (background) events. A score of -4 corresponds to candidate taus that are unmatched to electron candidates [80].

4.5 High-p_{T} tau candidates

Studies on the reconstruction of the hadronic decays of tau leptons are conducted primarily on low-p_{T} tau candidates from $Z \to \tau\tau$ decays, and therefore provide limited constraints on the modelling of hadronic taus at high-p_{T}. A conservative uncertainty, $\Delta\varepsilon^{3-prong}$, on the reconstruction efficiency of 3-prong high-p_{T} ($p_{\mathrm{T}}^{\tau} > 150$ GeV) tau candidates is applied via the equation:

$$(\Delta\varepsilon^{3-prong})^2 = (\Delta\varepsilon^{3-prong}_{low-p_{\mathrm{T}}})^2 + (0.000225/\text{ GeV} \times (p_{\mathrm{T}} - 100\text{ GeV}))^2 \tag{4.2}$$

where $\Delta\varepsilon^{3-prong}_{low-p_{\mathrm{T}}}$ is the uncertainty on the reconstruction of tau candidates with $p_{\mathrm{T}}^{\tau} \leq$ 150 GeV. The uncertainty is based on studies during Run-1 and estimated from simulated hadronic tau decays. It covers the effects of track merging, whereby tracks associated with the tau decay overlap, resulting in fewer tracks being associated with the tau candidate.

The performance of the tau identification algorithm at high-p_{T} is also investigated, and described in the rest of this section. At low-p_{T}, the performance of the tau identification algorithm is investigated in simulated $Z \to \tau\tau$ events, with systematic variations applied to the detector material and performance, the PU and the generator and shower simulation. Due to the low number of $Z \to \tau\tau$ events with high-p_{T} tau candidates, the performance of the tau identification algorithm is instead tested on jets through the misidentification rate, with the aim of investigating the agreement between data and simulation as a function of p_{T}. The study uses a tag and probe (T&P) method in an event selection dominated by dijet events where the 'tag' is the leading (highest-p_{T}) tau candidate, and the 'probe' is the subleading (second highest-p_{T}) tau candidate. The effect of the tau identification algorithm on the probe tau candidate is investigated.

The study is designed to quantify the fidelity of the simulation in modelling the tau misidentification in high-p_{T} jets by comparing the misidentification rate with data. As no significant discrepancy between data and simulation is observed, the uncertainty on the tau identification is inflated as a function of p_{T}.

4.5.1 Simulation and event selection

The dijet events are simulated using `PYTHIA` 8.1 [82] with the event samples differentiated according to the generator-level jet p_{T} as shown in Table 4.2. The cross sections of the simulated samples can be found in Appendix A.

A region enriched in dijet events is selected. The event must fire one of the single jet triggers with online p_{T} requirements, listed in Table 4.3 along with the corresponding trigger luminosity. All but the highest p_{T} single jet triggers are prescaled, and so to scale the simulated dijet background to the combination of triggers, each trigger is used in a specific lead jet p_{T} range, also listed in the table. The p_{T} range is selected to be a region in which the trigger has the lowest prescale whilst being at maximum efficiency.

The dijet selection cuts applied to data and simulation are:

- At least two tau candidates, and zero muons or electrons.

sample name	lead jet truth p_{T} range [GeV]
JZ2	60-160
JZ3	160-400
JZ4	400-800
JZ5	800-1300
JZ6	1300-1800
JZ7	1800-2500

Table 4.2: The various dijet simulation samples and lead jet generator-level p_{T} ranges used in the analysis.

Online p_{T} requirement [GeV]	Luminosity [pb^{-1}]	Lead jet p_{T} range [GeV]
110	1.39	150-200
150	5.18	200-250
200	19.03	250-300
260	66.06	300-350
320	184.79	350-400
360	3209.05	> 400

Table 4.3: The online p_{T} requirements of single jet triggers in the 2015 dataset and their effective luminosities accounting for prescale, along with the lead jet p_{T} range each trigger is used in.

- Tag object $p_{\mathrm{T}} > 150$ GeV.
- The number of tracks in the tag object must be greater than 1.
- The tag and probe are required to be produced back-to-back in the detector, satisfying $\cos(\Delta\phi_{\,tag-probe}) < -0.90$.
- The p_{T}-difference between the tag and probe objects is required to be below 20 %.
- An electron BDT veto is applied to the probe object.
- The probe candidate tau must have unit charge.
- The probe candidate tau must have 1 or 3 charged tracks.

The selection ensures a high purity of dijet events, with the tag and probe objects originating from the highest p_{T} vertex, whilst the requirements on the probe object maintain similarity to the selections applied to the reconstructed hadronic tau decays in analyses.

Figure 4.8 shows the number of tracks in the tag object after the full event selection is applied, and is shown separately for the cases of a 1-prong and 3-prong probe tau candidate. It is seen that the shape of the track distribution is successfully modelled for the tag object with the difference between data and simulation in the 3-prong case (and less so the 1-prong case) likely due to the fragmentation modelling of the jets in simulation. The issue is one of normalisation, and so should not bias the final result which compares the misidentification rates measured separately in data and simulation. For aesthetic purposes, in the following plots the simulated events are reweighted by the ratio of total number of data events to the total number of simulated events.

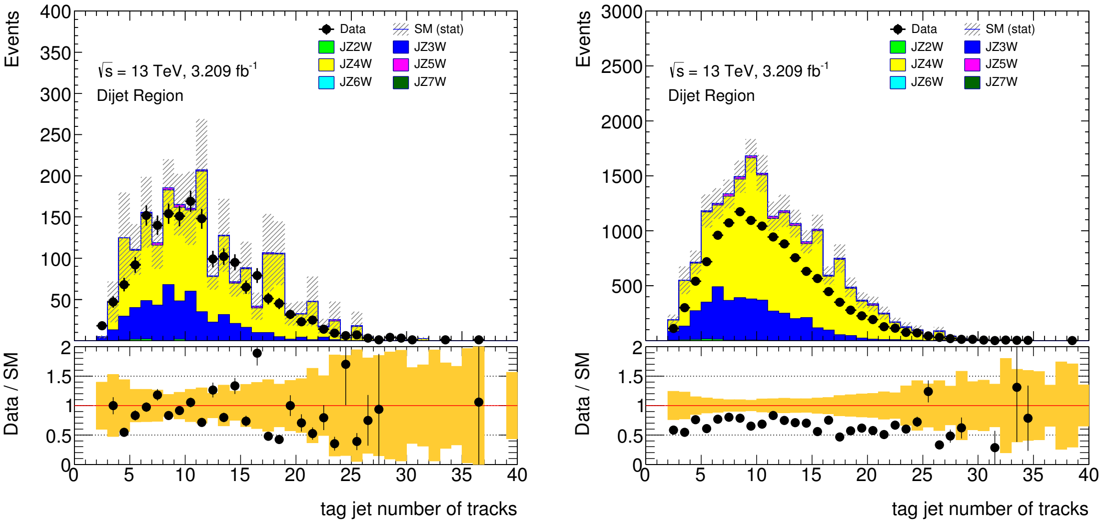

(a) Tag object (1-prong probe tau)

(b) Tag object (3-prong probe tau)

Figure 4.8: Distributions of number of tracks in the tag object in the case of a 1-prong probe tau candidate (left) and 3-prong probe tau candidate (right).

The p_T, η and ϕ distributions of the tag object and probe tau candidate are seen in Figure 4.9 and Figure 4.10 for cases where the probe tau candidate is 1-prong and 3-prong, respectively. These checks confirm that the kinematic distributions of the tag and probe objects are comparable in shape between data and simulation.

In Figures 4.11 and 4.12 the tau identification BDT score distribution of the probe tau candidate is shown for, respectively, 1-prong and 3-prong tau candidates recorded by the various single jet triggers. Reasonable agreement between data and simulation is seen in the case of the 1-prong and 3-prong probe candidate taus, and there is no significant deviation

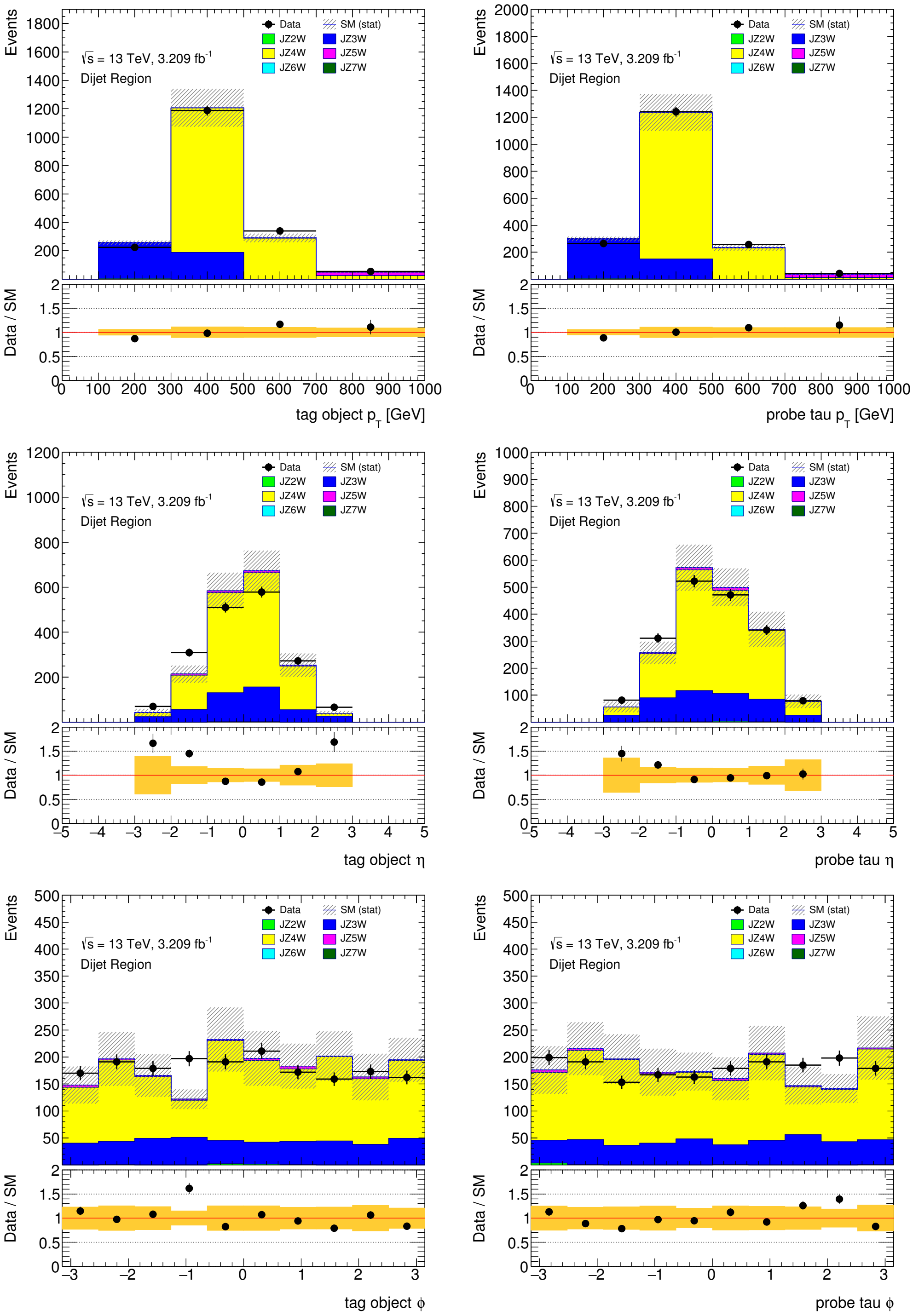

Figure 4.9: p_{T} (top), η (middle) and ϕ (bottom) distributions of the (left) tag, and (right) probe objects, for the case of a 1-prong probe tau.

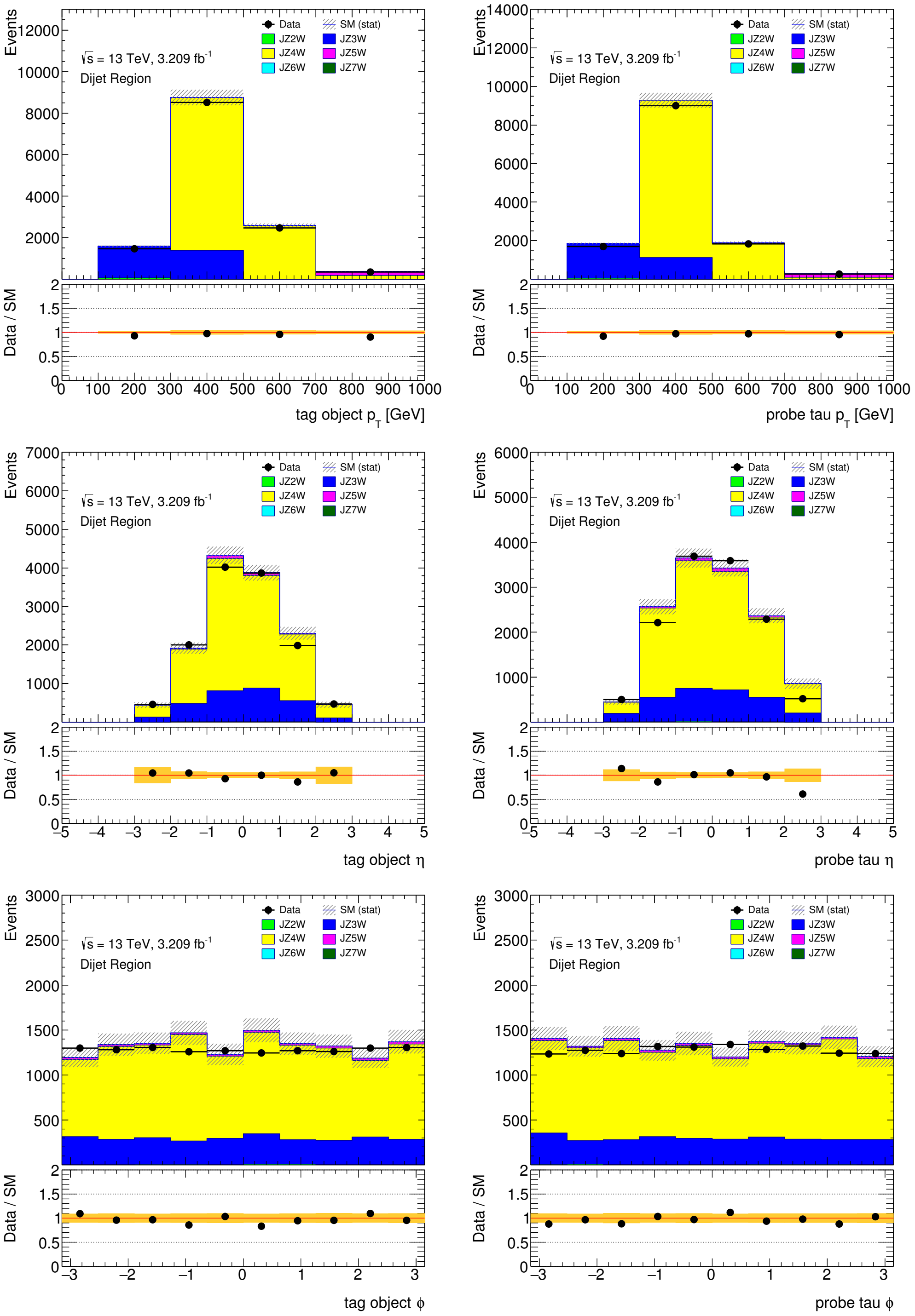

Figure 4.10: p_{T} (top), η (middle) and ϕ (bottom) distributions of the (left) tag, and (right) probe objects, for the case of a 3-prong probe tau.

in the tau-ID modelling between simulation and data.

4.5.2 Misidentification rate of tau particles

The misidentification rate of hadronically decaying tau leptons is the fraction of probe tau candidates that pass the tau identification. As described in Section 4.3, the loose, medium and tight working points that are used in the ATLAS identification of tau particles use a p_{T} dependent cut on this BDT score. Jets in general have a lower BDT score than tau leptons, as can be seen in Figure 4.5, and so instead of using the average working point score, a scan is performed across multiple BDT score cut values. Figure 4.13 shows the misidentification rate for selected BDT score cuts on the probe object as a function its p_{T}. A BDT score cut of 0.4 is shown for 1-prong tau candidates, and 0.25 for 3-prong tau candidates, with the full selection of plots in Appendix B.

In the figures, a linear function is fitted to the ratio of the data and simulation misidentification rates and the fit parameters are displayed. Across all the misidentification plots the gradient of the linear fit is consistent with zero. This is consistent with the assumption that the mismodelling of the tau misidentification rate between data and simulation is flat as a function of p_{T}, within the limits of the statistical uncertainty, and therefore the modelling of the tau identification does not significantly deteriorate at higher-p_{T}.

4.5.3 High-p_{T} tau uncertainty inflation

The uncertainty on the gradient parameters is used to quantify the statement that the modelling of the tau identification does not significantly degrade at high-p_{T}. In the $A/H \to \tau\tau$ analysis presented in Chapter 6, the leading and subleading tau identification efficiency after the rest of the event selection is approximately 85% for 1-prong taus, and 65% for 3-prong taus. A comparable misidentification fraction occurs for the dijet selection when cuts are applied to BDT scores of 0.40 in the case of 1-prong probe objects and 0.25 in the case of 3-prong probe objects. The tau identification uncertainty above 100 GeV is therefore inflated

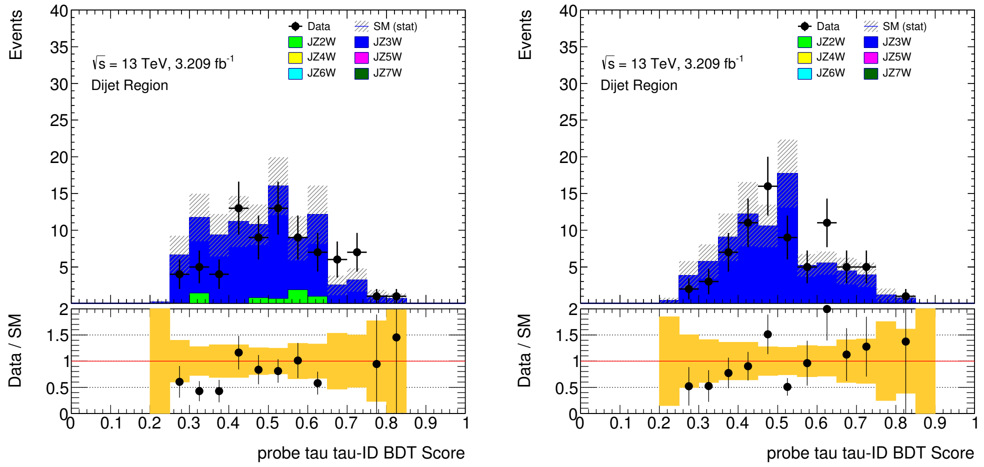

(a) Online jet p_{T} requirement, 110 GeV (b) Online jet p_{T} requirement, 150 GeV

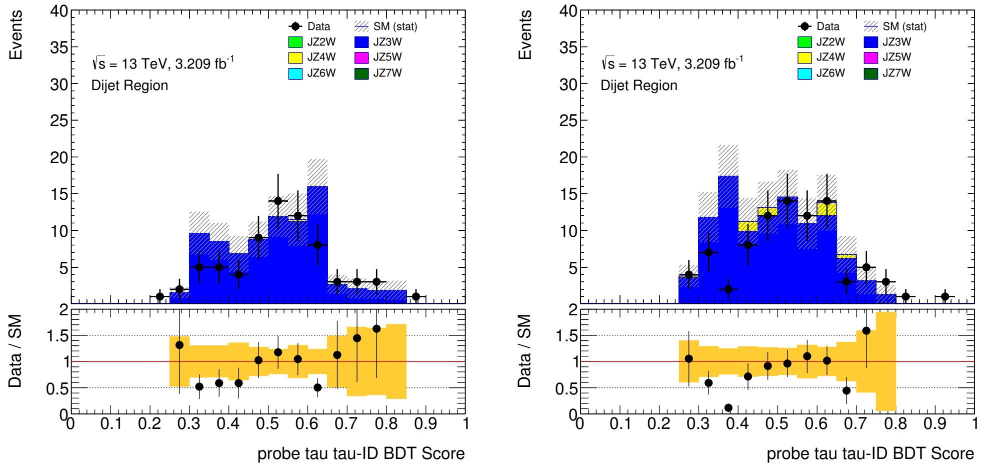

(c) Online jet p_{T} requirement, 200 GeV (d) Online jet p_{T} requirement, 260 GeV

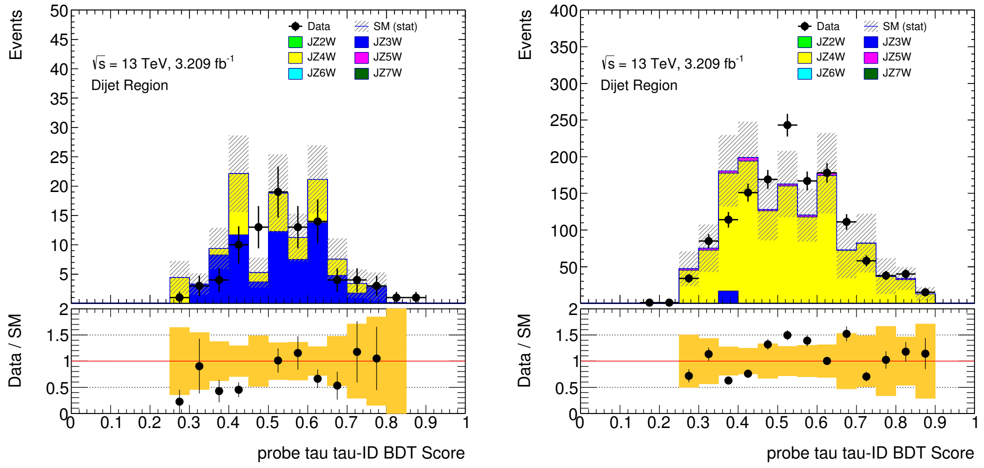

(e) Online jet p_{T} requirement, 320 GeV (f) Online jet p_{T} requirement, 360 GeV

Figure 4.11: Tau identification BDT scores of 1-prong probe tau candidates for various single jet triggers used in the dijet T&P analysis.

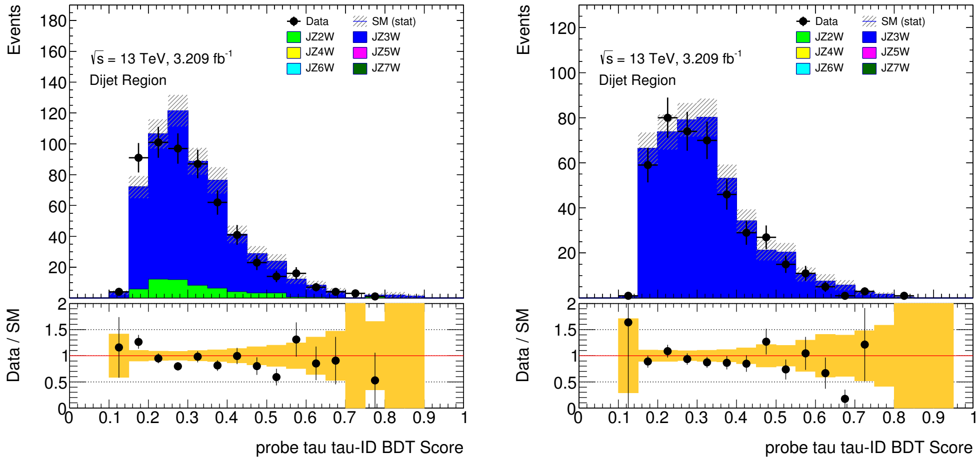

(a) Online jet p_{T} requirement, 110 GeV (b) Online jet p_{T} requirement, 150 GeV

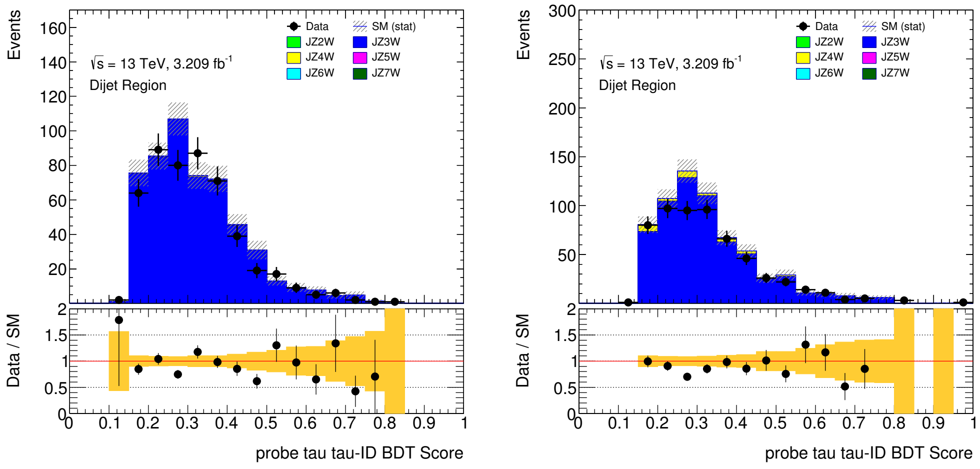

(c) Online jet p_{T} requirement, 200 GeV (d) Online jet p_{T} requirement, 260 GeV

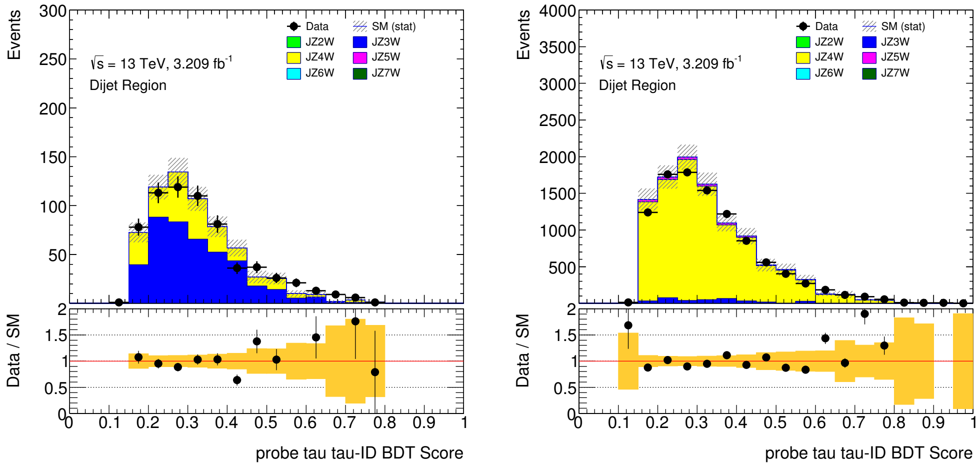

(e) Online jet p_{T} requirement, 320 GeV (f) Online jet p_{T} requirement, 360 GeV

Figure 4.12: Tau identification BDT scores of 3-prong probe tau candidates for various single jet triggers used in the dijet T&P analysis.

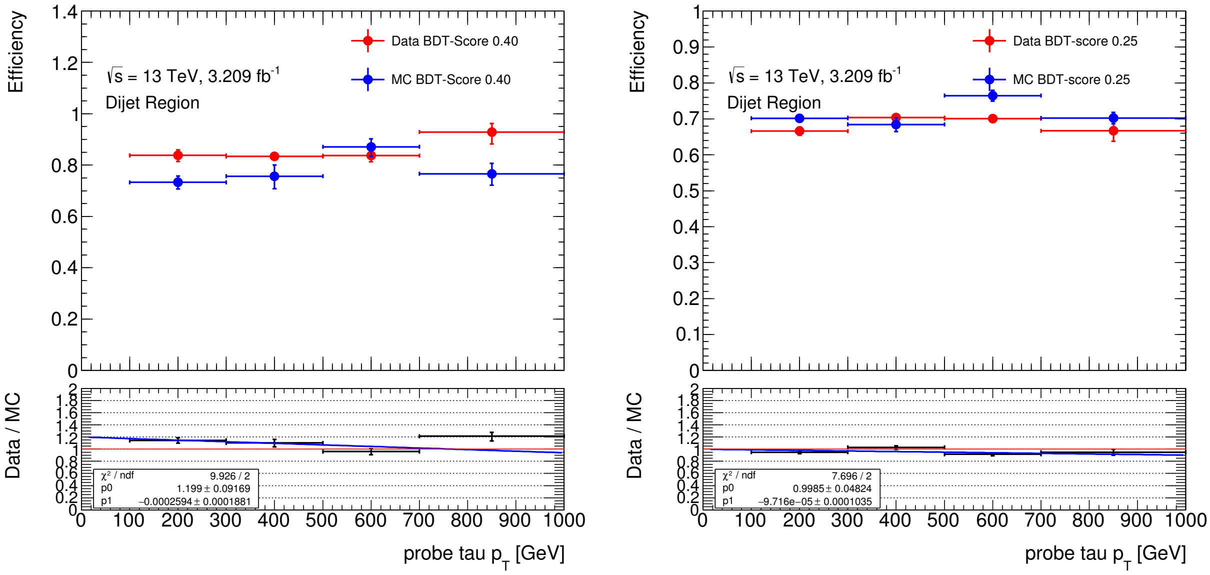

Figure 4.13: The misidentification rate of probe 1-prong (left) and 3-prong (right) tau candidates as a function of the probe object p_{T}, for cuts on the tau identification BDT scores of 0.40 and 0.25, respectively. Both data and simulation are shown as well as the ratio between the two. A linear fit is placed on the data-simulation ratio, and the relevant fit parameters displayed.

by the uncertainty on the gradient parameters, 0.019%/GeV for 1-prong tau candidates and 0.010%/GeV for 3-prong tau candidates, and is summed in quadrature with the asymmetric uncertainty on low-p_{T} tau candidates:

$$(\Delta\varepsilon^{1-prong})^2 = (\Delta\varepsilon^{1-prong}_{low-p_{\mathrm{T}}})^2 + (0.00019/\text{ GeV} \times (p_{\mathrm{T}} - 150\text{ GeV}))^2 \tag{4.3}$$

$$(\Delta\varepsilon^{3-prong})^2 = (\Delta\varepsilon^{3-prong}_{low-p_{\mathrm{T}}})^2 + (0.00010/\text{ GeV} \times (p_{\mathrm{T}} - 100\text{ GeV}))^2 \tag{4.4}$$

This inflation of the uncertainty accounts for the possibility of a deterioration in tau identification for high-p_{T} tau candidates. Figure 4.14 shows how the uncertainty on the tau identification increases as a function of the tau candidate p_{T}.

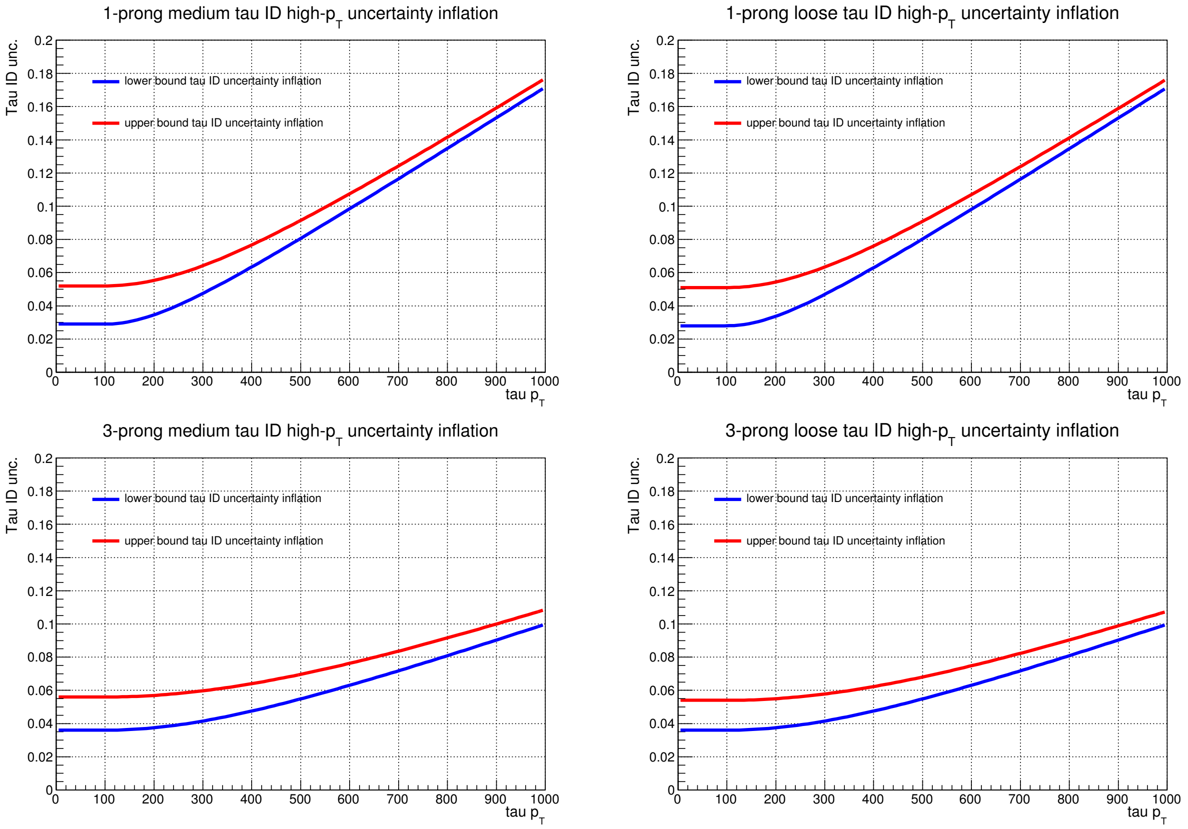

Figure 4.14: Inflation in the uncertainty on the identification of hadronic tau decays as a function of the 1-prong (left) and 3-prong (right) tau candidate p_{T} for the loose (above) and medium (below) identification working points. The upper and lower bounds refers to the upper and lower asymmetrical uncertainties on the tau ID for $p_{\mathrm{T}}^{\tau} < 100$ GeV.

Chapter 5

The Run-2 tau trigger system

The ATLAS trigger system, described in detail in Section 3.1.5, underwent a series of upgrades during LS1, and the tau trigger algorithms were redesigned in order to cope with an increase in backgrounds due to the rise in instantaneous luminosity and centre of mass energy. As discussed in Chapter 4, the high production rate of quark- and gluon-initiated jets forms a significant background in the identification of hadronically decaying tau leptons, and this background is present at the trigger-level (online). As in the case of the reconstruction and identification of tau candidates, the tau trigger targets the hadronic decays of tau leptons, and the muon and electron triggers are used to select the leptonic decays of tau leptons.

This section begins by describing the updated Run-2 tau trigger system [59] in Section 5.1. Before data taking began it was important to test the new algorithms in order to verify that they were behaving as expected. An emulation tool was therefore developed, as described in Section 5.1, and placed in the trigger monitoring software to monitor the data collection from the control room. The first proton-proton collisions of Run-2 occurred with a spacing of 50 ns between colliding proton bunches, and marked the first recorded collisions with a centre of mass energy of $\sqrt{s} = 13$ TeV. The online hadronic tau reconstruction was studied in this early Run-2 data, and Section 5.2 details the measurement of online trigger variables. As the tau trigger algorithms were developed and tested in simulation only, it is important to make comparisons between simulation and the Run-2 data. In Section 5.3, the performance of the tau trigger algorithms is measured in the complete 2015 dataset and compared with the expected performance in simulation.

Many important physics analyses are dependent on the tau trigger for data collection, in particular the SM and BSM Higgs boson searches. The work in this chapter details the development and operation of the tau trigger in the 2015 data-taking period.

5.1 Overview of the Run-2 tau trigger system

Two key changes to the trigger architecture during LS1 have enabled an improvement in the tau trigger strategy. Firstly, the introduction of a new central trigger processor (CTP) enables a greater number of L1 algorithms and L1 object combinations in comparison to Run-1, in particular for triggers dependent on topological information [58]. Secondly, the HLT is now a single processing system, rather than the two-tier system available in Run-1. This has enabled resource sharing, a faster processing time, and therefore more complex algorithms, similar to those of the offline selection. Additionally, the new IBL tracking layer is included in the trigger algorithms. A schematic diagram of the tau trigger system can be seen in Figure 5.1, and this section describes the different stages of the trigger, and the trigger nomenclature.

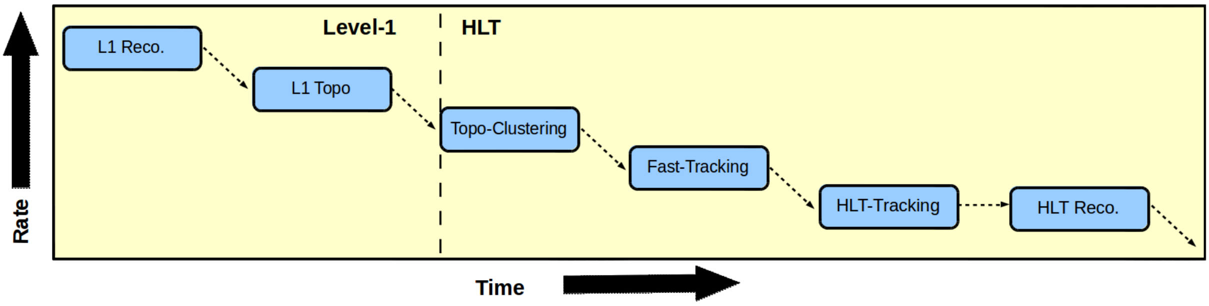

Figure 5.1: Schematic layout of the stages of the tau trigger system at L1 and HLT. The L1Topo system is still in commissioning.

5.1.1 L1 tau trigger

At L1, the first stage of the tau trigger, regions of interest (RoIs) are identified by applying cuts on the transverse energy deposits in summed calorimeter towers, seen in Figure 3.8. The rate for both single and combined (multi-object) tau triggers is reduced to $\lesssim 15$ kHz.

L1 tau trigger towers

The tau trigger RoI is defined by a set of 2×2 calorimeter towers, where at least one 2×1 or 1×2 set of electromagnetic calorimeter towers summed with a set of 2×2 hadronic calorimeter towers passes a pre-defined energy threshold. The energy threshold can be set to be dependent on $|\eta|$. An isolation ring is also defined in the EMCAL around the RoI, and an E_{T} dependent requirement can be placed on the energy in this region. Multiple L1 objects can be requested together, for example two L1 tau objects, or one tau and one muon object, allowing for lower energy thresholds compared to the single-object triggers.

L1 topological trigger

Some analyses, in particular the SM $H \rightarrow \tau\tau$ analysis, will be able to benefit from the L1 topological trigger once the commissioning of the L1Topo is completed. For example a ΔR or $\Delta\eta$ separation could be added between two L1 objects (e.g. between an L1 tau object and an L1 muon/electron/tau object). These requirements reduce the dominant QCD dijet background which tends to be broader in $|\eta|$ and back-to-back in ϕ, whilst the Higgs boson is often produced with transverse and longitudinal momentum, resulting in a smaller ΔR.

5.1.2 HLT tau trigger

The L1 tau RoIs are fed into the HLT where a sequence of ordered steps reduces the rate to $\lesssim 100$ Hz for single and combined tau triggers.

Topo-clustering

The HLT has access to the full-granularity calorimeter information in a $\Delta R < 0.2$ region around the L1 tau object. The topo-clustering [64] algorithm combines calorimeter cells above a certain energy threshold, and the clusters are calibrated at LC-scale. An online tau-specific energy calibration (TES) is applied to the clusters, and the position and energy redefined. A cut is then placed on the transverse energy of the HLT tau object.

Tracking

A multi-stage tracking system is used to reconstruct tracks in a sufficiently large ΔR cone around the tau candidate.

The first stage, referred to as fast-tracking (not to be confused with the Fast TracKer system, FTK, still in the commissioning stage), reconstructs tracks using trigger-specific pattern recognition algorithms. Two steps of fast-tracking occur. The first is used to identify the highest-p_{T} (leading) track in a narrow cone ($\Delta R < 0.1$) around the RoI and along the full beam-line in order to identify the event vertex. The second step reruns the fast-tracking software in an extended cone ($\Delta R < 0.4$) around the RoI, but with a narrow width along the beamline, centred around the event vertex. A requirement is made on the number of tracks within a core ($\Delta R < 0.2$) and isolation ($0.2 < \Delta R < 0.4$) region of $0 < N_{\mathrm{core}}^{\mathrm{tracks}} < 4$ and $N_{\mathrm{iso}}^{\mathrm{tracks}} < 2$, respectively.

Finally, the spacepoints and tracks identified in the fast-tracking stages are used as seeds for the HLT-tracking stage. HLT-tracking refers to the precision reconstruction of tracks with algorithms similar to those used in the offline reconstruction, and results in a significantly improved impact parameter resolution.

HLT Identification

The HLT precision track and calorimeter information is used to calculate a number of variables, which are input into a tau-trigger BDT after a pile-up (PU) correction. The variables used in the online BDT are the same as those used in the offline BDT, described in Section 4.3, and the same training has been used. As in the case of offline tau identification, three ID working points are available for 1-prong and 3-prong online tau candidates: loose, medium and tight.

HLT di-tau vertex separation

During the development of the tau trigger algorithms, a number of different strategies were attempted to reduce the rate whilst maintaining a high efficiency. In the new energy regime of Run-2, a particular concern was a high L1 rate overloading the HLT in the di-tau triggers (two tau objects at L1 and HLT), which have lower energy thresholds than the single-tau triggers. One strategy that was studied to mitigate this rate involved placing a requirement on the separation of the leading tracks of the L1 objects at the beginning of the HLT reconstruction algorithms.

Figure 5.2 shows the Δz separation between the vertices of the leading HLT fast-tracks for $Z \to \tau\tau$ and low-energy multi-jet events. The leading tracks are associated with a 20 GeV isolated L1 tau object and a 12 GeV isolated L1 tau object. The plot shows that there is no significant gain in placing a requirement on the separation of the leading tracks in the L1 objects, and the strategy was not pursued further.

5.1.3 Trigger strategy and nomenclature

Example primary tau triggers available in 2015 can be seen in Table 5.1, and are the main unprescaled triggers used in physics analyses. The tau trigger menu, that is, the list of L1 and HLT triggers available, also consists of a number of support triggers with various combinations of trigger-level tau objects, often prescaled and used for monitoring purposes, and a series of backup triggers which have tighter object selections and replace the primary triggers as the LHC moves to higher instantaneous luminosities and trigger rates. Finally, during the commissioning of new triggers, a set of alternative triggers with new algorithms

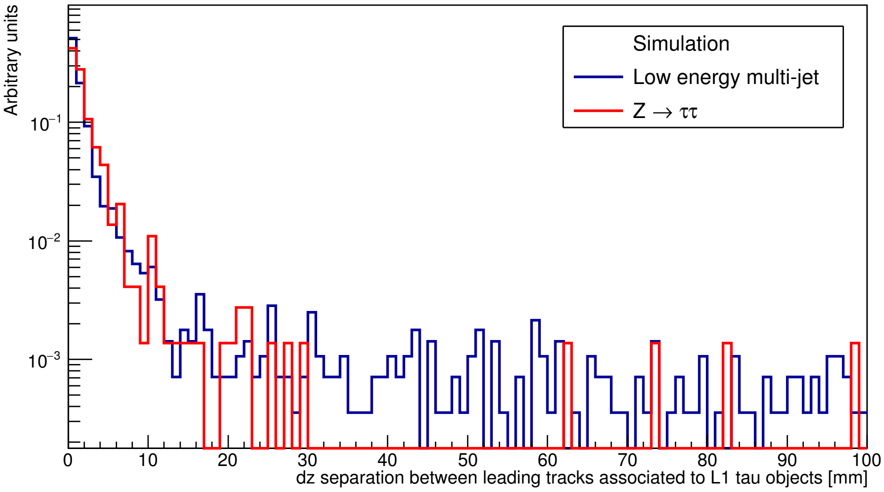

Figure 5.2: The separation along the beam line of the vertices of the highest-p_T tracks associated with two isolated L1 tau objects with transverse energies of 20 GeV and 12 GeV respectively.

to be tested may be included in the trigger menu.

Trigger type	Target analysis	Primary trigger name
Single-tau trigger	BSM $H/A \to \tau_\mathrm{had}\tau_\mathrm{had}$	HLT_tau80_medium1 L1_TAU60
Di-tau trigger	SM $H \to \tau_\mathrm{had}\tau_\mathrm{had}$	HLT_tau35_medium1_tau25_medium1 L1_TAU20IM_2TAU12IM
Tau + muon trigger	SM $H \to \tau_\mu\tau_\mathrm{had}$	HLT_mu14_iloose_tau25_medium1 L1_MU10_TAU12IM_J25_2J12
Tau + electron trigger	SM $H \to \tau_e\tau_\mathrm{had}$	HLT_e17_lhmedium_iloose_tau25_medium1 L1_EM15HI_2TAU12IM_J25_3J12
Tau + $E_\mathrm{T}^\mathrm{miss}$	BSM $H^\pm \to \tau_\mathrm{had}^\pm\nu$	HLT_tau35_medium1_xe70 L1_XE45_TAU20IM_2J20

Table 5.1: Example primary tau triggers used in 2015, and the main related analysis. Due to lower than expected trigger rates, not all triggers were used by the target analyses in 2015.

The naming of the triggers differs between L1 and HLT. The L1 objects are differentiated with capital letters, with 'TAU', 'J', 'EM', 'MU' and 'XE' referring to L1 tau, jet, electron, muon and $E_\mathrm{T}^\mathrm{miss}$ objects respectively. The number before the L1 object refers to the number of L1 objects used in the trigger chain, while the number after refers to the transverse energy requirement (in GeV). Following the name may be a series of letters, which refer to different types and levels of isolation: 'I', 'IL', 'IM', 'IT' refer respectively to a predefined maximum EMCAL energy and a variable maximum EMCAL energy dependent on object p_T with loose, medium and tight requirements, where the EMCAL energy is within an isolation ring surrounding the core 2×2 trigger towers; 'H' refers to a maximum energy requirement in an HCAL isolation ring.

When L1Topo requirements are applied, letters at the end of the trigger name refer to different topological requirements on the L1 trigger objects, and are separated by hyphens. 'DR' refers to a ΔR requirement on the two following objects ($0 < \Delta R < 2.8$ unless otherwise stated), while 'BOX' refers to a $\Delta\phi$ and $\Delta\eta$ requirement ($0 < \Delta\phi < 2.0$ and $0 < \Delta\eta < 2.0$ unless otherwise stated). The L1Topo triggers include 'disambiguation' algorithms that ensure that no two L1 objects are used twice in the trigger sequence (for example a TAU object also passing the J requirements).

The HLT trigger naming uses lower case letters for the HLT objects, followed by the online p_{T} requirement. The working point of the online ID requirement in the tau trigger is denoted by 'loose', 'medium' or 'tight'. Other triggers use a similar naming system, with a preceding 'i' referring to the level of isolation. For tau triggers, the type of tracking algorithm used in the chain may also be included in the name, with the default two-step tracking name, 'tracktwo', often omitted.

5.1.4 Preparation for Run-2 data-taking

In commissioning the new tau triggers for Run-2, it was important to confirm in simulation (and later in data) that the trigger-level decisions are as expected. This was particularly important for the L1 trigger decisions, where there was more uncertainty on the tau trigger rates. A 'trigger emulation tool' was designed that would take a trigger name and data or simulation file as input, and access the trigger-level objects to reconstruct the decisions using the object information. This could then be compared with the online algorithms in data and simulation, where the central trigger processor (CTP) is used in decision making.

The main purpose of the tool was to reproduce the trigger decisions in simulation, and later in data, in order to understand and verify that the trigger decisions were being made correctly (or at least as expected). By making the tool customisable, it could also be used in the design, optimisation and testing of future trigger chains, and potentially used in estimating simulated processes for certain analyses where the trigger information is not accessible.

In the process of developing the tool, the L1 algorithms were tested on samples of simulated events that were regularly updated with new releases of the trigger software. Issues were found in the calorimeter isolation algorithms, and were duly changed. Figure 5.3 shows the number of decisions where the emulation tool and the actual trigger differed, compared to the total number of trigger decisions, in a large sample of simulated $Z \to \tau\tau$ events. The tau-exclusive algorithms not using L1Topo show a 100% correspondence between the trigger and emulation. The L1Topo trigger chains were still in commissioning at the time of writing this thesis.

The trigger emulation tool was integrated into the online tau trigger monitoring software to assess the real-time performance of the tau trigger with data. Figure 5.4 shows the difference between emulation tool passes and trigger passes in the trigger monitoring software in the 2015 data. The mismatch between the number of events registered by the trigger and the number of events expected by the emulation tool is below 0.3%.

5.2 Early Run-2 commissioning of the tau trigger

As part of the commissioning of the online and offline Run-2 tau reconstruction and identification algorithms, a series of studies was completed on the early Run-2 data [4]. The recorded data for the first studies consisted of the first centre of mass $\sqrt{s} = 13$ TeV proton-proton collisions, had a spacing of 50 ns between proton bunches and had an instantaneous luminosity of 6.6 pb^{-1}. As more data came in, the studies were updated to use the full 78.3 pb^{-1} of 50 ns data [5]. The HLT variables were investigated to check that the online reconstruction of tau candidates in data was consistent with that expected in simulation. Additionally a first measurement of the trigger efficiency was made.

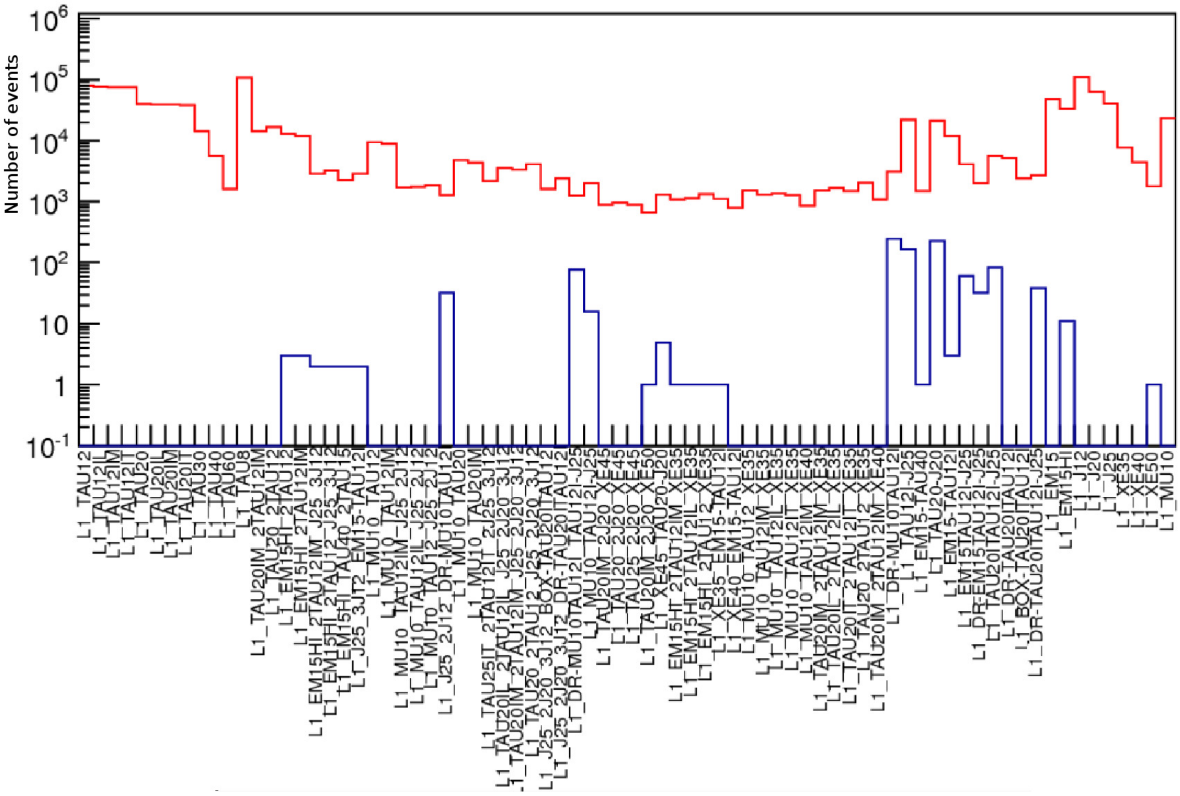

Figure 5.3: The number of trigger passes (red), and the number of differences between the trigger and tau trigger emulation (blue), for various L1 trigger chains in a sample of simulated $Z \to \tau\tau$ events.

5.2.1 Tag and probe method

The tag and probe (T&P) method is used to investigate the trigger-level variables of tau candidates, and the efficiency of the tau trigger. In this method, a sample of events enriched in $Z \to \tau_\mu \tau_h$ production is selected, where τ_h denotes the hadronic decay of the tau lepton and τ_μ denotes the muonic decay. A reconstructed and identified muon is required to pass the muon trigger, and is considered the 'tag' object. The leading tau candidate reconstructed and identified offline is then 'probed' to see if it geometrically matches ($\Delta R < 0.2$) a tau candidate reconstructed by the HLT and passing a certain tau trigger. The kinematic distributions associated with the HLT tau candidates are compared between data and simulation

In order to investigate the trigger-level reconstruction of quark- or gluon-initiated jets that are misidentified as tau candidates, a second T&P study is carried out on a sample enriched in $W(\to \mu\nu)$+jets events. Here the 'tag' object is as before, but the 'probe' object,

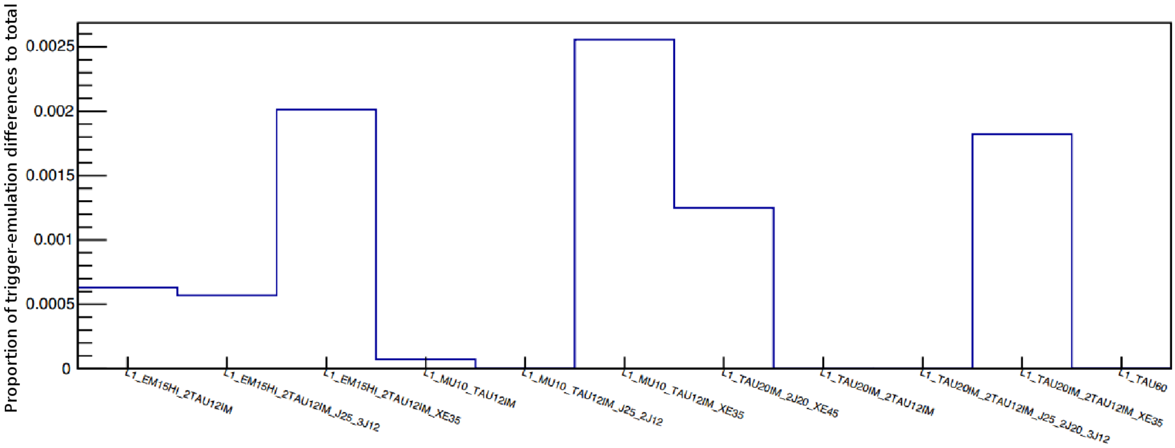

Figure 5.4: The ratio of the number of differences between the trigger and the emulation tool to the number of trigger passes for various L1 trigger chains in 2015 data. The difference is measured in the online tau trigger monitoring system.

a reconstructed offline tau candidate, is likely to be a misidentified jet associated with the hard-scatter process.

5.2.2 $Z \to \tau_\mu \tau_h$ tag and probe

The signal region requirements on the $Z \to \tau_\mu \tau_h$ T&P selection are designed to increase signal purity by reducing backgrounds, particularly from QCD jet production, and W+jets events. The requirements are as follows:

- Exactly one muon, at least one tau candidate and zero loose-ID electrons.
- The muon has a medium ID working point, fixed-threshold isolation and $p_\mathrm{T} > 22$ GeV.
- The muon passes the single-muon trigger with an online p_T threshold of 20 GeV (HLT_mu20_iloose_L1_MU15).
- The leading tau candidate has opposite-sign charge to the muon (OS), passes the offline medium tau-ID BDT working point, has 1 or 3 tracks (1-prong or 3-prong) and has a $p_\mathrm{T} > 20$ GeV.

- The tau candidate is geometrically matched to an online tau candidate passing the HLT_tau25_medium1_tracktwo_L1_TAU12IM trigger.

- The separation in η between the muon and tau candidate satisfies $|\Delta\eta(\mu, \tau_{\text{had}})| < 1.5$, and the difference in transverse momentum satisfies $\Delta p_{\text{T}} = p_{\text{T}}^{\tau_{\text{had}}} - p_{\text{T}}^{\mu} > -15$ GeV. The candidate taus and muons from $Z \to \tau\tau$ events tend to have a smaller separation in η and p_{T} due to the transverse momentum of the Z boson.

- The transverse mass of the muon and $E_{\text{T}}^{\text{miss}}$ system, $m_T(\mu, E_{\text{T}}^{\text{miss}})$, has the requirement $m_T(\mu, E_{\text{T}}^{\text{miss}}) = \sqrt{2p_T^{\mu} E_{\text{T}}^{\text{miss}}(1 - \cos\Delta\phi(\mu, E_{\text{T}}^{\text{miss}}))} < 50$ GeV. This reduces the W+jets background, which contains a significant amount of transverse mass.

- The sum of the cosines of the separation between the muon and $E_{\text{T}}^{\text{miss}}$ and the tau candidate and $E_{\text{T}}^{\text{miss}}$ satisfies $\sum_{\ell=\mu,\tau_{\text{had}}} \cos\Delta\phi(\ell, E_{\text{T}}^{\text{miss}}) > -0.5$. For $Z \to \tau\tau$ processes, the variable is centred at zero as the direction of the $E_{\text{T}}^{\text{miss}}$ tends to point in the direction of one the Z boson decay products. For W+jets production the value is generally negative as the direction of the $E_{\text{T}}^{\text{miss}}$ tends to point away from the muon and tau candidates.

- The reconstructed invariant mass of the muon and tau candidate 4-momenta, referred to as the visible mass, m_{vis}, must be within the range 45 GeV $< m_{vis}(\mu, \tau_{\text{had}}) <$ 85 GeV around the $Z \to \tau\tau$ peak.

The selection provides a high purity of $Z \to \tau\tau$ events whilst reducing backgrounds, particularly from QCD and W+jets processes.

Estimation of signal and background processes

The early 2015 data is compared to expected online distributions from SM processes. The signal process of $Z \to \tau\tau$ is modelled using the `Powheg-Box` v2 [83–85] generator, showered with `Pythia 8.186` [77,78]. The background resulting from QCD jets is modelled using data where the muon and tau candidate have the same-sign charge (SS). The background $Z \to$

$\ell\ell$ and W+jets processes are modelled by simulation in the same way as the signal process, whilst the $t\bar{t}$ background uses `Powheg-Box` v1 and `Pythia 6.428` [86]. The cross sections of the simulated samples can be found in Appendix A. The number of same-sign charge events predicted from these simulated processes is subtracted from the number of SS events in data, to avoid double counting in the SS background estimation procedure.

Results

A comparison between the data and expected SM reconstructed HLT distributions is shown in Figure 5.5 for several online kinematic variables. The figures show that there is a reasonable agreement between the expected and observed distributions, within the limits of statistical uncertainty. Appendix C shows the early tau trigger monitoring plots after the first week of data taking.

5.2.3 $W(\rightarrow \mu\nu)$+jets tag and probe

The signal region requirements on the $W(\rightarrow \mu\nu)$+jets T&P selection are as follows:

- Exactly one muon, at least one tau candidate and zero loose-ID electrons.
- The muon has medium ID working point, fixed-threshold isolation and $p_{\mathrm{T}} > 22$ GeV.
- The muon passes the single-muon trigger with an online p_{T} threshold of 20 GeV.
- The leading tau candidate has opposite-sign charge to the muon (OS), is 1-prong or 3-prong and has a $p_{\mathrm{T}} > 20$ GeV.
- The leading tau candidate is geometrically matched to an online tau candidate passing the HLT_tau25_medium1_tracktwo_L1_TAU12IM trigger.
- The transverse mass of the muon and $E_{\mathrm{T}}^{\mathrm{miss}}$ system satisfies $m_T(\mu, E_{\mathrm{T}}^{\mathrm{miss}}) > 50$ GeV.
- The missing transverse momentum satisfies $E_{\mathrm{T}}^{\mathrm{miss}} > 20$ GeV. The presence of the neutrino in $W+$jets events results in $E_{\mathrm{T}}^{\mathrm{miss}}$.

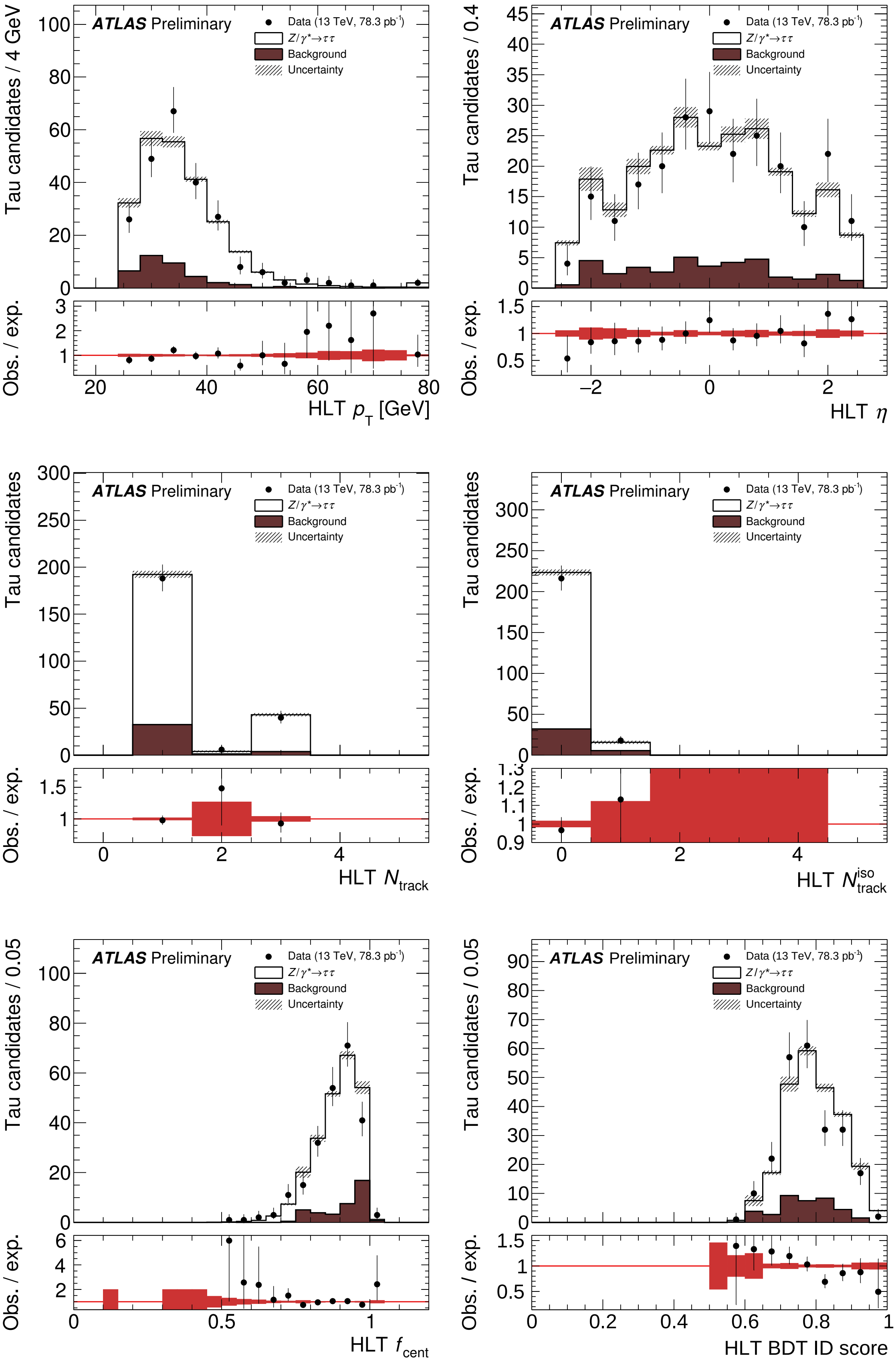

Figure 5.5: Kinematic distributions of online tau candidates measured in a sample enriched in $Z \to \tau_\mu \tau_h$ events. The data correspond to an integrated luminosity of 78.3 pb^{-1}. 'Background' refers to the sum of SS data and the simulated $Z \to \ell\ell$, W+jets and $t\bar{t}$ processes with the SS component subtracted. Only statistical uncertainties are shown.

Estimation of signal and background processes

Signal $W(\rightarrow \mu\nu)$+jets and background processes are modelled by simulation, using the same generators as in the case of $Z \rightarrow \tau_\mu \tau_h$ T&P. The background resulting from QCD jets is similarly estimated using data where the muon and tau candidate have the same charge sign. The simulated processes have this SS component subtracted to avoid double counting in the SS background.

Results

A comparison between the data and expected SM reconstructed HLT distributions is shown in Figure 5.6 for several online kinematic variables. The events shown are dominated by quark- and gluon-initiated jets misidentified by the HLT as tau candidates, and the figures show that there is a reasonable agreement between the expected and observed distributions, within the limits of statistical uncertainty.

5.2.4 Early Run-2 trigger efficiency

The trigger efficiency is defined as:

$$\epsilon_{\text{trigger}} = \frac{N_{\text{events passing trigger}}}{N_{\text{all events}}}, \tag{5.1}$$

where N is the number of events after a given event selection. For the tau trigger efficiency measurement, the event selection is designed to give a sample enriched in $Z \rightarrow \tau_\mu \tau_h$ processes, and the efficiency is measured in the early Run-2 data and compared to the efficiency expected from simulated $Z \rightarrow \tau\tau$ events. The T&P method is used, whereby a reconstructed muon passing the single-muon trigger constitutes the ‘tag’ object, and a hadronic tau decay reconstructed offline is probed to see if the tau trigger is passed. The event selection and estimation of signal and background processes is as described in Section 5.2.2. The measurement is made with respect to the transverse momentum of the tau candidate, reconstructed offline.

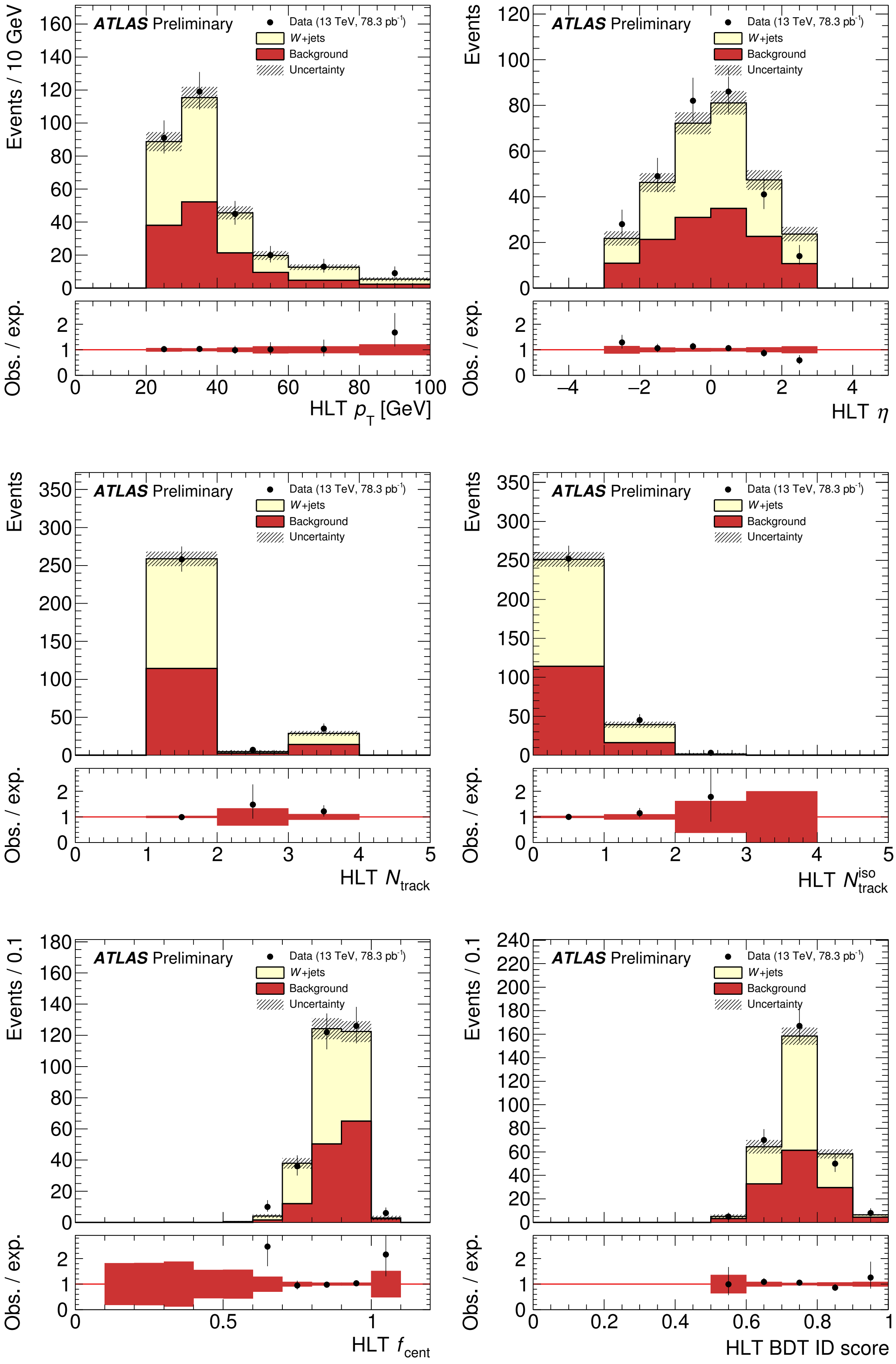

Figure 5.6: Kinematic distributions of online tau candidates measured in a sample enriched in $W(\rightarrow \mu\nu)$+jets events. The data correspond to an integrated luminosity of 78.3 pb^{-1}. 'Background' refers to the sum of SS data and the simulated Z+jets and $t\bar{t}$ processes with the SS component subtracted. Only statistical uncertainties are shown.

In this efficiency measurement, the HLT_tau25_medium1_L1_TAU12IM trigger is used, and is measured separately for the L1 and the combined L1+HLT components. The distributions of the transverse momentum of the tau candidate, reconstructed offline, are shown in Figure 5.7, for all events passing the selection without the tau trigger requirement (the denominator in Equation (5.1)) as well as events passing the L1 and L1+HLT (the numerators).

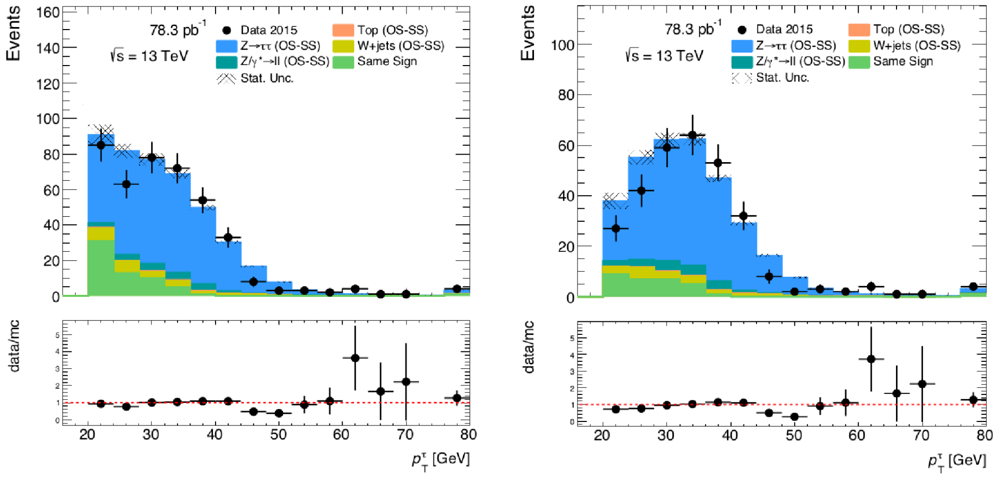

(a) All events

(b) L1_TAU12IM

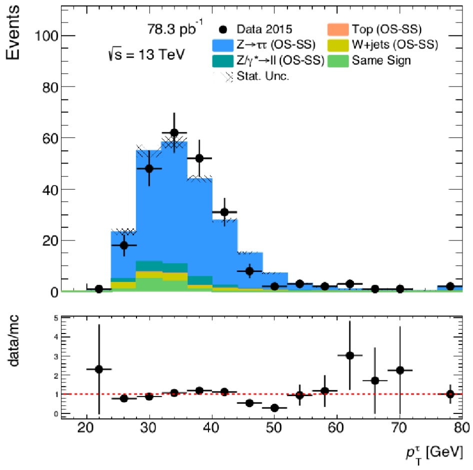

(c) HLT_tau25_medium1_L1_TAU12IM

Figure 5.7: The transverse momentum of tau candidates, reconstructed offline and passing the medium tau identification working point, passing various stages of the tau trigger. The events are taken from a sample enriched in $Z \rightarrow \tau_\mu \tau_h$ production. Only statistical uncertainties are shown. The plots are made in collaboration with a colleague.

To ensure that the trigger efficiency measurement in data is comparable with simulation, the expected number of signal region events from background (non-$Z \to \tau\tau$) processes, $N^{\text{background}}$, is first subtracted from the signal region data, N^{data}. Equation (5.1) is thus modified to:

$$\epsilon^{\text{data}}_{\text{trigger}} = \frac{N^{\text{data}}_{\text{events passing trigger}} - N^{\text{background}}_{\text{events passing trigger}}}{N^{\text{data}}_{\text{all events}} - N^{\text{background}}_{\text{all events}}}, \tag{5.2}$$

Figure 5.8 shows the trigger efficiency measured in data and compared with simulation with respect to the transverse momentum of the offline tau candidate. The efficiency measured in data and the expected efficiency from simulated $Z \to \tau\tau$ events are consistent within the limits of statistical uncertainty.

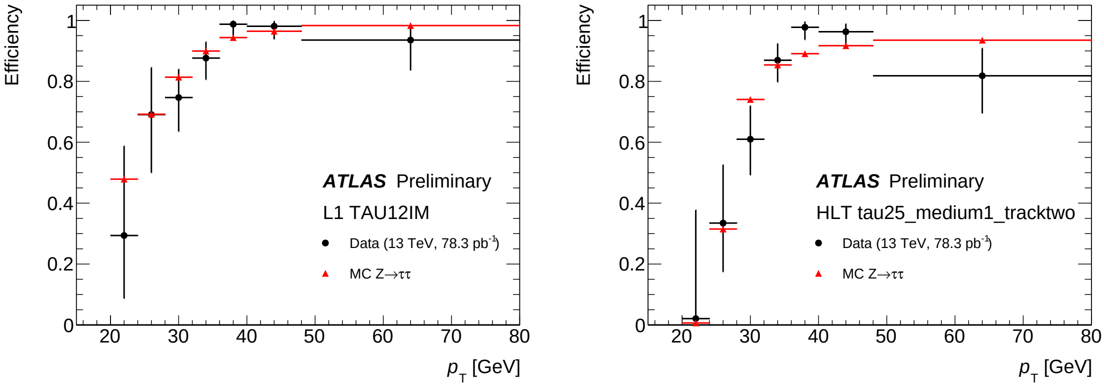

Figure 5.8: The L1 (left) and combined L1+HLT (right) single-tau trigger efficiencies measured in data and in a simulated sample of $Z \to \tau\tau$ events (MC), with respect to the transverse momentum of the tau candidate reconstructed offline. The events are taken from a sample enriched in $Z \to \tau_\mu\tau_h$ processes, and the data events have the estimated background from non-$Z \to \tau\tau$ processes subtracted. Only statistical uncertainties are shown. The plots are made in collaboration with a colleague.

5.3 Measurement of the tau trigger efficiency

A second measurement of the tau trigger efficiency is performed on the complete 2015 dataset, and uses the same T&P method as in the early Run-2 measurement. The trigger efficiency in data is measured in a selection of events designed to be enriched in $Z \to \tau_\mu\tau_h$ production and is compared to the trigger efficiency measured in a simulated sample of $Z \to \tau\tau$ events undergoing the same event selection. In the measurement in data, the estimated contribution of non-$Z \to \tau\tau$ processes after the event selection is subtracted from the data, in order to give a comparative sample of events.

The trigger scale factor, defined as the ratio of the trigger efficiency measured in data and simulation, quantifies the discrepancy in the trigger performance between data and simulation. The scale factor can be applied as a weighting to simulated events in order to correct the discrepancy between data and simulation.

This section describes the measurement of the trigger efficiency and scale factors for various tau triggers available in the 2015 data. First, the event selection is discussed, followed by a description of the method used to estimate signal and background processes. Finally the efficiencies and corresponding scale factors are presented for a variety of triggers.

5.3.1 Event selection

The signal region requirements for the $Z \to \tau_\mu \tau_h$ T&P selection are similar to those used in the early Run-2 measurement, and have been optimised and harmonised with the offline tau identification and tau energy scale performance measurements. In addition to the signal region, control regions are also defined and used in deriving scale factors for some of the background processes. The base requirements, common to both signal and control regions are as follows:

- Exactly one muon, at least one tau candidate, zero loose-ID electrons, and zero b-jets.
- The muon has a medium ID working point and has $p_{\mathrm{T}} > 22$ GeV.
- The muon passes the single-muon trigger with an online p_{T} threshold of 20 GeV (HLT_mu20_iloose_L1_MU15).
- The leading tau candidate passes a specific tau-ID BDT working point, is 1-prong or 3-prong and has $p_{\mathrm{T}} > 25$ GeV.

The additional selections which define the signal region are:

- The leading tau candidate has opposite-sign charge to the muon (OS).
- The muon has fixed-threshold isolation.
- The transverse mass of the muon and $E_{\mathrm{T}}^{\mathrm{miss}}$ system satisfies $m_T(\mu, E_{\mathrm{T}}^{\mathrm{miss}}) < 50$ GeV.
- The sum of the cosines of the separation between the muon and $E_{\mathrm{T}}^{\mathrm{miss}}$ and the tau candidate and $E_{\mathrm{T}}^{\mathrm{miss}}$ satisfies $\sum_{\ell=\mu,\tau_{\mathrm{had}}} \cos\Delta\phi(\ell, E_{\mathrm{T}}^{\mathrm{miss}}) > -0.5$.
- The visible mass of the combined muon and tau candidate system must be within the range 45 GeV $< m_{\mathrm{vis}}(\mu, \tau_{\mathrm{had}}) <$ 80 GeV.

The selection provides a high purity of $Z \to \tau\tau$ events whilst reducing backgrounds, particularly from QCD multi-jet and W+jets processes. In addition to the signal region, an orthogonal control region is defined, where the muon and leading tau candidate have the same-sign charge, and is referred to as the 'SS' control region.

In order to model the backgrounds from multi-jet and W+jets processes, additional control regions are defined with no overlap of signal region events. An 'anti-isolation' control region enriched in multi-jet events differs from the signal region by inversion of the fixed-threshold isolation requirement, and by dropping the requirement on the visible mass of the muon-tau system. A control region enriched in W+jets events is also defined by the requirements of $E_{\mathrm{T}}^{\mathrm{miss}} > 30$ GeV and $m_T(\mu, E_{\mathrm{T}}^{\mathrm{miss}}) > 60$ GeV, on top of the base requirements with the muon isolation requirement in place. It is referred to as the W+jets control region. Separate 'OS' and 'SS' anti-isolation and W+jets control regions are defined for the case where the muon and leading tau candidate have opposite and same charge signs.

In the numerator of the efficiency definition in Equation (5.1), the requirement is added that a specific trigger is passed and that the HLT tau candidate passing the trigger has a separation of $\Delta R < 0.2$ from the leading tau candidate. To measure the efficiency of prescaled triggers, the full 2015 dataset is used, with the trigger decision 'resurrected' in all events. A resurrected trigger means that the trigger decision is recomputed in the offline event reconstruction in all events, without the prescale applied.

The efficiency measurements were performed before the updated 2015 luminosity measurement was available, so the data correspond to an integrated luminosity of 3.3 fb^{-1}.

5.3.2 Estimation of signal and background processes

The main background processes to the signal $Z \to \tau\tau$ process come from QCD multi-jet, W+jets, $t\bar{t}$ and $Z \to \ell\ell$ (where $\ell =$ muon or electron) processes. The $Z \to \ell\ell$ and $t\bar{t}$ processes contribute minor backgrounds to the signal region and are estimated using simulated events. The W+jets background is also estimated using simulated events, but with a data-driven correction factor applied to the background. Due to the large cross section associated with the production of multi-jet events from QCD interactions and the inadequate modelling of these processes in simulation, a data-driven approach is used to estimate this background using SS control region events.

The simulation of signal and background processes is as described in Section 5.2.2, and the cross sections of the simulated samples can be found in Appendix A. The W+jets and QCD multi-jet estimation techniques are described in the rest of this section.

Same sign multi-jet estimation

The shape of the multi-jet background is taken from the SS control region, with a normalisation factor, r_{QCD}, applied to the events. The normalisation factor, calculated separately for 1-prong and 3-prong tau candidate events, is derived in the anti-isolation control region, and is the ratio of OS to SS events:

$$r_{\text{QCD}} = \left. \frac{N_{\text{OS}}^{\text{data}} - N_{\text{OS}}^{\text{non-multi-jet MC}}}{N_{\text{SS}}^{\text{data}} - N_{\text{SS}}^{\text{non-multi-jet MC}}} \right|_{\text{anti-isolation}}, \tag{5.3}$$

where $N_{\text{OS(SS)}}^{\text{data}}$ and $N_{\text{OS(SS)}}^{\text{non-multi-jet MC}}$ refer to the number of data and simulated non-multi-jet events, respectively, in the OS (SS) anti-isolation control region. The r_{QCD} normalisation factor is applied to events in the SS control region to give a data-driven estimate of multi-jet events in the signal region.

In order to prevent the double counting of SS events the number of same-sign charge events predicted from the simulated processes is subtracted from the number of SS events in data. Figure 5.9 shows the transverse momentum of the tau candidate in the OS anti-isolation control region with the multi-jet background estimated from SS events.

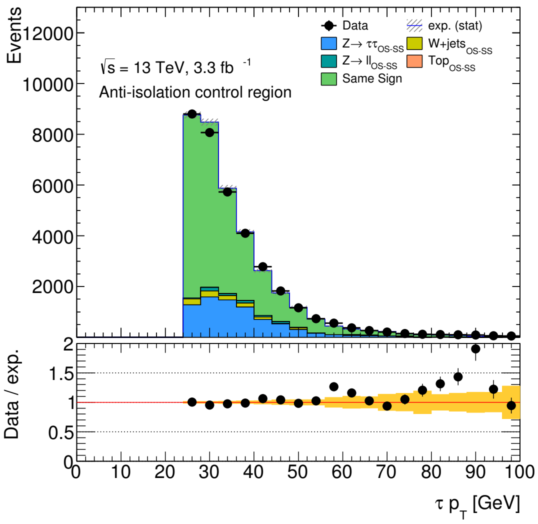

Figure 5.9: Distribution of the transverse momentum of the tau candidate in the OS anti-isolation region. The same sign component refers to the SS anti-isolation region events with a normalisation factor, the ratio of OS to SS events in the region, applied. The number of same-sign charge events predicted from the simulated processes is subtracted from the number of SS events in data. The data correspond to an integrated luminosity of 3.3 fb^{-1}. Only statistical uncertainties are shown.

W+jets estimation

The shape of the W+jets background is modelled using simulated events with a normalisation factor, k_{W}, applied. This normalisation factor is derived from the W+jets control region as the ratio between data (with expected non-W+jets events subtracted) to the expected number of W+jets events from simulation. It is extracted for both OS and SS control regions ($k_{\mathrm{W}}^{\mathrm{OS}}$ and $k_{\mathrm{W}}^{\mathrm{SS}}$), with the OS case defined as:

$$k_{\mathrm{W}}^{\mathrm{OS}} = \left. \frac{N_{\mathrm{OS}}^{\mathrm{data}} - N_{\mathrm{OS}}^{\text{non-}W\text{+jets MC}}}{N_{\mathrm{OS}}^{W\text{+jets MC}}} \right|_{W\text{+jets,OS}}, \tag{5.4}$$

where $N_{\text{OS}}^{\text{data}}$, $N_{\text{OS}}^{\text{non-}W\text{+jets MC}}$ and $N_{\text{OS}}^{W\text{+jets MC}}$ refer to the number of data events, simulated non-W+jets events and simulated W+jets events, respectively, in the OS W+jets control region. A similar definition for k_{W}^{SS} applies in the SS W+jets control region. Separate k_{W} values are calculated for 1-prong and 3-prong tau candidates.

Figure 5.10 shows the distributions of the transverse mass between the lepton and the $E_{\text{T}}^{\text{miss}}$ in the $W+$jets control region after the application of the k_{W} normalisation factors for the case of an offline medium ID tau candidate.

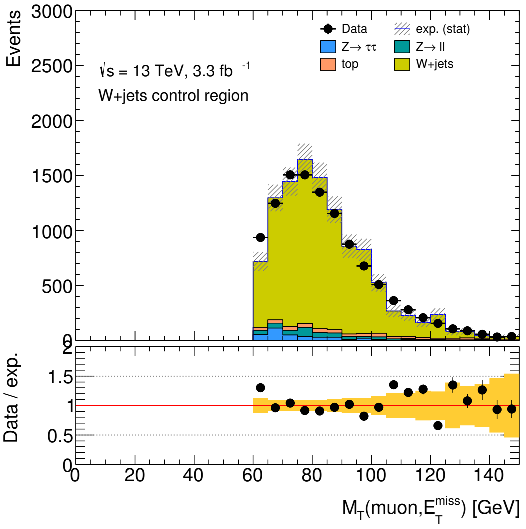

Figure 5.10: Distribution of the transverse mass between the muon and $E_{\text{T}}^{\text{miss}}$ in the OS $W+$jets control region after applying normalisation factors to simulated $W+$jets events. The plots correspond to the case where the reconstructed tau candidate is required to have offline medium tau ID. The data correspond to an integrated luminosity of 3.3 fb^{-1}. Only statistical uncertainties are shown.

Summary of background estimation

In summary, the expected number of signal region data events coming from signal and background processes is given by:

$$N_{\text{expected}} = r_{\text{QCD}} \times N_{\text{SS}}^{\text{data}} + N_{\text{OS-SS}}^{Z\to\tau\tau} + N_{\text{OS-SS}}^{W\text{+jets}} + N_{\text{OS-SS}}^{Z\text{+jets}} + N_{\text{OS-SS}}^{t\bar{t}},$$

where $N_{\text{SS}}^{\text{data}}$ refers to the number of data events in the same sign control region, and $N_{\text{OS-SS}}$ refers to the number of opposite-sign events with the number of same sign events subtracted, with the components for separate processes given by:

$$N^{Z\to\tau\tau}_{\text{OS-SS}} = N^{Z\to\tau\tau}_{\text{OS}} - r_{\text{QCD}} \times N^{Z\to\tau\tau}_{\text{SS}},$$

$$N^{Z\text{+jets}}_{\text{OS-SS}} = N^{Z\text{+jets}}_{\text{OS}} - r_{\text{QCD}} \times N^{Z\text{+jets}}_{\text{SS}},$$

$$N^{t\bar{t}}_{\text{OS-SS}} = N^{t\bar{t}}_{\text{OS}} - r_{\text{QCD}} \times N^{t\bar{t}}_{\text{SS}},$$

$$N^{W\text{+jets}}_{\text{OS-SS}} = k^{\text{OS}}_{\text{W}} \times N^{W\text{+jets}}_{\text{OS}} - k^{\text{SS}}_{\text{W}} \times r_{\text{QCD}} \times N^{W\text{+jets}}_{\text{SS}},$$

where N_{OS} is the number of signal region events for a given process, and N_{SS} is the number of same sign control region events.

5.3.3 Signal region distributions

The distributions of several kinematic variables are shown in Figure 5.11 after applying the signal region event selection to data and the estimated signal and background processes. The figures are shown for the case of the tau candidate identified with an offline medium working point. The reconstructed invariant mass of the visible muon and tau candidate system is shown before the application of the signal region invariant mass requirement. The signal region has a purity of $Z \to \tau_\mu \tau_h$ events of approximately 75% and the figures show that there is a reasonable agreement between the expected and observed distributions.

Figure 5.12 shows kinematic distributions in the signal region after the application of the HLT_tau25_medium1_tracktwo_L1_TAU12IM trigger and the matching ($\Delta R < 0.2$) of the online tau candidate to the leading tau reconstructed offline with medium ID. The BDT score of the online tau identification algorithms is also shown and is seen to be in agreement with the expected distribution.

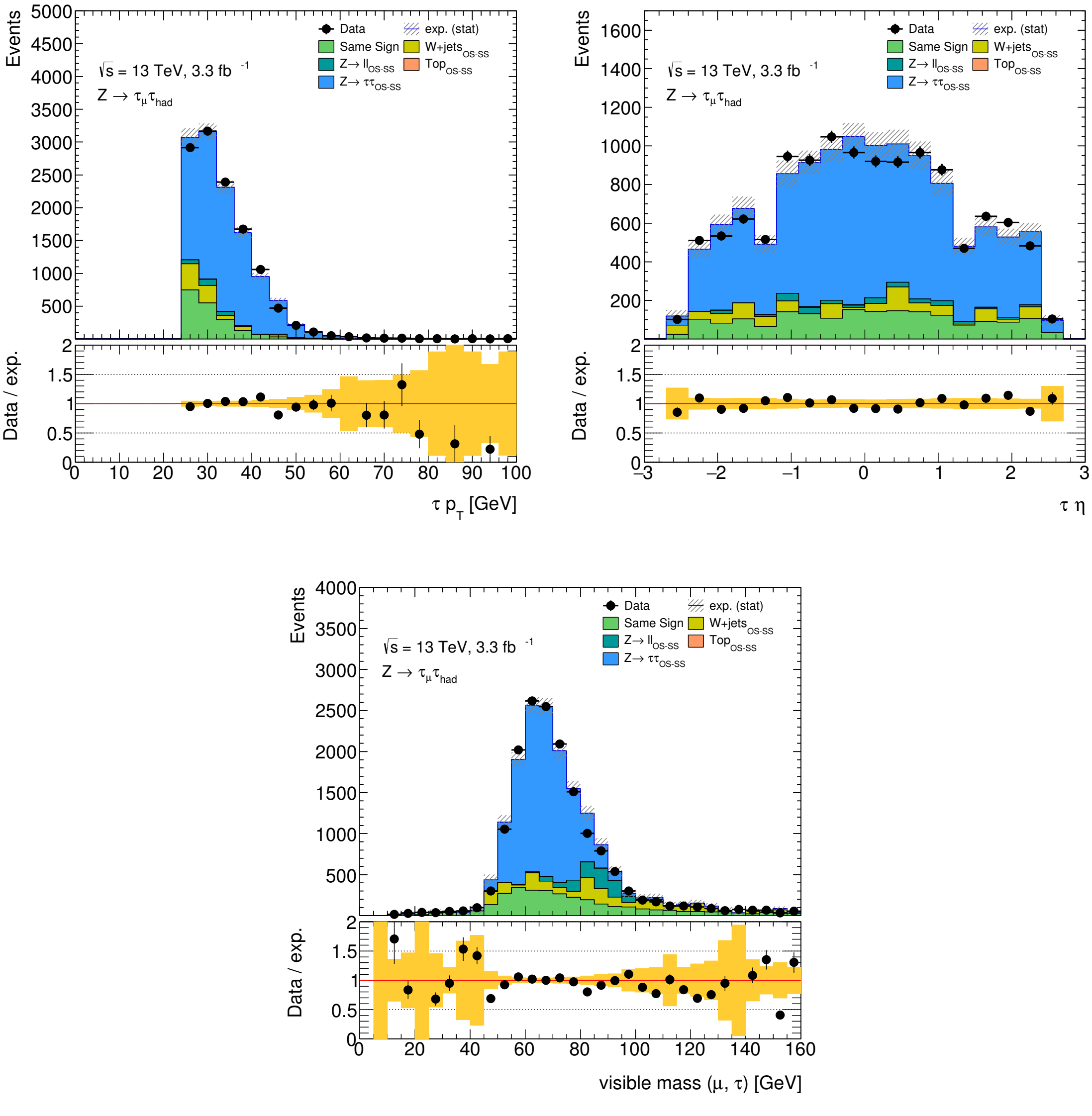

Figure 5.11: Various offline kinematic distributions of the offline medium ID tau candidate after a selection designed to enrich the signal region in $Z \to \tau_\mu \tau_h$ events. The plots show the tau candidate p_T (top left), pseudorapidity (top right) and the reconstructed invariant visible mass of the muon and tau candidate (bottom) with the final plot shown before the application of the selection requirement on the visible reconstructed mass. No tau trigger is applied in the selection. The data correspond to an integrated luminosity of 3.3 fb^{-1}. Only statistical uncertainties are shown.

5.3.4 Sources of systematic uncertainty

In the trigger efficiency measurement, systematic uncertainties associated with the modelling of the ATLAS detector and the SM processes enter through the subtraction of backgrounds from data. The largest source of systematic uncertainty considered is the uncertainty on the SS background modelling from the value of the normalisation factor. The uncertainty

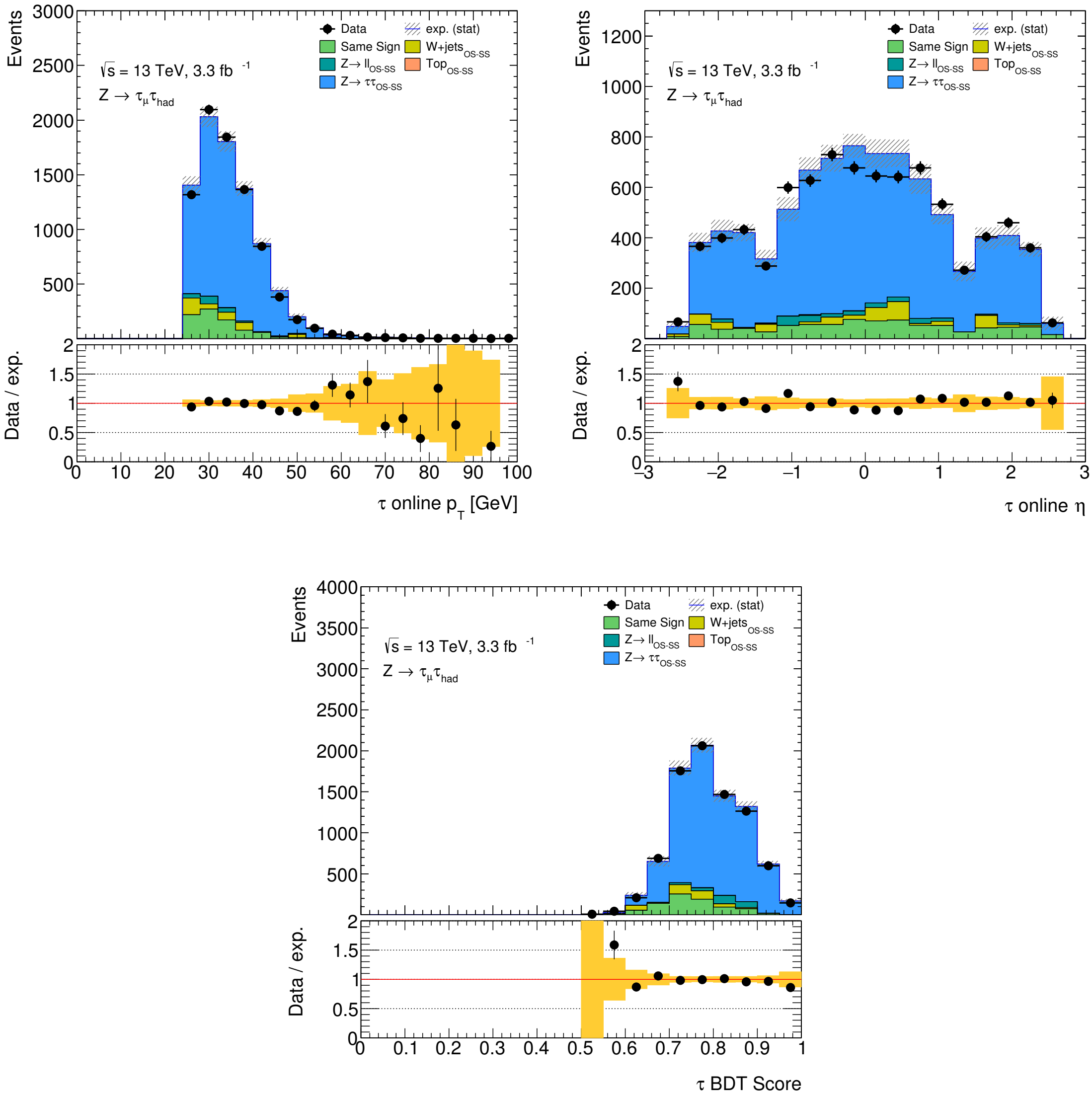

Figure 5.12: Various kinematic distributions of the online tau candidate geometrically matched to an offline medium ID tau candidate after a selection designed to enrich the signal region in $Z \to \tau_\mu \tau_h$ events. The plots show the online tau candidate p_{T} (top left), online pseudorapidity (top right) and the online tau identification BDT score (bottom). The HLT_tau25_medium1_tracktwo tau trigger is applied in the selection, which is seeded by the L1_TAU12IM trigger at L1. The data correspond to an integrated luminosity of 3.3 fb^{-1}. Only statistical uncertainties are shown.

on r_{QCD} combines a statistical component with a systematic component associated with the choice of isolation requirement used in defining the anti-isolation control region, and so covers the uncertainty in the assumption that the OS to SS ratio is the same between the isolation and anti-isolation regions. The systematic component is estimated from the range in the r_{QCD} value as the fixed-threshold isolation requirement on the muon, defined in

Section 3.2.3, is varied between $\Delta R < 0.01$ and $\Delta R < 0.4$. The normalisation factor for the $W+$jets control region is estimated in the same way by combining a statistical component and a component associated with the choice of transverse mass value used to define the W+jets control region. Sources of systematic uncertainty associated with the reconstruction of the muon and $E_{\mathrm{T}}^{\mathrm{miss}}$ were also considered.

5.3.5 Results

The efficiency of a given tau trigger is calculated in data using Equation (5.2) for each p_{T} bin, whilst the measurement in simulated $Z \rightarrow \tau\tau$ events uses Equation (5.1). The scale factor, the ratio of the efficiency measured in data to the measurement in simulation, is also calculated. Separate efficiencies and scale factors are calculated for 1-prong and 3-prong taus reconstructed offline, and the measurements can also be broken down between the data taking period (where there may be minor variations between the detector conditions), the pseudorapidity of the tau candidate, and level of offline identification on the tau candidate, depending on the requirements of a given analysis. The binning has been optimised for each variation to ensure a similar level of statistical uncertainty between bins.

Figure 5.13 shows the trigger efficiencies and corresponding trigger scale factors measured in the full 2015 dataset for 1-prong and 3-prong tau candidates with offline medium identification, inclusive in pseudorapidity. For the range in which the efficiency is flat as a function of the transverse momentum, the scale factors are found to be consistent with unity. The highest-p_{T} bin is used in the case of tau candidates beyond the p_{T}-range. Due to the low number of events with high-p_{T} tau candidates, there is a large statistical uncertainty associated with the scale factors of the HLT_tau80_medium1_tracktwo_L1_TAU60 trigger.

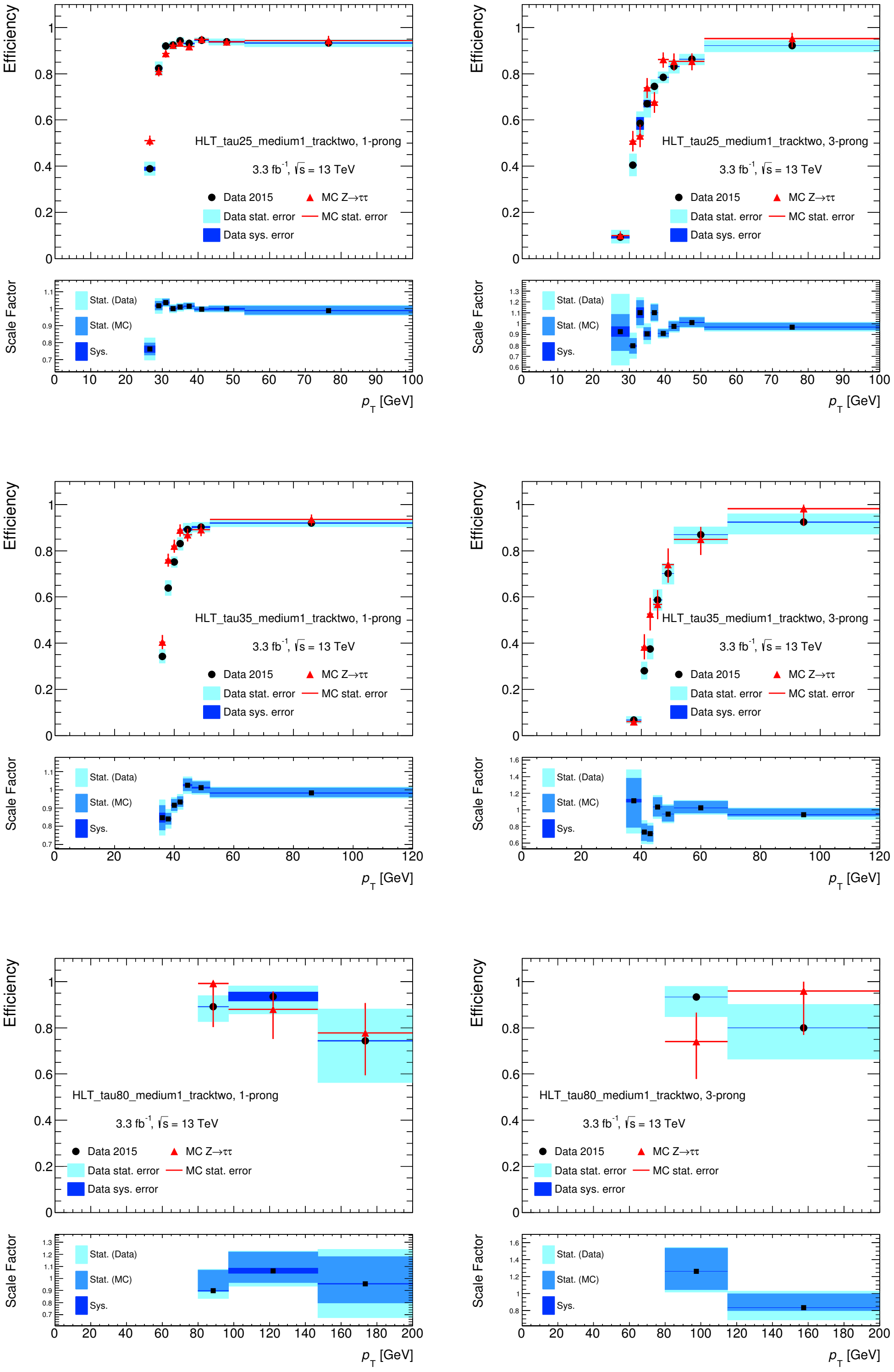

Figure 5.13: The efficiency of various tau triggers measured in simulated $Z \to \tau\tau$ events (MC) and in data with estimated backgrounds subtracted, after an event selection designed to be enriched in $Z \to \tau_\mu \tau_h$ events. The efficiency is measured as a function of the transverse momentum of the reconstructed 1-prong (left) and 3-prong (right) tau candidates, which are required to have a medium offline tau identification. The ratio of the efficiency in data to the efficiency in simulation, the tau trigger scale factor, is also shown. The data are collected by the single-muon trigger and correspond to an integrated luminosity of 3.3 fb^{-1}.

Chapter 6

The search for neutral high-mass Higgs bosons

This chapter describes the search for neutral Higgs bosons decaying via a pair of hadronically decaying tau leptons. The search is performed with 3.21 fb^{-1} of proton-proton collision data with a centre of mass energy of $\sqrt{s}$ =13 TeV recorded using the ATLAS detector, and is an update of the Run-1 analysis [31], following a similar methodology.

The aim of the analysis is to search for an excess of data events over the expected number of background events from Standard Model processes, after an event selection designed to contain a high proportion of potential $A/H \rightarrow \tau\tau$ events. If no excess is observed, the level of agreement between the data and estimated background can be used to set limits on the production cross section times branching fraction of the process, and constrain the MSSM parameter space. This chapter documents the analysis channel where the two tau leptons decay hadronically ($\tau_{\text{had}}\tau_{\text{had}}$). A separate analysis is performed for the final state where one tau lepton decays hadronically, and the other tau lepton decays via either an electron or muon ($\tau_{\text{lep}}\tau_{\text{had}}$). The limits of the two analysis channels are then combined.

Two separate analyses were completed with these search channels. First, an analysis was performed with a single final state category of two tau leptons (split into the channels mentioned above), and made public during the ATLAS and CMS 2015 End Of Year Event

(EOYE), a showcase event of LHC results [8]. The second analysis splits the final state into two further categories in order to increase the sensitivity, one in which there is at least one tagged b-jet in the final state (hereafter referred to as the b-tag category) and one in which there are no b-tagged jets in the final state (referred to as the b-veto category). The resulting paper is found in reference [10]. The limits of the updated analysis improve on those of the EOYE across the high-mass Higgs mass range, and as such is the only analysis discussed in this thesis.

The chapter is divided into several sections. Section 6.1, discusses the signal and background processes and their simulation in the analysis. The event selection is described in Section 6.2, and detailed information on the techniques used in estimating the backgrounds is in Section 6.3. The results of this background estimation after the full event selection is shown in Section 6.4. Section 6.5 explains some of the main sources of systematic uncertainty. The final results are interpreted as limits on the cross section times branching fraction of a scalar boson, and in terms of MSSM parameter space, in Section 6.6. The detector, object definitions and data are as discussed in previous chapters.

6.1 Signal and background processes

This section describes the signature and simulation of the processes that produce the $A/H \rightarrow \tau_{\text{had}}\tau_{\text{had}}$ decay. The decay of the Higgs boson to two hadronically decaying tau leptons produces a final state that can be mimicked by many SM processes. These processes are described in this section, which also provides an overview of how they are estimated.

6.1.1 Signal processes

In the analysis, two production modes of high-mass neutral Higgs bosons are considered: gluon-gluon fusion and b-associated production. Leading order LO Feynman diagrams for these processes are shown in Figure 2.3. The tau leptons resulting from the high-mass Higgs boson decay have opposite-sign charges and tend to be produced back-to-back in the detector and with a large momentum transverse to the beam axis. The tau neutrinos resulting from the decay of the tau leptons result in missing transverse momentum in the event.

The b-associated production models are simulated using the `MadGraph5_aMC@NLO 2.1.2` generator [87, 88] with the CT10nlo_nf4 PDF set [89], whilst the gluon fusion simulation is produced with the `Powheg-Box` v2 [83–85] generator and CT10 [90] PDF set. For both gluon fusion and b-associated production, the parton shower, underlying event and hadronisation processes are modelled using `Pythia 8.210` [91], with the AZNLO tune [92] used for the gluon fusion and the A14 tune [93] used for the b-associated production. For both production mechanisms, nine Higgs boson mass points spanning the range 200 GeV and 1.2 TeV are simulated.

The b-associated production passes through the `ATLFAST-II` [94] fast ATLAS simulation software, whereas `GEANT4` [76] is used for the gluon fusion and background processes.

The program `SusHi` (Supersymmetric Higgs) [95] is used to calculate the production cross sections for the various MSSM scenarios considered in the analysis for gluon fusion [96–108] and five-flavour b-associated production [109], whilst the b-associated production four-flavour scheme is calculated according to Refs. [110, 111]. The final b-associated cross section is then obtained using the methods described in Ref. [112]. The Higgs boson mass and couplings are calculated with `FeynHiggs` [113], and the branching fraction calculated as described in Ref. [114]. An exception is the hMSSM scenario which has the cross section calculated following the procedure in Ref. [115] and uses `HDECAY` [116] for the branching fraction calculation.

6.1.2 Background processes

Several SM interactions and decays result in the same detector signature as the $A/H \rightarrow \tau_{\text{had}}\tau_{\text{had}}$ process and are referred to as background processes. The sources of background considered in this analysis result from QCD and electroweak processes in which a jet or lepton is misidentified as a hadronically decaying tau particle, as well as processes that produce real tau leptons. Due to the possibility of mis-tagging b-jets, all the SM processes described form backgrounds to both the b-tag and b-veto categories. The methods used in the estimation of the background contribution to candidate signal events are discussed in Section 6.3. Appendix A lists the simulated samples used in this analysis and their associated cross sections.

Multi-jet events

The largest source of misidentified tau particles results from processes in which multiple hadronic jets are produced. This is due to the large cross section associated with QCD interactions in proton-proton collisions. Therefore, despite algorithms dedicated to the rejection of jet backgrounds, there are a large number of events in which quark- or gluon-initiated jets are misidentified as candidate taus.

Due to the large number of simulated events required to accurately model the jet rejection algorithms, and the inadequate theoretical modelling of multi-jet processes in high energy proton collisions, this background is estimated using data events where the subleading tau candidate (the second highest p_{T} tau candidate) fails the identification algorithm. A full description is given in Section 6.3.1.

$Z \to \tau\tau$ production

$Z \to \tau\tau$ processes in which both tau particles decay hadronically form an irreducible background due to sharing the same final state as the signal process. This background has similar kinematics to the signal process, but with the tau particles carrying a lower transverse momentum owing to the smaller mass of the Z boson. The leptonic decay of one or both of the tau particles also forms a background if an electron, muon, or an additional jet is misidentified as a hadronically decaying tau lepton, however this background is significantly smaller than the fully hadronic decay mode.

The process is modelled using events generated by the `Powheg-Box` v2 generator with the CT10 PDF set, interfaced to `Pythia 8.186` [77,78] with the AZNLO tune, and is normalised to next-to-next-to-leading-order (NNLO) cross section [117].

$Z \to \ell\ell$ production

As with the $Z \to \tau\tau$ background where the taus decay leptonically, $Z \to \ell\ell$ decays, where here ℓ refers to an electron or muon, can imitate the signal state when both ℓ, or an ℓ and a jet produced in association with the Z boson, are misidentified as tau leptons. The process is also estimated via simulation, and simulated with the same generator and conditions as the $Z \to \tau\tau$ background.

W+jets production

The production of $W \to \tau\nu$ can pass the signal selection when an associated jet is misidentified as a hadronically decaying tau lepton. A small background from $W \to \ell\nu$ arises when the lepton is also misidentified as a hadronic tau. W+jets processes are simulated using the `SHERPA 2.1.1` generator [118] with the CT10 PDF set, normalised to NNLO cross sections [119]. The matrix element calculations are performed with each parton multiplicity simulated at NLO for up to two additional partons and LO for up to four partons and merged using the `SHERPA` parton shower model with the `ME+PS@NLO` prescription [120].

Top quark production

The single or pair production of top quarks in the ATLAS detector contributes to the background of the search. Since the top quark decays almost exclusively to a W boson and a b-quark, the top backgrounds are particularly significant in the b-tag channel. The decay of the W boson produces a final state with either a real tau lepton, or a lepton or jet that can be misidentified as a tau particle. Additional jets associated with the production of the top quark cause further potential for the misidentification of tau particles.

The top production processes are modelled using simulated events generated by the `Powheg-Box` v2 generator with the CT10 PDF set, with the exception of t-channel single top quark events, simulated using the `Powheg-Box` v1 generator with the CT10f4 PDF set and with decay simulated using `MadSpin` [121]. The parton shower, fragmentation and underlying event are simulated with `Pythia 6.428` [86], with the CTQ6L1 PDF set, and the Perugia 2012 tune [122]. The top-quark mass is set to 172.5 GeV. The $t\bar{t}$ production sample is normalised to the NNLO cross section, including soft-gluon resummation to next-to-next-to-leading-logarithm accuracy [123].

Diboson events

The production of multiple W and Z bosons causes a background as two tau leptons may result from the decay of one or two bosons. Additionally, jets, electrons and muons associated with the W and Z decays may be misidentified as hadronic taus. Diboson production cross sections are relatively small. These processes are simulated by the `SHERPA 2.1.1` generator with the CT10 PDF set. The matrix element calculations are performed with each parton multiplicity simulated at NLO for up to one additional parton and LO for up to three additional partons and merged using the `SHERPA` parton shower model with the `ME+PS@NLO` prescription [120].

6.2 Event selection

The analysis follows a 'cut based' event selection, whereby only events that pass the full list of requirements described in this section are considered. The signal selection is similar to that optimised during the Run-1 analysis [31]. Separate selections are used in the estimation of scaling factors to background processes and are detailed in Section 6.3.

This section describes the details of the event selection used to select signal events with a high efficiency, and reject events from background processes. The physics objects used in the selection are the same as those described in Section 3.2 Chapter 4 and the selection is applied in the same way to both data and simulation, unless stated otherwise.

6.2.1 Trigger

The tau trigger system is described in detail in Chapter 5. Figure 6.1 shows the efficiency of various triggers in selecting signal events from the gluon fusion and b-associated production mechanisms for various Higgs boson mass points. The efficiency of the triggers is measured after an initial loose analysis selection, referred to as the preselection. The preselection requires the reconstruction of at least two hadronically decaying tau leptons with $p_{\mathrm{T}} >$ 100 GeV for the leading (highest p_{T}) tau candidate and $p_{\mathrm{T}} > 45$ GeV for the subleading tau candidate. Additionally a veto is placed on events which contain one or more reconstructed muon or electron objects with the loose ID requirement.

The significant gains to the analysis in using the HLT_tau80_medium1_L1_TAU60 trigger shown in the figures played an important role in the justification of keeping the trigger available for the full data collection period. The events are therefore selected using this single tau trigger (STT) which had the lowest p_{T} threshold available in the 2015 data. At HLT level, a requirement is made on the transverse momentum of reconstructed hadronic tau decays of $p_{\mathrm{T}} > 80$ GeV, and there is an online BDT medium identification (ID) requirement. The HLT reconstruction is seeded by an L1 trigger object with $p_{\mathrm{T}} > 60$ GeV. The leading tau candidate must be within a separation of $\Delta R < 0.2$ of the online tau candidate.

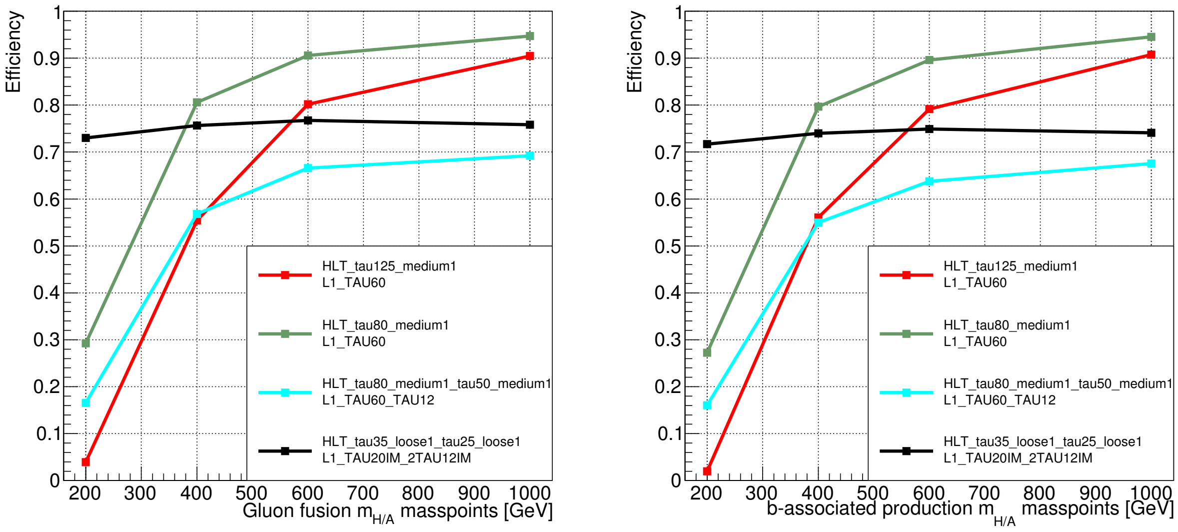

Figure 6.1: The efficiency of various triggers in selecting events from gluon fusion (left) and b-associated (right) production mechanisms as a function of the Higgs boson mass. The efficiency is measured after a loose preselection requiring at least two tau candidates and zero muons or electrons.

6.2.2 Analysis selection

A summary of the criteria required in the selection of events for the analysis, after the preselection, is given below:

1. Pass the STT described in Section 6.2.1.
2. Leading tau candidate passes the medium BDT ID criteria.
3. Leading tau candidate $p_{\mathrm{T}} > 110$ GeV.
4. Subleading candidate tau $p_{\mathrm{T}} > 55$ GeV.
5. $\Delta\phi(\tau^0_{had}, \tau^1_{had}) > 2.7$, where τ^0_{had} and τ^1_{had} are the leading and subleading tau candidates.
6. Subleading tau candidate passes the loose BDT ID criteria.
7. The leading and subleading tau candidates have OS charges.

Finally, the analysis is split into orthogonal signal regions. The b-tag category, which requires a jet with $p_{\mathrm{T}} > 20$ GeV tagged as a b-jet as described in Section 3.2.5, favours the

b-associated production mode, whilst the b-veto category, in which b-jets are vetoed, favours the gluon fusion production mechanism. The two categories do not uniquely contain the different production modes however. A significant number of signal events corresponding to the b-associated production mechanism may be present in the b-veto selection category due to inefficiencies in the b-tagging algorithm and the fact that for some production processes the b-jet is produced in the forward direction of the detector ($|\eta| > 2.5$) where it is not possible to use the tagging algorithms. Additionally, the production or misidentification of b-jets in events associated with the gluon fusion production mechanism means a small fraction ($< 2\%$) of events can contain b-tagged jets.

Tables 6.1 to 6.3 show the expected signal yields for the gluon fusion and b-associated production mechanisms in the b-veto and b-tag categories through the stages of the event selection, where the cross sections are set to 1 pb. The contribution of the gluon fusion production mechanism to the b-tag event yield is not shown due to the relatively low number of events. These are summarised in Tables 6.4 and 6.5, which show the signal selection efficiencies of the b-veto and b-tag selections respectively, for selected Higgs mass points. The lower acceptance of the b-associated production mode in the b-tag category is mainly a result of the η-coverage of the b-tagging algorithms.

6.2.3 Analysis validation and control regions

A validation region is defined orthogonal to the signal selection described above by inverting the charge requirement on the leading and subleading tau candidates such that they have the same sign charge (SS). The $A/H \to \tau\tau$ analysis was performed with the signal region event selection blind to reduce bias. This means that prior to the unblinding, where the signal region is examined and checked for excess events, the distributions and event yields after the event selection were unknown. The SS validation region enabled the verification of the some of the background estimation methods prior to the unblinding. The region is designed to be similar to the analysis selection in terms of kinematics and to contain a negligible amount of signal. There are separate SS validation regions in place for the b-tag and b-veto final states.

Mass hypothesis [GeV]	300	stat.	400	stat.	500	stat.	600	stat.
Preselection	396.7	3.8	491.3	4.2	533.4	4.4	563.1	5.1
Trigger & τ_{lead}^{ID}	178.9	2.6	266.0	3.1	301.4	3.3	328.5	3.8
Leading $\tau p_{\mathrm{T}} > 110$ GeV	122.5	2.1	228.9	2.9	278.9	3.1	312.9	3.7
Subleading $\tau p_{\mathrm{T}} > 55$ GeV	107.2	2.0	208.1	2.8	258.0	3.0	293.5	3.6
$\Delta\phi(\tau_{had}^{0}, \tau_{had}^{1}) > 2.7$	85.7	1.8	184.2	2.6	229.6	2.8	264.1	3.4
b-veto	84.4	1.8	182.1	2.6	226.1	2.8	259.6	3.3
sublead τ ID	64.3	1.5	147.1	2.3	187.1	2.6	215.0	3.0
Opposite Sign	63.6	1.5	145.3	2.3	184.4	2.5	211.7	3.0

Mass hypothesis [GeV]	700	stat.	800	stat.	1000	stat.	1200	stat.
Preselection	565.8	5.1	572.1	5.1	561.4	5.0	542.4	4.9
Trigger & τ_{lead}^{ID}	323.7	3.7	327.6	3.7	320.7	3.7	303.6	3.6
Leading $\tau p_{\mathrm{T}} > 110$ GeV	312.4	3.7	318.8	3.7	315.8	3.6	300.6	3.5
Subleading $\tau p_{\mathrm{T}} > 55$ GeV	296.6	3.6	304.1	3.6	301.5	3.5	287.4	3.5
$\Delta\phi(\tau_{had}^{0}, \tau_{had}^{1}) > 2.7$	264.5	3.4	273.8	3.4	272.4	3.4	259.6	3.3
b-veto	260.1	3.3	267.5	3.4	265.9	3.3	252.3	3.2
sublead τ ID	216.7	3.0	222.6	3.1	221.1	3.0	209.5	3.0
Opposite Sign	212.2	3.0	218.6	3.0	216.0	3.0	203.1	2.9

Table 6.1: Expected event yields and statistical uncertainties for simulated gluon fusion high-mass Higgs boson events in the signal region of the b-veto category. All cross sections are set to 1 pb and scaled to an integrated luminosity of 3.21 fb^{-1}.

Mass hypothesis [GeV]	300	stat.	400	stat.	500	stat.	600	stat.
Preselection	414.2	4.3	498.0	4.0	544.4	4.9	553.8	5.5
Trigger & τ_{lead}^{ID}	204.1	3.0	277.8	2.9	313.0	3.6	323.3	4.1
Leading $\tau p_{\mathrm{T}} > 110$ GeV	140.1	2.4	238.1	2.7	290.8	3.5	308.3	4.0
Sublead $\tau p_{\mathrm{T}} > 55$ GeV	121.1	2.3	214.4	2.6	268.7	3.3	289.9	3.9
$\Delta\phi(\tau_{had}^{0}, \tau_{had}^{1}) > 2.7$	96.3	2.1	175.0	2.4	225.4	3.1	247.6	3.6
b-tag	27.3	1.0	56.6	1.3	77.3	1.7	87.4	2.1
subleading τ ID	21.5	0.9	44.9	1.2	63.7	1.6	72.6	1.9
Opposite Sign	21.2	0.9	44.3	1.1	62.5	1.6	71.6	1.9

Mass hypothesis [GeV]	700	stat.	800	stat.	1000	stat.	1200	stat.
Preselection	561.0	5.6	565.5	5.6	548.5	4.9	519.7	5.2
Trigger & τ_{lead}^{ID}	334.6	4.1	338.2	4.1	321.1	3.6	294.0	3.8
Leading $\tau p_{\mathrm{T}} > 110$ GeV	323.6	4.1	331.2	4.1	316.6	3.6	291.9	3.8
Subleading $\tau p_{\mathrm{T}} > 55$ GeV	305.9	3.9	314.3	4.0	301.4	3.5	279.5	3.7
$\Delta\phi(\tau_{had}^{0}, \tau_{had}^{1}) > 2.7$	261.5	3.7	271.9	3.7	260.6	3.3	241.5	3.5
b-tag	96.5	2.2	105.5	2.2	106.2	2.0	99.3	2.2
Subleading τ ID	81.2	2.0	88.3	2.0	89.1	1.9	82.8	2.0
Opposite Sign	79.5	2.0	86.8	2.0	87.1	1.8	80.2	2.0

Table 6.2: Expected event yields and statistical uncertainties for simulated *b*-associated high-mass Higgs boson events in the signal region of the *b*-tag category. All cross sections are set to 1 pb and scaled to an integrated luminosity of 3.21 fb^{-1}.

Mass hypothesis [GeV]	300	stat.	400	stat.	500	stat.	600	stat.
Preselection	414.2	4.3	498.0	4.0	544.4	4.9	553.8	5.5
Trigger & τ_{lead}^{ID}	204.1	3.0	277.8	2.9	313.0	3.6	323.3	4.1
Leading $\tau p_{\mathrm{T}} > 110$ GeV	140.1	2.4	238.1	2.7	290.8	3.5	308.3	4.0
Subleading $\tau p_{\mathrm{T}} > 55$ GeV	121.1	2.3	214.4	2.6	268.7	3.3	289.9	3.9
$\Delta\phi(\tau_{had}^{0}, \tau_{had}^{1}) > 2.7$	96.3	2.1	175.0	2.4	225.4	3.1	247.6	3.6
b-veto	69.0	1.8	118.1	2.0	147.8	2.5	159.8	2.9
Subleading τ ID	54.4	1.6	95.7	1.8	123.5	2.3	132.7	2.7
Opposite Sign	53.9	1.6	94.5	1.8	121.9	2.3	130.8	2.6

Mass hypothesis [GeV]	700	stat.	800	stat.	1000	stat.	1200	stat.
Preselection	561.0	5.6	565.5	5.6	548.5	4.9	519.7	5.2
Trigger & τ_{lead}^{ID}	334.6	4.1	338.2	4.1	321.1	3.6	294.0	3.8
Leading $\tau p_{\mathrm{T}} > 110$ GeV	323.6	4.1	331.2	4.1	316.6	3.6	291.9	3.8
Subleading $\tau p_{\mathrm{T}} > 55$ GeV	305.9	3.9	314.3	4.0	301.4	3.5	279.5	3.7
$\Delta\phi(\tau_{had}^{0}, \tau_{had}^{1}) > 2.7$	261.5	3.7	271.9	3.7	260.6	3.3	241.5	3.5
b-veto	164.7	3.0	165.8	2.9	153.8	2.6	141.5	2.7
Subleading τ ID	138.0	2.7	141.4	2.7	129.8	2.4	117.2	2.5
Opposite Sign	135.4	2.7	138.3	2.7	126.8	2.3	114.0	2.4

Table 6.3: Expected event yields and statistical uncertainties for simulated b-associated high-mass Higgs boson events in the signal region of the b-veto category. All cross sections are set to 1 pb and scaled to an integrated luminosity of 3.21 fb^{-1}.

Mass hypothesis [GeV]	200	300	600	1000	1200
gluon fusion	0.13	4.70	15.62	16.01	14.98
b-associated prod.	0.15	4.01	9.71	9.40	8.50

Table 6.4: Signal selection efficiencies for the gluon fusion and b-associated high-mass Higgs production modes in percent for the b-veto category.

Mass Hypothesis [GeV]	200	300	600	1000	1200
gluon fusion	< 0.01	0.07	0.27	0.38	0.40
b-associated prod.	0.08	1.56	5.29	6.48	5.93

Table 6.5: Signal selection efficiencies for the gluon fusion and b-associated high-mass Higgs production modes in percent for the b-tag category.

Control regions, meanwhile, are used in the estimation of background contributions to the signal region, and are described in detail in Section 6.3.

6.2.4 Di-tau mass reconstruction

A discriminating mass reconstruction variable is important for separating the signal and background processes from each other, and so increase the sensitivity of the analysis. An accurate reconstruction of the mass of the di-tau mother particle is complicated by the production of tau neutrinos in the decay of tau leptons. The neutrinos carry an undetected portion of the system momentum through the detector, meaning the 4-momentum of the decay products is not fully known.

Several expressions related to the reconstruction of the decay system mass were considered for the analysis, such as the invariant mass of the visible decay products. Internal studies performed by a colleague show that the most sensitive technique at separating the signal and background processes is the total transverse mass.The total transverse mass of the system is defined as:

$$m_{\mathrm{T}}^{\mathrm{tot}} = \sqrt{m_{\mathrm{T}}^2(E_{\mathrm{T}}^{\mathrm{miss}}, \tau_0) + m_{\mathrm{T}}^2(E_{\mathrm{T}}^{\mathrm{miss}}, \tau_1) + m_{\mathrm{T}}^2(\tau_0, \tau_1)}, \tag{6.1}$$

where τ refers to the visible decay products of the tau particle, $E_{\mathrm{T}}^{\mathrm{miss}}$ is described in Section 3.2.7 and the transverse mass of a two particle system is defined as:

$$m_{\mathrm{T}}(a,b) = \sqrt{2p_{\mathrm{T}}(a)p_{\mathrm{T}}(b)(1-\cos\Delta\phi(a,b))}$$

for two particles, a and b.

6.3 Estimation of background processes

Key to any search for BSM physics processes is the understanding and accurate estimation of SM processes that contribute candidate signal selection events. As discussed in Section 6.1.2, the dominant background to the $A/H \rightarrow \tau_{\rm had}\tau_{\rm had}$ analysis is from multi-jet processes and is estimated using a data-driven method. The other backgrounds are estimated using simulated events with data-driven correction factors applied where relevant. This section describes how these backgrounds are estimated and shows the checks performed in the SS validation region.

6.3.1 Multi-jet estimation

Overview

In order to estimate the multi-jet background, control regions enriched in multi-jet processes are used. The purpose of the first control region, referred to as the multi-jet control region and defined below, is to determine the ratio of jets that are misidentified as the hadronic decays of tau leptons by the tau identification BDT, to those that do not pass the identification algorithms. This ratio is hereafter referred to as the 'fake factor'. This fake factor is calculated via the tag and probe (T&P) method. The 'tag' object is the leading tau candidate in the multi-jet control region, and the 'probe' object is the subleading tau candidate.

Inside this multi-jet control region, the fake factor is defined as:

$$f_{\tau-{\rm ID}}(p_{\rm T}, N_{\rm track}) \equiv \left. \frac{N^{{\rm pass}\ \tau-{\rm ID}}(p_{\rm T}, N_{\rm track})}{N^{{\rm fail}\ \tau-{\rm ID}}(p_{\rm T}, N_{\rm track})} \right|_{\rm multi-jet} \tag{6.2}$$

and is determined separately for 1-prong and 3-prong taus (denoted by $N_{\rm track}$) and dependent on the $p_{\rm T}$ of the misidentified tau candidate. The variables $N^{{\rm pass}\ \tau-{\rm ID}}$ and $N^{{\rm fail}\ \tau-{\rm ID}}$ refer to the number of tau candidates respectively passing and failing the tau ID requirement in the multi-jet control region.

A second control region, made orthogonal to the signal region and dominated by multi-jet events is defined by inverting the ID requirement on the subleading tau candidate in the signal selection, and is referred to as the inverted-ID control region. Contamination from non-multi-jet background events estimated by simulation are removed. The fake factor is then applied to the inverted-ID control region to give the shape and normalisation of the multi-jet contribution, $N_{\mathrm{multi-jet}}$, in a given kinematic variable:

$$N_{\mathrm{multi-jet}}(p_{\mathrm{T}}, N_{\mathrm{track}}) = f_{\tau-\mathrm{ID}}(p_{\mathrm{T}}, N_{\mathrm{track}}) \times \left(N^{\mathrm{fail}\ \tau-\mathrm{ID}}{}_{\mathrm{data}}(p_{\mathrm{T}}, N_{\mathrm{track}}) \right) \tag{6.3}$$

where $N^{\mathrm{fail}\ \tau-\mathrm{ID}}{}_{data}$ is the number of data events in the inverted-ID control region.

Multi-jet control region

The multi-jet control region is designed to be enriched in multi-jet events, whilst also having a selection similar to the signal region. The criteria are:

1. Pass any of the single jet triggers.
2. At least two tau candidates.
3. ‘Tag’ object $p_{\mathrm{T}} > 100$ GeV.
4. ‘Tag’ object fails the medium BDT ID.
5. Electron veto of the ‘tag’ object.
6. ‘Probe’ object $p_{\mathrm{T}} > 55$ GeV and $> 30\%$ of the ‘tag’ object p_{T}.
7. Probe object has unit charge.
8. Probe object has 1 or 3 charged tracks.

The single jet triggers have online p_{T} thresholds of 25, 35, 55, 60, 65, 85, 110, 150, 175, 200, 260, 300, 320, 330, and 360 GeV and with all but the last prescaled. Several of the requirements in the analysis signal region are relaxed for the control region in order to increase the number of data events available, after applying checks to ensure the measured fake factors do not have a significant dependence on the relevant variable. There is no distinction made between OS and SS tag and probe objects in the selection. Additionally no $\Delta\phi$ cut is placed on the tag and probe objects, unlike in the signal region event selection.

Fake factor values

The final fake factors are shown in Figure 6.2. The fake factors are determined separately for the 1-prong and 3-prong cases, and for the b-tag and b-veto categories by requiring either at least one or exactly zero b-jets, respectively. As the signal region event selection requires the subleading tau candidate to pass the loose BDT ID working point, the fake factors are measured as the ratio of probe candidates passing and failing the loose BDT ID. In Figure 6.3, a comparison is made between fake factors determined when the tag and probe object have OS and SS charges, whilst in Figure 6.4, the fake factors are compared for a selection in which the tag and probe object have a separation of $\Delta\phi > 2.7$ and $\Delta\phi < 2.7$. These relatively small differences in fake factors in these figures show that it is reasonable to merge the OS and SS categories, and use a selection inclusive in $\Delta\phi$.

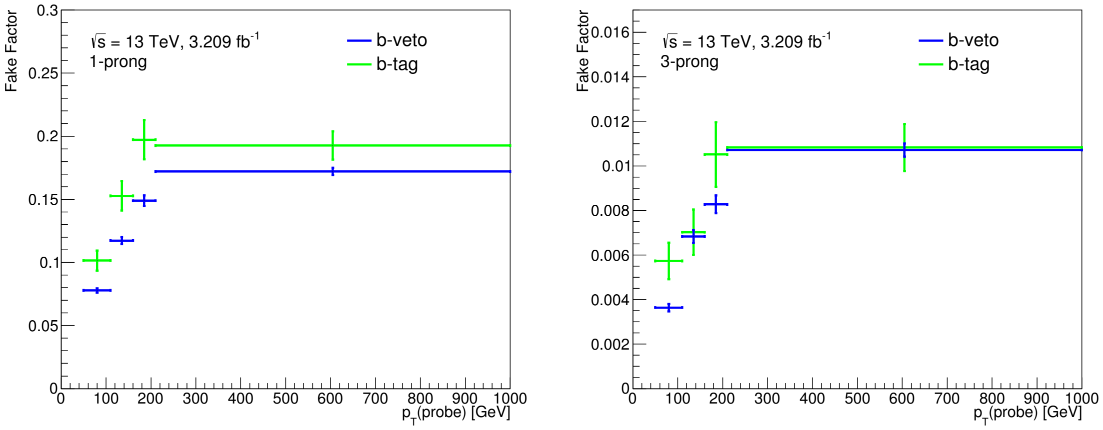

(a) 1-prong

(b) 3-prong

Figure 6.2: Fake factors, the ratio of probe tau candidates passing and failing the loose tau ID in the multi-jet control region, as a function of the probe tau candidate p_{T}. The fake factors are split between the b-tag and b-veto categories.

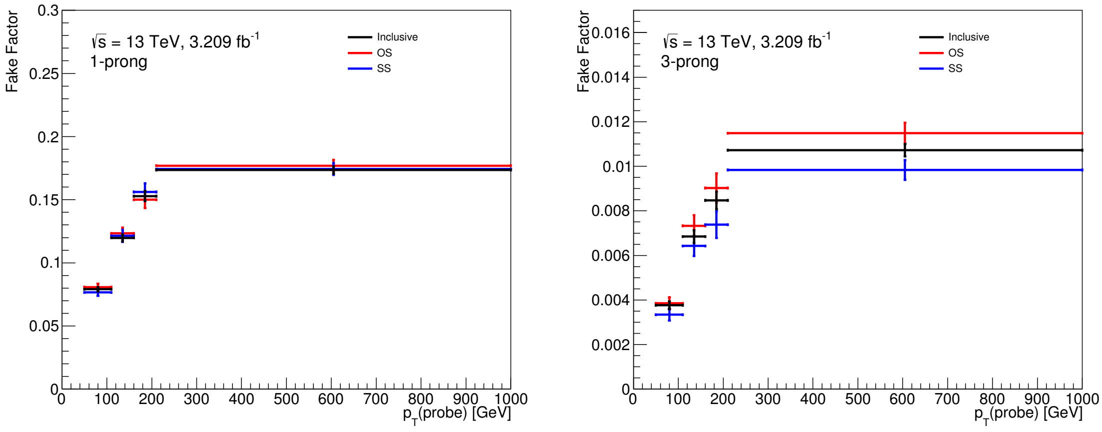

(a) 1-prong

(b) 3-prong

Figure 6.3: Fake factors, the ratio of probe tau candidates passing and failing the loose tau ID in the multi-jet control region, as a function of the probe tau candidate p_{T}. The fake factors are split between the cases where the tag and probe have SS and OS charges. No separation is made on the number of b-quarks in the event selection.

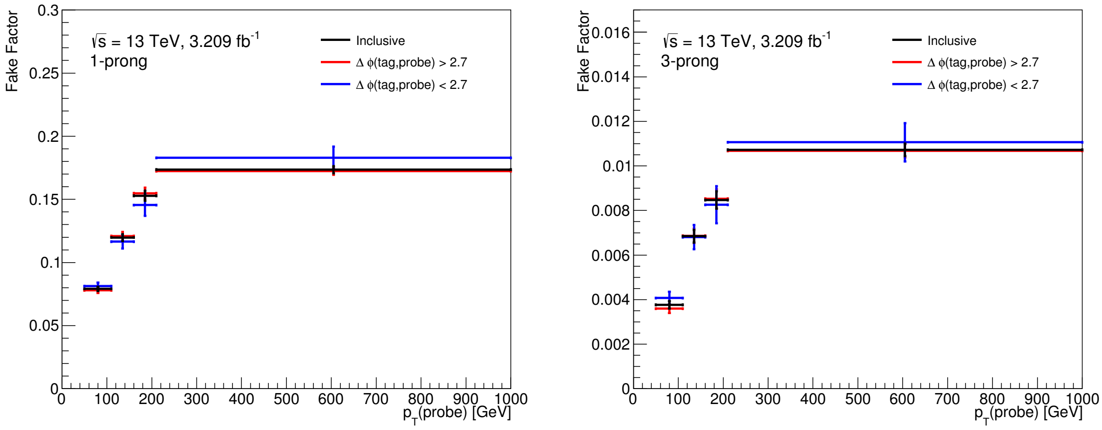

(a) 1-prong

(b) 3-prong

Figure 6.4: Fake factors, the ratio of probe tau candidates passing and failing the loose tau ID in the multi-jet control region, as a function of the probe tau candidate p_{T}. The fake factors are split between the cases where the tag and probe have a separation of $\Delta\phi > 2.7$ and $\Delta\phi < 2.7$. No separation is made on the number of b-quarks in the event selection.

Fake factor closure test

A closure test can be performed with the fake factors by applying them to data in the multi-jet control region. This shows that the fake factors are able to reconstruct the distributions observed in data for the hadronic tau kinematic variables. A comparison is made between data events in the control region in which the subleading tau candidate passes the loose tau ID working point, and the events in which the subleading tau candidate fails this ID requirement and has the relevant fake factor applied as an event weight. Figures 6.5 and 6.6 show this comparison for multi-jet control regions containing either zero or at least one b-jet, respectively.

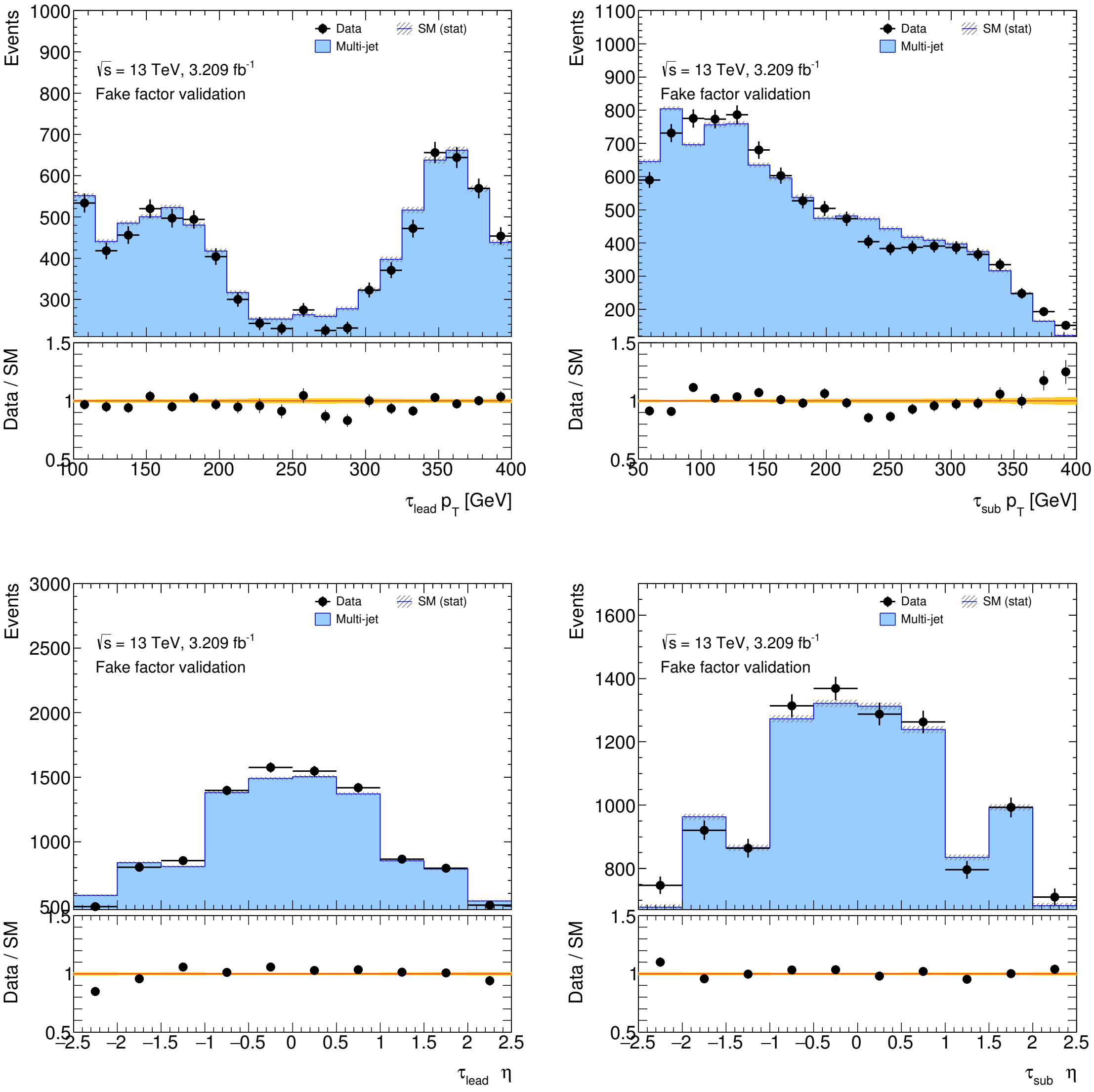

Figure 6.5: Closure test of the fake factors performed on data events in a multi-jet enriched control region with zero b-jets. The p_{T} (top) and η (bottom) distributions of the leading (left) and subleading (right) tau candidates are shown, with ‘data’ referring to data events in which tau ID algorithm is applied, and ‘multi-jet’ referring to the multi-jet distributions estimated with fake factors applied in place of the tau ID algorithms. Several jet triggers of varying prescales used in the collection of the data and the data correspond to an integrated luminosity of 3.21 fb^{-1}. Only statistical uncertainties are shown.

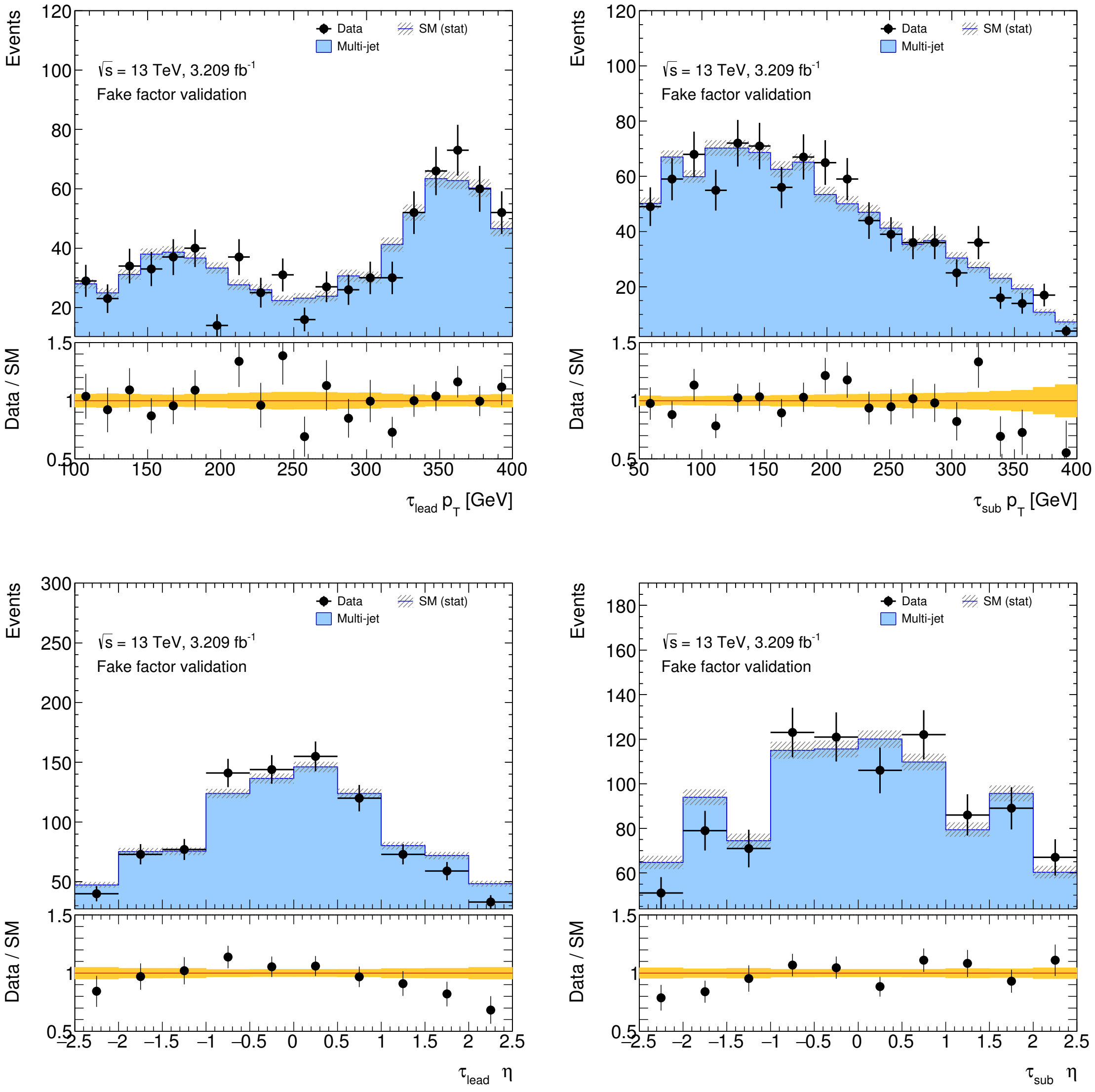

Figure 6.6: Closure test of the fake factors performed on data events in a multi-jet enriched control region with at least one b-jet. The p_{T} (top) and η (bottom) distributions of the leading (left) and subleading (right) tau candidates are shown, with 'data' referring to data events in which the tau ID algorithm is applied, and 'multi-jet' referring to the multi-jet distributions estimated with fake factors applied in place of the tau ID algorithms. Several jet triggers of varying prescales used in the collection of the data and the data correspond to an integrated luminosity of 3.21 fb^{-1}. Only statistical uncertainties are shown.

6.3.2 $W+$jets estimation

The $W+$jets background is estimated from simulation using the `SHERPA` generator, with a data-driven correction applied to improve the estimation of jets being misidentified as hadronically decaying tau leptons. The reason for this correction is that the misidentification of jets as hadronic tau decays is not well modelled in simulation. Further corrections are applied to the simulated events due to modelling issues, related to the `SHERPA` generator. Other generators were tested but found to have an insufficient number of simulated high transverse momentum taus.

$W(\to \tau\nu)$+jets correction for tau spin effects

In the version of `SHERPA` used in this analysis, `SHERPA 2.1.1`, the decay distributions of $W(\to \tau\nu)$+jets events are incorrectly modelled due to lack of spin correlation between the W boson and its decay products. This affects the angular distributions of the tau decay products, and so the transverse mass distribution. In order to reduce the time required to simulate sufficient numbers of $W(\to \tau\nu)$+jets, this spin correlation was disabled. The TauSpinnor Program [124–126] has been developed in order to correct the issue. The validation of the program is described in Ref. [127].

W+jets kinematic distribution reweighting

Modelling issues of kinematic distributions are observed in the simulation of W+jets events by the `SHERPA` generator when compared to both data and simulated events generated with the `Powheg` generator. A control region enriched in $W(\to \mu\nu)$+jets events is designed to compare the modelling by requiring the following:

1. Pass a muon trigger with either an online requirement of $p_{\mathrm{T}} > 50$ GeV, or an online requirement of $p_{\mathrm{T}} > 24$ GeV and a loose identification requirement.
2. Exactly one muon with $p_{\mathrm{T}} > 110$ GeV, medium identification level and gradient isolation.
3. A veto on events containing one or more electrons.
4. At least one tau candidate with $p_{\mathrm{T}} > 55$ GeV and 1 or 3 charged tracks.
5. A separation between the muon and the tau candidate of $\Delta\phi(\mu, \tau) > 2.4$.

In Figure 6.7 a clear discrepancy can be seen between data and events simulated with the `SHERPA` generator, whereas between data and events simulated with the `Powheg` generator a much closer agreement is observed. As such, a correction factor is derived and applied as a weighting to the `SHERPA` W+jets events. The correction factor is calculated in this control region by fitting as a function of $m_{\mathrm{T}}^{\mathrm{tot}}$, the ratio of data (with the simulated contributions of processes other than $W(\rightarrow \mu\nu)$+jets subtracted) to `SHERPA` simulated $W(\rightarrow \mu\nu)$+jets events. The reweighting function, is

$$f(m_{\mathrm{T}}^{\mathrm{tot}}) = \exp(0.321 - 2.03 \times m_{\mathrm{T}}^{\mathrm{tot}}) \tag{6.4}$$

As can be seen in the Figure 6.8, the correction significantly improves the data modelling.

W+jets correction for the misidentification of tau candidates

The misidentification rate of jets as hadronically decaying tau leptons is inadequately modelled in simulation, as seen in Figure 6.9. As such, a correction is applied in place of the tau identification requirement in cases where the tau candidate is not geometrically matched ($\Delta R < 0.2$) to a generator level (also referred to as true) tau lepton. Therefore, the generated tau particles that result from the decay of the W boson will in general have the loose or medium tau BDT identification requirement applied, whereas tau candidates that result from the misidentification of a quark- or gluon-initiated jet will have the misidentification correction applied instead.

This misidentification correction, also referred to as the misidentification rate or fake rate, is a data-driven estimate of the rate at which jets associated with the leptonic decays of W bosons are identified as tau candidates, and is expressed mathematically as:

$$FR(p_{\mathrm{T}}, N_{\mathrm{track}}) \equiv \left. \frac{N^{\mathrm{pass}\ \tau-\mathrm{ID}}(p_{\mathrm{T}}, N_{\mathrm{track}})}{N^{\mathrm{all}\ \tau-\mathrm{ID}}(p_{\mathrm{T}}, N_{\mathrm{track}})} \right|_{\mathrm{W}(\rightarrow\mu\nu)+\mathrm{jets}} \tag{6.5}$$

The number of data events in the control region is given by $N^{\mathrm{all}\ \tau-\mathrm{ID}}$, and the number of events passing a given tau BDT identification requirement is $N^{\mathrm{pass}\ \tau-\mathrm{ID}}$. The fake factor is measured in a dedicated control region enriched in $W(\rightarrow \mu\nu)$+jets events, and is applied as

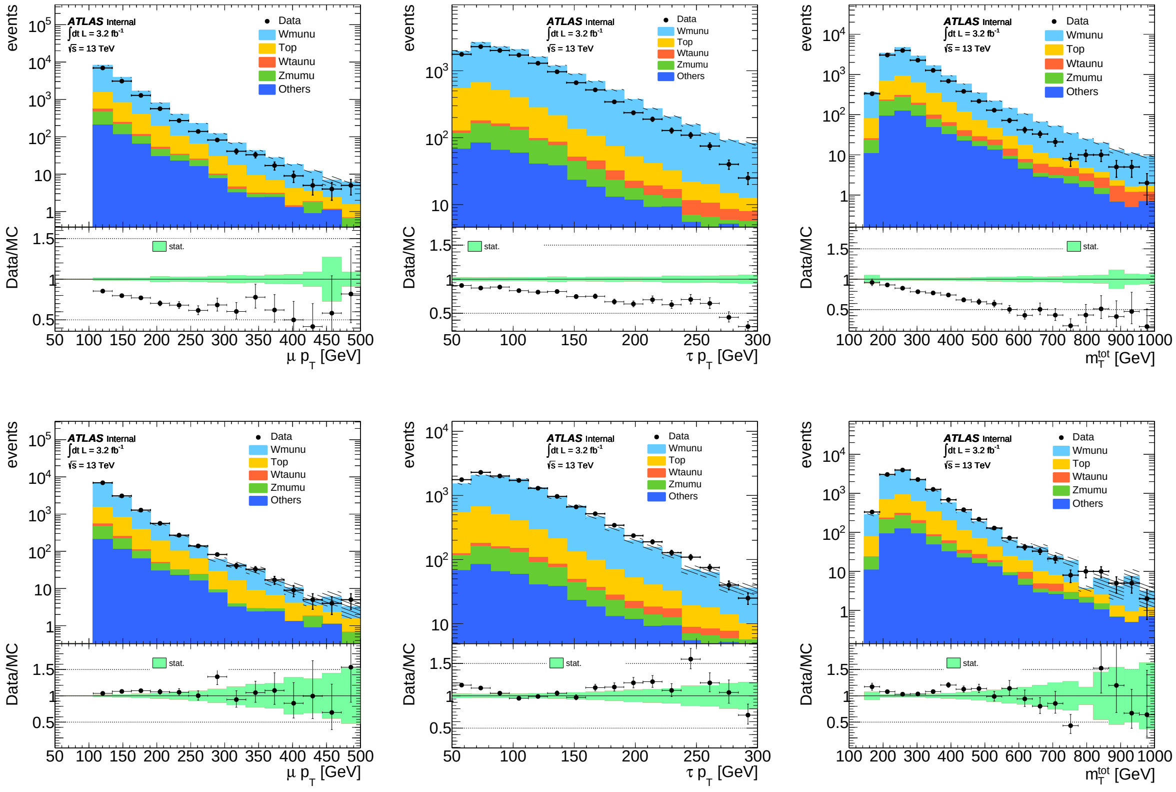

Figure 6.7: Distributions of selected kinematic variables in the W + jets control region using the `SHERPA` (top) and `Powheg` (bottom) generators to simulate W + jets events. The transverse momentum of the muon (left) and tau (centre) and the total transverse mass (right) are shown. The plots are produced by a collaborator.

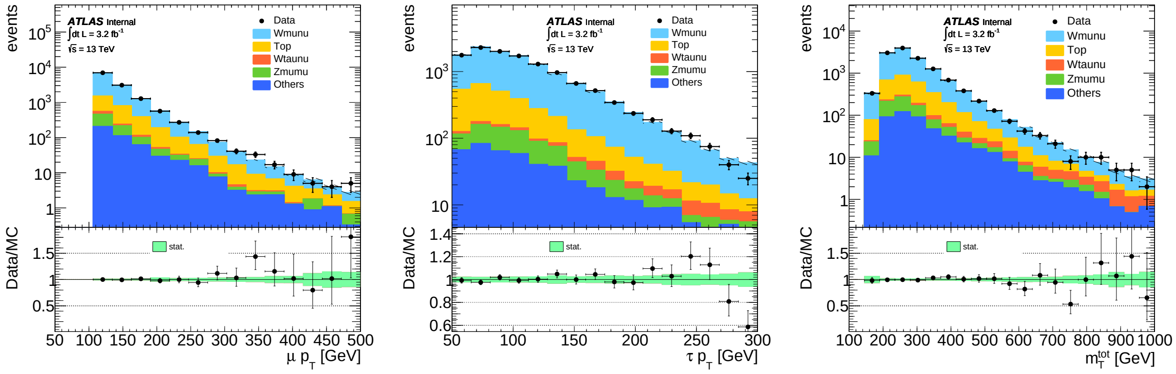

Figure 6.8: Distributions of selected kinematic variables in the W + jets control region using the `SHERPA` generator to simulate W + jets events, after the application of a reweighting function derived in data. The transverse momentum of the muon (left) and tau (centre) and the total transverse mass (right) are shown. The plots are produced by a collaborator.

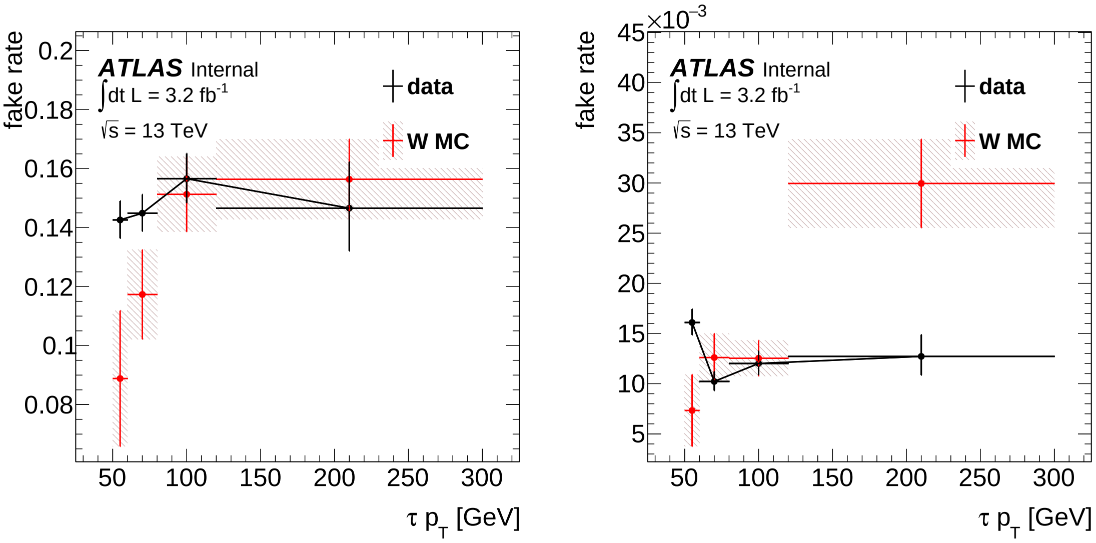

(a) 1-prong OS (b) 3-prong OS

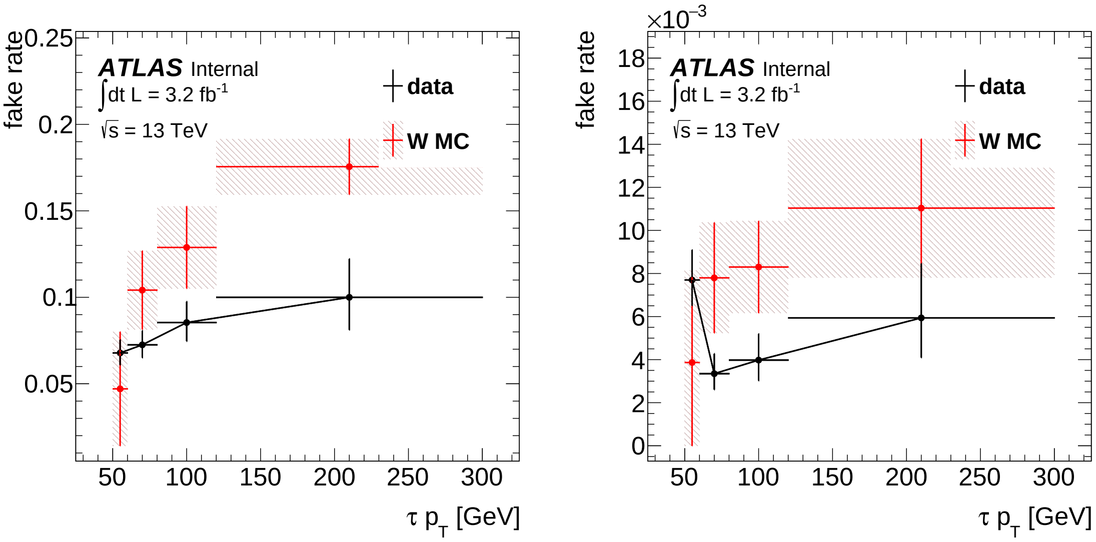

(c) 1-prong SS (d) 3-prong SS

Figure 6.9: The misidentification rate (fake rate) of candidate taus passing the loose tau ID working point in a control region dominated by $W(\to\mu\nu)$+jets events for data and simulated $W(\to\mu\nu)$+jets events. The events most likely contain jets associated with the W boson that are reconstructed as candidate taus. The misidentification rate is split into events in which the muon and candidate tau have opposite sign charges (top) and same sign charges (bottom), as well as the case where the tau candidate is 1-prong (left) and 3-prong (right). The plots are produced by a collaborator.

a weighting to the simulated event, dependent on the p_T and number of tracks (N_track), and calculated separately depending on the tau BDT identification requirement (i.e. loose or medium) in the event selection. The trigger also contains an online BDT tau identification requirement, and so the rate at which the jets are misidentified as passing the online tau identification algorithms is contained in the fake rate applied to the leading tau candidate, and the tau trigger requirement in the event selection is dropped.

The control region is similar to that used in the W+jets kinematic reweighting, but with the transverse momentum thresholds of the muon and tau candidate reduced to $p_\mathrm{T}^{\mu} > 55$ GeV and $p_\mathrm{T}^{\tau} > 50$ GeV. Further requirements are added such that there are no b-tagged jets, and that the sum of the cosines of the separation between the MET and both the muon and tau candidate is below zero, expressed as $\sum_{\ell=\mu,\tau} \cos \Delta\phi(\ell, E_\mathrm{T}^\mathrm{miss}) < 0$. This reduces $t\bar{t}$ and multi-jet contamination.

The measured fake rates for W+jets events are shown in Figure 6.10 for 1-prong and 3-prong tau candidates, with the two cases of loose and medium+trigger tau identification levels, and the rates are split between events in which the muon and tau candidate have OS and SS. The fake rates measured in a top control region, described in Section 6.3.3, are also shown.

6.3.3 Top background estimation

Backgrounds originating from the production of top quarks, in particular $t\bar{t}$ processes, form the second largest background to the b-tag category, and the largest background for high masses of the Higgs boson. Both $t\bar{t}$ and single top processes are estimated via simulation. Attempts were made to develop a dedicated $t\bar{t}$ control region in order to verify the modelling of the background, with various methods tested including variations on the number of b-jets and inversion of the signal region $\Delta\phi$. With the requirement that the control region be similar, yet orthogonal, to the signal region, it was found that there are insufficient data events to verify the modelling in a satisfactory way.

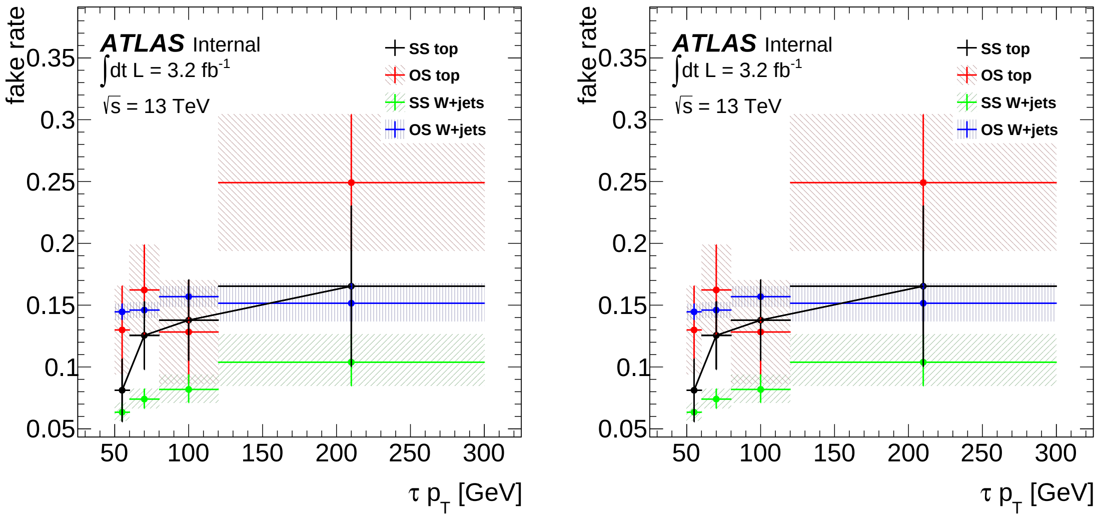

(a) Loose-ID 1-prong

(b) Loose-ID 3-prong

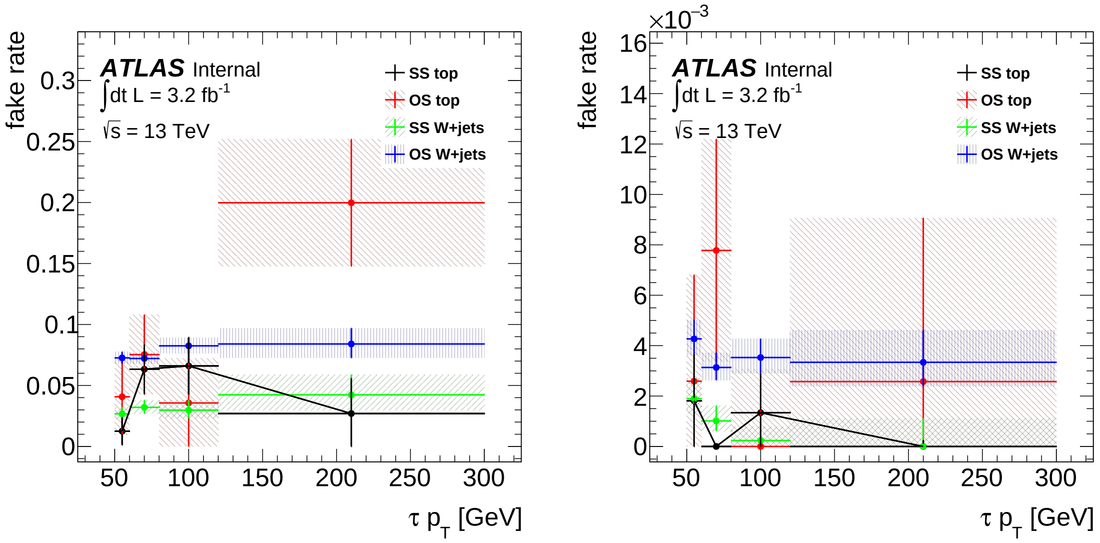

(c) Trigger+medium-ID 1-prong

(d) Trigger+medium-ID 3-prong

Figure 6.10: The rate at which jets are misidentified as a tau candidate, the fake rate, as measured in the $W(\rightarrow \mu\nu)$+jets and top control regions in data. The rates depend upon the working point of the online or offline tau identification algorithms, with the loose working point (top) and medium working point including the trigger (bottom) shown separately for 1-prong and 3-prong tau candidate particles and split by the charge product of the muon and tau candidate. The plots are produced by a collaborator.

Top background correction for the misidentification of tau candidates

As for the W+jets background, and with the same motivation, a correction is applied in place of the tau identification BDT in cases where the tau candidate is not geometrically matched to a generator level tau lepton. The correction applies to quark and gluon initiated jets that are reconstructed as tau candidate particles, whilst generator level tau particles generated from the simulated decays of W bosons (that result from the decay of t-quarks) will generally have the tau identification algorithm applied instead. The correction, or fake rate, is exactly the same as that described in Section 6.3.2, but measured in a separate but similar control region. The only differences in the control region described in Section 6.3.2 are that there must be at least one b-tagged jet in the final state, and that the $\sum_{\ell=\mu,\tau} \cos\Delta\phi(\ell, E_{\mathrm{T}}^{\mathrm{miss}}) < 0$ and $\Delta\phi(\mu,\tau) > 2.4$ requirements are dropped. The non-negligible contribution of events which contain real tau leptons, is estimated via simulation and subtracted from the control region.

The measured fake rates for the top control region are shown in Figure 6.10 for 1-prong and 3-prong tau candidates, with the case of loose and medium+trigger tau identification levels, and the rates are split between events in which the muon and tau candidate have OS and SS.

6.3.4 Z+jets and diboson background estimation

Backgrounds from Z+jets and diboson processes are estimated via simulation, with exactly the same misidentification rate correction as in the case of W+jets backgrounds in Section 6.3.2, derived in the W+jets control region. As such, events in which a simulated W boson or Z boson decays to a tau particle at generator level generally have the tau identification BDT applied, whereas events in which a jet is misidentified as a tau candidate are reweighted by the ‘fake rate’.

6.3.5 Validation of the background estimation in the SS validation region

The SS validation region is orthogonal to the signal region, with the event selection differing in that both tau candidates have the same sign charge. This validation region enables the performance of checks, particularly in regard to the multi-jet background estimation, before the unblinding of results in the signal region.

Figures 6.11 and 6.12 show selected distributions of kinematic variables used in constructing the mass discriminant after the full SS event selection for the b-veto category, whilst Figures 6.13 and 6.14 show the same kinematic distributions in the SS b-tag category. The invariant mass of the di-tau system, an alternative mass reconstruction method, is also checked, though is not used in the analysis.

Due to the relatively low number of events and large statistical uncertainty in the SS b-tag validation region, the figures are also shown for the SS b-tag validation region without the application of the $\Delta\phi(\tau^0_{had}, \tau^1_{had}) > 2.7$ requirement, and appear in Appendix D. Z+jets and W+jets processes where tau particles are not produced as a direct result of the boson decay, are classified with diboson processes under the heading ‘others’, due to the low yields from these background processes.

It can be seen that there is reasonably good agreement between the data and estimated backgrounds in the SS validation region.

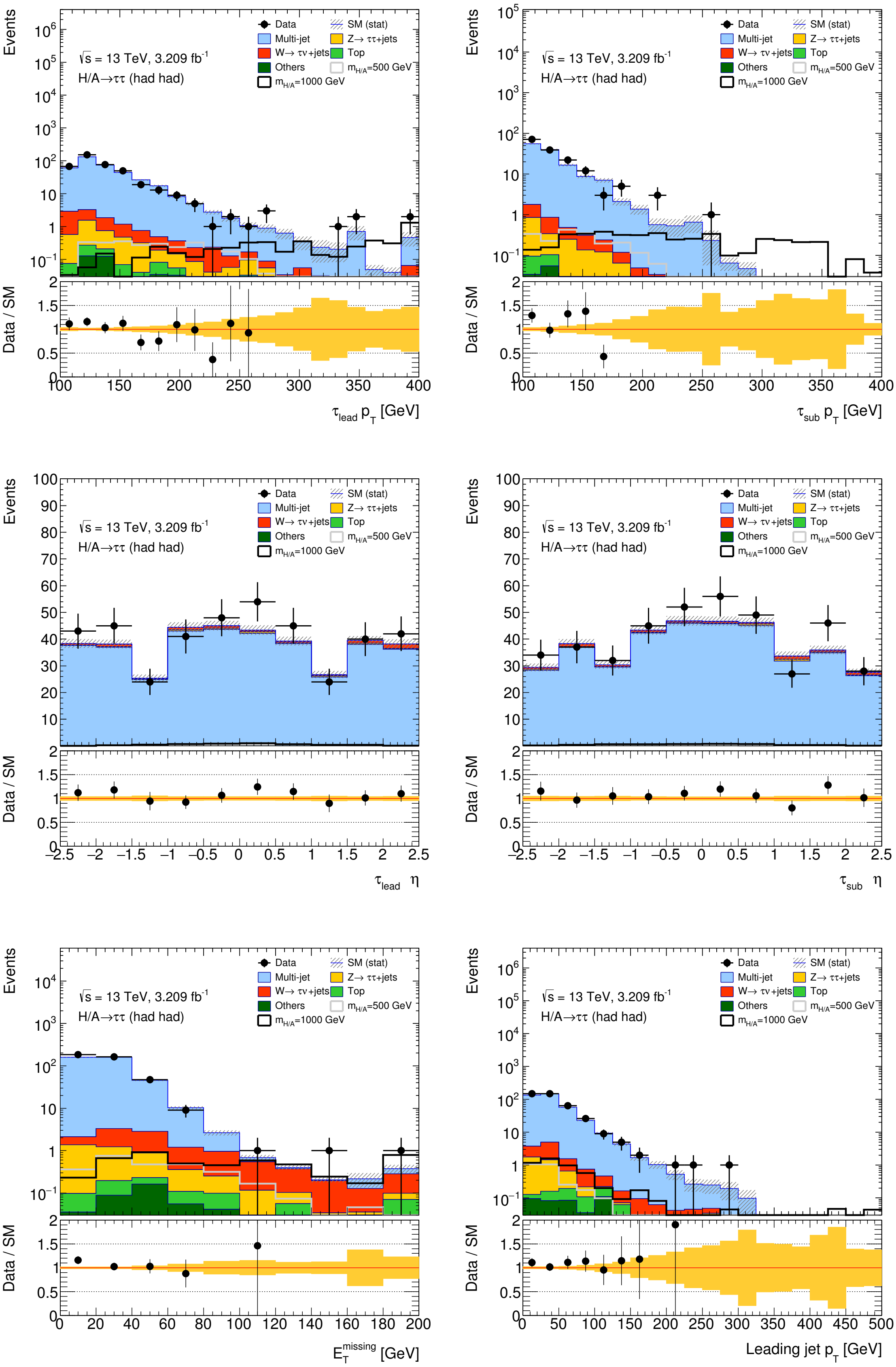

Figure 6.11: Various distributions of selected kinematic variables after the full event selection of the b-veto SS validation region. Two simulated gluon-gluon fusion signal mass points of 500 GeV and 1000 GeV are also shown for illustrative purposes, with cross section times branching fractions normalised to 1 pb. The data correspond to an integrated luminosity of 3.21 fb^{-1}. Only statistical uncertainties are shown.

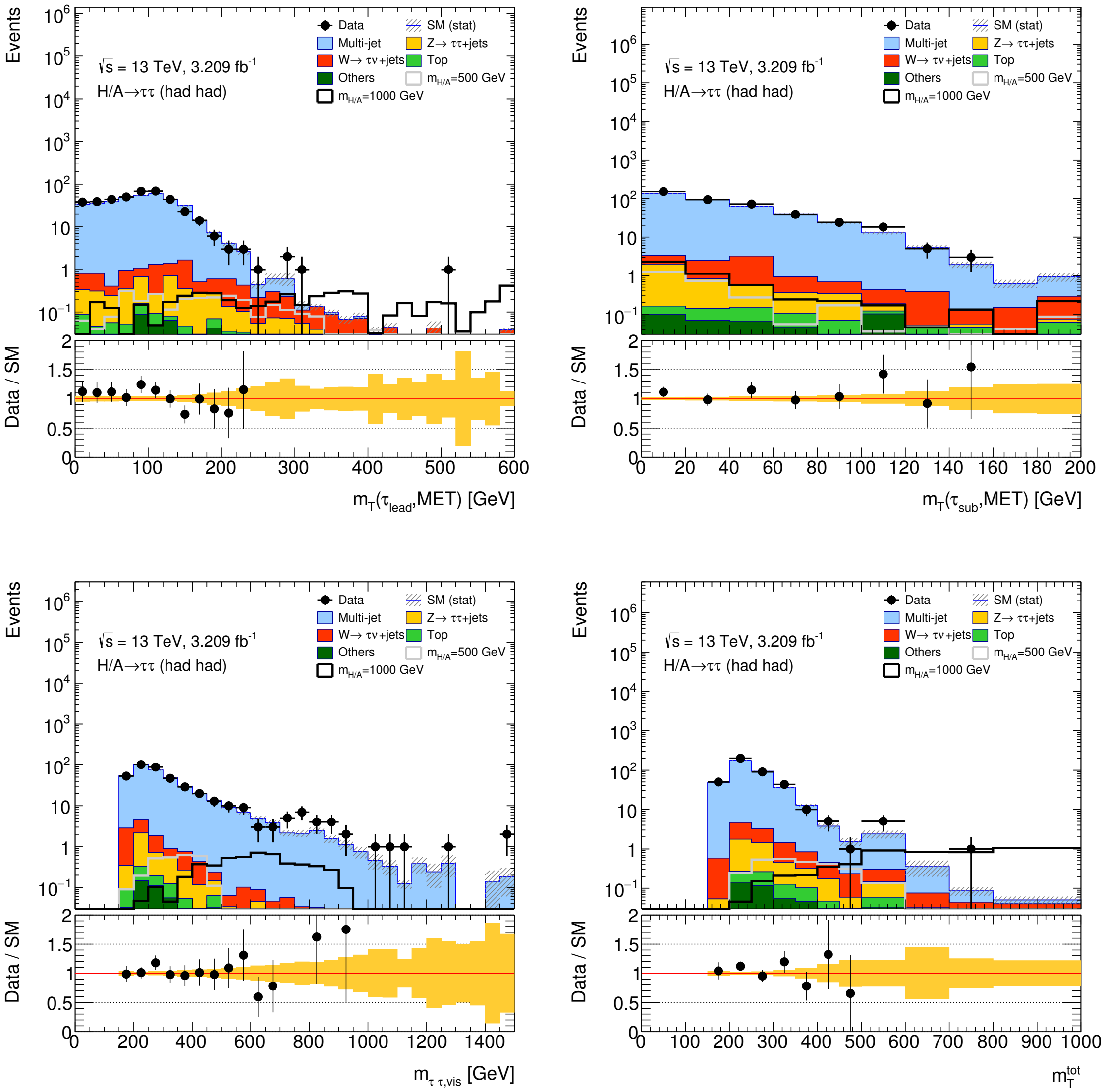

Figure 6.12: Various distributions of selected kinematic variables after the full event selection of the b-veto SS validation region. Two simulated gluon-gluon fusion signal mass points of 500 GeV and 1000 GeV are also shown for illustrative purposes, with cross section times branching fractions normalised to 1 pb. The data correspond to an integrated luminosity of 3.21 fb^{-1}. Only statistical uncertainties are shown.

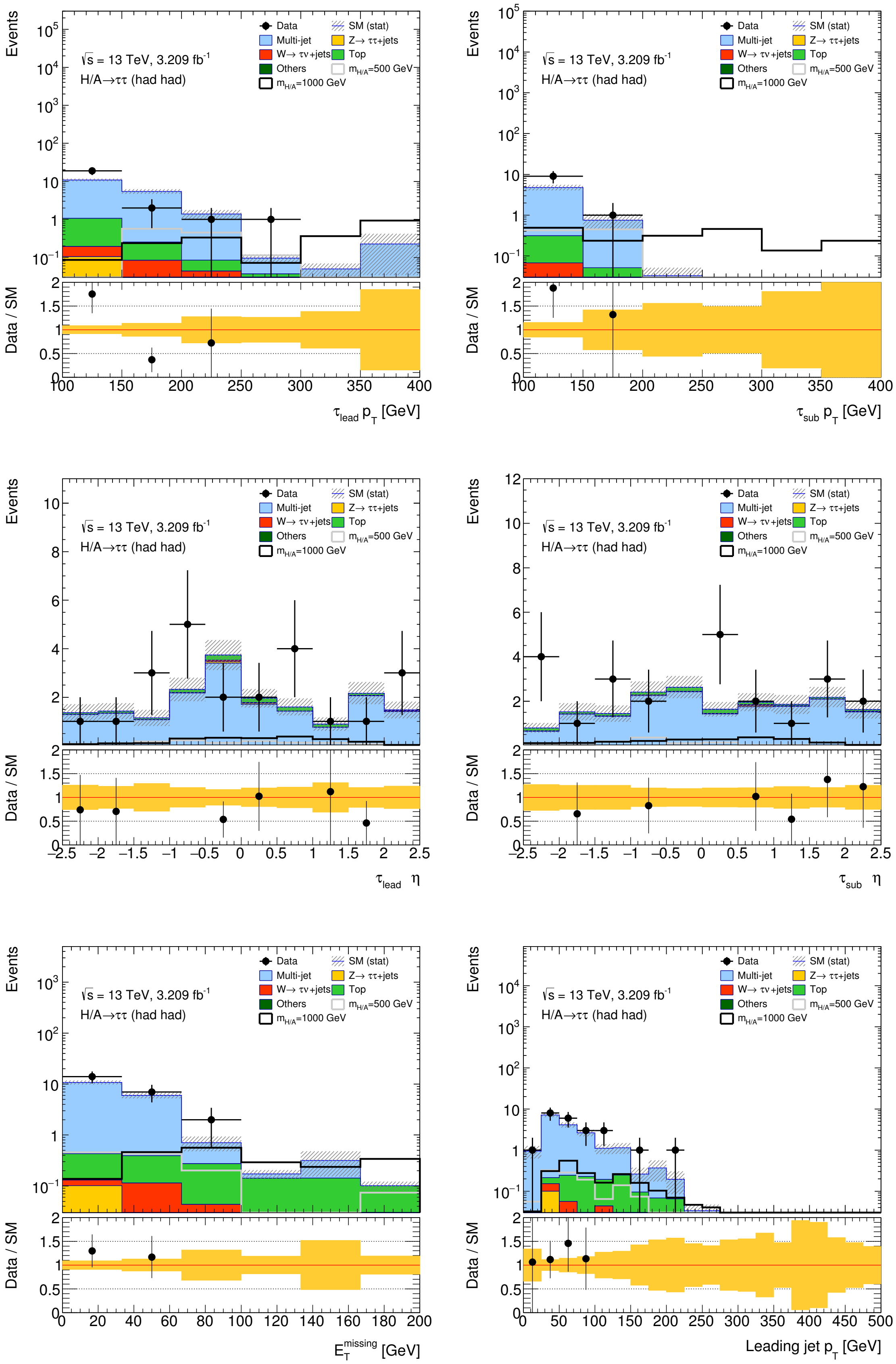

Figure 6.13: Various distributions of selected kinematic variables after the full event selection of the b-tag SS validation region. Two simulated b-associated production signal mass points of 500 GeV and 1000 GeV are also shown for illustrative purposes, with cross section times branching fractions normalised to 1 pb. The data correspond to an integrated luminosity of 3.21 fb^{-1}. Only statistical uncertainties are shown.

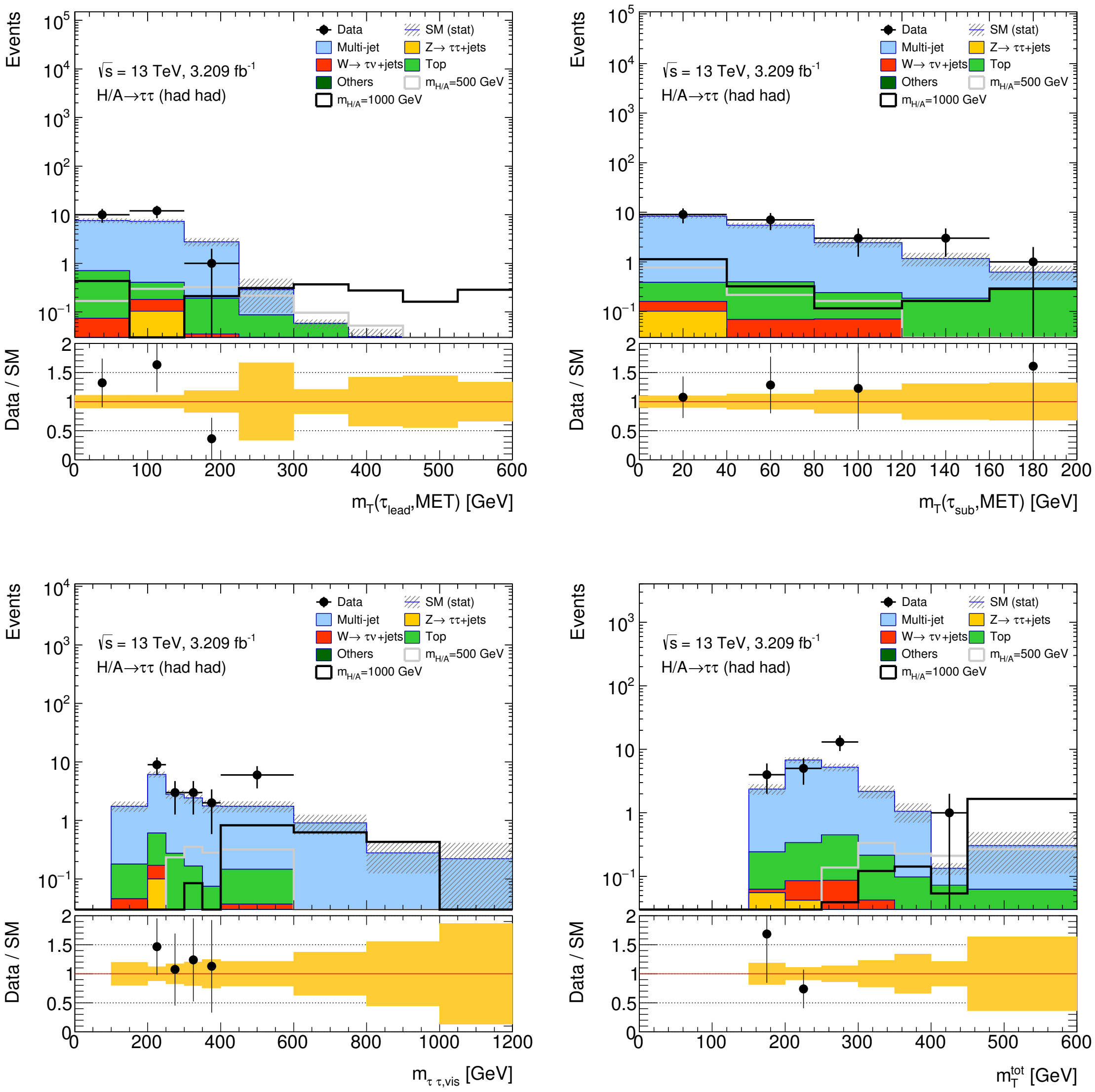

Figure 6.14: Various distributions of selected kinematic variables after the full event selection of the b-tag SS validation region. Two simulated b-associated production signal mass points of 500 GeV and 1000 GeV are also shown for illustrative purposes, with cross section times branching fractions normalised to 1 pb. The data correspond to an integrated luminosity of 3.21 fb^{-1}. Only statistical uncertainties are shown.

6.4 Results of the event selection and background estimation

This section displays the event yields and selected kinematic distributions after the b-veto and b-tag event selections described in Section 6.2.2. The methods described in Section 6.3 are used to estimate the major SM backgrounds after the event selections. Table 6.6 shows the data and estimated background yields at various stages of the event selection, for both the b-veto and b-tag categories. Also shown are the yields in the SS control region, where the charge product of the leading and subleading tau candidates is the same sign. Z+jets and W+jets processes where tau particles are not produced as a direct result of the boson decay, are classified with diboson processes under the heading ‘others’, due to the low yields from these background processes.

The statistical analysis of the results with the inclusion of sources of systematic uncertainty and their interpretation in terms of the MSSM parameter space, is carried out in Section 6.6.

6.4.1 Kinematic distributions in the b-veto signal region

Figures 6.15 and 6.16 show the distributions of selected kinematic variables after the complete event selection of the b-veto signal region, described in Section 6.2.2. The variables shown are used in constructing the mass discriminant, $m_{\mathrm{T}}^{\mathrm{tot}}$, used in the analysis. The invariant mass of the di-tau system, an alternative mass construction method, is also checked, though is not used in the analysis. Several selected signal Higgs boson mass points, produced by the gluon gluon fusion production mechanism, are also shown with an arbitrary cross section times branching fraction of 1 pb.

Selection criteria	Data	Multi-jet	stat.	$Z \to \tau\tau$	stat.	$W(\to \tau\nu)$	stat.	Top	stat.	Others	stat.
Preselection	2400154	-	-	17974.7	177.8	66067.8	677.1	73691.5	249.5	16170.7	387.5
Trigger & τ_{lead}^{ID}	236795	-	-	1407.4	44.4	3168.6	67.3	2955.9	19.3	343.9	10.8
Leading $\tau p_{\mathrm{T}} > 110$ GeV	106016	-	-	641.8	29.1	1208.5	32.0	775.5	9.3	86.3	3.8
Subleading $\tau p_{\mathrm{T}} > 55$ GeV	71177	-	-	509.1	25.6	902.6	28.8	548.8	7.9	61.1	3.4
$\Delta\phi(\tau_{had}^{0}, \tau_{had}^{1}) > 2.7$	50023	-	-	268.0	16.1	503.5	25.1	213.3	4.9	30.3	2.6
Expected event yields for SM backgrounds and observed events through the event selection common to both *b*-tag and *b*-veto categories											
b-veto	48270	-	-	260.6	15.8	489.1	25.0	63.7	2.6	28.2	2.4
Subleading τ ID	1034	759.9	7.4	111.1	2.0	46.0	2.2	4.6	0.6	4.5	0.4
Opposite Sign	628	393.4	5.4	107.4	1.9	38.7	2.0	3.8	0.5	4.0	0.4
Same Sign	406	366.5	5.1	3.7	0.4	7.3	1.0	0.8	0.1	0.5	0.1
b-tag	1753	-	-	7.2	3.0	14.4	1.2	149.6	4.2	2.1	1.1
Subleading τ ID	46	33.9	1.9	1.4	0.2	1.1	< 0.1	14.5	< 1.0	0.1	< 0.1
Opposite Sign	23	17.3	1.4	1.4	0.2	0.9	< 0.1	11.4	0.8	0.1	< 0.1
Same Sign	23	16.6	1.3	< 0.1	< 0.1	0.2	< 0.1	3.1	0.1	< 0.1	< 0.1

Table 6.6: Expected event yields for SM backgrounds and observed events in the event selection. The top section of the table shows the event selection common to both categories. The second section shows the continued event selection in the *b*-veto category and the split between opposite sign and same sign charges of the two tau particles. The third section shows the event selection in the *b*-tag category and the split between opposite sign and same sign charges of the two tau particles. The multi-jet background is not applicable until estimation via events failing the subleading tau identification stage. All numbers correspond to an integrated luminosity of 3.21 fb^{-1}.

6.4.2 Kinematic distributions in the *b*-tag signal region

Figures 6.17 and 6.18 show the distributions of selected kinematic variables, as discussed above, after the complete event selection of the b-tag signal region. Several selected signal Higgs boson mass points, produced by the b-associated production mechanism, are also shown with an arbitrary cross section times branching fraction of 1 pb. As the data and estimated background yield after the full event selection is relatively low, a second set of kinematic distributions without the application of the $\Delta\phi(\tau^0_{had}, \tau^1_{had}) > 2.7$ requirement is shown in Appendix E.

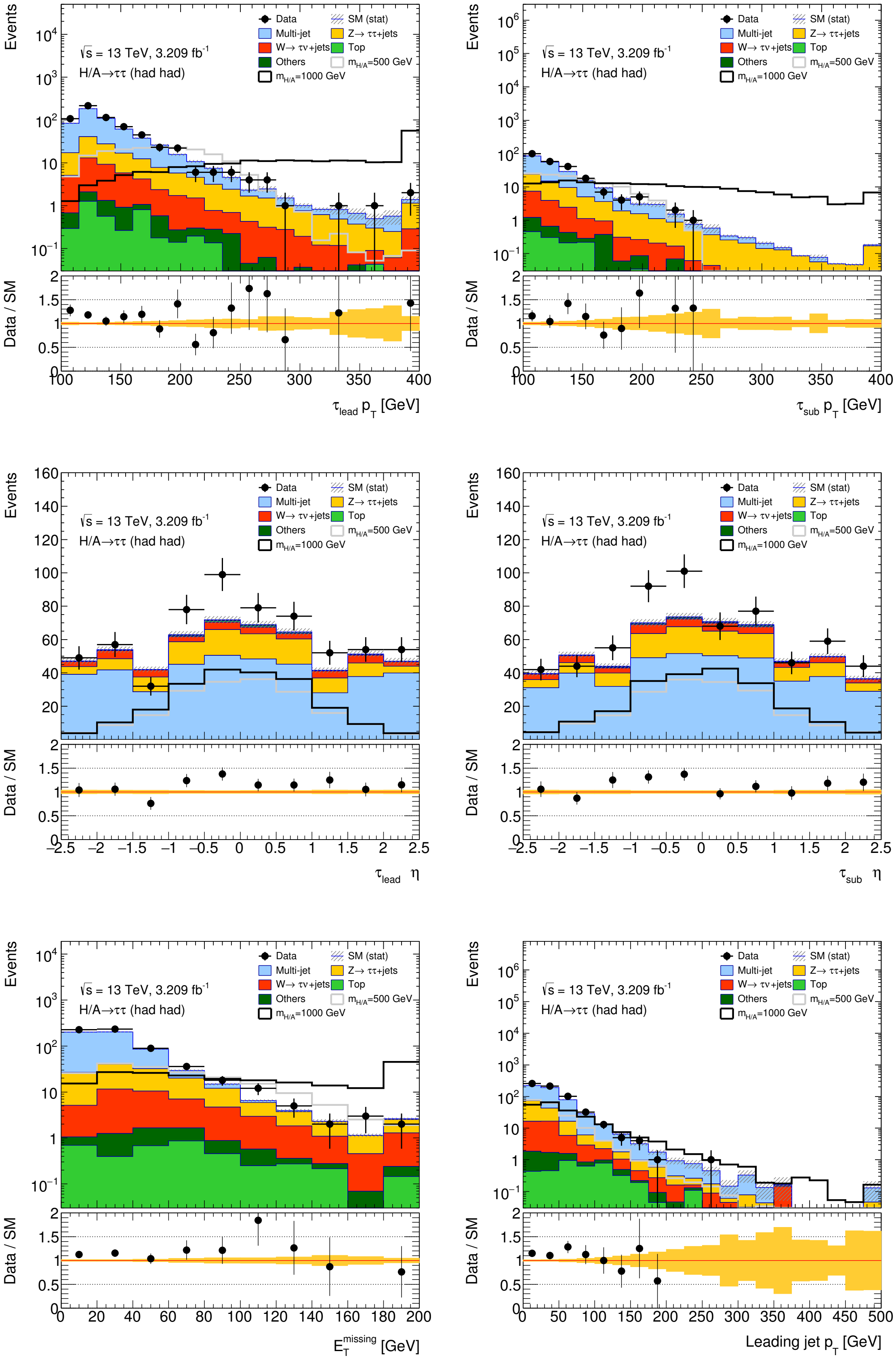

Figure 6.15: Various distributions of selected kinematic variables after the full event selection of the b-veto signal region. Two simulated gluon-gluon fusion signal mass points of 500 GeV and 1000 GeV are also shown for illustrative purposes, with cross section times branching fractions normalised to 1 pb. The data correspond to an integrated luminosity of 3.21 fb^{-1}. Only statistical uncertainties are shown.

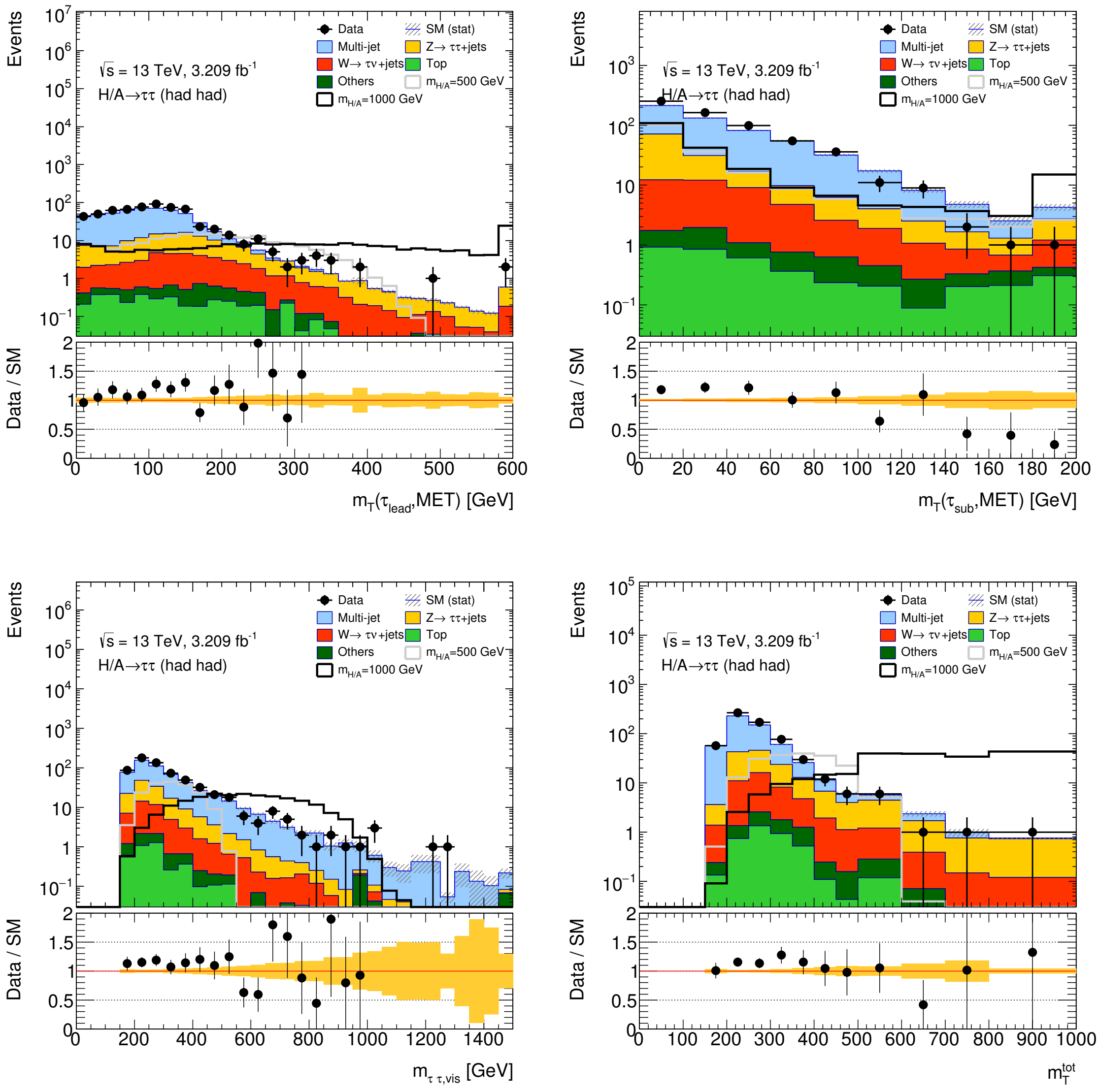

Figure 6.16: Various distributions of selected kinematic variables after the full event selection of the b-veto signal region. Two simulated gluon-gluon fusion signal mass points of 500 GeV and 1000 GeV are also shown for illustrative purposes, with cross section times branching fractions normalised to 1 pb. The data correspond to an integrated luminosity of 3.21 fb^{-1}. Only statistical uncertainties are shown.

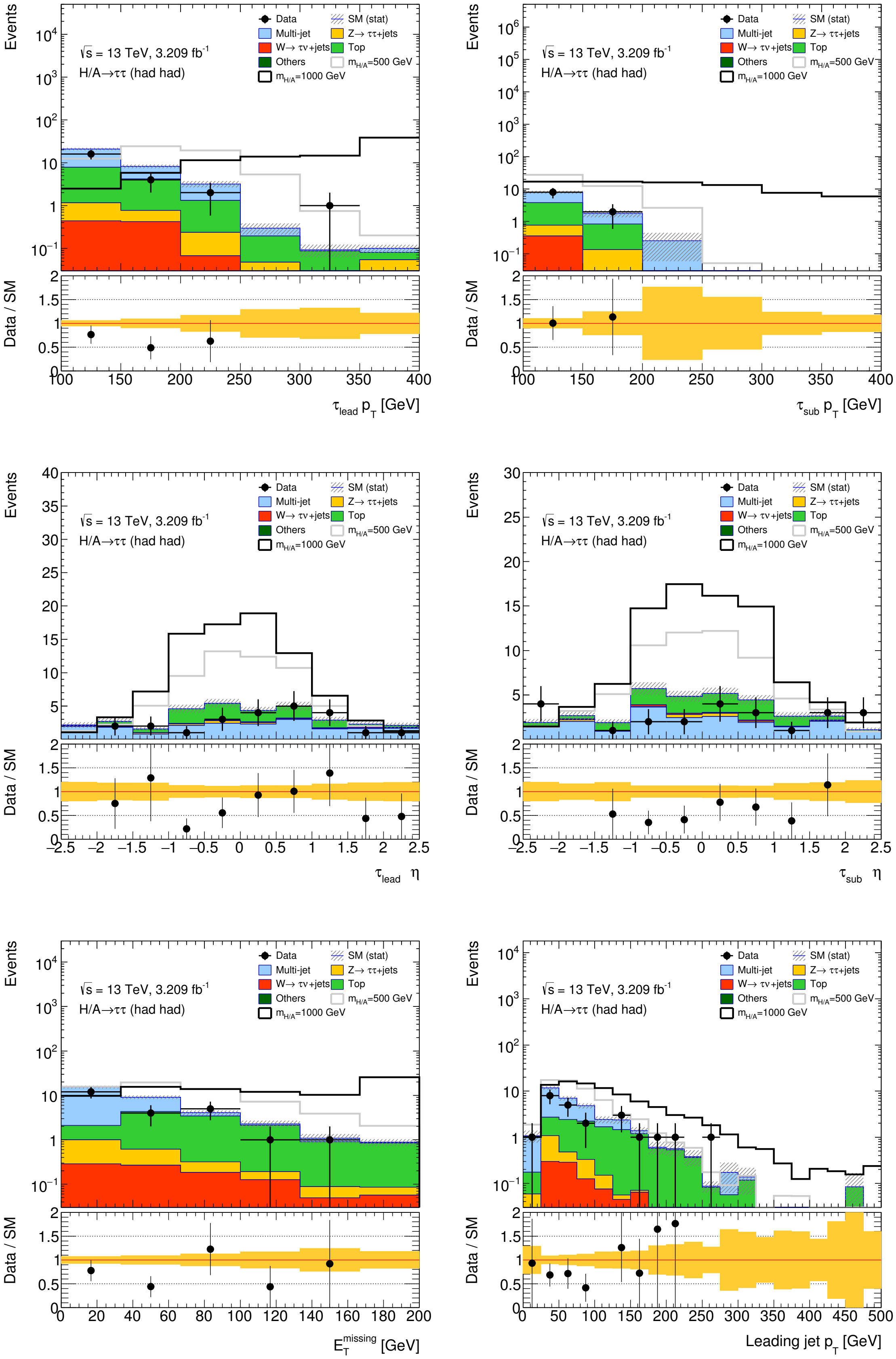

Figure 6.17: Various distributions of selected kinematic variables after the full event selection of the b-tag signal region. Two simulated b-associated production signal mass points of 500 GeV and 1000 GeV are also shown for illustrative purposes, with cross section times branching fractions normalised to 1 pb. The data correspond to an integrated luminosity of 3.21 fb^{-1}. Only statistical uncertainties are shown.

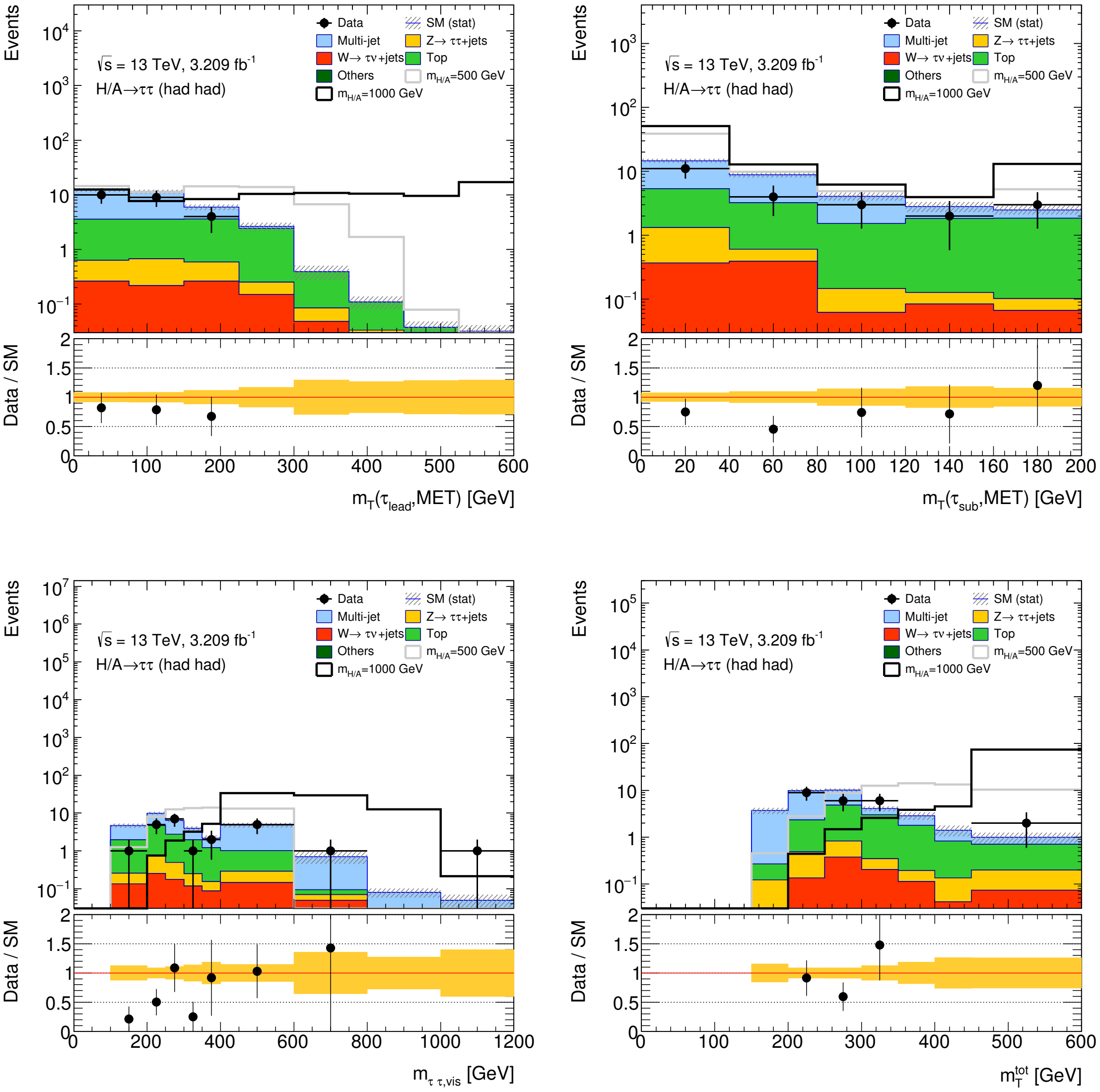

Figure 6.18: Various distributions of selected kinematic variables after the full event selection of the b-tag signal region. Two simulated b-associated production signal mass points of 500 GeV and 1000 GeV are also shown for illustrative purposes, with cross section times branching fractions normalised to 1 pb. The data correspond to an integrated luminosity of 3.21 fb^{-1}. Only statistical uncertainties are shown.

6.5 Sources of systematic uncertainty

The imperfect modelling of the ATLAS detector and estimated backgrounds results in several sources of systematic uncertainty that must be considered in the analysis along with the statistical uncertainty on the number of simulated events. These uncertainties can have an impact on both the normalisation and shape of the $m_{\mathrm{T}}^{\mathrm{tot}}$ reconstructed mass distribution. This section describes the sources of uncertainty considered in the analysis. Tables 6.7 and 6.8 display the leading systematics associated with the ATLAS detector, object reconstruction and background modelling, in the b-veto and b-tag categories respectively, in terms of their impact on the yield after the signal selection. Sources of uncertainty that have a negligible impact on the yields ($< 1\%$) are ignored.

6.5.1 Luminosity

The luminosity of the 2015 dataset is measured to be 3.21 fb^{-1}, with an uncertainty of 5% estimated using the methods described in Ref. [128].

6.5.2 Pile-up

The simulated backgrounds are generated with a specific pile-up (PU) distribution. This distribution is then reweighted in order to match the PU distribution observed in data more closely, and the imperfect reweighting contributes an uncertainty to the analysis that is determined by altering the reweighting factor.

6.5.3 Multi-jet estimation via fake factors

The uncertainty related to the multi-jet background estimation via fake factors, as described in Section 6.3.1, is taken as the sum in quadrature of the statistical uncertainty of the measurement of the fake factor and the difference between the OS and SS fake factors, which are shown in Figure 6.3. This covers the statistical uncertainty in the fake factor as

Systematic	multi-jet	Top	$W(\to \tau\nu)$	$Z \to \tau\tau$	Others	bbH [500 GeV]	ggH [500 GeV]
fake factor	$^{6.8}_{-6.8}$	-	-	-	-	-	-
tau trigger	-	$^{18.3}_{-15.9}$	$^{5.6}_{-4.6}$	$^{21.1}_{-18.2}$	$^{11.9}_{-10.4}$	$^{26.0}_{-23.9}$	$^{25.7}_{-23.5}$
tau ID	-	$^{10.5}_{-10.0}$	$^{6.6}_{-6.6}$	$^{12.5}_{-11.8}$	$^{6.9}_{-6.5}$	$^{12.0}_{-11.4}$	$^{11.9}_{-11.2}$
tau ID high-p_{T}	-	$^{1.0}_{-1.0}$	-	$^{1.5}_{-1.4}$	-	$^{2.3}_{-2.3}$	$^{2.3}_{-2.2}$
tau e-veto	-	$^{2.7}_{-2.6}$	$^{1.3}_{-1.3}$	$^{3.3}_{-3.2}$	$^{1.7}_{-1.7}$	$^{4.7}_{-4.7}$	$^{3.8}_{-3.8}$
tau reco.	-	$^{3.8}_{-3.7}$	$^{2.4}_{-2.4}$	$^{4.6}_{-4.5}$	$^{2.6}_{-2.5}$	$^{4.5}_{-4.4}$	$^{4.5}_{-4.4}$
TES ‘detector’	-	$^{6.7}_{-6.2}$	$^{5.4}_{-4.6}$	$^{11.0}_{-10.1}$	$^{6.1}_{-3.6}$	$^{1.4}_{-1.5}$	$^{2.0}_{-2.3}$
TES ‘model’	-	$^{0.8}_{-1.9}$	$^{1.2}_{-0.0}$	$^{1.4}_{-1.6}$	$^{2.0}_{-0.7}$	$^{0.3}_{-0.5}$	$^{0.4}_{-0.5}$
TES ‘in-situ’	-	$^{5.8}_{-5.5}$	$^{4.3}_{-2.4}$	$^{6.3}_{-4.9}$	$^{3.5}_{-2.4}$	$^{0.9}_{-0.8}$	$^{1.2}_{-1.4}$
fake rate	-	$^{5.4}_{-6.2}$	$^{9.5}_{-8.7}$	-	$^{8.0}_{-7.0}$	-	-
PU reweight	-	$^{-3.8}_{4.3}$	$^{6.1}_{1.7}$	-	$^{-1.5}_{1.2}$	-	$^{1.1}_{-0.6}$
JVF	-	$^{3.6}_{-3.4}$	$^{2.1}_{-2.0}$	$^{1.2}_{-1.2}$	$^{1.9}_{-1.8}$	$^{1.8}_{-1.8}$	$^{1.7}_{-1.6}$
JER	-	$^{1.9}_{-1.9}$	-	-	-	$^{0.6}_{-0.6}$	-
b-tag eff.(B0)	-	$^{4.4}_{-4.2}$	-	-	-	$^{1.7}_{-1.7}$	-
b-tag eff.(B1)	-	$^{1.6}_{-1.6}$	-	-	-	-	-

Table 6.7: The effect, in %, on the b-veto category final event yields for various signal and background processes as a result of shifting selected systematic uncertainties up and down by $\pm 1\sigma$. Only dominant uncertainties relating to the object reconstruction and background modelling are shown. Several different systematics contribute to the b-tagging efficiency. Many systematic uncertainties that have a very small effect ($< 1\,\%$) on the overall yield are not shown. The effects of some of the sources of systematic uncertainty listed were studied by collaborators.

Systematic	multi-jet	Top	$W(\rightarrow \tau\nu)$	$Z \rightarrow \tau\tau$	Others	bbH 500 [GeV]	ggH 500 [GeV]
fake factor	$^{17.1}_{-17.1}$	-	-	-	-	-	-
tau trigger	$^{-1.6}_{1.9}$	$^{18.0}_{-15.4}$	$^{7.2}_{-6.1}$	$^{21.9}_{-19.3}$	$^{8.4}_{-7.4}$	$^{26.3}_{-24.1}$	$^{24.9}_{-22.3}$
tau ID	-	$^{10.9}_{-10.3}$	$^{6.2}_{-6.2}$	$^{12.6}_{-11.9}$	$^{3.9}_{-3.9}$	$^{12.0}_{-11.3}$	$^{11.8}_{-11.1}$
tau ID high-p_{T}	-	$^{1.0}_{-1.0}$	-	$^{1.6}_{-1.6}$	-	$^{2.4}_{-2.4}$	$^{2.2}_{-2.2}$
tau e-veto	-	$^{2.7}_{-2.7}$	$^{1.5}_{-1.5}$	$^{3.3}_{-3.2}$	$^{1.0}_{-1.0}$	$^{4.7}_{-4.7}$	$^{4.0}_{-3.9}$
tau reco.	-	$^{3.9}_{-3.8}$	$^{2.5}_{-2.5}$	$^{4.7}_{-4.6}$	$^{1.5}_{-1.5}$	$^{4.5}_{-4.4}$	$^{4.6}_{-4.5}$
TES ‘detector’	-	$^{8.6}_{-7.4}$	$^{4.5}_{-4.8}$	$^{4.9}_{-10.8}$	$^{0.0}_{-0.8}$	$^{1.8}_{-2.2}$	$^{0.0}_{-4.5}$
TES ‘model’	-	$^{1.8}_{-0.4}$	$^{0.9}_{-1.7}$	$^{2.6}_{-0.1}$	$^{0.0}_{-0.0}$	$^{0.3}_{-0.4}$	$^{0.0}_{-0.0}$
TES ‘in-situ’	-	$^{6.8}_{-4.3}$	$^{2.3}_{-6.7}$	$^{4.5}_{-6.8}$	$^{0.0}_{-1.0}$	$^{1.2}_{-1.3}$	$^{0.0}_{-0.9}$
fake rate	-	$^{4.9}_{-5.7}$	$^{9.3}_{-8.5}$	-	$^{12.4}_{-11.0}$	-	-
PU reweight	-	$^{3.6}_{-3.4}$	$^{-15.5}_{2.1}$	$^{-5.1}_{4.6}$	$^{-25.9}_{2.1}$	$^{3.8}_{-1.7}$	$^{6.5}_{1.3}$
JVF	-	$^{3.9}_{-3.7}$	$^{3.9}_{-3.7}$	$^{2.9}_{-2.9}$	$^{4.6}_{-4.4}$	$^{3.4}_{-3.3}$	$^{3.6}_{-3.5}$
JER	-	$^{0.6}_{-0.6}$	$^{1.0}_{-1.0}$	$^{1.6}_{-1.6}$	$^{5.9}_{-5.9}$	$^{0.7}_{-0.7}$	$^{0.5}_{-0.5}$
b-tag eff.(L0)	-	-	$^{-3.8}_{3.8}$	$^{-4.5}_{4.5}$	$^{-7.6}_{7.6}$	-	$^{-5.9}_{5.9}$
b-tag eff.(L1)	-	-	-	-	-	-	$^{-1.2}_{1.2}$
b-tag eff.(B0)	-	$^{-2.2}_{2.1}$	$^{-2.3}_{2.3}$	$^{-1.9}_{1.9}$	$^{-1.4}_{1.3}$	$^{-3.6}_{3.6}$	$^{-2.8}_{2.8}$
b-tag eff.(C0)	-	-	$^{-4.6}_{4.6}$	$^{-4.1}_{4.2}$	$^{-3.9}_{3.8}$	-	$^{-3.1}_{3.0}$
b-tag eff.(C1)	-	-	$^{2.5}_{-2.5}$	$^{2.4}_{-2.4}$	$^{2.2}_{-2.2}$	-	$^{2.0}_{-2.0}$

Table 6.8: The effect, in %, on the b-tag category final event yields for various signal and background processes as a result of shifting selected systematic uncertainties up and down by $\pm 1\sigma$. Only dominant uncertainties relating to the object reconstruction and background modelling are shown. Several different systematics contribute to the b-tagging efficiency. Many systematic uncertainties that have a very small effect ($< 1\,\%$) on the overall yield are not shown. The effects of some of the sources of systematic uncertainty listed were studied by collaborators.

well as the uncertainty in the quark-gluon fraction of the jets.

6.5.4 Jet → τ fake rate

The method of estimating the rate at which jets are misidentified as tau candidates, the fake rate, is described in Sections 6.3.2 and 6.3.3. The systematic uncertainty related to the fake rate is taken as the statistical uncertainty on the fake rate measurement.

6.5.5 W+jets reweighting

A reweighting of the W+jets $m_{\mathrm{T}}^{\mathrm{tot}}$ distribution is applied in order to correct for the differences observed between data and the `SHERPA` generator, as described in Section 6.3.2. The systematic uncertainty on the reweighting is taken from the upper and lower uncertainties on the exponential fit parameters and covers the statistical uncertainty on the fit.

6.5.6 Tau candidates

Sources of systematic uncertainty associated with the reconstruction, energy calibration, and identification of tau candidates are described in Chapter 4, whilst the tau trigger efficiency measurement and associated uncertainty is described in Section 5.3.

Due to difficulties and delays in the $\tau_{\mathrm{lep}}\tau_{\mathrm{had}}$ analysis, instead of the systematic uncertainty associated with high-p_{T} taus described in Section 4.5, a precautionary, flat 20% uncertainty based on preliminary studies was placed on high-p_{T} tau candidates ($p_{\mathrm{T}}^{\tau} > 100$ GeV). For consistency, this precautionary high-p_{T} uncertainty was also used in the $\tau_{\mathrm{had}}\tau_{\mathrm{had}}$ analysis.

6.5.7 Jet reconstruction

The main uncertainties on jets result from the corrections and calibrations applied to them, as described in Section 3.2.4. The contribution has an effect on the analysis due to the categorisation by the number of b-jets. The JES contributes many uncertainties from the various corrections that enter the calculation [69]. The effect is taken from the up and down variations of the JES uncertainty for each jet. The uncertainty on the jet energy resolution (JER) is also taken into account in the same way, as well as the JVF. Systematic uncertainties associated with the b-tagging of jets contribute through calibrations measured from $t\bar{t}$ events [129]. Sources of uncertainty result from the tagging and mis-tagging scale factors for b-jets, c-jets, and light-flavour jets.

6.5.8 Electron and muon candidates and $E_{\mathrm{T}}^{\mathrm{miss}}$

Uncertainties related to the reconstruction, energy scale and identification of electron and muon candidates are found to have a negligible effect in the signal region. The uncertainties on these objects, as well as on the jet and tau candidates, are propagated onto the reconstruction of the $E_{\mathrm{T}}^{\mathrm{miss}}$, and the effect is also found to be negligible.

6.5.9 Cross section uncertainties for simulated backgrounds

The simulated backgrounds and their cross sections are shown in Appendix A. The simulated backgrounds have associated uncertainties resulting from the fixed order calculation. The uncertainties for the Z+jets and diboson cross sections are taken from [130] and are 5% and 6%, respectively. For the top backgrounds, the uncertainty is 6% and is evaluated using the recommended ATLAS approach [131, 132].

6.5.10 Top background modelling

The $t\bar{t}$ background is the dominant contribution to the overall top background in the b-tag category, contributing 89% of the total yield of the top background. Uncertainties related to $t\bar{t}$ modelling include the uncertainties associated with the shower radiation and hadronisation model, and the impact is estimated through comparison with the `POWHEG+Herwig` genera-

category	QCD scales	Shower generator	hard scatter generator	combined
b-tag	${}^{+26.6}_{-17.6}$	±4.5	±26.9	${}^{+38.1}_{-32.5}$
b-veto	${}^{+13.3}_{-17.1}$	±6.2	±3.4	${}^{+15.0}_{-18.5}$

Table 6.9: The effect on the final event yield of the total top background for the uncertainty arising from the choice of shower generator and hard scatter generator, given in percent.

tor [133]. The uncertainty related to the truncated perturbative cross section calculation is calculated by variation of the `POWHEG+Pythia6` factorisation and renormalisation scales by a factor of 2 up and down, Additional uncertainties, arising due to the hard scatter generation, are estimated by the comparison of a sample generated by MC@NLO [134] and showered using `Herwig++` [135] to the sample generated by `POWHEG` and showered by `Herwig++`.

Based on the samples available, no statistically significant shape effect on the top background is observed for these systematic variations, and therefore only the effect on the normalisation of the background yield is considered. The quadratically combined normalisation systematic was determined as ${}^{+15.0}_{-18.5}\,\%$ in b-veto and ${}^{+38.1}_{-32.5}\,\%$ in the b-tag category. The individual components are listed in Table 6.9.

6.5.11 Signal modelling

There are several sources of systematic uncertainty associated with the modelling of the b-associated production and gluon fusion signals. These include uncertainties associated with the renormalisation and factorisation scales, initial and final state radiation, and the parton distribution function (PDF). The effect of the renormalisation and factorisation scale uncertainties is taken as the variation on the event selection yield from doubling or halving the scales. The uncertainties relating to the initial and final state radiation are estimated from the `PYTHIA8` AZNLO [92] and A14 [93] tunes for the gluon fusion and b-associated production respectively. The uncertainty on the PDF of the simulated signal is estimated with the change in signal yield spanned by a 68% variation from alternative PDF sets in the PDF4LHC15_nlo_100 [136] set for gluon fusion. Due to the unavailability of the 4-flavour PDF4LHC15 scheme, a comparison is made amongst the NNPDF30_nlo_as_0118_nf_4 [136], CT14nlo_NF4 [89], MSTW2008nlo68cl_nf4 [137] and CT10_nlo_nf4 [90] sets for *b*-associated production. The systematics relating to the signal simulation are treated as normalisation systematics as no significant shape effect is found.

6.6 Statistical interpretation of the results

This section describes the statistical analysis of the results, and their interpretation in the context of the MSSM parameter space, discussed in Section 2.4. The final background yields and systematic uncertainties are shown in Table 6.10.

b-veto

Process	Yield	uncertainty			
		stat.	detector syst.	theory syst.	total
Multijet	393	5	18	0	19
$Z \to \tau\tau$	107	2	29	8	30
$W(\to \tau\nu)$	38.7	2.0	7.0	2.7	7.8
top, $t\bar{t}$	4.0	0.5	1.0	0.7	1.3
Others	5.2	0.5	0.9	0.4	1.1
Total SM	548	6	34	8	36
Data	628	25	0	0	25

b-tag

Process	Yield	uncertainty			
		stat.	detector syst.	theory syst.	total
Multijet	17.3	1.4	3.0	0.0	3.3
$Z \to \tau\tau$	1.42	0.20	0.40	0.10	0.46
$W(\to \tau\nu)$	0.90	0.12	0.19	0.06	0.24
top, $t\bar{t}$	11.4	0.8	2.7	4.1	5.0
Others	0.117	0.023	0.027	0.009	0.037
Total SM	31.1	1.6	4.0	4.1	6.0
Data	23	5	0	0	5

Table 6.10: Final yields for data and estimated backgrounds after the full event selection. The total uncertainty on the estimated backgrounds is displayed, in addition to the individual contributions of the theoretical and detector related components.

These values, and the distribution of the data and estimated backgrounds as a function of the discriminating variable, the total transverse mass, are used in determining the signal strength. The signal strength, μ, is defined as the ratio of the fitted signal cross section times branching fraction to the signal cross section times branching fraction for a specific MSSM benchmark scenario assumption. As such $\mu = 1$ would signify that the signal strength is as predicted by a given theoretical scenario, whilst a signal strength of zero, $\mu = 0$ would signify the absence of any signal.

6.6.1 Profile likelihood method

The statistical analysis uses the profile likelihood method [138]. A likelihood function, $\mathcal{L}$, is formed as a product of Poisson terms, constructed in bins of the $m_{\mathrm{T}}^{\mathrm{tot}}$ discriminant variable, with each bin contributing a separate Poisson term. The binning is the same as that used in the plots shown in Section 6.4. The systematic uncertainties, described in Section 6.5, enter as nuisance parameters, θ, constrained with Gaussian functions.

The likelihood is equivalent to the probability that a given set of mass bin values, $\vec{m}_{\mathrm{T}}^{\mathrm{tot}} = m_1, m_2...m_N$, are observed, assuming a specific signal strength hypothesis, μ, and is defined as:

$$\mathcal{L}(\mu, \vec{\theta}, \vec{\gamma} | \vec{m}_{\mathrm{T}}^{\mathrm{tot}}) = P(\vec{m}_{\mathrm{T}}^{\mathrm{tot}} | \mu, \vec{\theta}, \vec{\gamma}) = \mathcal{L}(\vec{\gamma})_{stat} \mathcal{L}(\vec{\theta})_{syst} \prod_{i=1}^{N} \frac{(\mu s_i + b_i)^{n_i}}{n_i!} e^{-(\mu s_i + b_i)} \tag{6.6}$$

where $\vec{m}_{\mathrm{T}}^{\mathrm{tot}}$ are the mass bins and n_i is the observed number of events in the i^{th} bin.

The expectation value of the number of observed events in the i^{th} bin is given by $(\mu s_i + b_i)$. The expected number of signal events in the i^{th} bin under a given hypothesis is s_i, while b_i is the expected number of background events in the i^{th} bin. The parameter s_i is dependent on the integrated luminosity, the model specific cross section times branching fraction and the signal probability density function $f_s(m_{\mathrm{T}}^{\mathrm{tot}}; \vec{\theta_s})$ where θ_s are nuisance parameters related to the systematic uncertainties affecting the signal. Similarly b_i is dependent on the integrated luminosity, the cross section times branching fraction of the background processes, and the background probability density function $f_b(m_{\mathrm{T}}^{\mathrm{tot}}; \vec{\theta_b})$ where θ_b are nuisance parameters related to the systematic uncertainties affecting the background.

The term $\mathcal{L}(\vec{\theta})_{syst}$ relates to the treatment of systematic uncertainties. Each source of systematic uncertainty introduces a nuisance parameter, θ, which may affect the yields of either the signal, the background, or both. The term $\mathcal{L}(\vec{\gamma})_{stat}$ relates to the treatment of statistical uncertainties, where the overall background in each bin is assigned a nuisance parameter, γ. The overall normalisation of the background is also treated as a nuisance parameter.

In order to find the maximum likelihood set of parameters, the negative log-likelihood distribution is instead minimised.

6.6.2 Limit Setting

The event selection yields, after the fitting procedure where a signal strength hypothesis of $\mu = 0$ is assumed, are shown in Table 6.11. The post-fit $m_{\mathrm{T}}^{\mathrm{tot}}$ distributions in the b-veto and b-tag categories are shown in Figure 6.19, and it can be seen that the data and estimated background are consistent with the background-only hypothesis, within the limits of uncertainty.

$\tau_{\mathrm{had}}\tau_{\mathrm{had}}$ channel

	b-tag category	b-veto category
$Z \to \tau\tau$+jets	1.9 ± 0.3	146 ± 20
Multi-jet	17 ± 3	396 ± 16
$W(\to \tau\nu)$ + jets	1.1 ± 0.2	45 ± 7
$t\bar{t}$ and single top quark	11 ± 3	4.5 ± 0.9
Others	0.13 ± 0.03	6.3 ± 0.8
Total prediction	31 ± 4	598 ± 21
Data	23	628
$ggH\ m_A = 500\mathrm{GeV}, \tan\beta = 20$	0.034 ± 0.014	2.2 ± 0.7
$bbH\ m_A = 500\mathrm{GeV}, \tan\beta = 20$	8 ± 3	15 ± 5

Table 6.11: Observed data and estimated background yields after the event selection and following the fitting procedure. The expected yield of gluon fusion and b-associated Higgs production processes under the $m_h^{\mathrm{mod}+}$ scenario are also shown for a Higgs mass of 500 GeV. Taken from [10].

As no significant excess is observed in the analysis, upper limits are calculated for the production cross section times branching fraction for the two Higgs production processes and for various Higgs mass points. To test the compatibility of the data with signal, a test statistic $\tilde{q}_\mu$ is defined as a ratio of likelihoods under the assumption of the signal strength being positive, i.e. $\mu > 0$, following the asymptotic approximation [138]:

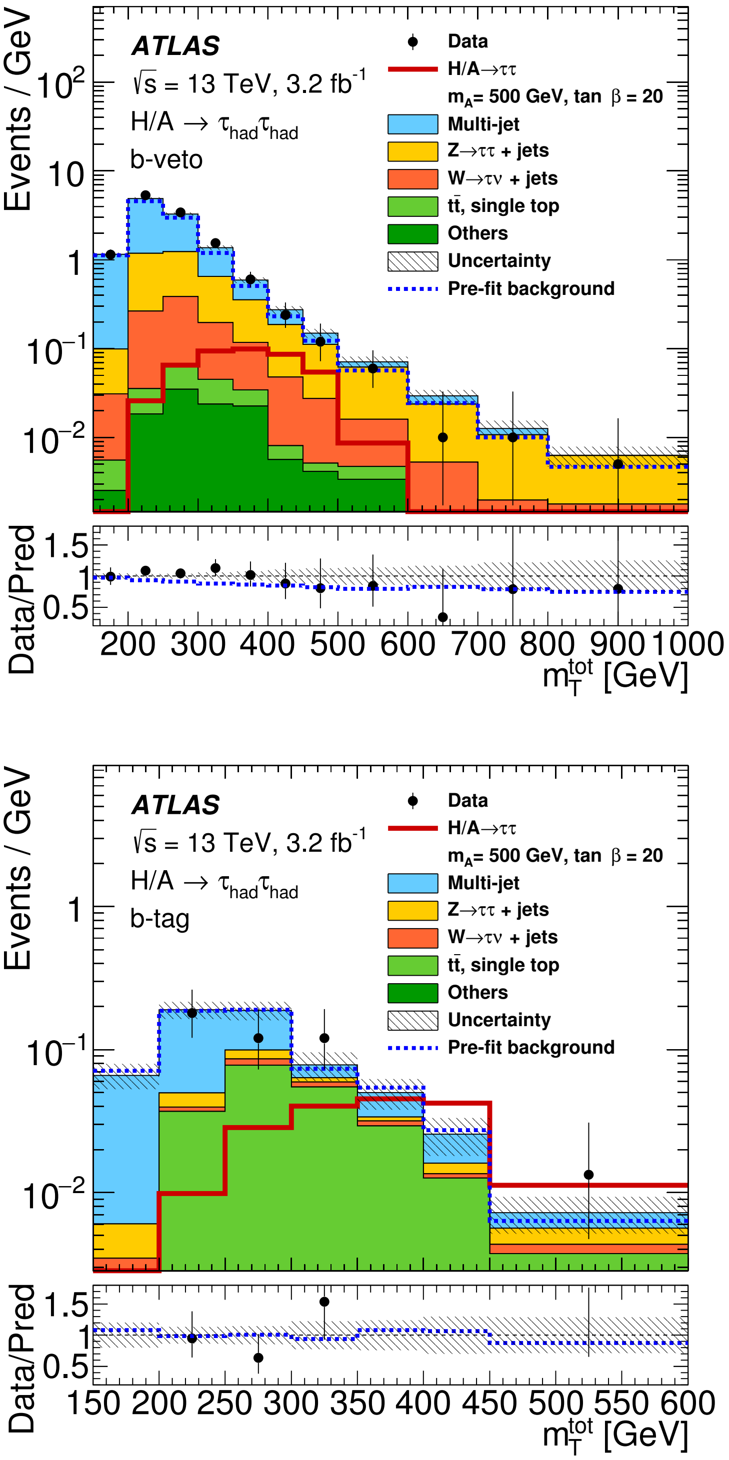

Figure 6.19: Distributions of the total transverse mass, $m_{\mathrm{T}}^{\mathrm{tot}}$, after the full event selection of the b-veto (above) and b-tag (below) categories with example gluon fusion and b-associated production signal processes shown in the respective categories. The pre-fit estimated background as well as the post-fit background, following the fitting procedure under the absence of a signal hypothesis, are shown. Taken from [10].

$$\tilde{q}_{\mu} = \begin{cases} -2\ln(\mathcal{L}(\mu, \hat{\hat{\vec{\theta}}}(\mu))/\mathcal{L}(0, \hat{\hat{\theta}}(0))) & \text{if } \hat{\mu} < 0 \\ -2\ln(\mathcal{L}(\mu, \hat{\hat{\vec{\theta}}}(\mu))/\mathcal{L}(\hat{\mu}, \hat{\vec{\theta}})) & \text{if } 0 \leq \hat{\mu} \leq \mu \\ 0 & \text{if } \hat{\mu} > \mu \end{cases}$$

The maximum likelihood estimator of μ is given by $\hat{\mu}$, while $\hat{\vec{\theta}}$ is the maximum likelihood estimator of the nuisance parameters. The conditional maximum likelihood estimators of the nuisance parameters under signal strength conditions of 0 and μ are given by $\hat{\hat{\vec{\theta}}}(0)$ and $\hat{\hat{\vec{\theta}}}(\mu)$ respectively. The test statistic has a probability density function computed under both the signal and background-only hypotheses.

The limits are calculated using the frequentist CL_s technique [139], which gives a 95% confidence limit exclusion for a given μ and is defined as:

$$CL_s = \frac{p_{\mu}}{1 - p_0} < \alpha \tag{6.7}$$

Where α is the confidence-level and p_0 is the p-value of the background-only hypothesis, the probability that the observed data, $\tilde{q}_{\mu,obs}$, has equal or poorer compatibility with the background-only hypothesis:

$$p_0 = P(\tilde{q}_{\mu} \leq \tilde{q}_{\mu,obs} | \mu = 0) \tag{6.8}$$

Similarly, p_{μ} is the p-value of the signal plus background hypothesis, the probability that the observed data has equal or poorer compatibility given the signal hypothesis, and given by:

$$p_{\mu} = P(\tilde{q}_{\mu} \geq \tilde{q}_{\mu,obs} | \mu) \tag{6.9}$$

Here we have assumed that the background-only distribution of the test statistic is shifted to the right of the signal plus background distribution. The signal is considered to be excluded at 95% confidence level where $\alpha = 0.05$.

The results are then combined with the results of the $\tau_{\text{lep}}\tau_{\text{had}}$ analysis, where the final state contains a hadronically decaying tau and either an electron or muon. The post-fit distributions of the total transverse mass in the $\tau_{\text{lep}}\tau_{\text{had}}$ analysis are shown in Appendix F. Figure 6.20 shows the upper limit on the cross section times branching fraction of the production of a scalar particle decaying to a pair of hadronically decaying tau leptons for various mass points whilst the limits in combination with the $\tau_{\text{lep}}\tau_{\text{had}}$ analysis are shown in Figure 6.21.

The results are also interpreted in the MSSM $m_A - \tan\beta$ space under the $m_h^{\text{mod+}}$ and hMSSM scenarios, with the 95% confidence level limits shown in Figure 6.22 for the $\tau_{\text{had}}\tau_{\text{had}}$ analysis. The impact of the systematic uncertainties on the fitted signal strenght as well as variations of the nuisance parameters from their nominal values are shown in Appendix G. Figure 6.23 shows the $\tan\beta$ limits as a function of m_A in combination with the $\tau_{\text{lep}}\tau_{\text{had}}$ final state analysis. The hMSSM benchmark scenario is shown with the Run-1 limit for comparison. For $m_A > 500$ GeV the Run-2 limit excludes significantly more $\tan\beta$ space and extends the limit from 1 TeV to 1.2 TeV. At the time of publication, this offered the strongest limits on $\tan\beta$ for high values of m_A.

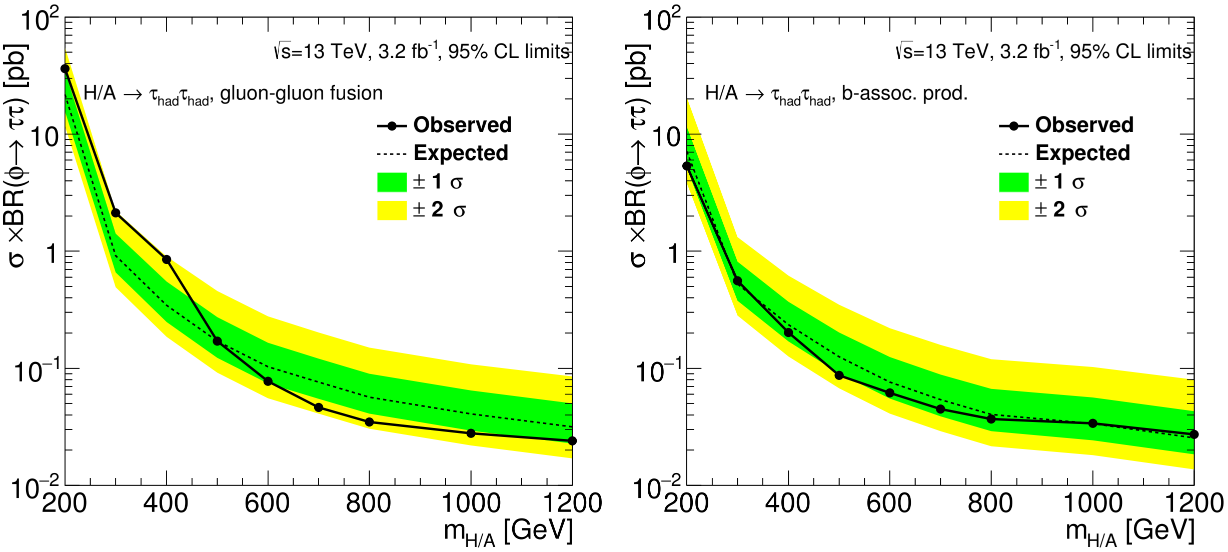

Figure 6.20: The observed and expected 95% confidence level upper exclusion limit on the cross section times branching fraction of the production of a H/A boson decaying to a pair of hadronically decaying tau leptons, as a function of the mass of the boson. The production cross sections correspond to gluon fusion (left) and b-associated production (right). The plots are produced by a collaborator.

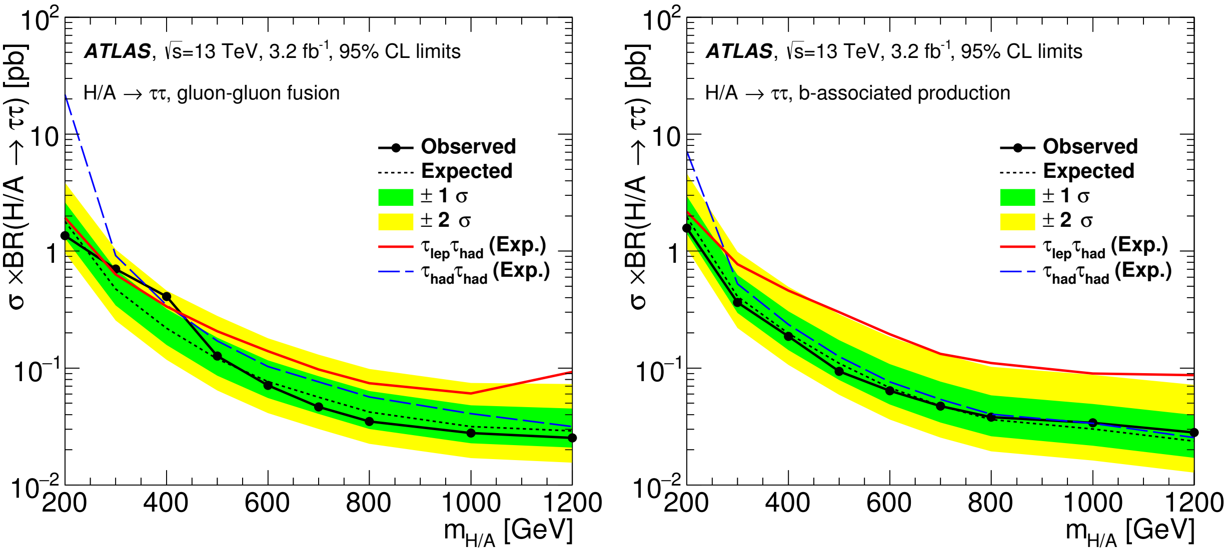

Figure 6.21: The observed and expected 95% confidence level upper exclusion limit on the cross section times branching fraction of the production of a H/A boson decaying to a pair of tau leptons, as a function of the mass of the boson. The expected limits of the analyses with $\tau_{\rm lep}\tau_{\rm had}$ (red) and $\tau_{\rm had}\tau_{\rm had}$ (blue) final states are shown as well as the combined expected and observed limits (black). The production cross sections correspond to gluon fusion (left) and b-associated production (right). Taken from [10].

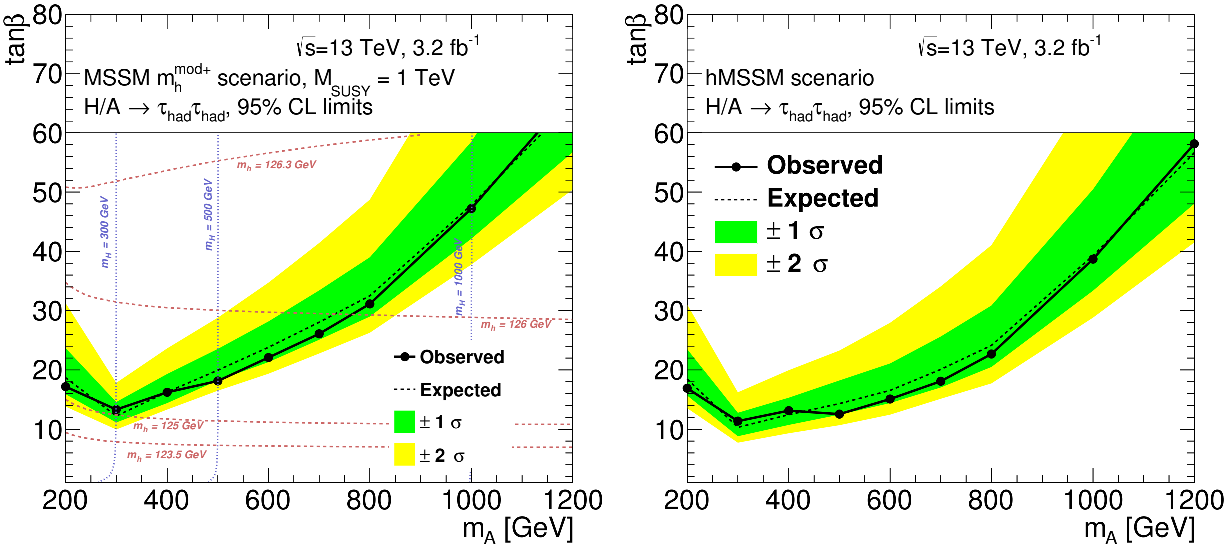

Figure 6.22: The observed and expected 95% confidence level limits on tanβ as a function of the mass of the neutral Higgs boson, m_A. The left plot shows the $m_h^{\text{mod}+}$ scenario, while the right plot shows hMSSM benchmark scenario limits. The plots are produced by a collaborator.

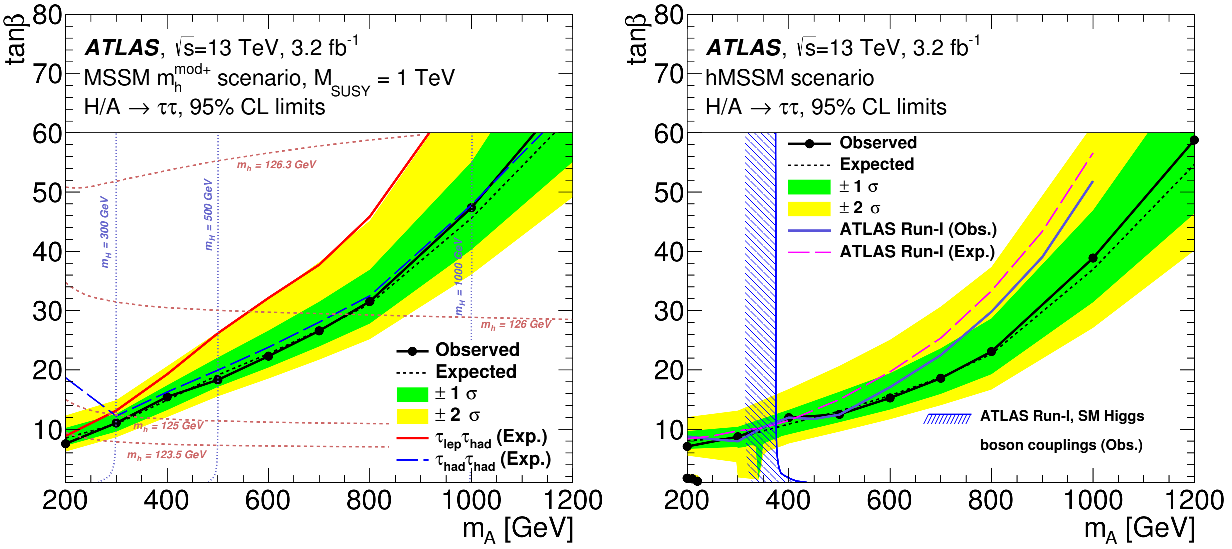

Figure 6.23: The observed and expected 95% confidence level limits on tanβ as a function of the mass of the neutral Higgs boson, m_A. The left plot shows the $m_h^{\text{mod}+}$ scenario, with the expected limits for the analyses with $\tau_{\text{lep}}\tau_{\text{had}}$ (red) and $\tau_{\text{had}}\tau_{\text{had}}$ (blue) final states, as well as the combined expected and observed limits (black). The right plot shows hMSSM benchmark scenario limits, as well as the Run-1 limits given by Ref. [31]. Also shown is the exclusion resulting from SM Higgs boson coupling measurements [140]. Taken from [10].

Chapter 7

Conclusions

The construction of the Large Hadron Collider has allowed proton-proton collisions to be studied in a new energy regime. This resulted in the discovery of a new scalar boson during Run-1, compatible with the Higgs boson predicted by the Standard Model, giving an insight into the mechanism of electroweak symmetry breaking. In the Minimal Supersymmetric extension to the Standard Model there are five physical Higgs bosons, and the parameter space can be described in terms of two parameters m_A, the mass of one of the Higgs bosons, and tanβ. The coupling of the Higgs field to down-type quarks and charged fermions, such as tau leptons, is expected to be enhanced for large values of tanβ. Of the five Higgs bosons in the MSSM, three are neutral, and it may be that the recently discovered scalar boson is one of these. During Run-1 a search for neutral high-mass Higgs bosons was performed using the ATLAS and CMS detectors, and 95% confidence limits were set on the production cross section times branching fraction, and on the MSSM parameter space in benchmark scenarios.

The upgrades to the LHC during the shutdown after Run-1 enabled proton-proton collisions to reach a record centre of mass energy of $\sqrt{s}$ = 13 TeV during 2015. This thesis presented a first search for neutral high-mass Higgs bosons decaying to pairs of hadronically decaying tau leptons in the new energy regime, using the ATLAS detector. No new particles were observed, and the results were combined with the results of the analysis where one of the tau leptons decays to a muon or electron, to set updated limits on the cross section times branching fraction. Interpreting the results in terms of the hMSSM benchmark scenario of the MSSM parameter space, limits are set on the value of tanβ as a function of the mass of the CP-odd Higgs, and mark an improvement on the Run-1 limits above $m_A > 500$ GeV. Additionally, the mass range in which limits are set on tanβ are extended from $m_A = 1$ TeV to $m_A = 1.2$ TeV.

In addition, the development and performance monitoring of the Run-2 tau trigger system was presented in Chapter 5. The collection of data for the $A/H \to \tau\tau$ analysis is dependent on the successful operation of the tau trigger system. The tau trigger system is also important for many other tau related searches during the continued operation of the LHC.

In May 2016, proton-proton collisions restarted at the LHC and by August, the ATLAS detector had collected 13.3 fb^{-1} of data. The techniques used in this thesis contributed to the analysis of the new data, presented in Ref. [141]. No new particles are observed, and the large increase in data results in a significant improvement in the limits on the MSSM parameter space. The updated plots can be found in Appendix H.

Whilst the analysis presented in this thesis has restricted the MSSM parameter space, a large amount of MSSM parameter space remains to be explored. As the LHC continues collecting data, the search for high-mass Higgs bosons decaying to tau leptons will continue to generate interest in the search for physics beyond the Standard Model.

Appendix

Appendix A

Simulated Samples

This appendix contains the dataset names and the cross sections of the simulated samples used.

Table A.1: `MC15` signal samples used in this thesis

DID	Sample name	cross section [pb]
341877	aMCNloPy8_bbH300_yb2_tautauhh	
341878	aMCNloPy8_bbH350_yb2_tautauhh	
341879	aMCNloPy8_bbH400_yb2_tautauhh	
341880	aMCNloPy8_bbH500_yb2_tautauhh	
341881	aMCNloPy8_bbH600_yb2_tautauhh	
341882	aMCNloPy8_bbH700_yb2_tautauhh	
341883	aMCNloPy8_bbH800_yb2_tautauhh	
341885	aMCNloPy8_bbH1000_yb2_tautauhh	
341917	aMCNloPy8_bbH1200_yb2_tautauhh	
342311	PoPy8_ggH300W2_tautauhh	
342313	PoPy8_ggH350W3_tautauhh	
342315	PoPy8_ggH400W5_tautauhh	
342317	PoPy8_ggH500W5_tautauhh	
342319	PoPy8_ggH600W10_tautauhh	
342321	PoPy8_ggH700W20_tautauhh	
342323	PoPy8_ggH800W20_tautauhh	
342327	PoPy8_ggH1000W30_tautauhh	
342331	PoPy8_ggH1200W40_tautauhh	
361022	Pythia8EvtGen_A14NNPDF23LO_jetjet_JZ2W	2433200000.0
361023	Pythia8EvtGen_A14NNPDF23LO_jetjet_JZ3W	26454000.0
361024	Pythia8EvtGen_A14NNPDF23LO_jetjet_JZ4W	254630.0
361025	Pythia8EvtGen_A14NNPDF23LO_jetjet_JZ5W	4553.5
361026	Pythia8EvtGen_A14NNPDF23LO_jetjet_JZ6W	257.53
361027	Pythia8EvtGen_A14NNPDF23LO_jetjet_JZ7W	16.215
361028	Pythia8EvtGen_A14NNPDF23LO_jetjet_JZ8W	0.62502
361029	Pythia8EvtGen_A14NNPDF23LO_jetjet_JZ9W	0.019639
361030	Pythia8EvtGen_A14NNPDF23LO_jetjet_JZ10W	0.0011962
361031	Pythia8EvtGen_A14NNPDF23LO_jetjet_JZ11W	4.2258e-05
361032	Pythia8EvtGen_A14NNPDF23LO_jetjet_JZ12W	1.0367e-06

Table A.2: `MC15` samples used in this thesis.

DID	Sample name	cross section [pb]
303437	Pythia8EvtGen_A14NNPDF23LO_DYtautau_120M180	1.3842e+01
303438	Pythia8EvtGen_A14NNPDF23LO_DYtautau_180M250	2.3352e+00
303439	Pythia8EvtGen_A14NNPDF23LO_DYtautau_250M400	8.6526e-01
303440	Pythia8EvtGen_A14NNPDF23LO_DYtautau_400M600	1.5594e-01
303441	Pythia8EvtGen_A14NNPDF23LO_DYtautau_600M800	2.9643e-02
303442	Pythia8EvtGen_A14NNPDF23LO_DYtautau_800M1000	8.3148e-03
303443	Pythia8EvtGen_A14NNPDF23LO_DYtautau_1000M1250	3.3072e-03
303444	Pythia8EvtGen_A14NNPDF23LO_DYtautau_1250M1500	1.0955e-03
303445	Pythia8EvtGen_A14NNPDF23LO_DYtautau_1500M1750	4.1817e-04
303446	Pythia8EvtGen_A14NNPDF23LO_DYtautau_1750M2000	1.7610e-04
303447	Pythia8EvtGen_A14NNPDF23LO_DYtautau_2000M2250	7.9838e-05
303448	Pythia8EvtGen_A14NNPDF23LO_DYtautau_2250M2500	3.8223e-05
303449	Pythia8EvtGen_A14NNPDF23LO_DYtautau_2500M2750	1.9088e-05
303450	Pythia8EvtGen_A14NNPDF23LO_DYtautau_2750M3000	9.8673e-06
303451	Pythia8EvtGen_A14NNPDF23LO_DYtautau_3000M3500	8.0521e-06
303452	Pythia8EvtGen_A14NNPDF23LO_DYtautau_3500M4000	2.4178e-06
303453	Pythia8EvtGen_A14NNPDF23LO_DYtautau_4000M4500	7.5696e-07
303454	Pythia8EvtGen_A14NNPDF23LO_DYtautau_4500M5000	2.4277e-07
303455	Pythia8EvtGen_A14NNPDF23LO_DYtautau_5000M	1.1662e-07

Table A.3: `MC15` samples used in this thesis.

DID	Sample name	cross section [pb]
301015	PowhegPythia8EvtGen_AZNLOCTEQ6L1_DYee_3500M4000	2.9e-06
301005	PowhegPythia8EvtGen_AZNLOCTEQ6L1_DYee_800M1000	0.010607
301017	PowhegPythia8EvtGen_AZNLOCTEQ6L1_DYee_4500M5000	3e-07
301003	PowhegPythia8EvtGen_AZNLOCTEQ6L1_DYee_400M600	0.1955
301013	PowhegPythia8EvtGen_AZNLOCTEQ6L1_DYee_2750M3000	1.25e-05
301002	PowhegPythia8EvtGen_AZNLOCTEQ6L1_DYee_250M400	1.082
301011	PowhegPythia8EvtGen_AZNLOCTEQ6L1_DYee_2250M2500	4.94e-05
301008	PowhegPythia8EvtGen_AZNLOCTEQ6L1_DYee_1500M1750	0.0005452
301004	PowhegPythia8EvtGen_AZNLOCTEQ6L1_DYee_600M800	0.037401
301007	PowhegPythia8EvtGen_AZNLOCTEQ6L1_DYee_1250M1500	0.0014219
301001	PowhegPythia8EvtGen_AZNLOCTEQ6L1_DYee_180M250	2.9212
301000	PowhegPythia8EvtGen_AZNLOCTEQ6L1_DYee_120M180	17.478
301010	PowhegPythia8EvtGen_AZNLOCTEQ6L1_DYee_2000M2250	0.0001039
301006	PowhegPythia8EvtGen_AZNLOCTEQ6L1_DYee_1000M1250	0.0042582
301012	PowhegPythia8EvtGen_AZNLOCTEQ6L1_DYee_2500M2750	2.45e-05
301009	PowhegPythia8EvtGen_AZNLOCTEQ6L1_DYee_1750M2000	0.0002299
301018	PowhegPythia8EvtGen_AZNLOCTEQ6L1_DYee_5000M	1e-07
301016	PowhegPythia8EvtGen_AZNLOCTEQ6L1_DYee_4000M4500	9e-07
301014	PowhegPythia8EvtGen_AZNLOCTEQ6L1_DYee_3000M3500	1e-05
301027	PowhegPythia8EvtGen_AZNLOCTEQ6L1_DYmumu_1250M1500	0.0014219
301026	PowhegPythia8EvtGen_AZNLOCTEQ6L1_DYmumu_1000M1250	0.0042582
301031	PowhegPythia8EvtGen_AZNLOCTEQ6L1_DYmumu_2250M2500	4.94e-05
301021	PowhegPythia8EvtGen_AZNLOCTEQ6L1_DYmumu_180M250	2.9212
301020	PowhegPythia8EvtGen_AZNLOCTEQ6L1_DYmumu_120M180	17.478
301038	PowhegPythia8EvtGen_AZNLOCTEQ6L1_DYmumu_5000M	1e-07
301022	PowhegPythia8EvtGen_AZNLOCTEQ6L1_DYmumu_250M400	1.082
301023	PowhegPythia8EvtGen_AZNLOCTEQ6L1_DYmumu_400M600	0.1955
301030	PowhegPythia8EvtGen_AZNLOCTEQ6L1_DYmumu_2000M2250	0.0001039
301033	PowhegPythia8EvtGen_AZNLOCTEQ6L1_DYmumu_2750M3000	1.25e-05
301024	PowhegPythia8EvtGen_AZNLOCTEQ6L1_DYmumu_600M800	0.037399
301028	PowhegPythia8EvtGen_AZNLOCTEQ6L1_DYmumu_1500M1750	0.0005452
301035	PowhegPythia8EvtGen_AZNLOCTEQ6L1_DYmumu_3500M4000	2.9e-06
301025	PowhegPythia8EvtGen_AZNLOCTEQ6L1_DYmumu_800M1000	0.010607
301037	PowhegPythia8EvtGen_AZNLOCTEQ6L1_DYmumu_4500M5000	3e-07
301034	PowhegPythia8EvtGen_AZNLOCTEQ6L1_DYmumu_3000M3500	1e-05
301032	PowhegPythia8EvtGen_AZNLOCTEQ6L1_DYmumu_2500M2750	2.45e-05
301029	PowhegPythia8EvtGen_AZNLOCTEQ6L1_DYmumu_1750M2000	0.0002299
301036	PowhegPythia8EvtGen_AZNLOCTEQ6L1_DYmumu_4000M4500	9e-07
301045	PowhegPythia8EvtGen_AZNLOCTEQ6L1_DYtautau_800M1000	0.010607
301053	PowhegPythia8EvtGen_AZNLOCTEQ6L1_DYtautau_2750M3000	1.25e-05
301058	PowhegPythia8EvtGen_AZNLOCTEQ6L1_DYtautau_5000M	1e-07
301044	PowhegPythia8EvtGen_AZNLOCTEQ6L1_DYtautau_600M800	0.037401
301041	PowhegPythia8EvtGen_AZNLOCTEQ6L1_DYtautau_180M250	2.9209
301057	PowhegPythia8EvtGen_AZNLOCTEQ6L1_DYtautau_4500M5000	3e-07
301054	PowhegPythia8EvtGen_AZNLOCTEQ6L1_DYtautau_3000M3500	1e-05
301048	PowhegPythia8EvtGen_AZNLOCTEQ6L1_DYtautau_1500M1750	0.0005452
301050	PowhegPythia8EvtGen_AZNLOCTEQ6L1_DYtautau_2000M2250	0.0001039
301042	PowhegPythia8EvtGen_AZNLOCTEQ6L1_DYtautau_250M400	1.082
301049	PowhegPythia8EvtGen_AZNLOCTEQ6L1_DYtautau_1750M2000	0.0002299
301047	PowhegPythia8EvtGen_AZNLOCTEQ6L1_DYtautau_1250M1500	0.001422
301055	PowhegPythia8EvtGen_AZNLOCTEQ6L1_DYtautau_3500M4000	2.9e-06
301040	PowhegPythia8EvtGen_AZNLOCTEQ6L1_DYtautau_120M180	17.48
301043	PowhegPythia8EvtGen_AZNLOCTEQ6L1_DYtautau_400M600	0.1955
301051	PowhegPythia8EvtGen_AZNLOCTEQ6L1_DYtautau_2250M2500	4.94e-05
301056	PowhegPythia8EvtGen_AZNLOCTEQ6L1_DYtautau_4000M4500	9e-07
301052	PowhegPythia8EvtGen_AZNLOCTEQ6L1_DYtautau_2500M2750	2.45e-05
301046	PowhegPythia8EvtGen_AZNLOCTEQ6L1_DYtautau_1000M1250	0.0042584

Table A.4: `MC15` samples used in this thesis.

DID	Sample name	cross section [pb]
361300	Sherpa_CT10_Wenu_Pt0_70_CVetoBVeto	2.138e+04
361301	Sherpa_CT10_Wenu_Pt0_70_CFilterBVeto	2.138e+04
361302	Sherpa_CT10_Wenu_Pt0_70_BFilter	2.138e+04
361303	Sherpa_CT10_Wenu_Pt70_140_CVetoBVeto	632.8
361304	Sherpa_CT10_Wenu_Pt70_140_CFilterBVeto	632.8
361305	Sherpa_CT10_Wenu_Pt70_140_BFilter	632.8
361306	Sherpa_CT10_Wenu_Pt140_280_CVetoBVeto	90.12
361307	Sherpa_CT10_Wenu_Pt140_280_CFilterBVeto	90.12
361308	Sherpa_CT10_Wenu_Pt140_280_BFilter	90.12
361309	Sherpa_CT10_Wenu_Pt280_500_CVetoBVeto	5.747
361310	Sherpa_CT10_Wenu_Pt280_500_CFilterBVeto	5.747
361311	Sherpa_CT10_Wenu_Pt280_500_BFilter	5.747
361312	Sherpa_CT10_Wenu_Pt500_700_CVetoBVeto	0.3479
361313	Sherpa_CT10_Wenu_Pt500_700_CFilterBVeto	0.3479
361314	Sherpa_CT10_Wenu_Pt500_700_BFilter	0.3479
361315	Sherpa_CT10_Wenu_Pt700_1000_CVetoBVeto	0.06107
361316	Sherpa_CT10_Wenu_Pt700_1000_CFilterBVeto	0.06107
361317	Sherpa_CT10_Wenu_Pt700_1000_BFilter	0.06107
361318	Sherpa_CT10_Wenu_Pt1000_2000_CVetoBVeto	0.006643
361319	Sherpa_CT10_Wenu_Pt1000_2000_CFilterBVeto	0.006643
361320	Sherpa_CT10_Wenu_Pt1000_2000_BFilter	0.006643
361321	Sherpa_CT10_Wenu_Pt2000_E_CMS_CVetoBVeto	2.659e-05
361322	Sherpa_CT10_Wenu_Pt2000_E_CMS_CFilterBVeto	2.659e-05
361323	Sherpa_CT10_Wenu_Pt2000_E_CMS_BFilter	2.659e-05
361324	Sherpa_CT10_Wmunu_Pt0_70_CVetoBVeto	2.138e+04
361325	Sherpa_CT10_Wmunu_Pt0_70_CFilterBVeto	2.138e+04
361326	Sherpa_CT10_Wmunu_Pt0_70_BFilter	2.138e+04
361327	Sherpa_CT10_Wmunu_Pt70_140_CVetoBVeto	632.8
361328	Sherpa_CT10_Wmunu_Pt70_140_CFilterBVeto	632.8
361329	Sherpa_CT10_Wmunu_Pt70_140_BFilter	632.8
361330	Sherpa_CT10_Wmunu_Pt140_280_CVetoBVeto	90.12
361331	Sherpa_CT10_Wmunu_Pt140_280_CFilterBVeto	90.12
361332	Sherpa_CT10_Wmunu_Pt140_280_BFilter	90.12
361333	Sherpa_CT10_Wmunu_Pt280_500_CVetoBVeto	5.747
361334	Sherpa_CT10_Wmunu_Pt280_500_CFilterBVeto	5.747
361335	Sherpa_CT10_Wmunu_Pt280_500_BFilter	5.747
361336	Sherpa_CT10_Wmunu_Pt500_700_CVetoBVeto	0.3479
361337	Sherpa_CT10_Wmunu_Pt500_700_CFilterBVeto	0.3479
361338	Sherpa_CT10_Wmunu_Pt500_700_BFilter	0.3479
361339	Sherpa_CT10_Wmunu_Pt700_1000_CVetoBVeto	0.06107
361340	Sherpa_CT10_Wmunu_Pt700_1000_CFilterBVeto	0.06107
361341	Sherpa_CT10_Wmunu_Pt700_1000_BFilter	0.06107
361342	Sherpa_CT10_Wmunu_Pt1000_2000_CVetoBVeto	0.006643
361343	Sherpa_CT10_Wmunu_Pt1000_2000_CFilterBVeto	0.006643
361344	Sherpa_CT10_Wmunu_Pt1000_2000_BFilter	0.006643
361345	Sherpa_CT10_Wmunu_Pt2000_E_CMS_CVetoBVeto	2.659e-05
361346	Sherpa_CT10_Wmunu_Pt2000_E_CMS_CFilterBVeto	2.659e-05
361347	Sherpa_CT10_Wmunu_Pt2000_E_CMS_BFilter	2.659e-05

Table A.5: `MC15` samples used in this thesis.

DID	Sample name	cross section [pb]
410000	PowhegPythiaEvtGen_P2012_ttbar_hdamp172p5_nonallhad	696.12
410001	PowhegPythiaEvtGen_P2012radHi_ttbar_hdamp345_down_nonallhad.merge	696.12
410002	PowhegPythiaEvtGen_P2012radLo_ttbar_hdamp172_up_nonallhad	696.12
410003	aMcAtNloHerwigppEvtGen_ttbar_nonallhad	696.12
410004	PowhegHerwigppEvtGen_UEEE5_ttbar_hdamp172p5_nonallhad	696.12
410006	PowhegPythia8EvtGen_A14_ttbar_hdamp172p5_nonallhad	696.12
410007	.PowhegPythiaEvtGen_P2012_ttbar_hdamp172p5_allhad	696.21
410011	PowhegPythiaEvtGen_P2012_singletop_tchan_lept_top	43.739
410012	PowhegPythiaEvtGen_P2012_singletop_tchan_lept_antitop	25.778
410013	PowhegPythiaEvtGen_P2012_Wt_inclusive_top	34.009
410014	PowhegPythiaEvtGen_P2012_Wt_inclusive_antitop	33.989
410015	PowhegPythiaEvtGen_P2012_Wt_dilepton_top	3.5835
410016	PowhegPythiaEvtGen_P2012_Wt_dilepton_antitop	3.5814
407018	PowhegPythiaEvtGen_P2012CT10_Wt_inclusive_top_HT500	3.00848
407019	PowhegPythiaEvtGen_P2012CT10_Wt_inclusive_top_MET200	0.383707
407020	PowhegPythiaEvtGen_P2012CT10_Wt_inclusive_tbar_HT500	3.00514
407021	PowhegPythiaEvtGen_P2012CT10_Wt_inclusive_tbar_MET200	0.382686
410025	PowhegPythiaEvtGen_P2012_SingleTopSchan_noAllHad_top	2.0517
410026	PowhegPythiaEvtGen_P2012_SingleTopSchan_noAllHad_antitop	1.2615
361106	PowhegPythia8EvtGen_AZNLOCTEQ6L1_Zee	97.5316
361107	PowhegPythia8EvtGen_AZNLOCTEQ6L1_Zmumu	97.5316
361108	PowhegPythia8EvtGen_AZNLOCTEQ6L1_Ztautau	97.5316
361063	Sherpa_CT10_llll	12.583
361064	Sherpa_CT10_lllvSFMinus	1.8446
361065	Sherpa_CT10_lllvOFMinus	3.6235
361066	Sherpa_CT10_lllvSFPlus	2.5656
361067	Sherpa_CT10_lllvOFPlus	5.0169

Table A.6: `MC15` samples used in this thesis.

DID	Sample name	cross section [pb]
361348	Sherpa_CT10_Wtaunu_Pt0_70_CVetoBVeto	2.138e+04
361349	Sherpa_CT10_Wtaunu_Pt0_70_CFilterBVeto	2.138e+04
361350	Sherpa_CT10_Wtaunu_Pt0_70_BFilter	2.138e+04
361351	Sherpa_CT10_Wtaunu_Pt70_140_CVetoBVeto	632.8
361352	Sherpa_CT10_Wtaunu_Pt70_140_CFilterBVeto	632.8
361353	Sherpa_CT10_Wtaunu_Pt70_140_BFilter	632.8
361354	Sherpa_CT10_Wtaunu_Pt140_280_CVetoBVeto	90.12
361355	Sherpa_CT10_Wtaunu_Pt140_280_CFilterBVeto	90.12
361356	Sherpa_CT10_Wtaunu_Pt140_280_BFilter	90.12
361357	Sherpa_CT10_Wtaunu_Pt280_500_CVetoBVeto	5.747
361358	Sherpa_CT10_Wtaunu_Pt280_500_CFilterBVeto	5.747
361359	Sherpa_CT10_Wtaunu_Pt280_500_BFilter	5.747
361360	Sherpa_CT10_Wtaunu_Pt500_700_CVetoBVeto	0.3479
361361	Sherpa_CT10_Wtaunu_Pt500_700_CFilterBVeto	0.3479
361362	Sherpa_CT10_Wtaunu_Pt500_700_BFilter	0.3479
361363	Sherpa_CT10_Wtaunu_Pt700_1000_CVetoBVeto	0.06107
361364	Sherpa_CT10_Wtaunu_Pt700_1000_CFilterBVeto	0.06107
361365	Sherpa_CT10_Wtaunu_Pt700_1000_BFilter	0.06107
361366	Sherpa_CT10_Wtaunu_Pt1000_2000_CVetoBVeto	0.006643
361367	Sherpa_CT10_Wtaunu_Pt1000_2000_CFilterBVeto	0.006643
361368	Sherpa_CT10_Wtaunu_Pt1000_2000_BFilter	0.006643
361369	Sherpa_CT10_Wtaunu_Pt2000_E_CMS_CVetoBVeto	2.659e-05
361370	Sherpa_CT10_Wtaunu_Pt2000_E_CMS_CFilterBVeto	2.659e-05
361371	Sherpa_CT10_Wtaunu_Pt2000_E_CMS_BFilter	2.659e-05

Appendix B

Misidentification rate of high-p_T tau candidates

This appendix contains the misidentification rates of high-p_T tau candidates undergoing a dijet event selection. The misidentification rate is measured in data and in simulated dijet events, and the ratio is shown and fitted with a linear function.

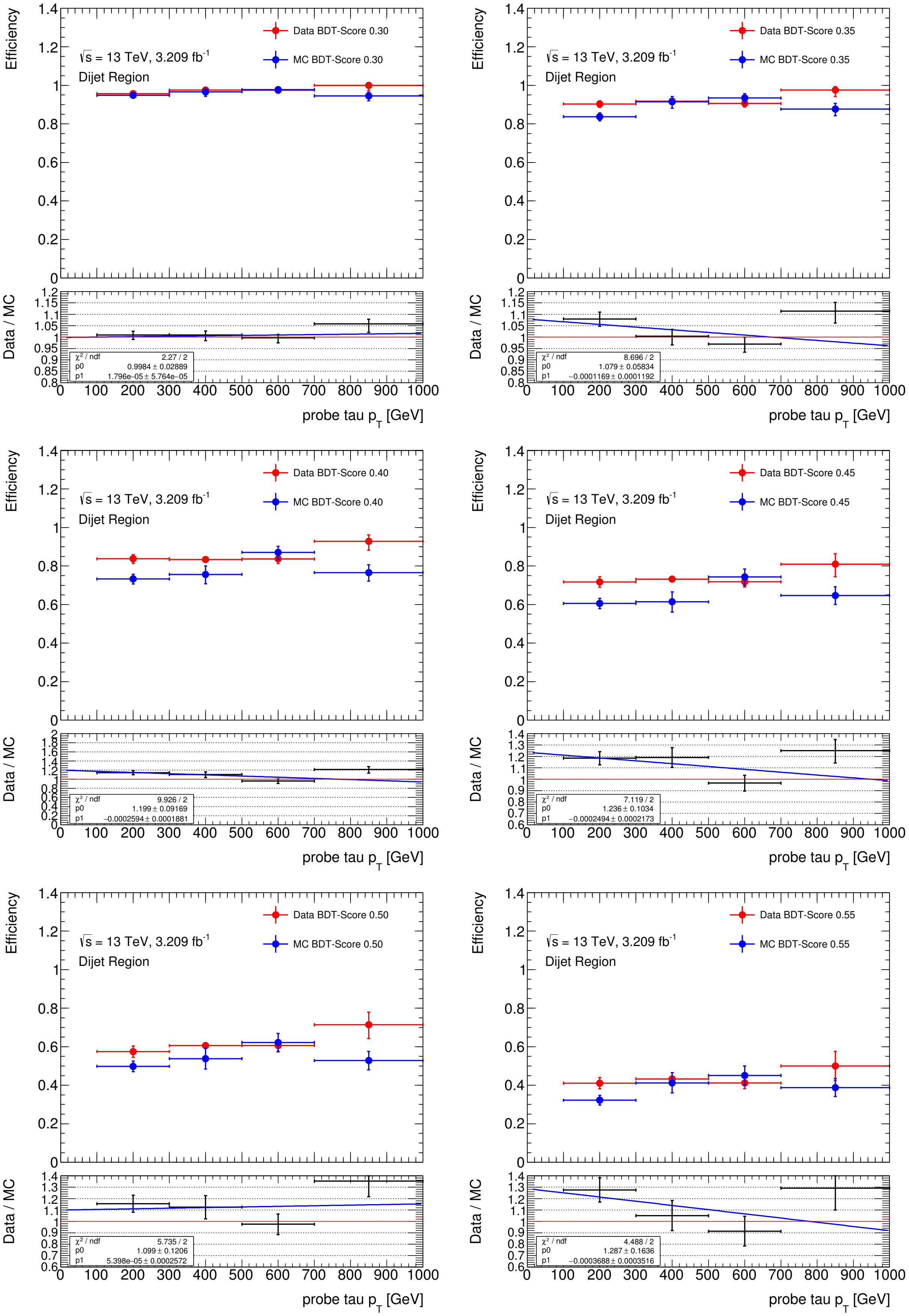

Figure B.1: Misidentification rates of probe 1-prong tau candidates for cuts on various different tau identification BDT scores, as a function of the probe object p_T. Both data and simulation are shown as well as the ratio between the two. A linear fit is placed on the data-simulation ratio, and the relevant fit parameters displayed.

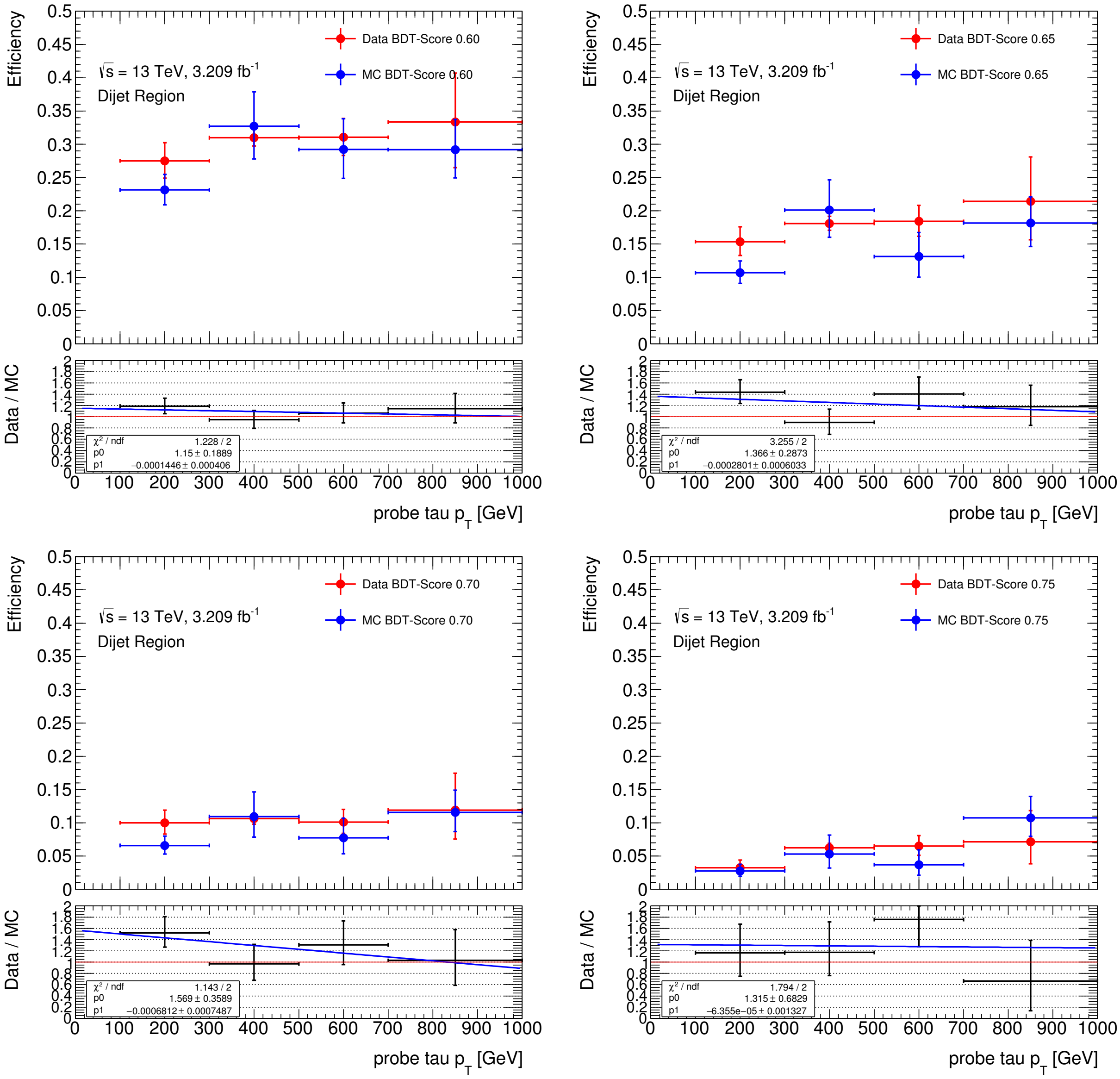

Figure B.2: Misidentification rates of probe 1-prong tau candidates for cuts on various different tau identification BDT scores, as a function of the probe object p_T. Both data and simulation are shown as well as the ratio between the two. A linear fit is placed on the data-simulation ratio, and the relevant fit parameters displayed.

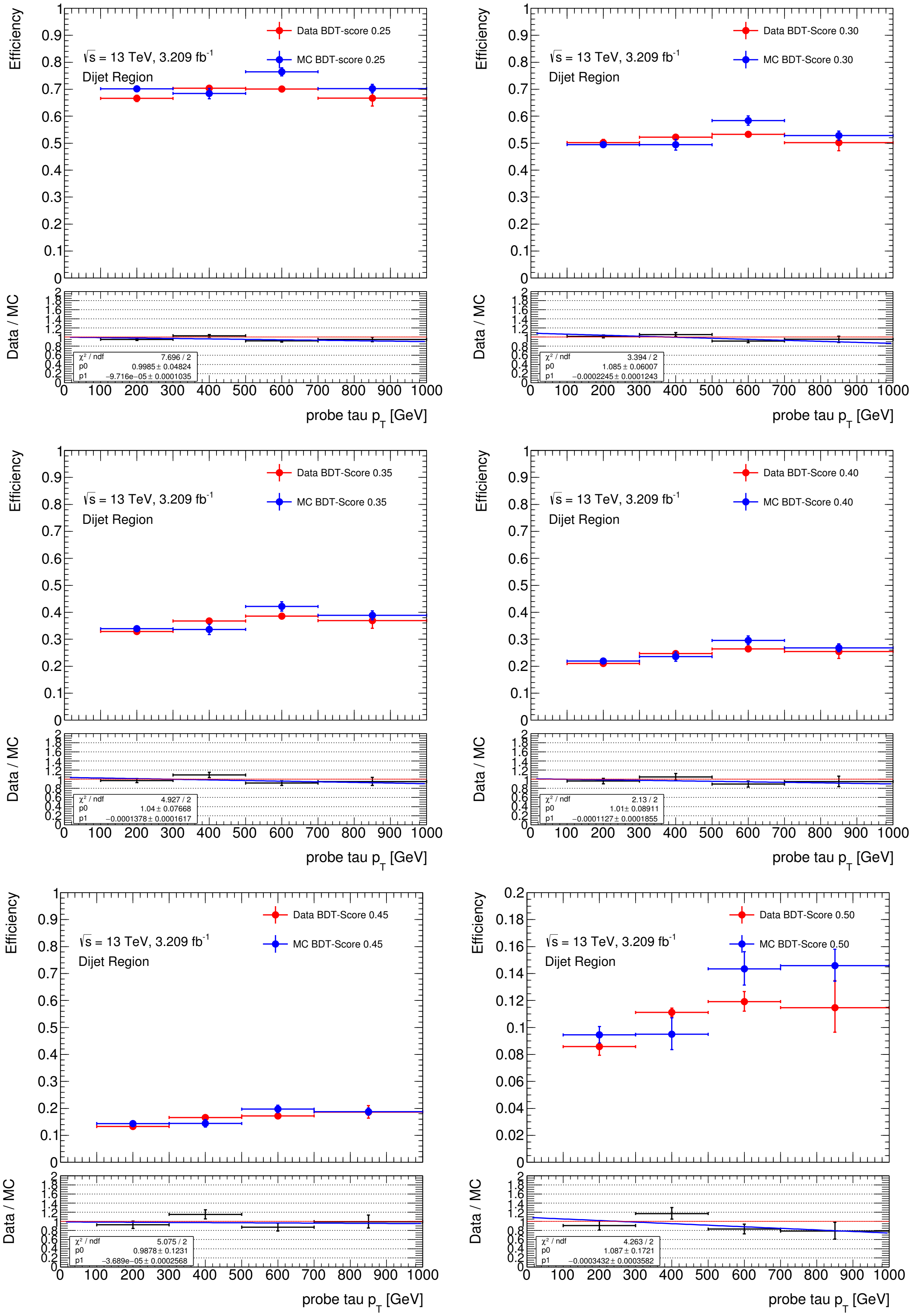

Figure B.3: Misidentification rates of probe 3-prong tau candidates for cuts on various different tau identification BDT scores, as a function of the probe object p_T. Both data and simulation are shown as well as the ratio between the two. A linear fit is placed on the data-simulation ratio, and the relevant fit parameters displayed.

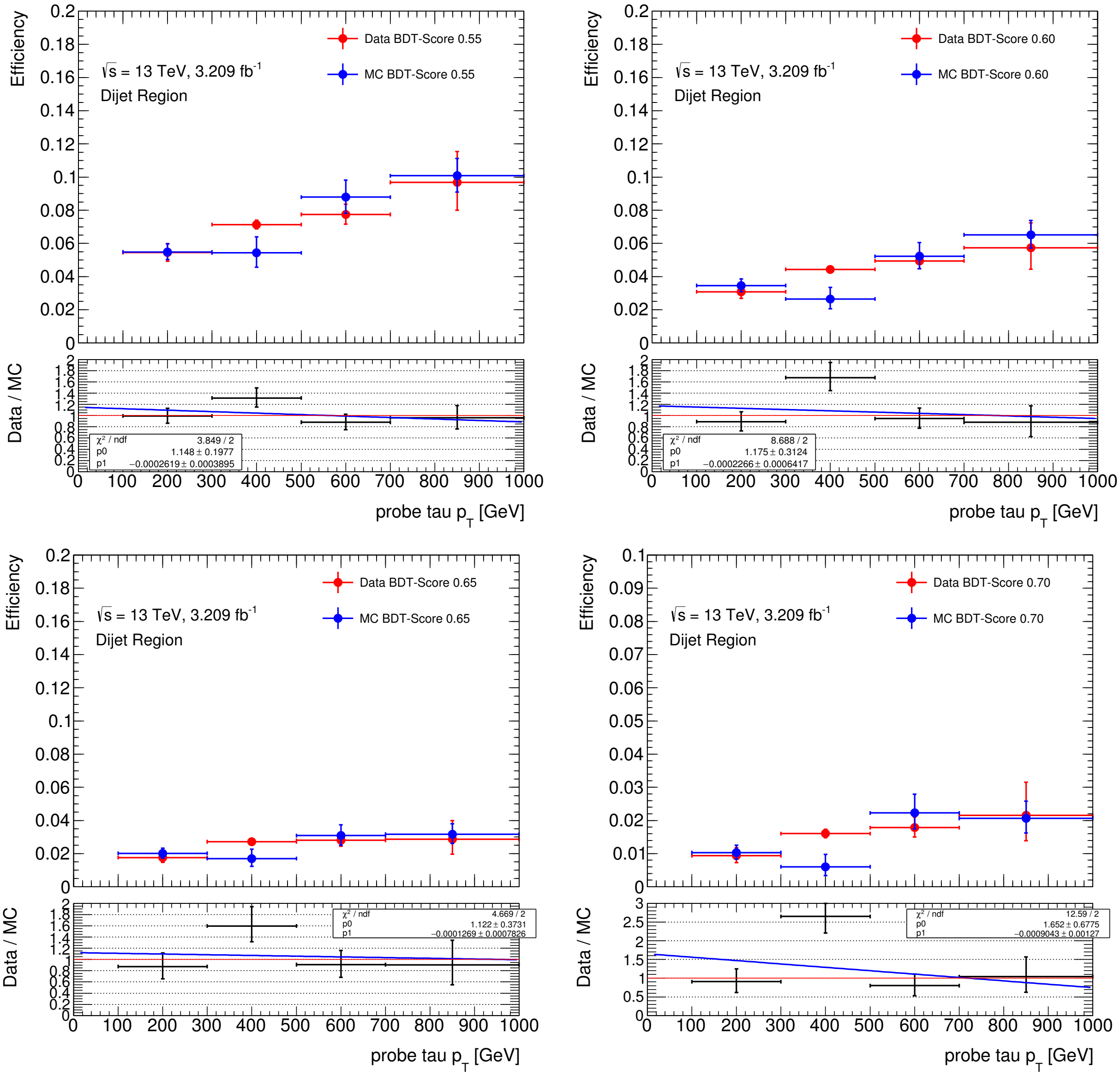

Figure B.4: Misidentification rates of probe 3-prong tau candidates for cuts on various different tau identification BDT scores, as a function of the probe object p_T. Both data and simulation are shown as well as the ratio between the two. A linear fit is placed on the data-simulation ratio, and the relevant fit parameters displayed.

Appendix C

Early Run-2 trigger monitoring

This appendix contains the tau trigger monitoring plots after the first week of data taking. The data corresponds to an integrated lumiosity of 6.6 pb^{-1}.

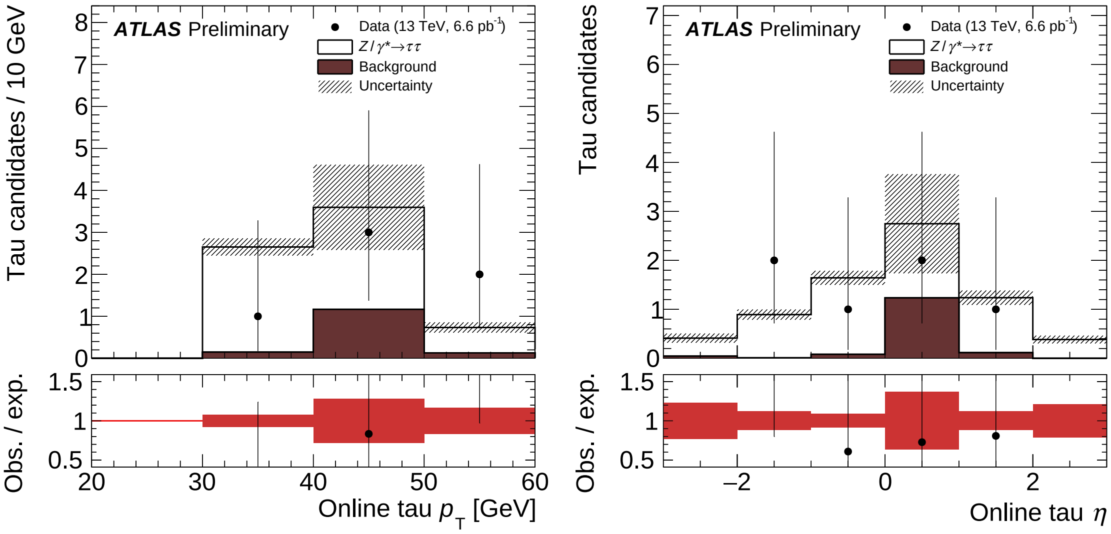

Figure C.1: Kinematic distributions of online tau candidates measured in a sample enriched in $Z \to \tau_\mu \tau_h$ events. The data correspond to an integrated luminosity of 6.6 pb^{-1}. 'Background' refers to the sum of SS data and simulated $Z \to \ell\ell$, W+jets, and $t\bar{t}$ processes with the SS component subtracted. Only statistical uncertainties are shown.

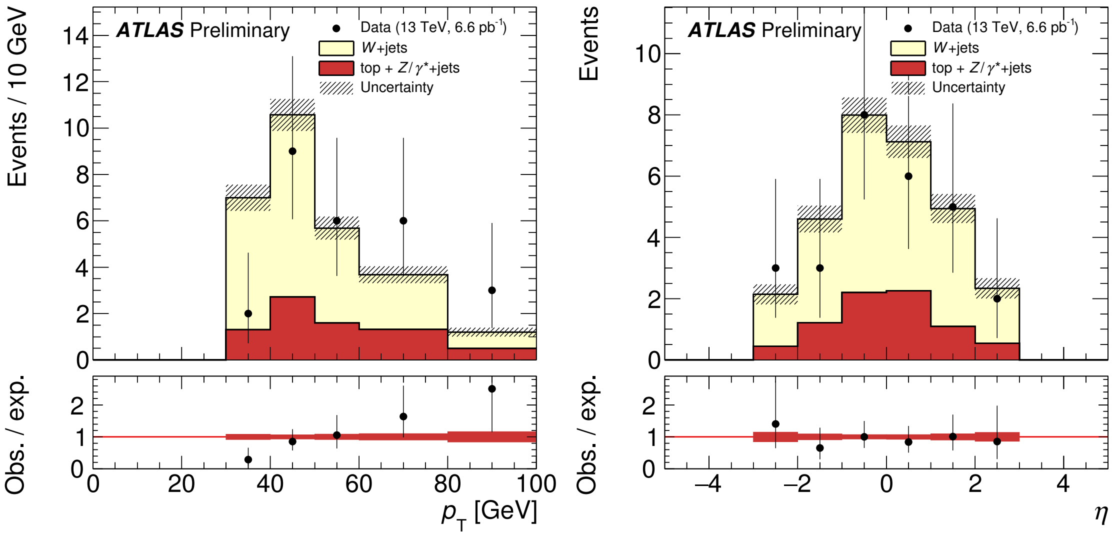

Figure C.2: Kinematic distributions of online tau candidates measured in a sample enriched in $W(\to \mu\nu)$+jets events. The data correspond to an integrated luminosity of 6.6 pb^{-1}. Only statistical uncertainties are shown.

Appendix D

Extra SS control region validation figures

The following distributions show the SS b-tag validation region without the application of the $\Delta\phi(\tau^{0}_{had}, \tau^{1}_{had}) > 2.7$ requirement. Although this $\Delta\phi$ inclusive selection is loosened compared to the signal selection used in the analysis, it offers a further check on the distributions of the kinematic variables.

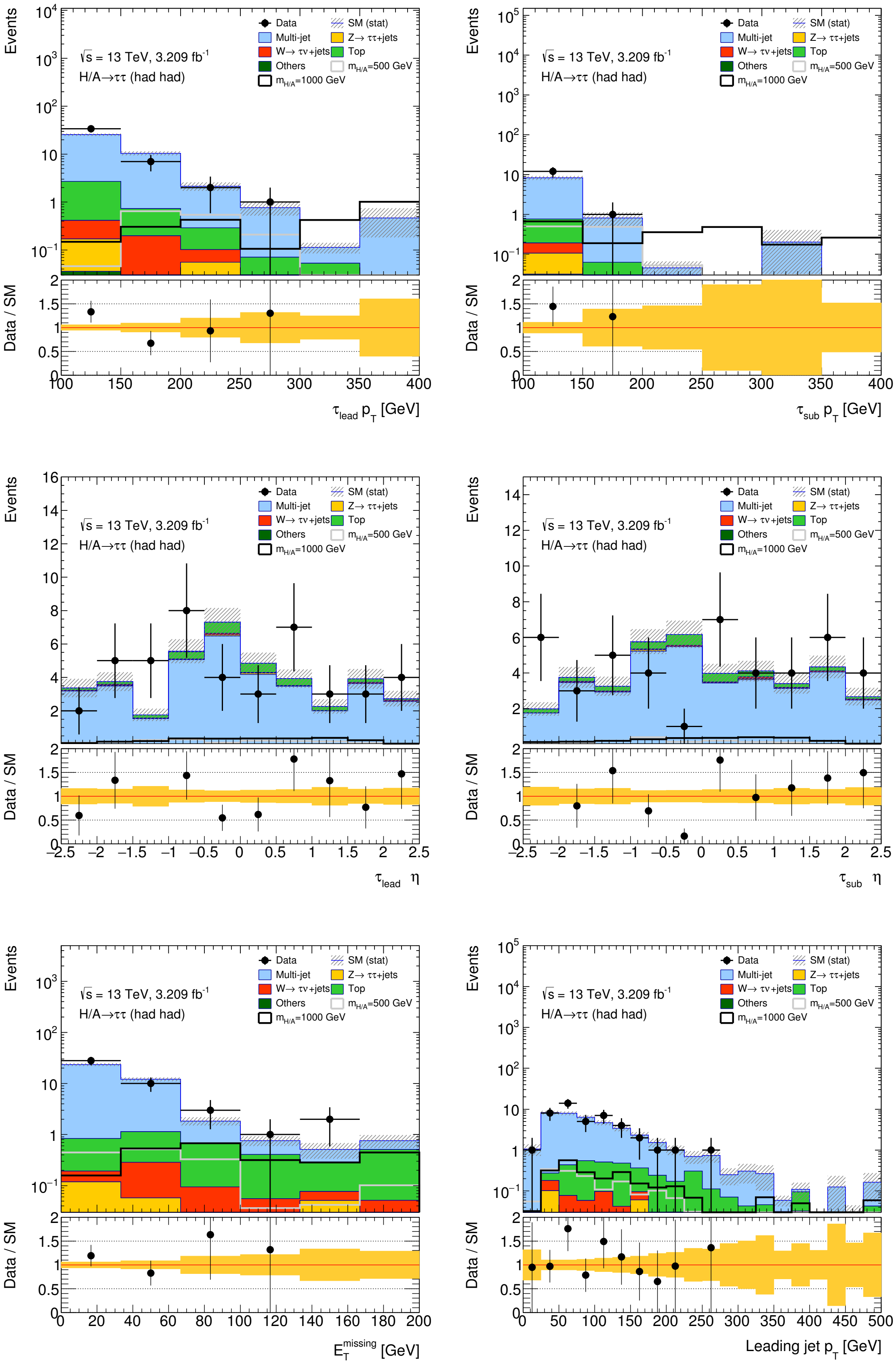

Figure D.1: Various distributions of selected kinematic variables after the full event selection, excluding the $\Delta\phi(\tau^0_{had}, \tau^1_{had})$ requirement, of the *b*-tag SS validation region. Two simulated *b*-associated production signal mass points of 500 GeV and 1000 GeV are also shown for illustrative purposes, with cross section times branching fractions normalised to 1 pb. The data correspond to an integrated luminosity of 3.21 fb^{-1}. Only statistical uncertainties are shown.

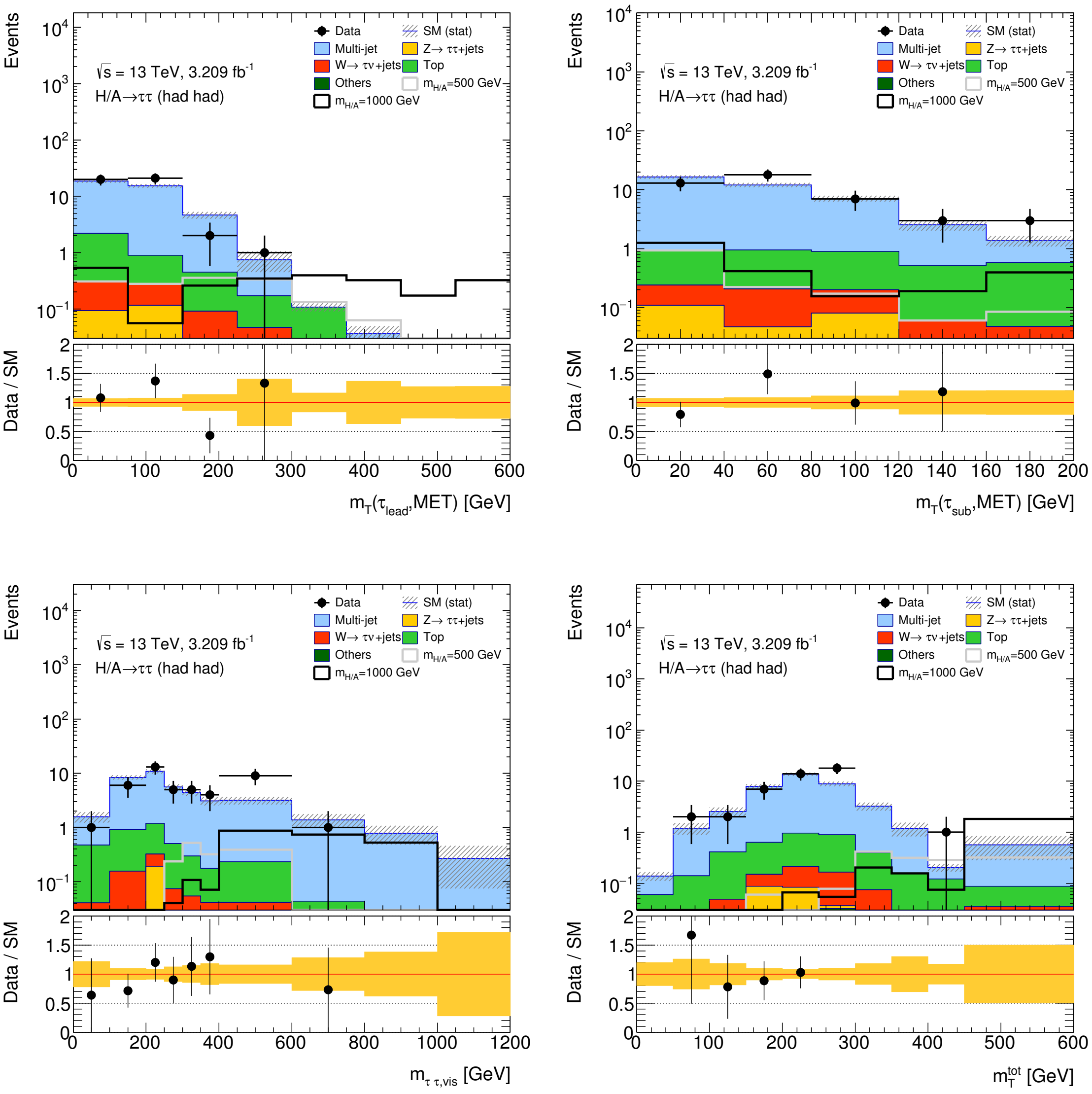

Figure D.2: Various distributions of selected kinematic variables after the full event selection, excluding the $\Delta\phi(\tau^0_{had}, \tau^1_{had})$ requirement, of the b-tag SS validation region. Two simulated b-associated production signal mass points of 500 GeV and 1000 GeV are also shown for illustrative purposes, with cross section times branching fractions normalised to 1 pb. The data correspond to an integrated luminosity of 3.21 fb^{-1}. Only statistical uncertainties are shown.

Appendix E

Extra signal region kinematic distributions

The following distributions show the *b*-tag signal region without the application of the $\Delta\phi(\tau^0_{had}, \tau^1_{had}) > 2.7$ criteria. Although this $\Delta\phi$ inclusive selection is loosened compared to the signal selection used in the analysis, it offers a useful check on the distributions of kinematic variables.

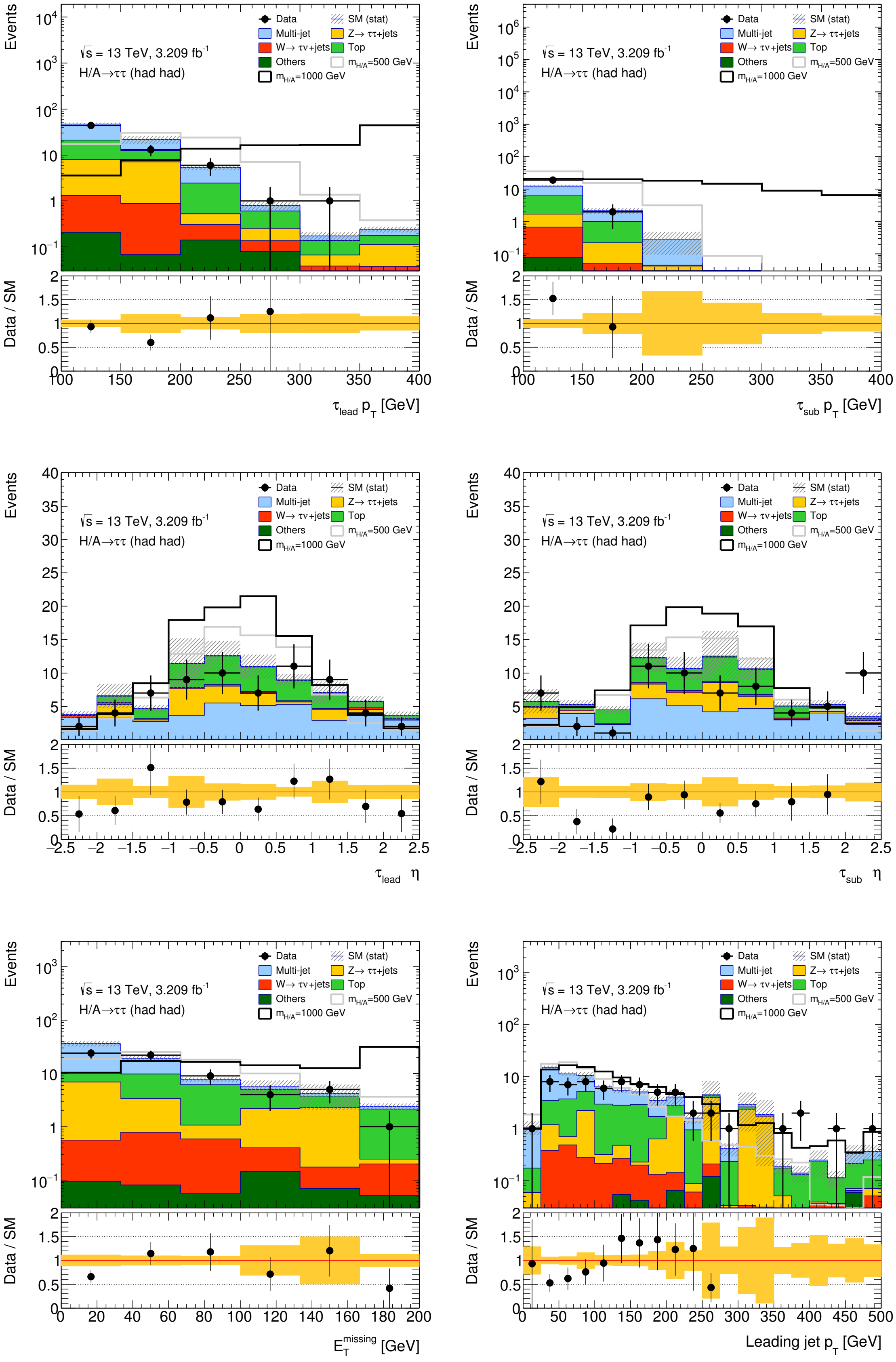

Figure E.1: Various distributions of selected kinematic variables after the full event selection, excluding the $\Delta\phi(\tau^0_{had}, \tau^1_{had})$ requirement, of the b-tag signal region. Two simulated b-associated production signal mass points of 500 GeV and 1000 GeV are also shown for illustrative purposes, with cross section times branching fractions normalised to 1 pb. The data correspond to an integrated luminosity of 3.21 fb^{-1}. Only statistical uncertainties are shown.

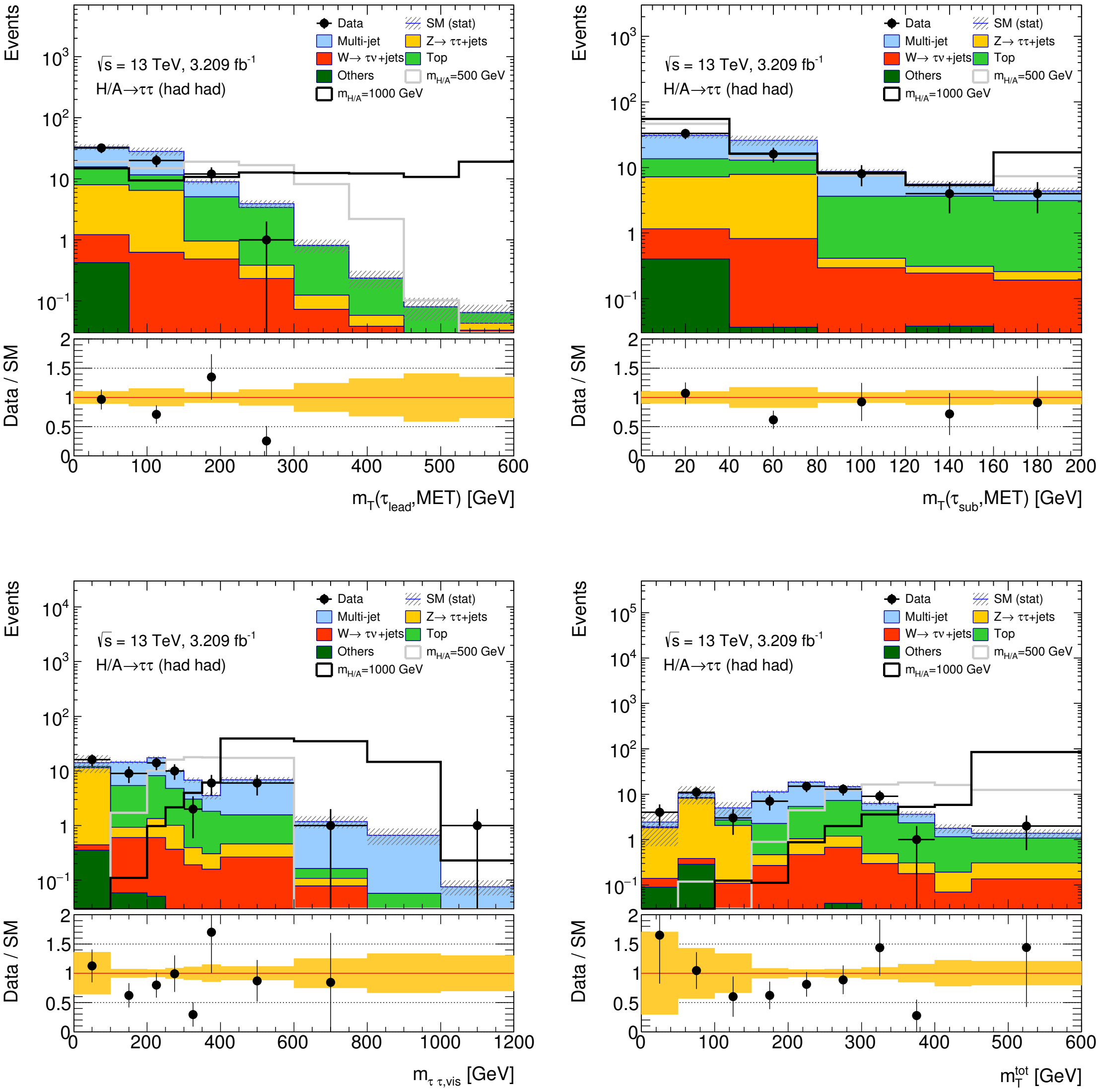

Figure E.2: Various distributions of selected kinematic variables after the full event selection, excluding the $\Delta\phi(\tau^0_{had}, \tau^1_{had})$ requirement, of the b-tag signal region. Two simulated b-associated production signal mass points of 500 GeV and 1000 GeV are also shown for illustrative purposes, with cross section times branching fractions normalised to 1 pb. The data correspond to an integrated luminosity of 3.21 fb^{-1}. Only statistical uncertainties are shown.

Appendix F

Distributions of the total transverse mass in the $A/H \rightarrow \tau_{\text{lep}}\tau_{\text{had}}$ analysis

This appendix shows the post-fit distributions of the total transverse mass in the $A/H \rightarrow \tau\tau$ analysis where one of the tau leptons decays hadronically, and the other decays to an electron or muon.

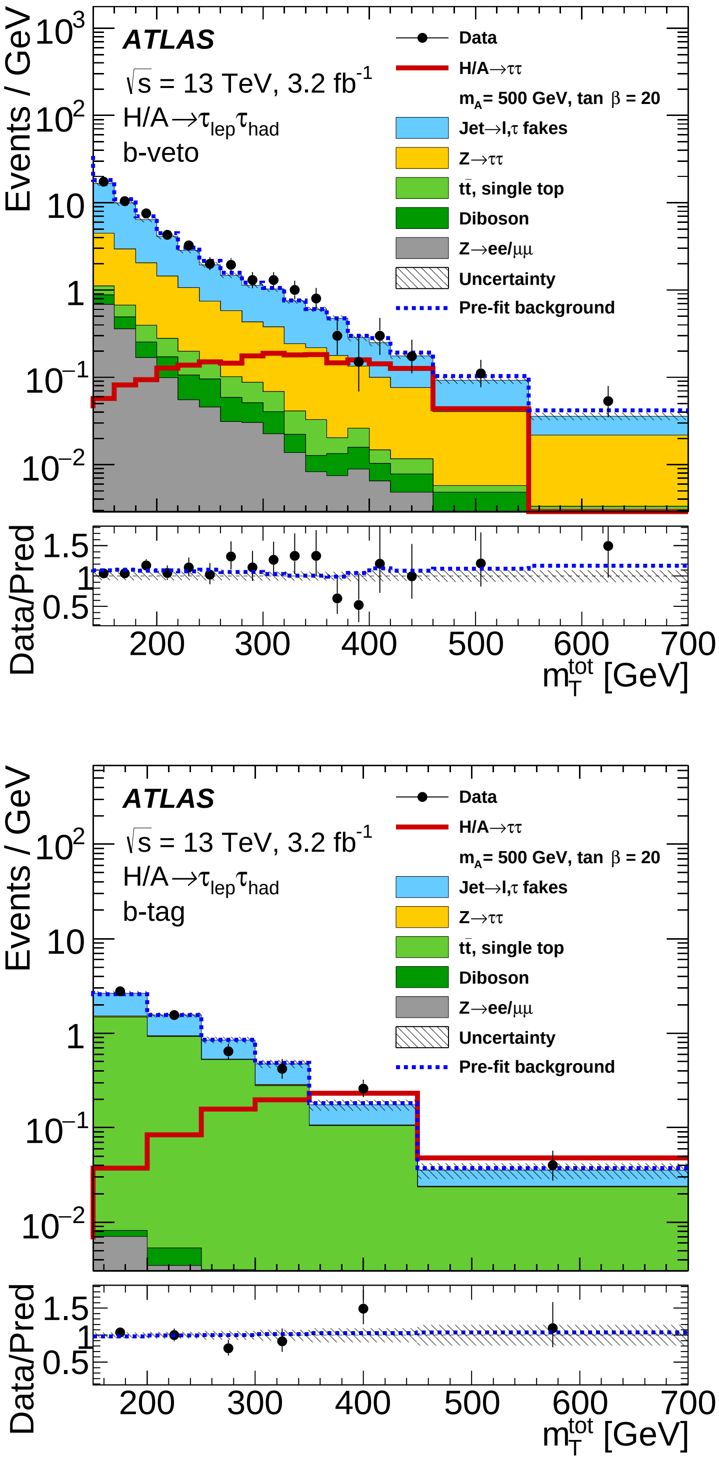

Figure F.1: Distributions of the total transverse mass, $m_{\mathrm{T}}^{\mathrm{tot}}$, after the full event selection of the b-veto (above) and b-tag (below) categories in the $\tau_{\mathrm{lep}}\tau_{\mathrm{had}}$ analysis with example gluon fusion and b-associated production signal processes shown in the respective categories. The pre-fit estimated background as well as the post-fit background, following the fitting procedure under the absence of a signal hypothesis, are shown. Taken from [10].

Appendix G

Impact of systematic uncertainties on the signal strength

This appendix shows the impact of the systematic uncertainties on the fitted signal strength and variations of the nuisance parameters from their nominal values under different signal assumptions.

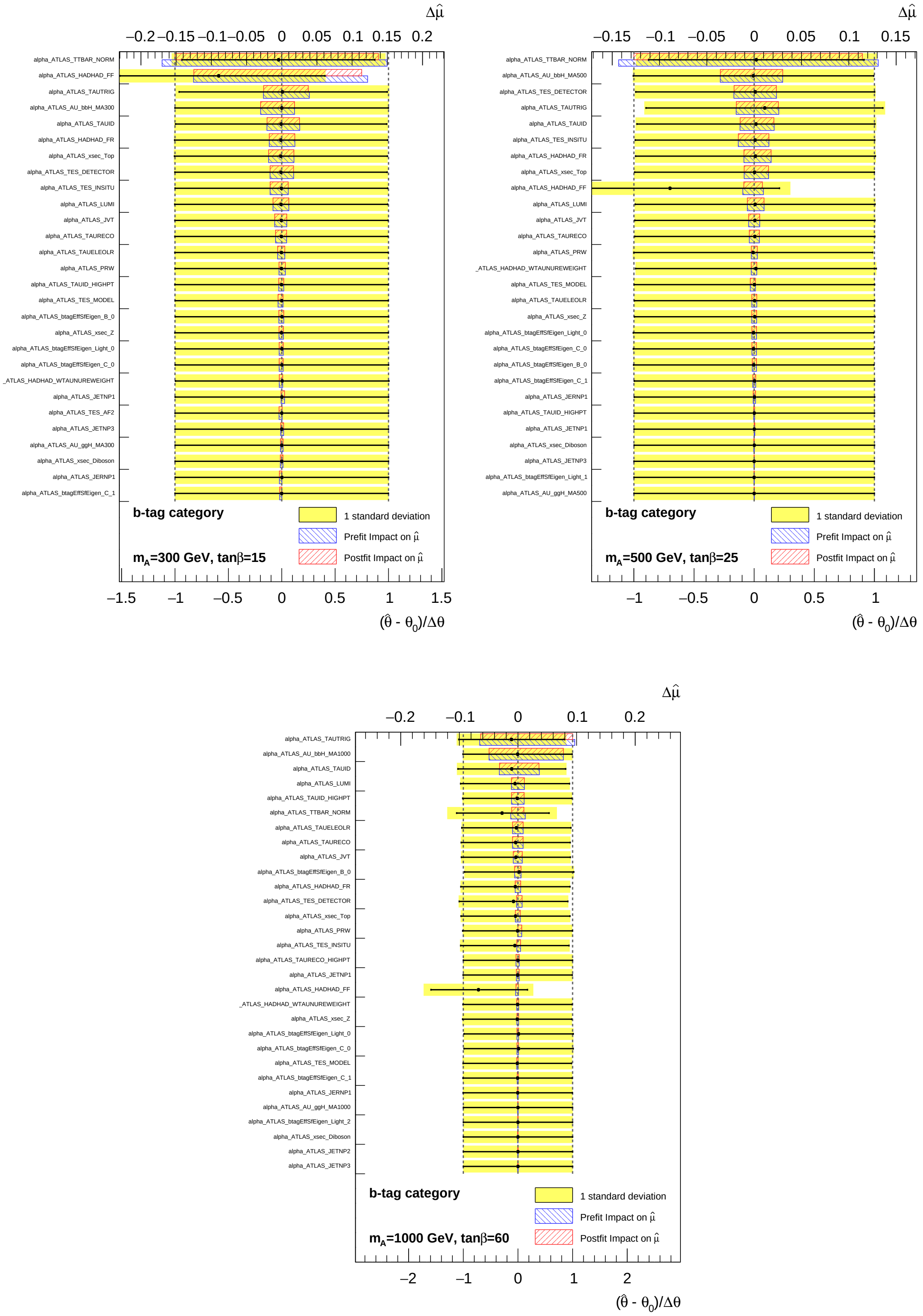

Figure G.1: The impact of the systematic uncertainties on the fitted signal strength and variations of the nuisance parameters from their nominal values in units of their uncertainty values. The plots show several signal mass points in the b-tag category, $m_{A/H} = 300$ GeV, 500 GeV and 1000 GeV, with the values of $\tan\beta$ chosen to be close to the expected limit in the $m_h^{\text{mod+}}$ scenario. The plots are produced by a collaborator.

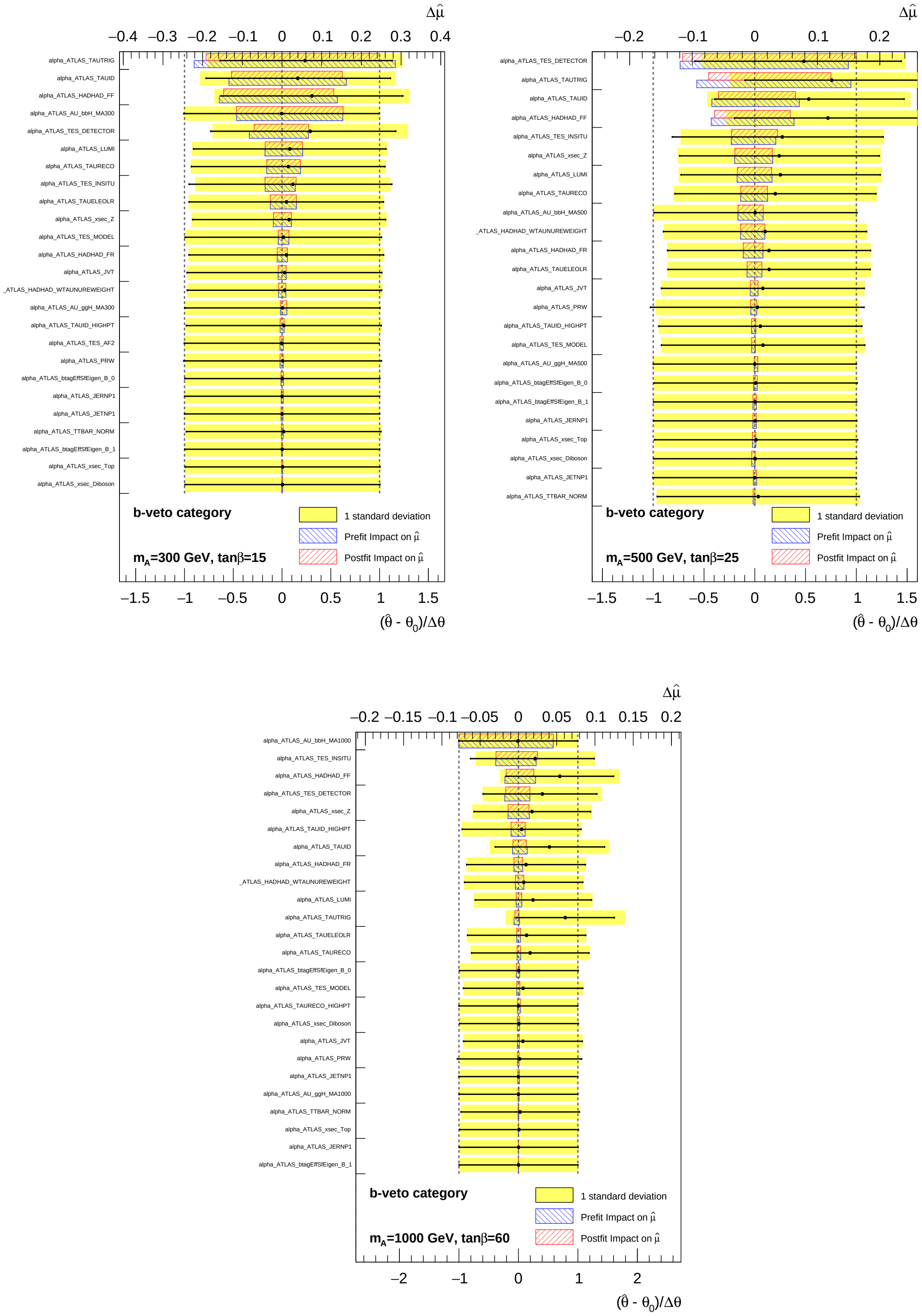

Figure G.2: The impact of the systematic uncertainties on the fitted signal strength and variations of the nuisance parameters from their nominal values in units of their uncertainty values. The plots show several signal mass points in the b-veto category, $m_{A/H} = 300$ GeV, 500 GeV and 1000 GeV, with the values of $\tan\beta$ chosen to be close to the expected limit in the $m_h^{\text{mod+}}$ scenario. The plots are produced by a collaborator.

Appendix H

Updated Run-2 limits

This appendix contains the updated results of the $A/H \to \tau\tau$ using data corresponding to an instantaneous luminosity of 13.3 fb^{-1} [141]. The distributions of the total transverse mass in the signal region are shown, as well as the updated limits in the $m_h^{\text{mod}+}$ and hMSSM scenarios.

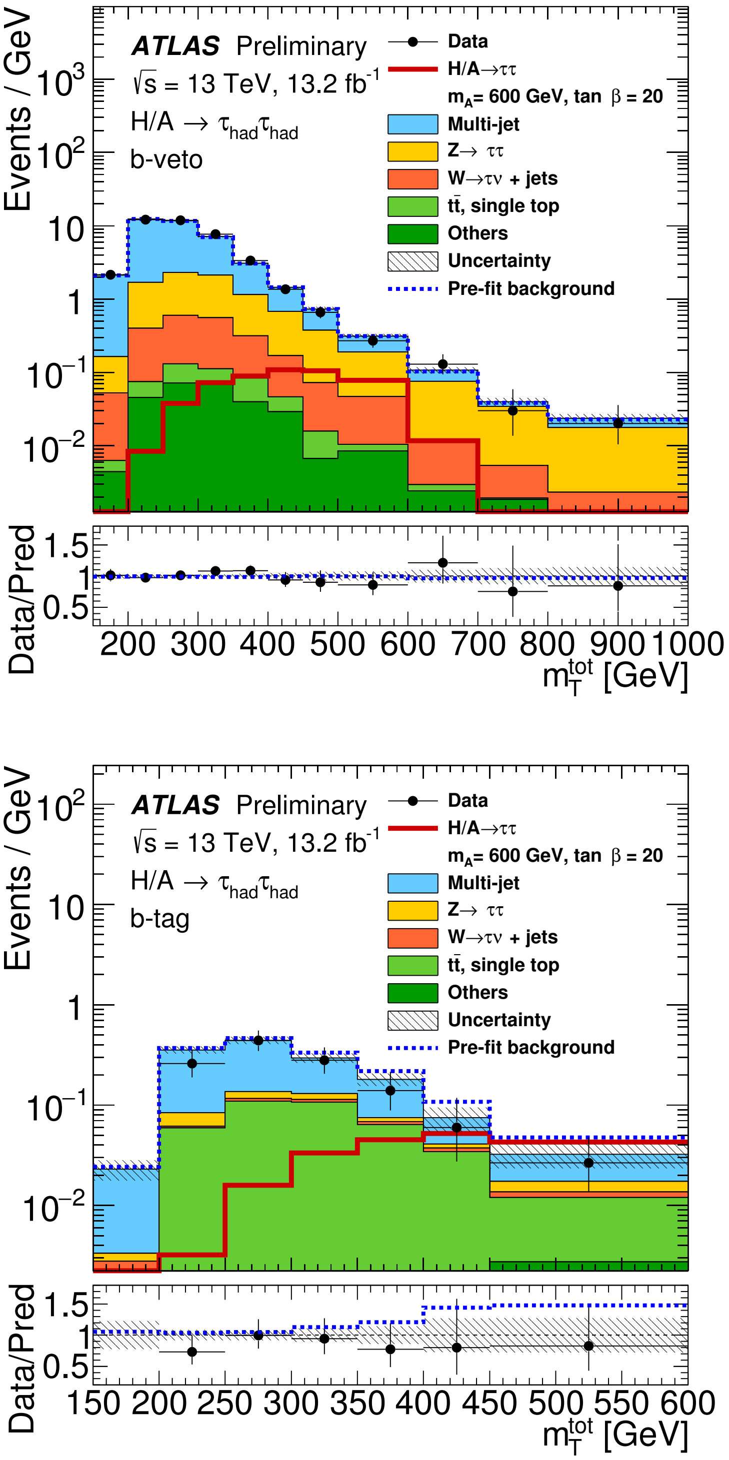

Figure H.1: Distributions of the total transverse mass, $m_{\mathrm{T}}^{\mathrm{tot}}$, after the full event selection of the b-veto (above) and b-tag (below) categories with example gluon fusion and b-associated production signal processes shown in the respective categories. The pre-fit estimated background as well as the post-fit background, following the fitting procedure under the absence of a signal hypothesis, are shown. Taken from [141].

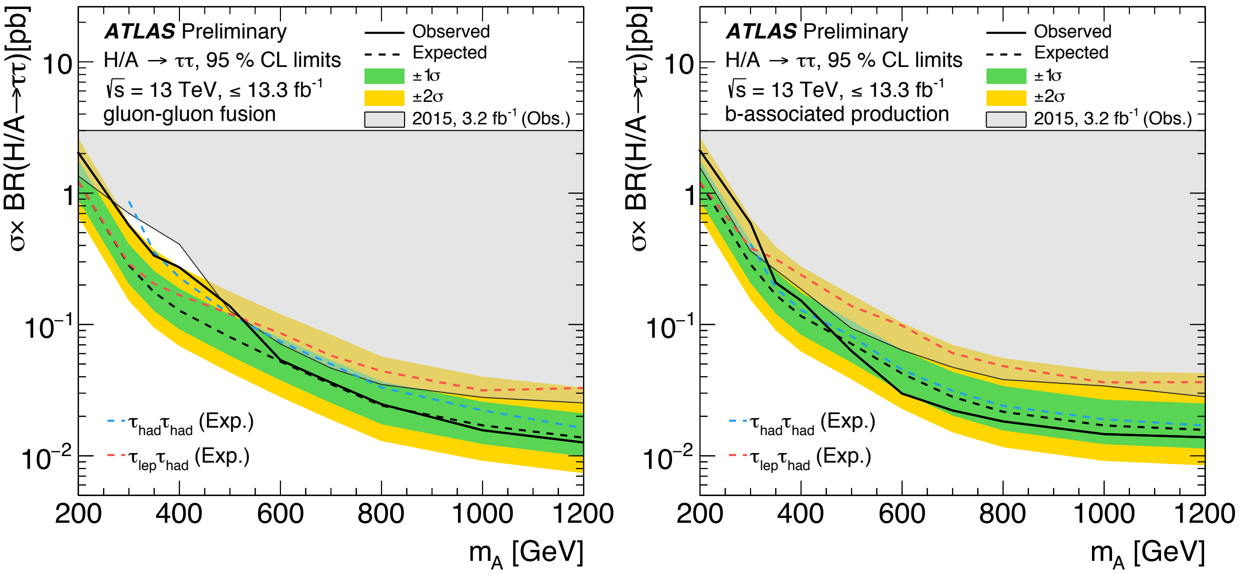

Figure H.2: The observed and expected 95% confidence level upper exclusion limit on the cross section times branching fraction of the production of a H/A boson decaying to a pair of tau leptons, as a function of the mass of the boson. The expected limits of the $\tau_{\text{lep}}\tau_{\text{had}}$ (red) and $\tau_{\text{had}}\tau_{\text{had}}$ (blue) final states are shown as well as the combined expected and observed limits (black). The production cross sections correspond to gluon fusion (left) and b-associated production (right) and the limits of the analysis using 2015 data are also shown. Taken from [141].

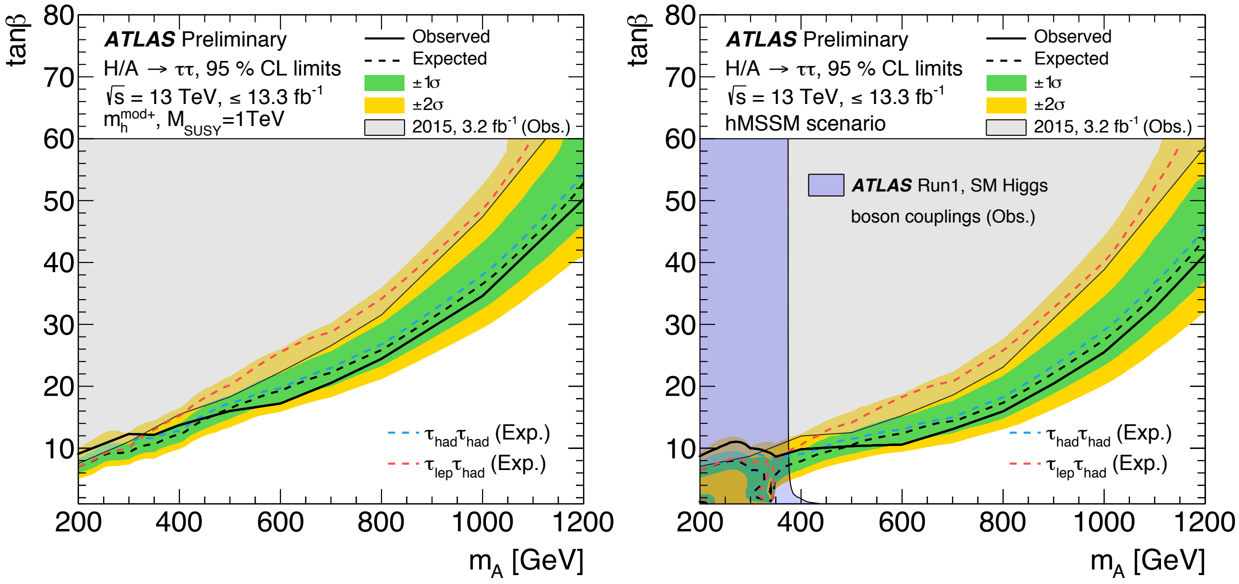

Figure H.3: The observed and expected 95% confidence level limits on tanβ as a function of the mass of the neutral Higgs boson, m_A. The left plot shows the $m_h^{\text{mod}+}$ scenario, with the expected limits for the $\tau_{\text{lep}}\tau_{\text{had}}$ (red) and $\tau_{\text{had}}\tau_{\text{had}}$ (blue) final states, as well as the combined expected and observed limits (black). The right plot shows hMSSM benchmark scenario limits. Also shown is the exclusion resulting from SM Higgs boson coupling measurements [140] and the limits of the analysis using 2015 data. Taken from [141].

Bibliography

[1] M. Shochet, L. Tompkins, V. Cavaliere, et al., *Fast TracKer (FTK) Technical Design Report*, Tech. Rep. CERN-LHCC-2013-007. ATLAS-TDR-021, Jun, 2013. https://cds.cern.ch/record/1552953. ATLAS Fast Tracker Technical Design Report.

[2] M. A. Pickering, *The ATLAS Hadronic Tau Trigger: Initial Run-2 Strategy and Performance*, Tech. Rep. ATL-DAQ-PROC-2015-042, CERN, Geneva, Oct, 2015. https://cds.cern.ch/record/2058716.

[3] M. A. Pickering, *The ATLAS Hadronic Tau Trigger: Initial Run-2 Strategy and Performance*, Proceedings of 27th International Symposium on Lepton Photon Interactions at High Energies, Aug. 17, 2015 (2015). pos.sissa.it/archive/conferences/245/067/LeptonPhoton2015_067.pdf.

[4] *Commissioning of the reconstruction of hadronic tau lepton decays in ATLAS using pp collisions at* $\sqrt{s} = 13\ TeV$, Tech. Rep. ATL-PHYS-PUB-2015-025, CERN, Geneva, Jul, 2015. https://cds.cern.ch/record/2037716.

[5] M. Beckingham, D. Zanzi, T. Ikai, et al., *Tau Trigger Performance Plots with 50ns 13 TeV Collisions*, Tech. Rep. ATL-COM-DAQ-2015-125, CERN, Geneva, Aug, 2015. https://cds.cern.ch/record/2040905.

[6] W. Davey, P.-O. Deviveiros, M. Beckingham, et al., *Offline Tau and Tau Trigger Performance Plots with 25ns 13TeV Collisions*, Tech. Rep. ATL-COM-PHYS-2015-1392, CERN, Geneva, Nov, 2015. https://cds.cern.ch/record/2103755.

[7] T. Mitani, M. A. Pickering, L. Zhang, et al., *Measurement of the tau lepton reconstruction and identification performance in the ATLAS experiment using pp collisions at* $\sqrt{s} = 13\ TeV$, Tech. Rep. ATL-COM-PHYS-2016-929, CERN, Geneva, Jul, 2016. https://cds.cern.ch/record/2199788.

[8] *Search for Neutral Minimal Supersymmetric Standard Model Higgs Bosons* $H/A \to \tau\tau$ *produced in pp collisions at* $\sqrt{s} = 13\ TeV$ *with the ATLAS Detector*, Tech. Rep. ATLAS-CONF-2015-061, CERN, Geneva, Dec, 2015. http://cds.cern.ch/record/2114827.

[9] ATLAS Collaboration, M. A. Pickering, *ATLAS High-mass MSSM* $H/A \to \tau\tau$ *search at 13 TeV*,. https://cds.cern.ch/record/2162419.

[10] ATLAS Collaboration, M. Aaboud et al., *Search for Minimal Supersymmetric Standard Model Higgs bosons H/A and for a Z′ boson in the ττ final state produced in pp collisions at* $\sqrt{s} = 13$ *TeV with the ATLAS Detector*, `arXiv:1608.00890 [hep-ex]`.

[11] *D. Alvarez Piqueras, M. Beckingham, U. Blumenschein, W. Davey, E. Drechsler, D. Duschinger, L. Fiorini, A. Goussiou, C. Gwilliam, G. Hamity, L. Hauswald, R. Hyneman, S. Jabbar, K. Koneke, H. Liu, W. Mader, A. McCarn, R. Moore, T. Mori, M. Morinaga, J. Pakela, M. Pickering, A. Pranko, N. Rompotis, P. Sales De Bruin, T. Schwarz, A. Straessner, J. Tanaka, T. Vickey, L. Zhang and Z. Zinonos,.*

[12] ATLAS Collaboration, *Observation of a new particle in the search for the Standard Model Higgs boson with the ATLAS detector at the LHC*, Physics Letters B **716** no. 1, (2012) 1 – 29.

[13] CMS Collaboration, *Observation of a new boson at a mass of 125 GeV with the CMS experiment at the LHC*, Physics Letters B **716** no. 1, (2012) 30 – 61.

[14] Particle Data Group Collaboration, K. A. Olive et al., *Review of Particle Physics*, Chin. Phys. **C38** (2014) 090001. and 2015 update.

[15] ATLAS Collaboration and CMS Collaboration, *Combined Measurement of the Higgs Boson Mass in pp Collisions at* $\sqrt{s} = 7$ *and 8 TeV with the ATLAS and CMS Experiments*, Phys. Rev. Lett. **114** (2015) 191803. `http://link.aps.org/doi/10.1103/PhysRevLett.114.191803`.

[16] J. Baglio, *Phenomenology of the Higgs at the hadron colliders: from the Standard Model to Supersymmetry.* PhD thesis, Orsay, LPT, 2011. `arXiv:1111.1195 [hep-ph]`. `http://inspirehep.net/record/944641/files/arXiv:1111.1195.pdf`.

[17] S. P. Martin, *A Supersymmetry primer*, `arXiv:arXiv:hep-ph/9709356 [hep-ph]`.

[18] F. Goertz, *Warped Extra Dimensions: Flavor, Precision Tests and Higgs Physics.* PhD thesis, Mainz U., Inst. Phys., 2011. `arXiv:1112.6387 [hep-ph]`. `https://inspirehep.net/record/1082990/files/arXiv:1112.6387.pdf`.

[19] ATLAS Collaboration, G. Aad et al., *Summary of the ATLAS experiments sensitivity to supersymmetry after LHC Run 1 interpreted in the phenomenological MSSM*, JHEP **10** (2015) 134, `arXiv:1508.06608 [hep-ex]`.

[20] CMS Collaboration, V. Khachatryan et al., *Phenomenological MSSM interpretation of CMS searches in pp collisions at sqrt(s) = 7 and 8 TeV*, Submitted to: JHEP (2016), `arXiv:1606.03577 [hep-ex]`.

[21] G. Degrassi, S. Heinemeyer, W. Hollik, P. Slavich, and G. Weiglein, *Towards high precision predictions for the MSSM Higgs sector*, Eur. Phys. J. **C28** (2003) 133–143, `arXiv:hep-ph/0212020 [hep-ph]`.

[22] M. Carena, S. Heinemeyer, O. Stl, C. E. M. Wagner, and G. Weiglein, *MSSM Higgs Boson Searches at the LHC: Benchmark Scenarios after the Discovery of a Higgs-like Particle*, Eur. Phys. J. **C73** no. 9, (2013) 2552, `arXiv:1302.7033 [hep-ph]`.

[23] A. Djouadi, L. Maiani, G. Moreau, et al., *The post-Higgs MSSM scenario: Habemus MSSM?*, Eur. Phys. J. **C73** (2013) 2650, `arXiv:1307.5205 [hep-ph]`.

[24] LHC Higgs Cross Section Working Group Collaboration, *LHC Higgs Cross Section WG Picture Gallery*,. `https://twiki.cern.ch/twiki/bin/view/AtlasPublic/RunStatsPublicResults2010#2015`.

[25] S. Myers, *The LEP collider, from design to approval and commissioning*, in *Proceedings of CERN Accelerator School, Nov. 26, 1990, CERN yellow report 91-08*. `https://cas.web.cern.ch/cas/John%20Adams'%20Lectures/Myers.pdf`.

[26] R. R. Wilson, *The Tevatron*, Phys. Today **30N10** (1977) 23–30.

[27] L. Evans and P. Bryant, *LHC Machine*, JINST **3** (2008) S08001.

[28] DELPHI, OPAL, ALEPH, LEP Working Group for Higgs Boson Searches, L3 Collaboration, S. Schael et al., *Search for neutral MSSM Higgs bosons at LEP*, Eur. Phys. J. **C47** (2006) 547–587, `arXiv:hep-ex/0602042 [hep-ex]`.

[29] CDF Collaboration, D0 Collaboration, Tevatron New Physics Higgs Working Group Collaboration, *Combined CDF and D0 upper limits on MSSM Higgs boson production in tau-tau final states with up to 2.2 fb-1*, Tech. Rep. arXiv:1003.3363, Mar, 2010. `https://cds.cern.ch/record/1249675`.

[30] ATLAS Collaboration, G. Aad et al., *Search for the neutral Higgs bosons of the Minimal Supersymmetric Standard Model in pp collisions at* $\sqrt{s} = 7$ *TeV with the ATLAS detector*, JHEP **02** (2013) 095, `arXiv:1211.6956 [hep-ex]`.

[31] ATLAS Collaboration, G. Aad et al., *Search for neutral Higgs bosons of the minimal supersymmetric standard model in pp collisions at* $\sqrt{s} = 8$ *TeV with the ATLAS detector*, JHEP **11** (2014) 056, `arXiv:1409.6064 [hep-ex]`.

[32] CMS Collaboration, V. Khachatryan et al., *Search for neutral MSSM Higgs bosons decaying to a pair of tau leptons in pp collisions*, JHEP **10** (2014) 160, `arXiv:1408.3316 [hep-ex]`.

[33] CMS Collaboration, V. Khachatryan et al., *Search for neutral MSSM Higgs bosons decaying into a pair of bottom quarks*, JHEP **11** (2015) 071, `arXiv:1506.08329 [hep-ex]`.

[34] LHCb Collaboration, R. Aaij et al., *Limits on neutral Higgs boson production in the forward region in pp collisions at* $\sqrt{s} = 7$ *TeV*, JHEP **05** (2013) 132, `arXiv:1304.2591 [hep-ex]`.

[35] ATLAS, *The ATLAS Experiment at the CERN Large Hadron Collider*, JINST **3** (2008) S08003.

[36] CMS Collaboration, *The CMS experiment at the CERN LHC*, Journal of Instrumentation **3** no. 08, (2008) S08004. `http://stacks.iop.org/1748-0221/3/i=08/a=S08004`.

[37] L. R. Evans and P. Bryant, *LHC Machine*, J. Instrum. **3** (2008) S08001. 164 p. `https://cds.cern.ch/record/1129806`. This report is an abridged version of the LHC Design Report (CERN-2004-003).

[38] ALICE Collaboration, *The ALICE experiment at the CERN LHC*, Journal of Instrumentation **3** no. 08, (2008) S08002. `http://stacks.iop.org/1748-0221/3/i=08/a=S08002`.

[39] LHCb Collaboration, *The LHCb Detector at the LHC*, Journal of Instrumentation **3** no. 08, (2008) S08005. `http://stacks.iop.org/1748-0221/3/i=08/a=S08005`.

[40] P. Mouche, *Overall view of the LHC. Vue d'ensemble du LHC*,. `https://cds.cern.ch/record/1708847`. General Photo.

[41] ATLAS Collaboration, *Luminosity Public Results*,. `https://twiki.cern.ch/twiki/bin/view/AtlasPublic/LuminosityPublicResults`.

[42] ATLAS Collaboration, *Luminosity Public Results in Run-2*,. `https://twiki.cern.ch/twiki/bin/view/AtlasPublic/LuminosityPublicResultsRun2`.

[43] J. Pequenao, *Computer generated image of the whole ATLAS detector*,. `https://cds.cern.ch/record/1095924`.

[44] C. Lefevre, "LHC: the guide (English version). Guide du LHC (version anglaise)." Feb, 2009.

[45] J. Pequenao, *Computer generated image of the ATLAS inner detector*,. `https://cds.cern.ch/record/1095926`.

[46] F. Hugging, *The ATLAS Pixel Detector*, IEEE Transactions on Nuclear Science **53** (2006) 1732–1736, `physics/0412138`.

[47] ATLAS Collaboration, "ATLAS Insertable B-Layer Technical Design Report." CERN-LHCC-2010-013, ATLAS-TDR-19, 2010. `http://cdsweb.cern.ch/record/1291633`.

[48] ATLAS Collaboration, *Operation and performance of the ATLAS semiconductor tracker*, JINST **9** (2014) P08009, `arXiv:1404.7473 [hep-ex]`.

[49] ATLAS Collaboration, *The ATLAS Transition Radiation Tracker (TRT) proportional drift tube: design and performance*, Journal of Instrumentation **3** no. 02, (2008) P02013. `http://stacks.iop.org/1748-0221/3/i=02/a=P02013`.

[50] B. Mindur, *ATLAS Transition Radiation Tracker (TRT): Straw Tubes for Tracking and Particle Identification at the Large Hadron Collider*, Tech. Rep. ATL-INDET-PROC-2016-001, CERN, Geneva, Mar, 2016. `https://cds.cern.ch/record/2139567`.

[51] J. Pequenao, *Computer generated image of the ATLAS calorimeter*,. `https://cds.cern.ch/record/1095927`.

[52] ATLAS Collaboration, N. Nikiforou, *Performance of the ATLAS Liquid Argon Calorimeter after three years of LHC operation and plans for a future upgrade*, in *Proceedings, 3rd International Conference on Advancements in Nuclear Instrumentation Measurement Methods and their Applications (ANIMMA 2013)*. 2013. `arXiv:1306.6756 [physics.ins-det]`. `http://inspirehep.net/record/1240499/files/arXiv:1306.6756.pdf`.

[53] ATLAS Collaboration, A. e. a. Airapetian, *ATLAS detector and physics performance: Technical Design Report, 1.* Technical Design Report ATLAS. CERN, Geneva, 1999. https://cds.cern.ch/record/391176.

[54] ATLAS Collaboration, *ATLAS tile calorimeter: Technical Design Report.* Technical Design Report ATLAS. CERN, Geneva, 1996. https://cds.cern.ch/record/331062.

[55] J. Pequenao, *Computer generated image of the ATLAS Muons subsystem,*. https://cds.cern.ch/record/1095929.

[56] ATLAS Collaboration, *ATLAS muon spectrometer: Technical Design Report.* Technical Design Report ATLAS. CERN, Geneva, 1997. https://cds.cern.ch/record/331068.

[57] B. Stelzer, *The New Small Wheel Upgrade Project of the ATLAS Experiment*, Tech. Rep. ATL-MUON-PROC-2014-008, CERN, Geneva, Oct, 2014. https://cds.cern.ch/record/1958265.

[58] ATLAS Collaboration, *Technical Design Report for the Phase-I Upgrade of the ATLAS TDAQ System*, Tech. Rep. CERN-LHCC-2013-018. ATLAS-TDR-023, Sep, 2013. https://cds.cern.ch/record/1602235. Final version presented to December 2013 LHCC.

[59] *2015 start-up trigger menu and initial performance assessment of the ATLAS trigger using Run-2 data*, Tech. Rep. ATL-DAQ-PUB-2016-001, CERN, Geneva, Mar, 2016. https://cds.cern.ch/record/2136007.

[60] M. Backes, *The ATLAS Trigger System - Ready for Run-2*, Tech. Rep. ATL-DAQ-PROC-2015-041, CERN, Geneva, Oct, 2015. https://cds.cern.ch/record/2058618.

[61] M. Cacciari, G. P. Salam, and G. Soyez, *The Anti-k(t) jet clustering algorithm*, JHEP **04** (2008) 063, arXiv:0802.1189 [hep-ph].

[62] T. Cornelissen, M. Elsing, S. Fleischmann, et al., *Concepts, Design and Implementation of the ATLAS New Tracking (NEWT)*, Tech. Rep. ATL-SOFT-PUB-2007-007. ATL-COM-SOFT-2007-002, CERN, Geneva, Mar, 2007. https://cds.cern.ch/record/1020106.

[63] ATLAS Collaboration, *Electron efficiency measurements with the ATLAS detector using the 2012 LHC proton-proton collision data,*. https://cds.cern.ch/record/1706245.

[64] W. Lampl, S. Laplace, D. Lelas, et al., *Calorimeter Clustering Algorithms: Description and Performance,*. https://cds.cern.ch/record/1099735.

[65] ATLAS Collaboration, *Electron identification measurements in ATLAS using $\sqrt{s}$ = 13 TeV data with 50 ns bunch spacing,*. https://cds.cern.ch/record/2048202.

[66] ATLAS Collaboration, G. Aad et al., *Muon reconstruction performance of the ATLAS detector in protonproton collision data at $\sqrt{s}$ =13 TeV*, Eur. Phys. J. **C76** no. 5, (2016) 292, arXiv:1603.05598 [hep-ex].

[67] ATLAS Collaboration, *Jet energy measurement with the ATLAS detector in proton-proton collisions at $\sqrt{s} = 7$ TeV*, Eur.Phys.J. **C73** (2013) 2304, `arXiv:arXiv:hep-ex/1112.6426 [hep-ex]`.

[68] T. Barillari, E. Bergeaas Kuutmann, T. Carli, et al., *Local Hadronic Calibration*, Tech. Rep. ATL-LARG-PUB-2009-001-2. ATL-COM-LARG-2008-006. ATL-LARG-PUB-2009-001, CERN, Geneva, Jun, 2008. `https://cds.cern.ch/record/1112035`.

[69] ATLAS Collaboration, *Jet Calibration and Systematic Uncertainties for Jets Reconstructed in the ATLAS Detector at $\sqrt{s} = 13$ TeV*,. `https://cds.cern.ch/record/2037613`.

[70] ATLAS Collaboration, *Expected performance of the ATLAS b-tagging algorithms in Run-2*,. `https://cds.cern.ch/record/2037697`.

[71] L. Breiman, J. Friedman, R. Olshen, and C. Stone, *Classification and Regression Trees*. Chapman & Hall, New York, 1984.

[72] Y. Freund and R. E. Schapire, *A decision-theoretic generalization of on-line learning and an application to boosting*, J. Comput. Syst. Sci. **55** (1997).

[73] ATLAS Collaboration, *Expected performance of missing transverse momentum reconstruction for the ATLAS detector at $\sqrt{s} = 13$ TeV*,. `https://cds.cern.ch/record/2037700`.

[74] ATLAS Collaboration, *Data Quality Public Results in Run-2*,. `https://twiki.cern.ch/twiki/bin/view/AtlasPublic/RunStatsPublicResults2010#2015`.

[75] ATLAS Collaboration, *The ATLAS simulation infrastructure*, Eur. Phys. J. **C 70** (2010) 823–874, `arXiv:1005.4568 [physics.ins-det]`.

[76] GEANT4 Collaboration, Agostinelli et al., *GEANT4: A simulation toolkit*, Nucl. Instrum. Meth. **A506** (2003) 250–303.

[77] T. Sjostrand, S. Mrenna, and P. Skands, *PYTHIA 6.4 physics and manual*, JHEP **0605** (2006) 026, `arXiv:arXiv:hep-ph/0603175`.

[78] T. Sjostrand, S. Mrenna, and P. Z. Skands, *A Brief Introduction to PYTHIA 8.1*, Comput.Phys.Commun. **178** (2008) 852–867, `arXiv:arXiv:hep-ph/0710.3820 [hep-ph]`.

[79] ATLAS Collaboration, G. Aad et al., *Identification and energy calibration of hadronically decaying tau leptons with the ATLAS experiment in pp collisions at $\sqrt{s}$=8 TeV*, Eur. Phys. J. **C75** no. 7, (2015) 303, `arXiv:1412.7086 [hep-ex]`.

[80] *Reconstruction, Energy Calibration, and Identification of Hadronically Decaying Tau Leptons in the ATLAS Experiment for Run-2 of the LHC*, Tech. Rep. ATL-PHYS-PUB-2015-045, CERN, Geneva, Nov, 2015. `https://cds.cern.ch/record/2064383`.

[81] *Determination of the tau energy scale and the associated systematic uncertainty in proton-proton collisions at $\sqrt{s} = 8$ TeV with the ATLAS detector at the LHC in 2012*, Tech. Rep. ATLAS-CONF-2013-044, CERN, Geneva, Apr, 2013. `https://cds.cern.ch/record/1544036`.

[82] T. Sjöstrand, S. Mrenna, and P. Z. Skands, *A Brief Introduction to PYTHIA 8.1*, Comput. Phys. Commun. **178** (2008) 852, `arXiv:0710.3820 [hep-ph]`.

[83] P. Nason, *A New method for combining NLO QCD with shower Monte Carlo algorithms*, JHEP **11** (2004) 040, `arXiv:hep-ph/0409146 [hep-ph]`.

[84] S. Frixione, P. Nason, and C. Oleari, *Matching NLO QCD computations with Parton Shower simulations: the POWHEG method*, JHEP **11** (2007) 070, `arXiv:0709.2092 [hep-ph]`.

[85] S. Alioli, P. Nason, C. Oleari, and E. Re, *A general framework for implementing NLO calculations in shower Monte Carlo programs: the POWHEG BOX*, JHEP **06** (2010) 043, `arXiv:1002.2581 [hep-ph]`.

[86] T. Sjöstrand, S. Mrenna, and P. Z. Skands, *PYTHIA 6.4 physics and manual*, JHEP **05** (2006) 026, `arXiv:hep-ph/0603175`.

[87] J. A. et al, *The automated computation of tree-level and next-to-leading order differential cross sections, and their matching to parton shower simulations*, JHEP **07** (2014) 079, `arXiv:1405.0301 [hep-ph]`.

[88] M. Wiesemann et al, *Higgs production in association with bottom quarks*, JHEP **02** (2015) 132, `arXiv:1409.5301 [hep-ph]`.

[89] S. Dulat, T.-J. Hou, J. Gao, et al., *New parton distribution functions from a global analysis of quantum chromodynamics*, Phys. Rev. **D93** no. 3, (2016) 033006, `arXiv:1506.07443 [hep-ph]`.

[90] H.-L. Lai, M. Guzzi, J. Huston, et al., *New parton distributions for collider physics*, Phys. Rev. **D82** (2010) 074024, `arXiv:1007.2241 [hep-ph]`.

[91] T. S. et al., *An Introduction to PYTHIA 8.2*, Comput.Phys.Commun. **191** (2015) 159–177, `arXiv:1410.3012 [hep-ph]`.

[92] ATLAS Collaboration, G. Aad et al., *Measurement of the Z/γ^* boson transverse momentum distribution in pp collisions at $\sqrt{s} = 7$ TeV with the ATLAS detector*, JHEP **09** (2014) 145, `arXiv:1406.3660 [hep-ex]`.

[93] ATLAS Collaboration, *ATLAS Run 1 Pythia8 tunes*, ATL-PHYS-PUB-2014-021 (2014). `https://cds.cern.ch/record/1966419`.

[94] W. Lukas, *Fast Simulation for ATLAS: Atlfast-II and ISF*, CERN. CERN, Geneva, 2012. `http://cdsweb.cern.ch/record/1458503/files/ATL-SOFT-PROC-2012-065.pdf`.

[95] R. V. Harlander, S. Liebler, and H. Mantler, *SusHi: A program for the calculation of Higgs production in gluon fusion and bottom-quark annihilation in the Standard Model and the MSSM*, Comput. Phys. Commun. **184** (2013) 1605–1617, `arXiv:1212.3249 [hep-ph]`.

[96] R. V. Harlander and W. B. Kilgore, *Next-to-next-to-leading order Higgs production at hadron colliders*, Phys. Rev. Lett. **88** (2002) 201801, `arXiv:hep-ph/0201206 [hep-ph]`.

[97] M. Spira, A. Djouadi, D. Graudenz, and P. M. Zerwas, *Higgs boson production at the LHC*, Nucl. Phys. **B453** (1995) 17–82, `arXiv:hep-ph/9504378 [hep-ph]`.

[98] C. Anastasiou and K. Melnikov, *Higgs boson production at hadron colliders in NNLO QCD*, Nucl. Phys. **B646** (2002) 220–256, `arXiv:hep-ph/0207004 [hep-ph]`.

[99] V. Ravindran, J. Smith, and W. L. van Neerven, *NNLO corrections to the total cross-section for Higgs boson production in hadron hadron collisions*, Nucl. Phys. **B665** (2003) 325–366, `arXiv:hep-ph/0302135 [hep-ph]`.

[100] R. V. Harlander and W. B. Kilgore, *Production of a pseudoscalar Higgs boson at hadron colliders at next-to-next-to leading order*, JHEP **10** (2002) 017, `arXiv:hep-ph/0208096 [hep-ph]`.

[101] C. Anastasiou and K. Melnikov, *Pseudoscalar Higgs boson production at hadron colliders in NNLO QCD*, Phys. Rev. **D67** (2003) 037501, `arXiv:hep-ph/0208115 [hep-ph]`.

[102] U. Aglietti, R. Bonciani, G. Degrassi, and A. Vicini, *Two loop light fermion contribution to Higgs production and decays*, Phys. Lett. **B595** (2004) 432–441, `arXiv:hep-ph/0404071 [hep-ph]`.

[103] R. Bonciani, G. Degrassi, and A. Vicini, *On the Generalized Harmonic Polylogarithms of One Complex Variable*, Comput. Phys. Commun. **182** (2011) 1253–1264, `arXiv:1007.1891 [hep-ph]`.

[104] R. V. Harlander and M. Steinhauser, *Supersymmetric Higgs production in gluon fusion at next-to-leading order*, JHEP **09** (2004) 066, `arXiv:hep-ph/0409010 [hep-ph]`.

[105] R. Harlander and P. Kant, *Higgs production and decay: Analytic results at next-to-leading order QCD*, JHEP **12** (2005) 015, `arXiv:hep-ph/0509189 [hep-ph]`.

[106] G. Degrassi and P. Slavich, *NLO QCD bottom corrections to Higgs boson production in the MSSM*, JHEP **11** (2010) 044, `arXiv:1007.3465 [hep-ph]`.

[107] G. Degrassi, S. Di Vita, and P. Slavich, *NLO QCD corrections to pseudoscalar Higgs production in the MSSM*, JHEP **08** (2011) 128, `arXiv:1107.0914 [hep-ph]`.

[108] G. Degrassi, S. Di Vita, and P. Slavich, *On the NLO QCD Corrections to the Production of the Heaviest Neutral Higgs Scalar in the MSSM*, Eur. Phys. J. **C72** (2012) 2032, `arXiv:1204.1016 [hep-ph]`.

[109] R. V. Harlander and W. B. Kilgore, *Higgs boson production in bottom quark fusion at next-to-next-to leading order*, Phys. Rev. **D68** (2003) 013001, `arXiv:hep-ph/0304035 [hep-ph]`.

[110] S. Dittmaier, M. Kramer, 1, and M. Spira, *Higgs radiation off bottom quarks at the Tevatron and the CERN LHC*, Phys. Rev. **D70** (2004) 074010, `arXiv:hep-ph/0309204 [hep-ph]`.

[111] S. Dawson, C. B. Jackson, L. Reina, and D. Wackeroth, *Exclusive Higgs boson production with bottom quarks at hadron colliders*, Phys. Rev. **D69** (2004) 074027, `arXiv:hep-ph/0311067 [hep-ph]`.

[112] R. Harlander, M. Kramer, and M. Schumacher, *Bottom-quark associated Higgs-boson production: reconciling the four- and five-flavour scheme approach*, `arXiv:1112.3478 [hep-ph]`.

[113] S. Heinemeyer, W. Hollik, and G. Weiglein, *FeynHiggs: A Program for the calculation of the masses of the neutral CP even Higgs bosons in the MSSM*, Comput. Phys. Commun. **124** (2000) 76–89, `arXiv:hep-ph/9812320 [hep-ph]`.

[114] LHC Higgs Cross Section Working Group Collaboration, J. R. Andersen et al., *Handbook of LHC Higgs Cross Sections: 3. Higgs Properties*, `arXiv:1307.1347 [hep-ph]`.

[115] E. Bagnaschi, F. Frensch, S. Heinemeyer, et al., *Benchmark scenarios for low* $\tan\beta$ *in the MSSM*, Tech. Rep. LHCHXSWG-2015-002, CERN, Geneva, Aug, 2015. `https://cds.cern.ch/record/2039911`.

[116] A. Djouadi, J. Kalinowski, and M. Spira, *HDECAY: A Program for Higgs boson decays in the standard model and its supersymmetric extension*, Comput. Phys. Commun. **108** (1998) 56–74, `arXiv:hep-ph/9704448 [hep-ph]`.

[117] R. Gavin, Y. Li, F. Petriello, and S. Quackenbush, *FEWZ 2.0: A code for hadronic Z production at next-to-next-to-leading order*, Comput. Phys. Commun. **182** (2011) 2388–2403, `arXiv:1011.3540 [hep-ph]`.

[118] T. Gleisberg et al., *Event generation with SHERPA 1.1*, JHEP **02** (2009) 007, `arXiv:0811.4622 [hep-ph]`.

[119] K. Melnikov and F. Petriello, *Electroweak gauge boson production at hadron colliders through O(alpha(s)**2)*, Phys. Rev. **D74** (2006) 114017, `arXiv:hep-ph/0609070 [hep-ph]`.

[120] S. Hoeche, F. Krauss, M. Schonherr, and F. Siegert, *QCD matrix elements + parton showers: The NLO case*, JHEP **04** (2013) 027, `arXiv:1207.5030 [hep-ph]`.

[121] P. Artoisenet, R. Frederix, O. Mattelaer, and R. Rietkerk, *Automatic spin-entangled decays of heavy resonances in Monte Carlo simulations*, JHEP **03** (2013) 015, `arXiv:1212.3460 [hep-ph]`.

[122] P. Z. Skands, *Tuning Monte Carlo Generators: The Perugia Tunes*, *Phys. Rev.* **D 82** (2010) 074018, `arXiv:1005.3457 [hep-ph]`.

[123] M. Czakon and A. Mitov, *Top++: a program for the calculation of the top-pair cross-section at hadron colliders*, Comput. Phys. Commun. **185** (2014) 2930, `arXiv:1112.5675 [hep-ph]`.

[124] Z. Czyczula, T. Przedzinski, and Z. Was, *TauSpinner Program for Studies on Spin Effect in tau Production at the LHC*, Eur.Phys.J. **C72** (2012) 1988, `arXiv:1201.0117 [hep-ph]`.

[125] A. Kaczmarska, J. Piatlicki, T. Przedzinski, E. Richter-Was, and Z. Was, *Application of TauSpinner for Studies on* τ*-Lepton Polarization and Spin Correlations in* Z, W *and* H *Decays at the LHC*, Acta Phys.Polon. **B45** no. 10, (2014) 1921–1946, `arXiv:1402.2068 [hep-ph]`.

[126] S. Banerjee, J. Kalinowski, W. Kotlarski, T. Przedzinski, and Z. Was, *Ascertaining the spin for new resonances decaying into tau+ tau- at Hadron Colliders*, Eur.Phys.J. **C73** no. 2, (2013) 2313, `arXiv:1212.2873 [hep-ph]`.

[127] P. Bechtle, A. Kastanas, W. Liebig, et al., *Search for strongly produced supersymmetry in 13 TeV pp collisions with tau-leptons, jets and missing transverse energy in the final state.*, Tech. Rep. ATL-COM-PHYS-2015-1126, CERN, Geneva, Sep, 2015. `https://cds.cern.ch/record/2050716`. support note for planned SUSY CONF or paper on 2015 LHC data.

[128] ATLAS Collaboration, *Improved luminosity determination in pp collisions at $\sqrt{s}$ = 7 TeV using the ATLAS detector at the LHC*, Eur.Phys.J. **C73** (2013) 2518, `arXiv:arXiv:hep-ex/1302.4393 [hep-ex]`.

[129] ATLAS Collaboration, "Calibration of the performance of b-tagging for c and light-flavour jets in the 2012 ATLAS data." ATLAS-CONF-2014-046, 2014.

[130] J. Butterworth, E. Dobson, U. Klein, et al., *Single Boson and Diboson Production Cross Sections in pp Collisions at sqrts=7 TeV*, Tech. Rep. ATL-COM-PHYS-2010-695, CERN, Geneva, Aug, 2010. `https://cds.cern.ch/record/1287902`.

[131] ATLAS Single Top Cross Section Twiki. `https://twiki.cern.ch/twiki/bin/view/LHCPhysics/SingleTopRefXsec#Predictions_at_7_8_13_and_14_TeV`.

[132] ATLAS Ttbar Cross Section Twiki. `https://twiki.cern.ch/twiki/bin/view/LHCPhysics/TtbarNNLO#Top_quark_pair_cross_sections_at`.

[133] G. Corcella et al., *HERWIG 6.5 release note*, 2002.

[134] S. Frixione and B. Webber, *The MC@NLO 3.2 event generator*, `arXiv:arXiv:hep-ph/0601192`.

[135] M. Bahr et al., *Herwig++ Physics and Manual*, Eur. Phys. J. **C58** (2008) 639–707, `arXiv:arXiv:hep-ph/0803.0883 [hep-ph]`.

[136] NNPDF Collaboration, R. D. Ball et al., *Parton distributions for the LHC Run II*, JHEP **04** (2015) 040, `arXiv:1410.8849 [hep-ph]`.

[137] A. D. Martin, W. J. Stirling, R. S. Thorne, and G. Watt, *Heavy-quark mass dependence in global PDF analyses and 3- and 4-flavour parton distributions*, Eur. Phys. J. **C70** (2010) 51–72, `arXiv:1007.2624 [hep-ph]`.

[138] G. Cowan, K. Cranmer, E. Gross, and O. Vitells, *Asymptotic formulae for likelihood-based tests of new physics*, Eur. Phys. J. **C71** (2011) 1554, `arXiv:1007.1727 [physics.data-an]`. [Erratum: Eur. Phys. J.C73,2501(2013)].

[139] A. L. Read, *Presentation of search results: The CL(s) technique*, J.Phys. **G28** (2002) 2693–2704.

[140] ATLAS Collaboration, G. Aad et al., *Constraints on new phenomena via Higgs boson couplings and invisible decays with the ATLAS detector*, JHEP **11** (2015) 206, `arXiv:1509.00672 [hep-ex]`.

[141] ATLAS Collaboration, *Search for Minimal Supersymmetric Standard Model Higgs Bosons H/A in the $\tau\tau$ final state in up to 13.3 fb^1 of pp collisions at $\sqrt{s}$= 13 TeV with the ATLAS Detector*, Tech. Rep. ATLAS-CONF-2016-085, CERN, Geneva, Aug, 2016. `https://cds.cern.ch/record/2206278`.